

# QUARK-GLUON PLASMA and HEAVY ION COLLISIONS



*A meeting held in the framework of the activities of*



*the Italian Working Group on Strong Interactions*

*Editors*

Wanda Maria Alberico, Marzia Nardi  
& Maria-Paola Lombardo

QUARK-GLUON PLASMA  
and  
HEAVY ION COLLISIONS

This page is intentionally left blank

# QUARK-GLUON PLASMA and HEAVY ION COLLISIONS

*A meeting held in the framework of the activities of*



*the Italian Working Group on Strong Interactions*

*Laboratori Nazionali di Frascati dell'INFN  
Frascati, Italy      14–18 January 2002*

*Editors*

Wanda Maria Alberico & Marzia Nardi  
University of Torino and INFN, Torino

Maria-Paola Lombardo  
INFN, Padova

*Published by*

World Scientific Publishing Co. Pte. Ltd.

P O Box 128, Farrer Road, Singapore 912805

*USA office:* Suite 1B, 1060 Main Street, River Edge, NJ 07661

*UK office:* 57 Shelton Street, Covent Garden, London WC2H 9HE

**British Library Cataloguing-in-Publication Data**

A catalogue record for this book is available from the British Library.

**QUARK-GLUON PLASMA AND HEAVY ION COLLISIONS**

Copyright © 2002 by World Scientific Publishing Co. Pte. Ltd.

*All rights reserved. This book, or parts thereof, may not be reproduced in any form or by any means, electronic or mechanical, including photocopying, recording or any information storage and retrieval system now known or to be invented, without written permission from the Publisher.*

For photocopying of material in this volume, please pay a copying fee through the Copyright Clearance Center, Inc., 222 Rosewood Drive, Danvers, MA 01923, USA. In this case permission to photocopy is not required from the publisher.

ISBN 981-238-174-0

This book is printed on acid-free paper.

Printed in Singapore by Mainland Press

## CONTENTS

<i>Preface</i>	ix
Quark liberation	
<i>N. Cabibbo</i>	1
Physics perspectives of the ALICE experiment at the large hadron collider	
<i>L. Riccati and M. Masera</i>	4
Hard probes of matter in QCD	
<i>H. Satz</i>	19
<b>Phenomenology of heavy ion collisions and observables</b>	<b>29</b>
Heavy ion collision phenomenology I: soft observables	
<i>F. Becattini</i>	31
Heavy ion collision phenomenology II: hard probes	
<i>M. Nardi</i>	47
<b><i>Topical talks</i></b>	
Non-conventional statistical effects in relativistic heavy-ion collisions	
<i>W.M. Alberico, A. Lavagno and P. Quarati</i>	59
Strangeness production in a constituent quark model	
<i>F. Becattini and G. Pettini</i>	65
Double parton collisions in $NN$ and $NA$ interactions	
<i>A. Del Fabbro and D. Treleani</i>	71
Sequential charmonium suppression	
<i>S. Fortunato</i>	77

Inclusive distributions and collective phenomena in heavy ion collisions <i>R. Ugoccioni</i>	84
<b>Many-body theories and the nuclear equation of state</b>	<b>91</b>
Randomness in nuclei and in the quark-gluon plasma <i>A. De Pace and A. Molinari</i>	93
Quantum Monte Carlo and nuclear astrophysics <i>S. Fantoni, A. Sarsa and K. Schmidt</i>	117
Is the equation of state of strongly interacting matter observable? <i>O. Benhar</i>	136
Isospin effects at finite baryon density <i>M. Di Toro, M. Colonna, V. Greco and F. Matera</i>	152
Semiclassical description of the quark-gluon plasma <i>S. Terranova, A. Bonasera, M. Colonna and T. Maruyama</i>	170
<b>Topical talks</b>	
The relevance of the deconfined phase for the mass of neutron stars <i>M. Baldo</i>	179
Mixed quark-hadron phase in neutron-rich matter <i>A. Drago and A. Lavagno</i>	186
Spin-polarized states of nuclear matter <i>W. Zuo, U. Lombardo and C.W. Shen</i>	192
<b>The QCD phase diagram</b>	<b>199</b>
An introduction to QCD at non-zero temperature and density <i>M.-P. Lombardo</i>	201

Effective fields in dense quantum chromodynamics <i>G. Nardulli</i>	216
Aspects of the quantum chromodynamics phase diagram <i>F. Sannino</i>	233
The $U(1)$ axial symmetry and the chiral transition in QCD <i>E. Meggiolaro</i>	249
Mechanisms of confinement <i>L. Del Debbio</i>	259
<b><i>Topical talks</i></b>	
Vector spectrum and color screening in two-color QCD at non-zero $T$ and $\mu$ <i>B. Allés, M. D'Elia, M.-P. Lombardo and M. Pepe</i>	271
Study of confinement using the Schröedinger functional <i>P. Cea and L. Cosmai</i>	280
Imaginary chemical potential in QCD at finite temperature <i>M. D'Elia and M.-P. Lombardo</i>	286
Effective description of the LOFF phase of QCD <i>M. Mannarelli</i>	294
Deconfinement transition and high temperature phase in lattice gauge theories <i>A. Papa</i>	300
Vector condensation at large chemical potential <i>F. Sannino and W. Schäfer</i>	308

This page is intentionally left blank

## PREFACE

In recent years many efforts have been devoted to the search for the Quark Gluon Plasma, a new, deconfined phase of hadronic matter, through ultra-relativistic heavy ion collisions. In 1986 the Alternate Gradient Synchrotron in Brookhaven started accelerating nuclei, thus beginning the Era of high energy nucleus-nucleus collisions. Since then, many experiments developed, with increasing luminosity and energy of the ion beams: the Large Hadron Collider, expected to be completed by 2007 at CERN will allow to study Pb-Pb collisions at  $\sqrt{s} \sim 5.5$  TeV/nucleon.

Ultra-relativistic heavy ion collisions offer a unique possibility to investigate nuclear matter under extreme conditions of temperature and density in laboratory. This issue poses an extraordinary challenge to theoretical physicists as well, both in the field theory approaches and in the phenomenological analysis of the observables.

Within this framework, the Meeting “Quark Gluon Plasma and Heavy Ion Collisions”, held in Frascati (Italy) in January 2002, has been conceived to bring together the most recent expertise on the behaviour of strong interacting systems in various thermo-dynamical conditions : topics included field theoretic approaches to the QCD phase diagram, many-body techniques and applications, dynamics of phase transitions and phenomenological analysis of relativistic heavy ion collisions, offering a few examples of how the seeds of the deconfined state are looked for in relativistic heavy ion collisions.

A common basis for future work was offered by several pedagogical talks, appropriately complemented by topical seminars on the most recent developments. This material is collected here, with the purpose and hope that the book will represent a useful tool both as a textbook, suitable for beginners in the field, as well as a reference source for experienced researchers.

We choose to arrange the material into three chapters, corresponding to the main research fields and perspectives from which the Quark Gluon Plasma can be investigated, the distinction among them being mostly methodological:

1. Phenomenology of heavy ion collisions and observables.
2. Many body theories and nuclear physics perspectives.
3. Field theoretic approaches.

A short introduction given at the beginning of each chapter offers a quick overview of the scientific contents, and (tries to) put it in the general perspective of the book. Once more, there is no pretense of being exhaustive:

the various themes are widely developed in textbooks and Proceedings of topical Conferences. We emphasize that our focus is on interdisciplinarity and complementarity.

Finally we wish to thank all participants and contributors, who shared our efforts in realizing this volume, our colleagues in the Organizing Committee, O. Benhar, G. Pancheri, F. Palumbo and S. Petrarca, and the Conveners of the three working sessions, F. Becattini, A. Bonasera, A. Fabrocini, A. Papa and F. Sannino. We also express our acknowledgments to the Secretaries, Angela Mantella, Concetta Nuncibello and Roberta Soldatelli, the INFN for financial support of the Meeting through funds of the IV National Committee, the National Laboratory of INFN in Frascati, which hosted the Meeting with precious logistic and staff support, the MURST research funds of COFIN, contract N. 2001024324-007, for partial support of publication charges.

W.M. Alberico, M.P. Lombardo, M. Nardi

## QUARK LIBERATION

NICOLA CABIBBO

*University of Rome - La Sapienza  
and INFN, Sezione di Roma*

The experiments with colliding beams of relativistic ions make it possible to explore the behaviour of nuclear matter at extreme densities, and at the same time extreme energy density and temperature. We are now at a particularly exciting time with two new high energy colliders, RHIC at Brookhaven, which is entirely dedicated to relativistic ion collisions, and in a few years, LHC at CERN, which will devote part of its running time to relativistic ion collisions.

I have not been active in the field for very many years, but I probably started it with a paper I wrote with Giorgio Parisi in 1975<sup>1</sup>, entitled: "Exponential Hadronic Spectrum and Quark Liberation". To my knowledge this was the first proposal of the existence, within quark models, of different phases of hadronic matter. The low temperature – low baryon density phase is the familiar one, where quarks are confined within hadrons. In high temperature or high baryon number phases quarks would not be confined, and could freely move in space. A phase of this kind is now called a quark-gluon plasma phase. In 1975 we argued for the existence of one such phase, but we have now well-founded arguments which point to the existence of more than one high density phase, and this will indeed be one of the themes of this meeting, with a working group devoted to the phase diagram of quark-gluon matter.

A few years after, at the beginning of the APE project, with Giorgio, Maria Paola Lombardo, and other members of the APE group, we engaged in the early lattice simulations of high temperature gluon phases, a line of work which gave interesting results over the years, and remains today the only known method to study high-temperature QCD from first principles. This was my last meeting with quark-gluon plasmas. I will use this opportunity to say a few words about the 1975 paper, referring to it for more details.

The main point of ref. <sup>1</sup> was that an exponential spectrum of hadronic states, i.e a level density

$$w(E) \propto \exp(\beta_C E) \tag{1}$$

implies that the temperature  $T_C = 1/K\beta_C$  is either a limiting temperature, as proposed by Hagedorn<sup>2</sup>, or the critical temperature for a phase transition.

The free energy density can be expressed in terms of  $w(E)$  as

$$F(\beta) = \int dE w(E) \exp(-\beta E) \quad (2)$$

It is clear that the exponential spectrum of eq. (1) leads to a singularity of  $F(\beta)$  at  $\beta = \beta_C$ . Which kind of singularity depends on the leading behaviour of  $w(E)$  as  $E \rightarrow \infty$ . If we assume that

$$w(E) \rightarrow E^{\alpha-3} \exp(\beta_C E) \quad (E \rightarrow \infty) \quad (3)$$

we find a free energy density which behaves in the vicinity of the critical temperature as

$$F(\beta) = A(\beta - \beta_C)^{2-\alpha} \quad (4)$$

and a density of internal energy

$$U(\beta) = \frac{d}{d\beta} F(\beta) = (2 - \alpha) A(\beta - \beta_C)^{1-\alpha} \quad (5)$$

We then see that for  $\alpha < 1$ ,  $U(\beta)$  reaches a finite limit for  $T \rightarrow T_C$ , and the singularity must be interpreted as a phase transition, while for  $\alpha > 1$  the energy density diverges as  $T \rightarrow T_C$  and  $T_C$  represents a true limiting temperature.

As shown in ref. <sup>1</sup> the behaviour in eq. (3) is the one suggested by R. Hagedorn's bootstrap condition. In his original paper on hadron thermodynamics <sup>2</sup> Hagedorn had found eq. (3) with  $\alpha = 2$ , and had thus been led to propose the existence of a limiting temperature for hadronic matter.

In our paper we argued that in quark models where hadrons have a finite volume one would expect a phase transition rather than a limiting temperature. This is for example clear in the MIT bag model where hadrons are bubbles of space (bags) in the interior of which quarks can move freely. The Bag model has an exponential spectrum, and the volume of hadrons results proportional to the mass. We have shown that the bag model offers a model of the quark liberation phase transition which is closely parallel to Fischer's droplet model of the gas-liquid transition. Alternatively we argued that since confinement is associated with a broken symmetry (the chiral symmetry), one would expect the existence on an high energy phase where the symmetry is restored, and the quarks deconfined.

The existence of a quark liberation transition requires an exponential hadron spectrum as in eq. (3), and the indications collected in this direction by Hagedorn and his collaborators could in 1975 be interpreted as evidence for the existence of such a phase transition. Only today we are seeing the first

manifestations of what could become a more direct test of these ideas, and this is the subject of this meeting.

### **References**

1. N. Cabibbo and G. Parisi, Phys Lett. B, **59**, 67 (1975).
2. R. Hagedorn, Nuovo Cimento Suppl. , **3**, 147 (1965).

# PHYSICS PERSPECTIVES OF THE ALICE EXPERIMENT AT THE LARGE HADRON COLLIDER

L. RICCATI

*I.N.F.N., Via Pietro Giuria 1, I-10125 Torino, Italy*

*E-mail: riccati@to.infn.it*

M. MASERA

*Dipartimento di Fisica Sperimentale dell'Università and I.N.F.N.*

*Via Pietro Giuria 1, I-10125 Torino, Italy E-mail: masera@to.infn.it*

The Large Hadron Collider (LHC) under construction at CERN will deliver ion beams up to centre of mass energies of the order of 5.5  $TeV$  per nucleon, in case of lead. If compared to the available facilities for the study of nucleus–nucleus collisions (SpS and RHIC), this represents a huge step forward in terms of both volume and energy density that can be attained in nuclear interactions. ALICE (A Large Ion Collider Experiment) is the only detector specifically designed for the physics of nuclear collisions at LHC, even though it can also study high cross section processes occurring in proton–proton collisions. The main goal of the experiment is to observe and study the phase transition from hadronic matter to deconfined partonic matter (Quark Gluon Plasma — QGP). ALICE is conceived as a general-purpose detector and will address most of the phenomena related to the QGP formation at LHC energies: to this purpose, a large fraction of the hadrons, leptons and photons produced in each interaction will be measured and identified.

## 1 Introduction

Ultrarelativistic heavy-ion collisions have been studied for fifteen years with a rich experimental programme both at the AGS (Brookhaven National Laboratories) and at the SPS (CERN). It turned out that in these collisions very high energy densities can be reached and there are experimental evidences that in Pb-Pb collisions at the SPS a new state of matter in which quarks and gluons are deconfined was formed<sup>1</sup>. The Relativistic Heavy Ion Collider (RHIC) at BNL began its activity in 2000 opening a new horizon for studying nucleus-nucleus interactions. The centre of mass energy ( $\sqrt{s} = 200\text{ GeV}$  per nucleon) is one order of magnitude higher than what can be achieved at the SPS hence the temperature reached in the collision should well exceed the critical value for the phase transition to the QGP. The amount of available experimental results from RHIC is already impressive<sup>2</sup>. The next step towards really high energies will be made by the Large Hadron Collider (LHC) that will be ready for physics in the year 2006. The available centre of mass energy will be 5.5  $TeV$  per nucleon with Pb beams, 27.5 times higher if com-

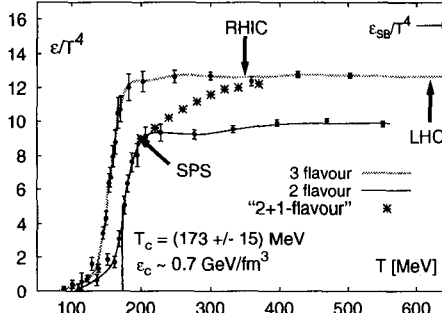


Figure 1. Lattice QCD phase transition (F.Karsch in [11])

pared to RHIC. The ALICE (A Large Ion Collider Experiment) experiment is focused on heavy-ion physics at the LHC, even though it is able to address relevant high cross section p-p phenomena<sup>3</sup>. Its physics perspectives, as far as nucleus-nucleus interactions are concerned, will be presented in this paper.

## 2 A Heavy-Ion experiment at the LHC: why?

Some of the parameters characterizing a nucleus-nucleus collision for SPS, RHIC and LHC are listed in Table 1 (adapted from<sup>5</sup>) which has to be considered as an order-of-magnitude comparison tool. The extrapolation from SPS to RHIC was far from being obvious; for instance many predictions for particle multiplicity have been done starting from several models with different assumptions on the QCD dynamics leading to results spanning over a rather wide range ( $600 < dN_{ch}/d\eta < 1500$ ) of values with a general tendency to overestimate the multiplicity actually observed at RHIC<sup>4</sup>. Even though the data from RHIC are useful to tune and possibly rule out models, they do not reduce too much the uncertainties on the predictions for multiplicity at LHC, which vary from slightly below 2000 up to 8000 charged particles per unit of rapidity. The particle production in nucleus-nucleus collisions scales with the number of the participants at SPS energies, where soft processes dominate. The role of hard processes, which are dependent on the number of collisions ( $N_{coll} \propto A^{4/3}$ ) also increases with increasing  $\sqrt{s}$  and it is expected to be dominant at LHC. Another factor that contributes to enhance the multiplicity at high energy is related to the fact that the structure functions increase steeply with decreasing  $x_{BJ}$ . This leads to an enhanced number of partons taking part in the interaction. The effect of this increase in the number of

Table 1. Comparison of parameters characterising A–A collisions. See text for details.

Parameters for central A–A collisions	SPS	RHIC	LHC
$\sqrt{s}/A$ (GeV)	17	200	5500
$dN_{ch}/d\eta$	400	650	$2 \div 8 \cdot 10^3$
$\epsilon$ (GeV/fm $^3$ )	2.9	25	200
$V_f$ (fm $^3$ )	few 10 $^3$	few 10 $^4$	few 10 $^5$
$\tau_{QGP}$ (fm/c)	< 2	2 $\div$ 4	$\geq 10$
$\tau_0^{QGP}$ (fm/c)	1	0.2	0.1

partons is somewhat reduced by the shadowing. It should be noted that at LHC, for moderate  $Q^2 \sim 10$  GeV $^2$ , we will reach  $x_{BJ}$  values in the range of  $5 \cdot 10^{-4}$  in the central region and down to almost  $10^{-5}$  in the forward region (ALICE muon spectrometer), where shadowing effects are strong. Moreover, phenomena like parton saturation and jet quenching should be particularly relevant at the LHC. The uncertainties on these processes do not allow to make a reliable evaluation of the multiplicities. The value  $dN_{ch}/d\eta = 8000$  is therefore used in the simulations for ALICE as an upper limit at which the detector must still be functional.

The thermalization time ( $\tau_0^{QGP}$ ) decreases with increasing  $\sqrt{s}$  essentially for two reasons. On one hand the formation time of partons is inversely proportional to the transverse momentum which, in turn, increases slowly with  $\sqrt{s}$  and on the other hand higher parton densities (mainly gluons at LHC) lead to a higher interaction rate. As a consequence the temperature and the energy density are expected to be very high at LHC. In Fig. 1 the temperature dependence of  $\epsilon$  as computed in lattice QCD is shown under different assumptions: two and three light quarks and two light quarks plus one heavier quark (s). In Fig. 1 the expected behaviour is indicated by the stars: at temperatures  $T \simeq T_c = 173 \pm 15$  MeV, the quark s does not contribute to the thermodynamics due to its mass whereas at high temperature the energy density is essentially given by 3-light flavour QCD. At the LHC, the colliding system is expected to be well within the plateau at  $T \sim 3T_c$  with a vanishing baryochemical potential at  $y \sim 0$ . In this regime of  $\mu_B \ll T$  the equation of state approaches the better understood case of  $\mu_B = 0$ . The ideal limit of a Stefan–Boltzmann gas of quarks and gluons is not reached even at the highest temperatures indicating that non perturbative effects are still relevant. The high temperature reached at LHC extends also the lifetime and the volume of the formed QGP since it has to expand while cooling down to the freeze-

out temperature, which is independent of the energy of the collision. Longer lifetime and volume imply that signals coming from the plasma phase should be strongly enhanced at LHC.

At LHC energies, perturbative QCD can be applied: hard processes with high momentum transfers are already significant at RHIC and will be dominant at LHC. The hard signals, namely heavy flavours and high  $p_T$  jets, are created at early times and probe the medium formed after the collision. The

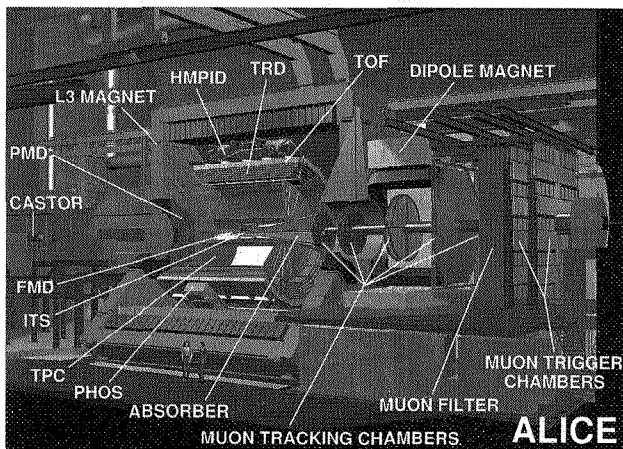


Figure 2. The ALICE experimental apparatus

study of charmonium states, initiated at the SPS, will be extended at LHC to the  $\Upsilon$  family since the production cross section will be sufficiently high and the melting point expected for these resonances will be exceeded at the LHC. A direct measurement of open charm will be feasible after indirect hints of its possible enhancement already at SPS energy. The open charm detection will provide also a normalization for the  $J/\Psi$ . Finally, the relative abundance analysis of hadrons via particle ratios will be extended to charmed particles. The energy loss of high  $p_T$  partons can be studied via jet measurements: the expected *jet quenching* due to this phenomenon is in fact a probe that can be fully exploited at LHC energies. The possibility of measuring several observables on a event-by-event basis increases with the number of produced particles so at LHC the event-by-event physics will be a precision tool suitable for searches of non statistical fluctuations which are expected to occur at the phase transition.

### 3 The ALICE experiment

ALICE is the only experiment at LHC especially conceived to study the physics of strongly interacting matter and the QGP. For this reason it has to cover as much observables as possible. It is operated by an international collaboration formed by more than 900 physicists from 77 institutions of 28 different countries. Few weeks per year ( $\sim 10^6$  s) will be devoted to nucleus-nucleus physics at a luminosity that is limited to  $\mathcal{L} = 10^{27} \text{ cm}^{-2} \text{s}^{-1}$  for Pb-Pb. With a  $\sigma_I = 8 b$ , the expected number of interactions per second is  $\sim 8000$  ( $\sim 10\%$  being central).

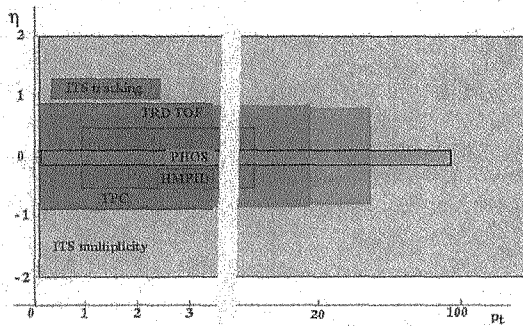


Figure 3. ALICE central barrel detectors: acceptances

#### 3.1 Observables

The ALICE physics goals can be summarized, albeit not exhaustively, as follows:

- *Global event features.* Multiplicities, very forward energy flow (0 degree) and rapidity distributions allow to determine the centrality, the number of participants in the interaction and to specify the initial energy density.
- *The geometry and space-time evolution of the emitting source.* The space-time structure of the collision fireball will be studied with two-particle momentum correlations.
- *Degrees of freedom* as a function of temperature. Quantities related to the dynamical evolution of the hadronic phase like  $p_T$  spectra and particle

ratios of identified hadrons ( $\pi, \eta, \omega, \phi, p, K, \Lambda, \Xi, \Omega$ ) and direct photons will be measured.

- *Non statistical fluctuations and critical behaviour.* This topic will be addressed by event-by-event analyses, including some spectra and particle ratios. Distortions of  $N_\gamma - N_{\text{charged}}$  correlations will be suitable for the detection of Disoriented Chiral Condensates (DCC). Searches for anomalies like the *Centauro* events will be also performed.
- *Chiral symmetry restoration.* It will be searched through the study of the resonance decays.
- *Collective effects:* elliptic and directed flow will be investigated by various sub detectors.
- *Hard probes.* Open charm and beauty, high  $p_T$  spectra, jets and jet quenching will be measured. Spectroscopy of the  $J/\Psi$  and  $\Upsilon$  families will provide a tool particularly sensitive to deconfinement.

These physics goals imply a good particle identification capability of both hadrons and leptons over a wide acceptance and an extended  $p_T$  domain. As a difference from the other LHC experiments, the sensitivity to low  $p_T$  particles is relevant for many of the physics issues addressed by ALICE. Therefore the main experimental challenge consists in tracking and identify virtually all the produced stable particles in an environment in which these particles could be as many as 8000 per unit of rapidity.

### 3.2 The experimental apparatus

The experimental layout is represented in Fig. 2. The relatively low interaction rate expected with nuclear beams together with the high particle density lead to a solution based on a Time Projection Chamber (TPC) used for tracking in the central rapidity region. This detector, which is able to sustain the foreseen rate has a high granularity over a wide region. It extends longitudinally from  $-2.5\text{ m}$  to  $2.5\text{ m}$  and radially from  $90\text{ cm}$  up to  $250\text{ cm}$  in order to have a  $dE/dx$  resolution  $< 10\%$  for electron identification. The design and the choice of the gas are optimised for a good double-track resolution. The total number of channels is  $5.7 \cdot 10^6$  feeding the DAQ with an amount of information of  $\sim 60\text{ MB}$  for a central event, corresponding to 12000 tracks. The pseudorapidity coverage (see Fig. 3) of the TPC and the other detectors of the central barrel is  $|\eta| < 0.9$ , which is adequate for studying particle ratios,  $p_T$  spectra and HBT correlations.

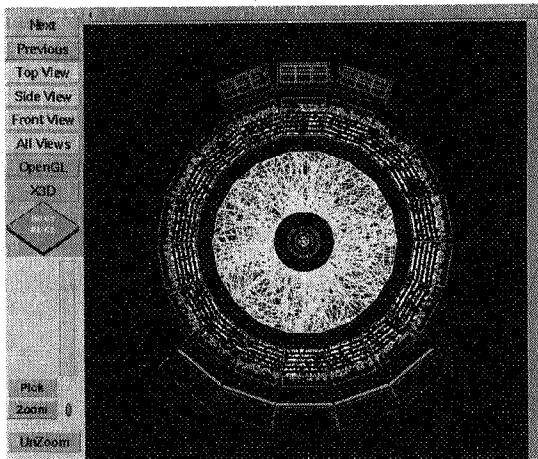


Figure 4. AliRoot event display. Particles are generated with a polar angle  $\theta$  in the range  $85 < \theta < 95$  with a density corresponding to the maximum foreseen value. Starting from the beam axis, ITS, TPC, TRD and TOF are displayed. PHOS and HMPID are below and above the beam axis respectively

The magnetic field necessary for momentum measurements is provided by the magnet of the L3 experiment: it generates a weak solenoidal field ( $B < 0.5\text{ T}$ ) over the whole region of the barrel. This choice allows a low momentum cut-off ( $\sim 100\text{ MeV}/c$ ) and, at the same time, a good tracking efficiency and momentum resolution.

The six layers of silicon detectors forming the Inner Tracking System (ITS) are used for track reconstruction close to the vertex. The innermost layer is located at a radius  $r = 4\text{ cm}$ , only  $1\text{ cm}$  from the beam pipe, while the sixth layer is located at  $r = 44\text{ cm}$ . The main goal of the ITS is to reconstruct secondary vertices from hyperons,  $K_0^S$  and charmed mesons decays, hence the vertexing resolution must be  $< 100\text{ }\mu\text{m}$ . This constraint, together with the high track density, led to the choice of detectors that provide a bidimensional information such as silicon pixels in the first two layers and silicon drift detector for the third and fourth layers. The last two layers, due to the relatively large surface to be equipped, employ double sided silicon strip detectors. The ITS is also needed for low momentum particle identification through  $dE/dx$  measurements in layers 3 to 6 and to improve the momentum resolution at large momenta.

As it is illustrated in Fig. 3, the particle identification (PID) is performed

by using several detectors exploiting all methods available to this purpose, since PID is one of the key issues of this experiment. A Time Of Flight (TOF) detector, located in the barrel at  $3.7\text{ m}$  from the beam axis, identifies  $\pi^\pm$ ,  $K^\pm$ , protons and contributes to  $e/\pi$  rejection. The TOF is made with multi-gap

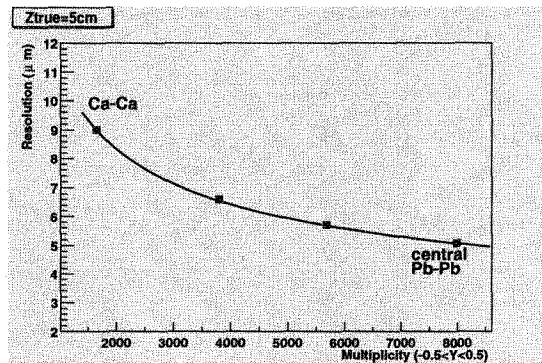


Figure 5. Resolution on the primary vertex Z coordinate as a function of the multiplicity in the central unit of rapidity. The full line is a fit with the function  $\sigma_z = B + A/\sqrt{dN_{ch}/d\eta}$  with  $A = 292$  and  $B = 1.8$

resistive plate chambers with an intrinsic time resolution  $< 100\text{ ps}$ . The extension of the hadron identification into the semi-hard region (good  $p, K$  separation for  $p_T < 5\text{ GeV}/c$ ) is achieved, with a reduced acceptance, by means of a proximity focusing RICH detector (HMPID) located at  $\sim 4.5\text{ m}$  from the beam axis. The electron identification in the barrel is complemented at high  $p_T$  ( $p_T > 1\text{ GeV}/c$ ) by a dedicated Transition Radiation Detector (TRD) consisting of six layers of radiator foil stacks followed by Time Expansion Chambers, providing a  $\pi$  rejection  $> 50$  at the maximum occupancy. As a fast response detector, it can be used for triggering on high momentum electrons ( $p > 3\text{ GeV}/c$ ).

Detection of direct photons and of neutral mesons ( $p_T > 1\text{ GeV}/c$ ) like  $\pi^0$  and  $\eta$  through their  $2\gamma$  decay mode is achieved with a single arm, high resolution electromagnetic calorimeter (PHOS) placed  $4.6\text{ m}$  from the vertex. The detector is made by 17920 crystals of  $PbWO_4$  scintillator grouped in 5 modules. The choice of this material is due to the requirement of a Molière radius as small as possible, together with a good light output.

The muon channel will be studied by a dedicated forward muon spectrometer in the pseudorapidity range  $2.4 < \eta < 4$ . It consists of a hadronic absorber  $\simeq 10\lambda_f$  thick starting close to the interaction region in order to re-

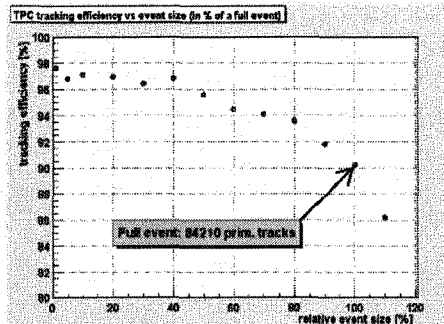


Figure 6. Tracking efficiency in the TPC as a function of the size of the event.

duce the combinatorial background from  $\pi^\pm$  and  $K^\pm$  decays. The absorber, which is composite, is designed in order to minimize both the multiple scattering and the leakage. Muons are then tracked in a  $0.7\text{ }T$  dipole magnet (for an overall  $3\text{ }Tm$ ) by means of 10 Cathode Pad Chambers. A second absorber, placed at the end of the spectrometer, followed by four planes of Resistive Plate Chambers is used for muon identification and triggering. The main goal of the spectrometer is the study of the charmonium and bottomonium states. A mass resolution of  $100\text{ MeV}/c^2$  at the  $\Upsilon$  mass is required for this purpose<sup>6</sup>.

The apparatus is complemented by several smaller detecting systems placed at forward rapidities: the impact parameter of the collision is measured by a set of 4 small calorimeters to be installed in the machine tunnel at both sides of the interaction region at a distance of  $\sim 100\text{ m}$ . Electromagnetic and transverse energy at high rapidity ( $5.3 < \eta < 7.3$ ) are measured by the CASTOR calorimeter. The pseudorapidity distribution of charged particles will be determined by the Forward Multiplicity Detector for  $-5.1 < \eta < -1.7$  and  $1.7 < \eta < 3.4$ . Searches for non statistical fluctuations in the ratio of photons and charged particles, the study of collective flow and the determination of the interaction plane will be carried out by the Photon Multiplicity Detector (PMD)<sup>7</sup>. Finally, the time of the event will be measured by the T0 and V0 detectors. A complete description of the current status of the apparatus can be found in<sup>8</sup>.

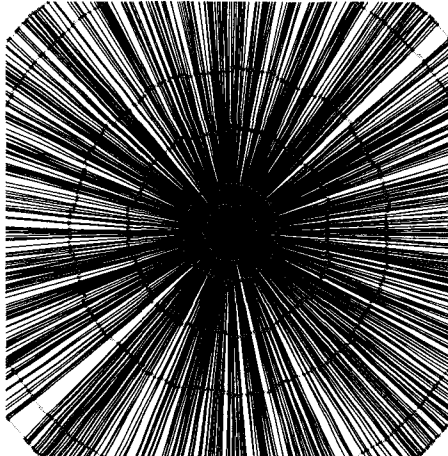


Figure 7. Reconstructed tracks in ITS ( $p_T > 1 \text{ GeV}/c$ )

### 3.3 Expected performances

The evaluation of the physics performances of ALICE is a process that began with the preparation of the Technical Proposal<sup>9</sup> of the experiment, continued with the Technical Design Reports<sup>10</sup> of the single subsystems and it is the goal of a dedicated report (PPR) that is in preparation now<sup>11</sup>. The most recent summaries can be found in <sup>12</sup> for hadronic signals and in <sup>13</sup> for heavy quark measurements. The development of the offline framework necessary for the PPR represents a major challenge for the Collaboration, given the complexity of the apparatus and the large amount of information involved. Since 1998 a new Object Oriented framework, AliRoot<sup>14</sup> is being developed starting from ROOT<sup>15</sup>, which is a C++ package written for high energy physics. AliRoot provides an interface with event generators like Pythia<sup>16</sup> and Hijing<sup>17</sup>, with simulation programs like GEANT3, FLUKA and GEANT4. Relic Fortran code is wrapped in C++ user interfaces, so all new code has been written in C++. Reconstruction and analysis phases are also done in the AliRoot environment. This package, which is in continuous evolution, has been already used for most of the simulations needed for the Technical Design Reports. A large scale simulation, spread over several computing centres around the world started in October 2001 for the preparation of the PPR<sup>11</sup>.

In Fig. 4, a  $10^\circ$  polar slice of a central Pb–Pb event is displayed: it is clear that tracking in the central barrel is the real challenge for ALICE, since

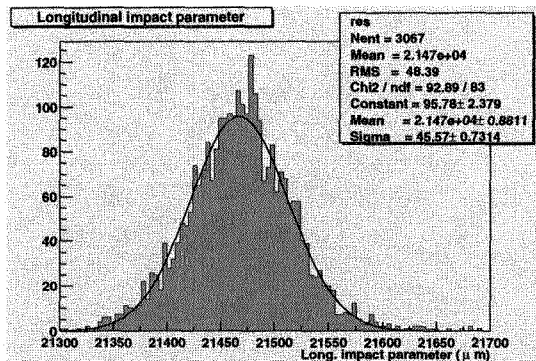


Figure 8. Distribution of the  $Z$  coordinate of the reconstructed tracks, extrapolated to the primary vertex

most of the physical observables addressed by this experiment depend on the tracking capabilities of the apparatus.

The status of tracking in the barrel will be reported here; the reader is referred to the papers mentioned above for a complete report.

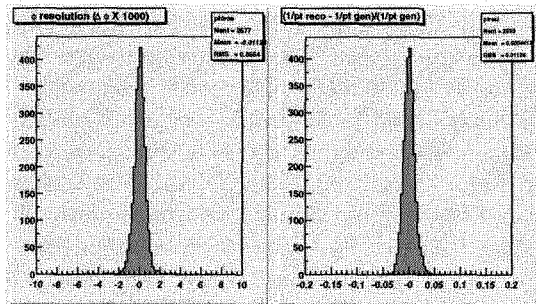


Figure 9. Resolutions in azimuth and  $p_T$  for tracking in TPC+ITS

A tracking efficiency of the order of 90% for particles with transverse momenta greater than  $100 - 150 \text{ MeV}/c$  and a momentum resolution  $\delta p/p \sim 1 - 2\%$  are the design requirements for the reconstruction in the TPC and the ITS. The method now implemented in AliRoot is based on the Kalman filter<sup>18</sup>: it has the advantage of being a track finding and a track fitting method at the same time. Furthermore, there is no need of having a track model and there

is no need of manipulating all the measured points belonging to the same track together, since the Kalman filter is a local tracking method. Incorrect space points, due to noise or to failures of the cluster finding algorithms can be rejected during the track finding without using an additional track fitting pass, which would be needed with global tracking approaches. Each track is represented at a given point by 5 numbers and the size of the covariance matrix to be handled is  $5 \times 5$  in contrast to what happens with a global method in which matrices of the size of the number of measured points must be inverted during fit. Stochastic effects are naturally taken into account in the filtering process and the propagation of tracks from a subdetector to another is relatively easy. The price to pay is that this technique cannot be used with raw data, so a cluster finding algorithm must be applied in advance and this is not generally an easy task. For instance in the inner sectors of the TPC, the occupancy is  $\sim 40\%$  and some clusters may be lost or displaced. Moreover, the track finding has to be initiated with track segments which have to be preliminarily determined. This operation is called *seeding*. In ALICE, the track seeding can be performed by combining the clusters on two predetermined pad rows of the TPC so the reconstruction in the entire barrel starts from this detector.

To this purpose the vertex position in the interaction region must be known, even though the vertex constraint for seeding is not applied strictly in order to be able to reconstruct also secondary particles. As illustrated in Fig. 5 the position of the primary vertex can be measured with very good accuracy by means of the first two high granularity layers of the ITS: the algorithm is very simple and makes use of the correlation among silicon pixels belonging to the two different layers. The higher is the multiplicity the better is the accuracy. The resolution in the  $r - \varphi$  plane is of the order of  $25 \mu m$ . The resolution is more than adequate for the tracking procedures and this technique can still be applied in the case of p-p events, where the resolution is  $\sim 150 \mu m$ . The tracking efficiency in the TPC is shown in Fig. 6 as a function of the generated particle multiplicity. The efficiency is computed with respect to the number of particles which produce a sufficient number of clusters in the TPC (*trackable* particles). A relative event size of 100% corresponds to a central multiplicity density of 8000 charged particles. In this case the overall number of particles is more than 80000 and the efficiency is still 90%. The reconstruction in the ITS is carried out starting from the tracks actually found in the TPC. The method adopted in the ITS is not purely local, since a vertex constraint is applied in order to cope with the track density. A track is found when there is a matching on all the 6 layers of the ITS. In Fig. 7, reconstructed tracks in the ITS with a transverse momentum higher than  $1 GeV/c$  are displayed:

the first five silicon layers are clearly visible. In Fig. 8, the distribution of the coordinate along the beam axis of the reconstructed vertex after tracking in the TPC+ITS is shown. The distribution width is  $\sim 50 \mu m$ . With this resolution, the detection of secondary vertices is possible, also in cases in which the  $c\tau \simeq 120 \mu m$  as for  $D^0 \rightarrow K^- \pi^+$ . This decay channel of  $D^0$  meson is actually the most promising one to study hadronic charm production in ALICE<sup>13</sup>. In Fig. 9 both the resolution in azimuth and  $p_T$  for a central Pb-Pb event are shown. With a magnetic field  $B = 0.4 T$  the  $p_T$  and  $\varphi$  resolutions are  $\sim 1\%$  and  $\sim 0.5 mrad$  respectively. These are very preliminary evaluations that must be reassessed by using the large amount of simulated data now available. In Fig. 10 reconstructed  $p_T$  spectra are shown. The event

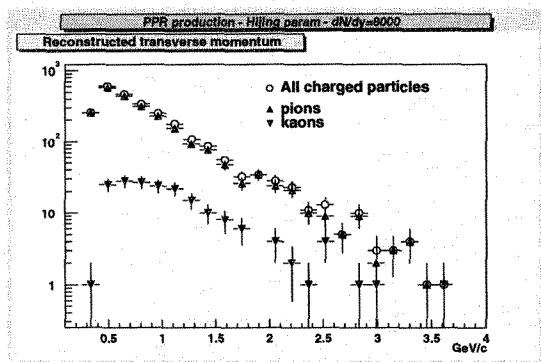


Figure 10. Reconstructed  $p_T$  in ITS+TPC. The event has been generated with a Hijing parametrization with  $dN_{ch}/d\eta = 8000$

generator used is a parametrization of Hijing and only  $K$  and  $\pi$  were actually generated. When comparing reconstructed spectra with generated ones, it turns out that the reconstruction does not introduce distortions. The tracks obtained in TPC+ITS are then backpropagated to the outer barrel detectors. For instance, in Fig. 11 the invariant mass spectrum of dielectron pairs from  $T$  decay is plotted. The invariant mass has been obtained in the TRD after a complete tracking in the barrel and the application of a trigger momentum cutoff.

The good tracking performance in the barrel is necessary also for studying jets in ALICE. Usually jets are reconstructed by means of electromagnetic and hadronic calorimeters, but in ALICE there are no hadronic calorimeters and the acceptance of PHOS is limited. Since particles with  $p_T$  up to  $\sim 40 GeV$  can be measured with good resolution, jets can be found by looking for the

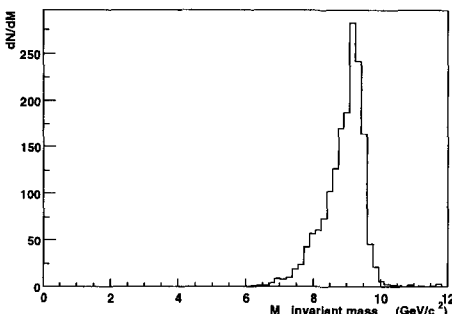


Figure 11. Invariant mass  $e^+e^-$  distribution in case of  $\Upsilon \rightarrow e^+e^-$

leading particle. A jet finding procedure with leading particles is presently under test. Reconstructed particles in the TPC with  $p_T > 4\text{ GeV}/c$  are used as a seed for jet finding. All the particles with  $p_T > 2\text{ GeV}/c$  belonging to a cone of width  $\Delta R = \sqrt{\Delta\varphi^2 + \Delta\eta^2} < \Delta R_0$  centered on the “seed” particle are associated to the jet ( $\Delta R_0 = 0.7$  in the present tests). The momentum vectors of the found particles are summed up. This procedure is repeated iteratively till no more seeds are left. The first results are good and a trigger for high  $p_T$  jets based on the TRD is under study. Another possibility of studying jets in ALICE is to use the PHOS to tag jets originating from  $\gamma q$  and  $\gamma g$  topologies: in these cases an energetic photon in the PHOS is associated to a hadronic jet in the TPC.

#### 4 Conclusions

With the advent of the LHC it will be possible to study the QGP well above the energy density of the phase transition. There will be a sizeable improvement in all the parameters related to the quark gluon plasma formation and to the possibility of studying it on a more stable theoretical ground. The ALICE experiment just ended its research and development phase and entered the construction phase. The design of the apparatus is now well defined and the available simulation and analysis tools have reached a high level of accuracy and reliability: the Collaboration is making a great effort to study in detail the physics capabilities of the experiment. The results obtained so far are confirming that ALICE will be able to exploit the possibilities of studying strongly interacting matter available at the LHC.

## References

1. U. Heinz and M. Jacob, nucl-th/0002042, 16/02/2000
2. See contributions to these Proceedings of B.Back (PHOBOS), I.Barden (BRAHMS), H.Caines (STAR) and A.Drees (PHENIX)
3. J.P. Revol, these Proceedings
4. K. J. Eskola, Nucl. Phys. **A698** (2002) 78 [hep-ph/0104058]
5. J. Schukraft, Nucl. Phys. **A698** (2002) 287 [CERN-ALI-2001-009]
6. P. Crochet, these Proceedings
7. B. Mohanty, these Proceedings; S. Raniwala, these Proceedings
8. P.Giubellino for the ALICE Collaboration, Proc. of the III International Symposium on LHC Physics and Detectors, Chia, Italy, October 25–27, 2001
9. ALICE Collaboration, Technical Proposal, CERN/LHCC/95–71 (1995); Addendum to the Technical Proposal CERN/LHCC/96–32 (1996)
10. ALICE Collaboration, Technical Design Reports. HMPID: CERN/LHCC/98–19 (1998); PHOS: CERN/LHCC/99–4 (1999); ZDC: CERN/LHCC/99–5; ITS: CERN/LHCC/99–12; MUON: CERN/LHCC/99–22 (1999) and CERN/LHCC/2000–046 (2000); PMD: CERN/LHCC/99–32 (1999); TPC: CERN/LHCC/2000–001 (2000); TOF: CERN/LHCC/2000–012 (2000); TRD: CERN/LHCC/2001/021 (2001)
11. Alice Collaboration, Physics Performance Report, in preparation
12. P.Foka for the ALICE Collaboration, Proc. of the III International Symposium on LHC Physics and Detectors, Chia, Italy, October 25–27, 2001
13. P. Crochet for the ALICE Collaboration, Proc. of the III International Symposium on LHC Physics and Detectors, Chia, Italy, October 25–27, 2001
14. AliRoot: source code and documentation available at <http://AliSoft.cern.ch/offline>
15. Root: source code and documentation available at <http://root.cern.ch>
16. T. Sjöstrand, Comput. Phys. Commun. **82** (1994) 74; T. Sjöstrand, hep-ph/0108264 (2001)
17. X.N. Wang and M. Gyulassy, Phys. Rev. **D44** (1991) 3501; X.N. Wang and M. Gyulassy, Comput. Phys. Commun. **83** (1994) 307
18. P. Billoir, Nucl. Instrum. Methods **225** (1984) 352; P. Billoir, S. Qian, Nucl. Instrum. Methods **A294** (1990) 219; B. Batyunya et al, ALICE Internal Note ALICE/97–24 (1997)

# HARD PROBES OF MATTER IN QCD

HELMUT SATZ

*Fakultät für Physik, Universität Bielefeld  
D-33501 Bielefeld, Germany*

We discuss how hard processes can be used as probes for the hot deconfined state of matter predicted by QCD. Hard processes are first defined in hadronic collisions; next, modifications due to known normal nuclear matter are obtained from  $pA$  collisions. This then allows the search for additional effects caused by the new medium produced in high energy  $AA$  collisions.

## 1 Introduction

What is a hard process? Hadrons are extended and composite objects; they have a radius of about one fermi and consist of quarks, antiquarks and gluons. *Soft processes* are those which proceed on rather long space-time scales, of the order of the intrinsic hadronic scale  $\Lambda_{\text{QCD}}^{-1} \sim 1 \text{ fm}$ . Examples are elastic  $pp$  scattering, where the entire proton has to know that it was hit, or the production process  $pp \rightarrow \pi + X$ , where the pion must be formed as an extensive object. Both require times of at least a fermi. *Hard processes*, on the other hand, are governed by a sub-hadronic scale much smaller than  $\Lambda_{\text{QCD}}^{-1}$ ; they consist of interactions between partons, which occur in very short space-time intervals. One example is the Drell-Yan production of a heavy dilepton pair, which dominantly occurs through  $q\bar{q}$  annihilation into a heavy virtual photon, with  $M_\gamma \geq 4 \text{ GeV}$ . Another is open charm production, mainly due to gluon fusion  $gg \rightarrow c\bar{c}$ ; here the threshold scale is  $2m_c \sim 3 \text{ GeV}$ . The associated production times are the inverse of these scales and with  $t_{\text{hard}} \sim 0.05 \text{ fm}$  much shorter than was the case for soft processes.

In QCD matter, deconfinement occurs when the density of constituents is so high that all long range effects are screened. The quark-gluon plasma (QGP) is thus a medium of very short space-time scales, and to study it, we need probes which are hard enough to resolve these short scales. Soft probes would simply not be able to “see it”. A further advantage of hard probes is that because of the short scales, perturbative calculations of the partonic processes become possible, so that for most phenomena one has quantitative predictions.

All hard processes have a common basic structure. In the collision of two hadrons, a parton from one collision partner interacts with a parton from the other. The parton content of the hadrons is specified by the parton dis-

tribution functions (PDF's)  $g(x)$ ,  $q(x)$  and  $\bar{q}(x)$ , for gluons, quarks and anti-quarks, respectively. These PDF's are determined from data on deep inelastic scattering of leptons on hadrons, making use of sum rules derived from the conservation of momentum, charge, etc. Given the PDF's and the perturbative interaction between the partons, all but the final hadronization of a hard process is determined. In the next section, we shall see specific examples of this structure.

## 2 Normalizing the Probe

We first want to study hard processes “without medium”, to verify that the combination of PDF's from deep inelastic scattering and perturbatively calculated partonic interactions indeed gives a correct description of the different possible reactions <sup>1</sup>. In particular, one can consider the following (inclusive) processes:

- direct photons:  $pp \rightarrow \gamma + X$
- Drell-Yan dileptons:  $pp \rightarrow \{\gamma \rightarrow e^+e^- (\mu^+\mu^-)\} + X$
- open charm/beauty:  $pp \rightarrow c\bar{c}(b\bar{b}) + X$
- quarkonium:  $pp \rightarrow J/\psi(\Upsilon) + X$
- hard jets:  $pp \rightarrow \text{jet} + X$

Let us consider the characteristic features and problems for some representative reactions.

The cross-section for Drell-Yan dilepton production through  $pp$  collisions at cms energy  $\sqrt{s}$  is in lowest order given as  $q\bar{q}$  annihilation,

$$\frac{d\sigma}{dM^2} = \int dx_1 dx_2 \frac{d\hat{\sigma}}{dM^2} \sum_k e_k^2 [q_k(x_1)\bar{q}_k(x_2) + q_k(x_2)\bar{q}_k(x_1)], \quad (1)$$

where

$$\frac{d\hat{\sigma}}{dM^2} = \left[ \frac{4\pi\alpha^2}{9M^2} \right] \delta(\hat{s} - M^2) \quad (2)$$

and  $\hat{s} = x_1 x_2 s$ . Here  $q(x)$  and  $\bar{q}(x)$  denote the proton quark and antiquark distribution functions of the Bjorken variable  $x$ , and  $e_k$  specifies the electric charge of the given quark. With the PDF's from deep inelastic scattering, the cross-section is thus completely specified and can be compared to data.

Such a comparison shows first of all that indeed  $M^4 d\sigma/dM^2 = f(M^2/s)$  scales as function of  $M^2/s$ . One further finds that the functional behavior of

the cross-section is correctly described, but that the numerical values differ by about a factor two:

$$\left( \frac{d\sigma}{dM^2} \right)_{\text{exp}} / \left( \frac{d\sigma}{dM^2} \right)_{\text{LO}} \equiv K \simeq 2. \quad (3)$$

This so-called K-factor arises when data is compared to the lowest order (LO) cross-section; the inclusion of higher orders brings also numerical agreement. The transverse momentum ( $k_T$ ) distribution of Drell-Yan production is reproduced for small  $k_T$  by the lowest order expression if the incident partons are given an intrinsic transverse momentum of about 0.7 GeV; for large  $k_T$ , higher order terms have to be included. We can thus conclude that Drell-Yan production in  $pp$  collisions is understood and fully predictable.

The situation is similar for the production of open charm. Here the lowest order term (at high energy) is gluon fusion to a  $c\bar{c}$  pair. However, here the (unobservable) mass  $m_c$  of the charm quark enters, and the K-factor depends on the value of this mass. A pragmatic approach is to compare the cross-section calculated up to higher orders with data and fix  $m_c$  to fit the data at one value of the collision energy. For all other  $s$ , the cross-section is then determined, and the resulting form agrees with the energy dependence measured at central rapidity. Little is known about large rapidities or transverse momentum distributions. With this reservation, we again conclude that open charm production in  $pp$  collisions is understood and predictable.

Charmonium production starts the same way as that of open charm; but now the produced  $c\bar{c}$  pair, which is generally colored, has to undergo color neutralisation to form a physical resonance. This color neutralisation process is found to be non-perturbative and introduces a principal uncertainty into the theoretical description.

The total “hidden charm” cross-section

$$\sigma_{c\bar{c}}^{\text{HC}} \equiv \int_{4m_c^2}^{4m_D^2} d\hat{s} \int dx_1 dx_2 g(x_1) g(x_2) \hat{\sigma}(\hat{s}) \delta(\hat{s} - x_1 x_2 s) \quad (4)$$

is found to contribute dominantly to open charm production, with the  $c\bar{c}$  system acquiring the missing energy for  $D\bar{D}$  production from the color field in the collision process. Only about 10 % of the hidden charm actually goes into charmonium production.

The color evaporation <sup>2</sup> model does not attempt to specify the color neutralisation process, but simply assumes that each charmonium state  $i$  gets a fixed fraction of the cake:

$$\sigma_i(s) = f_i \sigma_{c\bar{c}}^{\text{HC}}(s), \quad (5)$$

where  $i = J/\psi, \chi_c, \dots$  and the  $f_i$  are constants. The first prediction of the model, the energy independence of production ratios of different charmonium states is found to be well satisfied for  $\psi'/(J/\psi)$  and  $\chi/(J/\psi)$ . The values of  $f_i$  can thus be determined at one collision energy to predict the energy dependence of the cross-sections. This energy dependence is also found to agree well with all data. We thus conclude that charmonium production in  $pp$  collisions is predictable, but not fully understood: what is the dynamics of color neutralisation, how do the  $f_i$  arise?

One promising attempt to fill this gap is provided by the color octet model<sup>3</sup>. It assumes that the color octet  $c\bar{c}$  combines with a gluon to form a color singlet  $c\bar{c}g$  state. This “pre-resonance” is a higher Fock space excitation of a charmonium state, which subsequently decays into the ground state color singlet  $c\bar{c}$ . Life-time and size of the pre-resonance charmonium are estimated to be around 0.25 fm.

We conclude: the evaluation of hard processes in hadronic collisions requires in general of three elements. Using the parton distribution functions determined from deep inelastic scattering, we describe a hard partonic interaction by means of perturbative QCD. Up to here, everything is rather under control. The final hadronisation stage brings in some model dependence, particularly for quarkonium production. However, the color evaporation model, though not theoretically derivable, provides good quantitative predictions.

### 3 Hard Probes in Nuclear Matter

The next step is to see how our prospective hard probes react when we study them not in vacuum (i.e., in an elementary reaction), but in a known medium, standard nuclear matter. To do this, we have to consider the probes in  $pA$  interactions as function of  $A$ . The simplest theoretical argument would suggest that hard processes are not affected by a nuclear medium, and based on this idea, many early hard scattering experiments used nuclear targets to increase the production rates. Unfortunately, the conjecture is wrong. While experiments indeed showed so far that for the overall Drell-Yan cross section

$$\sigma_{DY}^{pA} \simeq A \sigma_{DY}^{pp}, \quad (6)$$

they found a nuclear transverse momentum broadening,

$$\langle p_T^2 \rangle_{DY}^{pA} > \langle p_T^2 \rangle_{DY}^{pp}, \quad (7)$$

as well as nuclear modifications of parton distribution functions; in particular for quarks one has

$$q_A(x)/q_N(x) \neq 1 \quad (8)$$

(nuclear shadowing, EMC effect). Finally, there is “normal  $J/\psi$  suppression” in nuclear matter, with

$$\left( \frac{d\sigma_{J/\psi}^{pA}}{dy} \right)_{y=0} / A \left( \frac{d\sigma_{J/\psi}^{pN}}{dy} \right)_{y=0} < 1. \quad (9)$$

Clearly these consequence of normal nuclear matter should be understood and taken into account correctly before a hard process in  $AA$  collisions can be used to probe for new effects.

One origin of nuclear transverse momentum broadening is the scattering of the incident partons as they pass through the nuclear target before undergoing the hard process we want to study. This leads to

$$\langle p_T^2 \rangle_{pA} = \langle p_T^2 \rangle_{pp} + \nu(A) \delta_0^2, \quad (10)$$

where  $\nu(A)$  counts the number of scatterings and  $\delta_0$  the “kick” received by the parton each time. By studying Drell-Yan and open charm production in  $pA$  collisions, one can determine the value of  $\delta_0$  for quarks and gluons, respectively. Charmonium production can suffer a further final state broadening through interactions of the nascent charmonium with nuclear target matter.

The nuclear modification of parton distributions arises conceptually because a multiple scattering picture breaks down for fast partons in matter. When the mean free path of the parton in matter becomes less than the “coherence” length travelled by the parton in the time it needs to react to the scattering (e.g., by emitting a gluon), then the parton gets hit many times before it has had a chance to recover. This phenomena (Landau-Pomeranchuk-Migdal effect <sup>4</sup>) leads to interference and as a result to an effective change of the PDF’s. This is evidently also an initial state effect, and the modified PDF’s can be obtained from deep inelastic lepton-hadron studies and from Drell-Yan and open charm measurements in  $pA$  collisions.

In contrast, normal  $J/\psi$  suppression is a final state effect. We had seen that charmonia are presumably produced in a pre-resonance state; the life-time of this stage is estimated to be some 0.2 - 0.3 fm, which in the target rest frame becomes dilated to 5 - 10 fm for the charmonia at  $x_F \gtrsim 0.1$  - 0.2 as measured in present fixed target experiments. The nuclear target thus only sees this pre-resonance, which because of rather universal binding dynamics has the same size and life-time for the different charmonium states ( $J/\psi$ ,  $\chi$ ,  $\psi'$ ). The pre-resonance break-up cross-section in nuclear matter is found to be  $\sigma_{PR} \sim 5$  - 7 mb, either through geometric estimates or from data analyses. The resulting survival probability,

$$S_A \simeq \exp\{-n_0 \sigma_{PR} L_A\}, \quad (11)$$

describes well the  $A$ -dependence of  $J/\psi$  and  $\psi'$  suppression in  $pA$  collisions<sup>5</sup>. Moreover, the observed equality of  $J/\psi$  and  $\psi'$  suppression here arises naturally because of the pre-resonance passage; for physical resonances,  $\sigma_{\psi} \gtrsim 4\sigma_{J/\psi}$ , so that one would expect very different suppression rates.

In conclusion, hard processes are affected by normal nuclear matter, with both initial state effects ( $p_T$ -broadening, PDF modifications) and final state effects (pre-resonance quarkonium absorption, nuclear jet quenching). These effects must be taken into account before the process can be used as QGP probe. In order to make sure that this is done correctly, it is essential that all experiments provide the  $pA$  counterpart to any  $AA$  data to be interpreted.

#### 4 Probing the Hot Medium in AA Collisions

Different hard probes have different functions in probing the medium produced in  $AA$  collisions. Hard photons, Drell-Yan dileptons, open charm/beauty, and eventually even  $Z$ 's can be used to test

- if initial state effects are under control: they define the amount of nuclear interference (shadowing) and  $p_T$ -broadening;
- if there are secondary hard production processes involving partons from different nucleon-nucleon collisions (hard color interconnection).

Quarkonia and hard jets, on the other hand, can test if there are final state effects beyond those already seen in nuclear matter, and in particular, if there is color deconfinement. The crucial features allowing this are:

- quarkonium dissociation ( $J/\psi$  suppression) depends on the state of the medium, and
- the energy loss of hard jets (jet quenching) depends on the state of the medium.

Let us consider these two deconfinement probes in a little more detail.

In a hot QGP, color screening dissolves the binding of the  $J/\psi$ , so that the  $c$  and the  $\bar{c}$  separate and lose each other. The large charm quark mass rules out thermal production of further  $c\bar{c}$  pairs, so that at hadronisation, the broken pair leads to  $D$  and  $\bar{D}$  formation. Hence QGP formation leads to  $J/\psi$  suppression<sup>6</sup>.

On a more microscopic level, the small spatial size of the  $J/\psi$  ( $r_{J/\psi} \simeq 0.2$  fm) and tight binding ( $2M_D - M_{J/\psi} \simeq 0.65$  GeV) requires hard gluons for resolution and break-up. The hadronic PDF's strongly damp the gluon momentum, so that a confined medium does not contain hard enough gluons for  $J/\psi$  dissociation. On the other hand, in a deconfined medium of temperature

$T \sim 0.2 - 0.3$  GeV, the gluon momenta peak at values of 0.6 - 0.9 GeV, so that a gluonic equivalent of the photo-effect can readily break-up a  $J/\psi$ . We thus conclude that only deconfined media can lead to  $J/\psi$  suppression<sup>7</sup>.

The  $J/\psi$ 's produced in hadronic collisions originate in part from the decay of higher excited states. This feed-down leads to a very characteristic sequential in-medium suppression pattern, whose different steps moreover serve as thermometer for the medium. About 60% of hadronic  $J/\psi$  production is direct  $1S$  production, with about 30% coming from  $\chi$  and 10% from  $\psi'$  decay; because of the narrow widths of charmonia, these decays occur in nuclear collision well outside any produced medium. This medium thus records the passage of the different states. The increasing size and decreasing binding energy as we go from  $J/\psi$  to  $\chi$  to  $\psi'$  implies for the dissociation temperatures  $T_{J/\psi} > T_\chi > T_{\psi'}$  and results in a step-wise suppression of the form shown in Fig. 1.

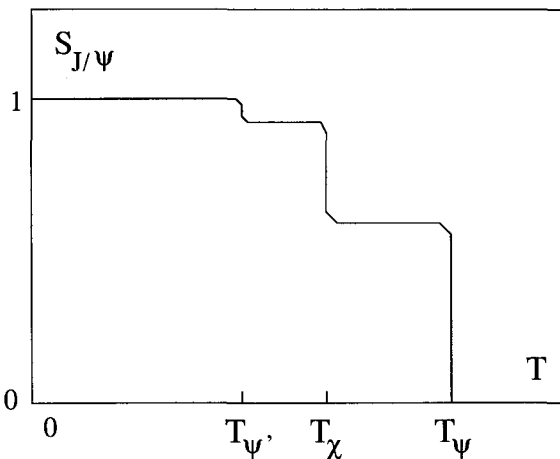


Figure 1. Sequential  $J/\psi$  suppression: a schematic view of the  $J/\psi$  survival probability in a hot medium

For bottomonium production, the greater number of sub-threshold  $b\bar{b}$  bound states ( $\Upsilon, \Upsilon', \Upsilon''; \chi_b, \chi'_b$ ) provides an even richer structure with more steps<sup>10</sup>. The combination of charmonium and bottomonium production can thus play for nuclear collisions a role similar to that of the analysis of stellar spectra for determining stellar temperatures.

The actual application of this tool to heavy ion data requires the consideration of various further features introduced by the collision geometry, the experimental resolution, possible in-medium changes of the open charm threshold, etc. It is outside the scope of this report; see e.g. <sup>9</sup> for further studies.

Turning now to jet quenching <sup>11</sup>, we first recall a crucial feature concerning the radiative energy loss of a fast charge passing through a medium. Each scattering of the charge leads to the emission of a gluon, whose energy  $\omega$  is proportional to the energy  $E$  of the charge. The total radiative energy loss is thus  $\Delta E = \nu\omega \sim E$ , where  $\nu$  denotes the number of successive scatterings. This multiple scattering picture breaks down, however, when the time  $t_{\text{coll}}$  between two successive interactions of the charge becomes shorter than the characteristic gluon emission time  $t_0$ ; this is once more the Landau-Pomeranchuk-Migdal effect already mentioned above <sup>4</sup>. Now the charge does not have the time to react to a given interaction before it is hit again. In this case, the square of the scattering amplitude for the sequence of interactions does not reduce to a sum of squared successive interactions: there now is (destructive) interference between scatterings, which reduces the energy loss of fast charges passing dense media.

Taking the LPM effect into account, the energy loss of a hard jet passing a dense medium is found to have the form <sup>12,13</sup>

$$-\frac{dE}{dz} \simeq \hat{q} z_0 \quad L > z_0, \quad (12)$$

$$\simeq \hat{q} L, \quad L < z_0, \quad (13)$$

where  $L$  specifies the size of the medium and  $z_0$  the distance the charge travels in the medium during its emission time  $t_0$ . The transport coefficient

$$\hat{q} = n(T) \int dq_T^2 q_T^2 \frac{d\sigma}{dq_T^2} \quad (14)$$

is determined by the density  $n(T)$  of the medium and the scattering strength of the medium: the integral in eq. (14) effectively measures the transverse kick the charge receives per interaction.

To analyse jet quenching in different media, we thus have to know the density of the medium and the corresponding scattering strength. Recent studies <sup>14</sup> show that a hot QGP leads to quenching an order of magnitude higher than found for hadronic matter. It is not yet known, however, if the onset of deconfinement leads to an observable discontinuity in the quenching rate.

As in the case of quarkonium suppression, the actual use of jet quenching in the analysis of data (just coming from RHIC at this time) requires the consideration of collision features and experimental possibilities. In particular, data from  $pA$  are essential to determine the normal quenching in nuclear matter; only then can one look for further consequence of hot produced media.

## 5 Summary

In hard processes, partonic constituents of hadrons interact on scales allowing perturbative QCD calculations. The parton content of the hadrons is given by distribution functions determined in deep inelastic scattering. Where subsequent hadronisation comes in, phenomenological models provide confirmed quantitative extrapolations in energy.

The effect of a nuclear medium on hard processes is defined by  $pA$  interactions; hence data on these are necessary to fix the “normal” reference behavior. Such effects can modify the effective parton distributions (shadowing), can influence the perturbative calculation stage (multiple initial state parton scattering), and it can affect the hadronisation (final state scattering of the probe).

With probes thus defined and understood in normal nuclear matter, one can then look for additional final state effects due to the medium produced in nuclear collisions. The principal phenomena here are quarkonium dissociation and jet quenching; both lead to a behavior crucially dependent on the confinement/deconfinement nature of the medium.

## References

1. For an overview of this program, see H. Satz and X.-N. Wang (Eds.), *Hard Processes in Hadronic Interactions*, *Int. J. Mod. Phys. A* **10**, 2881–3090 (1995)
2. M. B. Einhorn and S. D. Ellis, *Phys. Rev. D* **12**, 2007 (1975); H. Fritzsch, *Phys. Lett. 67B*, 217 (1977); M. Glück, J. F. Owens and E. Reya, *Phys. Rev. D* **17**, 2324 (1978); J. Babcock, D. Sivers and S. Wolfram, *Phys. Rev. D* **18**, 162 (1978).
3. G. T. Bodwin, E. Braaten and G. P. Lepage, *Phys. Rev. D* **51**, 1125 (1995); E. Braaten and S. Fleming, *Phys. Rev. Lett.* **74**, 3327 (1995); E. Braaten, S. Fleming and T.-C. Yuan, *Ann. Rev. Nucl. Sci.* **46**, 197 (1996).
4. L. P. Landau and I. Ya. Pomeranchuk, *Doklad. Akad. Nauk SSSR* **92**,

- 535, 735 (1953); A. B. Migdal, *Phys. Rev.* **103**, 1811 (1956); E. L. Feinberg and I. Ya. Pomeranchuk, *Suppl. Nuovo Cim. III, Ser. X*, N. **4**, 652 (1956).
5. D. Kharzeev and H. Satz, *Phys. Lett.* **B 366**, 316 (1996).
  6. T. Matsui and H. Satz, *Phys. Lett.* **B 178**, 416 (1986).
  7. D. Kharzeev and H. Satz, *Phys. Lett.* **B 334**, 155 (1994).
  8. F. Karsch, M. T. Mehr and H. Satz, *Z. Phys.* **C 37**, 617 (1988); F. Karsch and H. Satz, *Z. Phys.* **C 51**, 209 (1991); S. Gupta and H. Satz, *Phys. Lett.* **B 283**, 439 (1992).
  9. D. Kharzeev *et al.*, *Z. Phys.* **C 74**, 307 (1997); H. Satz, *Rep. Progr. Phys.* **63**, 1511 (2000).
  10. S. Digal, P. Petreczky and H. Satz, *Phys. Rev.* **D 64**, 094015 (2001).
  11. J. D. Bjorken, Fermilab-Pub-82/59-THY (1982) and Erratum, unpublished.
  12. R. Baier *et al.*, *Phys. Lett.* **B 345**, 277 (1995); *Nucl. Phys.* **B 483**, 291 (1997); *Nucl. Phys.* **B 484**, 265 (1997); *Nucl. Phys.* **B 531**, 403 (1998).
  13. B. G. Zakharov, *JETP Letters* **63**, 952 (1996); *JETP Lett.* **65**, 615 (1997).
  14. D. Schiff, Lectures at the 1999 Zakopane Summer School, to appear in the Proceedings.

## PHENOMENOLOGY OF HEAVY ION COLLISIONS AND OBSERVABLES

*The ultrarelativistic heavy ion collisions are the unique chance of creating and studying the quark-gluon plasma in the laboratory. The presentation of the relevant phenomenology and experimental observables ("soft" and "hard" probes) introduces the main themes of this chapter.*

*The analysis of the experimental data is so complicated that it is necessary to start from simpler reactions, like nucleon-nucleon or nucleon-nucleus collisions and, successively, to implement their phenomenological analysis in understanding nucleus-nucleus interactions. It should be possible, in this way, to have a good description of elementary processes and to disentangle the effects already present in ordinary hadronic matter from the genuine QGP signals. The contribution of Del Fabbro and Treleani is precisely a discussion of the multiple parton collisions in N-N and N-A scattering at high energy; the importance of such a study for the consequences on heavy ion collisions is evident.*

*One of the most popular signature of deconfinement is strangeness enhancement. Becattini and Pettini present a systematic study of strangeness production, both in elementary and heavy ion interactions, assuming statistical hadronization. With a small number of free parameters, they successfully describe the observed hadron multiplicity. This analysis reveals the peculiarity of nuclear reactions with respect to elementary interactions.*

*Among the RHIC first data, a special attention has been devoted to the charged particle production. The model presented by Ugoccioni is based on the Dual String Model, which has already been successfully applied to SPS data. At RHIC energy a new phenomenon occurs: saturation. In the Dual String Model this effect is implemented by string fusion, giving a good description of experimental dependence of charged particle rapidity distribution on the centrality of the collision.*

*Finally, Alberico, Lavagno and Quarati propose a new analysis of transverse mass spectrum and momentum fluctuations of particles produced in nuclear collisions at SPS. They invoke a non-extensive statistical mechanics instead of the standard one (Boltzmann-Gibbs) to reveal properties such as long range forces and memory effects, in the statistical analysis of heavy ion interactions.*

This page is intentionally left blank

# HEAVY ION COLLISION PHENOMENOLOGY I

## - SOFT OBSERVABLES -

F. BECATTINI

*Università di Firenze and INFN Sezione di Firenze  
Via G. Sansone 1, I-50019, Sesto F.no, Firenze, Italy  
E-mail: becattini@fi.infn.it*

The physics of heavy ion collisions with regard the soft probes of the Quark-Gluon Plasma is reviewed.

## 1 Introduction

The aim of the heavy ion collision (HIC) programme is to create a new state of matter, the so-called Quark-Gluon Plasma (QGP), in which quarks and gluons can freely travel several fermi's, i.e. they are no longer confined within a typical hadronic volume. The generally accepted theory of strong interactions, Quantum-Chromo-Dynamics (QCD), predicts that interaction between partons weakens as they get closer to each other and energy-momentum transfer gets larger. This implies that quarks and gluons become weakly interacting particles at very high density and temperature and this is then the regime where they are supposed to unbind from hadrons. It is still not clear from lattice calculations whether the transition from a confined to a deconfined phase in the thermodynamic limit is a first-order, second-order, or rather a smooth continuous transition<sup>1</sup>.

In order to reach the needed high values of temperature and density and to create a system which is large enough to be properly defined as a medium where partons can travel many hadronic volumes, the best found option in terrestrial laboratories is the collision of large-sized nuclei at a suitably high energy. Thus, an extensive programme of experimental heavy ion collisions has been and is being carried out over a large range of nucleon-nucleon centre-of-mass energy in the relativistic and ultrarelativistic regime, from few GeV up to several TeV. For the present, the main beam facilities are SIS in GSI Darmstadt ( $\sqrt{s}_{NN} \approx 1$  GeV), AGS at BNL ( $\sqrt{s}_{NN}$  up to 6 GeV), SPS at CERN ( $\sqrt{s}_{NN}$  from 8 to 20 GeV) and RHIC at BNL ( $\sqrt{s}_{NN}$  from 130 to 200 GeV). The next generation experiments will be operated at the LHC collider at CERN with a  $\sqrt{s}_{NN}$  of several TeV.

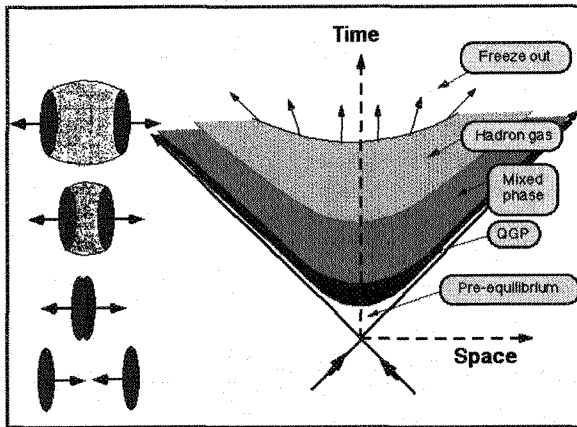


Figure 1. Evolution in space and time of a heavy ion collision

## 2 Heavy ion collisions and models

A heavy ion collision is a dynamical process which is very far from the ideal thermodynamical system assumed in lattice QCD simulations. The current wisdom models this process as outlined in Fig. 1. The QGP, if any, should be formed as a result of the huge energy deposition in the core of the collision after the time needed for thermal equilibration. Thereafter, the system rapidly cools and expands and QGP hadronizes soon after energy density overcomes a critical value. After a possible stage of mixed phase, a weakly interacting expanding gas of hadrons is left. When the further expansion gets hadrons far enough that inelastic scatterings are cut off, hadronic multiplicities of the different species get frozen and this event is defined as *chemical freeze-out*. When also elastic scatterings cease, one speaks about *kinetic freeze-out* in that also momentum distributions cannot undergo further changes. Of course, chemical and kinetic freeze-outs are not indeed sharp occurrences for all hadronic species at the same time and one should rather consider different freeze-outs for different particles.

In fact, what is observed in the detectors are the freely streaming hadrons emerging from the kinetic freeze-out. Hopefully, their distributions should keep memory of the QGP formation in the early stage of the collision. A great deal of modelling is thus necessary to trace back QGP from the measured particles. In principle, it would be desirable to reconstruct the whole process and study how different initial conditions (e.g. QGP or not QGP) affect the

final distributions to be compared with the data. Because of their ability of getting through the intermediate evolution without being sizeably affected, some observables can give a more direct clue of QGP formation and these are certainly the most interesting ones and the most highly-prized to find. Nevertheless, a detailed description with suitable models is necessary for a fully understanding of what goes on in the collision. Yet, there is no single model which can be used to calculate the whole process and several models are used in combination, each with a different range of applicability.

- *Parton Cascade Models* This model is mainly used to describe the pre-equilibrium stage of the collision, in order to estimate how fast partons belonging to incoming nucleons multiply and thermalize. Quarks and gluons are treated as weakly interacting particles undergoing independent collisions, i.e. interference effects are neglected. The space-time evolution of the partonic system is described by a relativistic transport equation whose collision term is calculated through the leading-order perturbative QCD. According to the actual calculations, kinetic equilibration is quite fast ( $\simeq 3 - 5$  fm/c at RHIC energy) whereas chemical equilibration needs longer times and the initial plasma seems to be too gluon rich. Higher orders in the perturbative expansion are generally not included.
- *Hydrodynamics* The hydrodynamical regime sets in possibly after the establishment of thermal (but not necessarily chemical) equilibrium at partonic level. Of course, this approach demands the existence of locally equilibrated cells consistently larger than parton mean free path (roughly:  $>> (3\alpha_S(T)T)^{-1}$ ). Thermal equilibrium is a general assumption throughout the evolution which is calculated on the basis of the local conservation equations:

$$\frac{\partial T^{\mu\nu}}{\partial x^\mu} = 0 \quad \frac{\partial N_i^\mu}{\partial x^\mu} = 0 \quad (1)$$

where  $T^{\mu\nu}$  is the energy-momentum tensor and  $N_i^\mu$  the four-vector current for the  $i^{\text{th}}$  ( $i = 1, \dots, n$ ) conserved internal quantity, like, e.g., baryon number. If one takes the ideal fluid approximation, there are  $5+n$  independent variables and  $4+n$  conservation equations. Therefore, with the equation of state, there are as many variables as equations and the system can be solved once initial and boundary conditions are known. Such conditions are usually provided by models of the pre-equilibrium stage yielding the equilibration time, the initial temperature, chemical potentials and four-velocity distribution. The hydrodynamical approach is usually employed in the QGP phase as well as in the early hadronic

phase. A special simplified hydrodynamical model of the collisions, the Bjorken longitudinal boost-invariant model, is commonly used to estimate the initial produced energy density in the collision by means of the formula:

$$\varepsilon(\tau_0) = \frac{1}{\pi R^2 \tau_0} \frac{dE_T}{dy} \quad (2)$$

where  $\tau_0$  is the proper thermalization time,  $\pi R^2$  is the section of the cylinder undergoing boost invariant longitudinal expansion and  $dE_T/dy$  is the transverse energy per unit of rapidity at midrapidity, which is measurable. By using  $\tau_0 = 1$  fm/c and  $R$  as the radius of a lead nucleus, an initial energy density of about 3 GeV/fm<sup>3</sup> can be estimated for Pb–Pb collisions at top SPS energy ( $\sqrt{s_{NN}} = 17.2$  GeV) with a corresponding temperature of 210–200 MeV. At RHIC, with  $\sqrt{s_{NN}} = 130$  GeV, the initial temperature may have been as high as 350 MeV<sup>2</sup>.

- *Microscopic Transport Models* In these models a heavy ion collision is described as a sequence of binary/N-ary collisions of “conventional” objects, such as hadrons, resonances and constituent quarks and di-quarks, which are assumed to propagate with classical trajectories in phase space. Hence, this approach provides a useful baseline for QGP search for it allows to assess whether a single observable shows evidence of non-hadronic physics. The initial particle production is usually modelled via string fragmentation. Much physical input is needed: hadronic total and differential cross sections, masses and widths of resonances, and the parameters of the string model which should be tuned to elementary collisions. Calculations can be performed only by means of Monte-Carlo codes.
- *Statistical-thermal Models* In this approach no attempt is done to reconstruct either all or part of the evolution of the collision. Rather, one tries to extract information from the observed final system of particles by assuming global and/or local (partial) chemical and thermal equilibrium. This statistical-thermal ansatz allows to determine the parameters  $T$  and  $\mu_B$  at chemical and kinetic freeze-out. Generally speaking, the multiplicities of different particle species yield information on the chemical freeze-out point, whilst hadronic spectra carry information on the kinetic freeze-out point. There are different versions of the statistical-thermal model according to inclusion or not of chemical non-equilibrium effects, application to full phase space or limited kinematical regions etc.

Often, these models are used in combination. For instance, hydrodynamical evolution is merged with hadronic transport models with special matching

conditions: pre-hadronic evolution is calculated hydrodynamically and the hadronic distributions at the phase transition point are used as input for the hadronic transport model which predicts the further evolution of the system by re-scattering hadrons up to the freeze-out points.

### 3 Soft observables and QGP signatures

The possible creation of QGP in the highly dynamical process of a heavy ion collision is a transient which should hopefully be traced by means of final-state observables measured by detectors surrounding the interaction region. Physicists involved in this field have striven hard for almost 20 years to find the most effective physical observables proving the formation of QGP in HIC. In this section, I will review the main so-called *soft probes* of QGP, namely those involving the observation of the bulk of light hadrons produced in the collision. Amongst such soft observables, I have singled out four main items: inclusive particle production, strangeness enhancement, collective flow and Bose-Einstein correlations, also known as Hanbury Brown-Twiss (HBT) interferometry. For each of those, I will try to give a brief introduction and to summarize the state of the art in what concerns measurements and analysis and interpretation of the data.

#### 3.1 Thermal particle production

The basic idea is as follows: if a phase transition occurs and the system is equilibrated, a thermal spectrum of hadrons from the emitting source after freeze-out should be observed (hadronic black-body radiation). This simple idea can be tested by applying a statistical-thermal analysis to a hopefully large set of measured average multiplicities of hadronic species. The statistical-thermal analysis must take into account that hadrons are by no means emitted from one thermally and chemically equilibrated region (a *fireball*) globally at rest in the centre-of-mass frame, rather from several such regions at statistical equilibrium with different global momentum, charges, masses and volumes. However, as long as Lorentz-invariant quantities, like hadronic multiplicities, are involved, one can take advantage of their independence on fireball's momentum and try to establish a mathematical equivalence between the average actual set of fireballs and one equilibrated fireball at rest in the centre-of-mass frame. This equivalence applies only if the actual distribution of fireball charges and masses for given volumes has a special form<sup>4</sup>. If this is the case, and volume and mass of the equivalent global fireball are large enough, the average primary multiplicities of any hadron is given by the grand-canonical

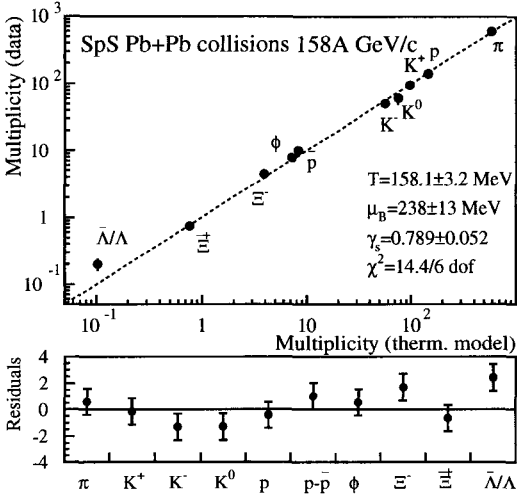


Figure 2. Measured vs fitted hadron multiplicities and fitted parameters in Pb-Pb collisions at  $\sqrt{s}_{NN} = 17.3$  GeV<sup>3</sup>.

formula (in the Boltzmann limit):

$$\langle n_j \rangle = \frac{(2J_j + 1)V}{(2\pi)^3} \gamma_S^{N_{sj}} \int d^3p \exp[-\sqrt{p^2 + m_j^2}/T] \exp(-\sum_i \mu_i q_{ij}/T) \quad (3)$$

where  $V$  is the sum of the proper volumes of all fireballs,  $T$  the temperature and  $\mu_i$  is the chemical potential relevant to the  $i^{\text{th}}$  charge  $q_{ij}$  (electric, baryon number and strangeness). By comparing the measured multiplicities with the above theoretical estimates and taking into account the subsequent decays, the parameters  $T$ ,  $\mu_i$  and  $V$  can be obtained. The factor  $\gamma_S$  in Eq. (3), which is powered to the number of strange quarks in the hadron  $j$ , is a phenomenological put-by-hand extra strangeness suppression parameter, which is needed to reproduce the data. It must be pointed out that, in this approach, full-phase-space integrated multiplicities, namely  $4\pi$  full-acceptance measurements or extrapolations, must be used.

On a different approach to the statistical-thermal analysis, it is envisaged that each fireball is endowed with different temperatures and chemical potentials. By selecting hadronic multiplicities measured in a central rapidity

window, one should be able to draw information especially on the central fireball which is supposed to be the QGP actual formation place. This scheme is attractive but has some drawbacks: it does not allow a full-phase-space analysis unless  $T$  and  $\mu$  are constant; each fireball should be large enough for a grand-canonical description in terms of  $T$  and  $\mu_B$  to apply (this is not required in the previous scheme) and the fluctuations of mass and charge are anyway fixed in the grand-canonical ensemble; finally, the choice of a central rapidity window does not ensure the isolation of the central fireball as hadrons from nearby fireballs can get into it anyway.

The statistical-thermal analysis of average multiplicities has been done by many authors in the two aforementioned approaches with generally consistent results. In fact, hadrons seem to be emitted from a thermally and chemically (except strangeness, this will be discussed later) equilibrated source as shown in Fig. 2.

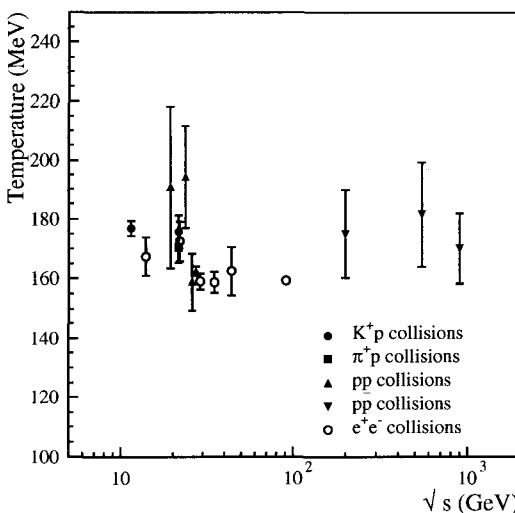


Figure 3. Temperatures fitted in elementary collisions (from ref.<sup>5</sup>).

On the other hand, it has been shown that this applies to elementary systems as well ( $e^+e^-$ ,  $pp$ ,  $p\bar{p}$  etc.)<sup>7</sup>, provided that the grand-canonical formalism is replaced with the appropriate canonical one, i.e. with exact enforcement of initial charges. The obtained temperature value is fairly constant (see Fig. 3)

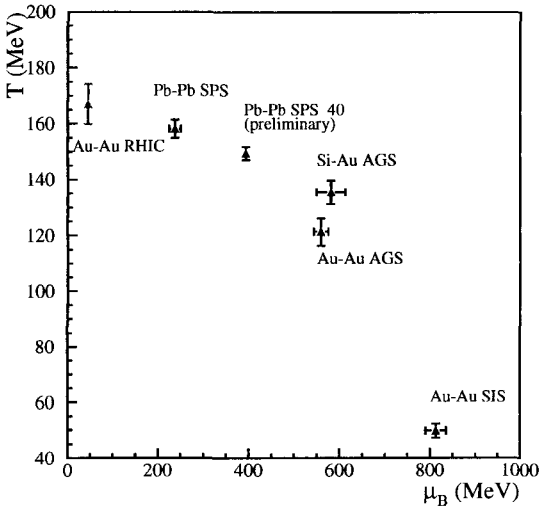


Figure 4. Temperatures and baryon-chemical potentials at chemical freeze-out fitted in heavy ion collisions. The RHIC point has been fitted by using hadron yields at midrapidity, unlike all other points which have been determined by using full-phase-space multiplicities (from ref.<sup>6</sup>).

and amazingly close to the expected QCD critical temperature. This unexpected result has certainly disqualified the observation of a thermal hadron radiation in HIC as a phase transition signature but has provided much interesting information on hadronisation mechanism in both EC and HIC. The strikingly good agreement between statistical-thermal *ansatz* and data in elementary collisions has been interpreted as an evidence of pure statistical filling of available multi-hadronic phase space of pre-hadronic clusters once they reach a critical value of energy density (corresponding to the critical QCD temperature  $T_c \simeq 160$  MeV)<sup>7,8,9</sup>. Otherwise stated, hadronisation process itself creates hadrons in a state of apparent equilibrium<sup>10</sup> at the QCD critical energy density, as a post-hadronisation equilibration via inelastic collisions is ruled out by the high expansion rate. The close values of fitted temperatures in EC and high energy HIC at low baryon-chemical potential also indicate that hadron inelastic rescattering hardly changes the primordial hadron abundances generated when QGP hadronizes. This is confirmed by

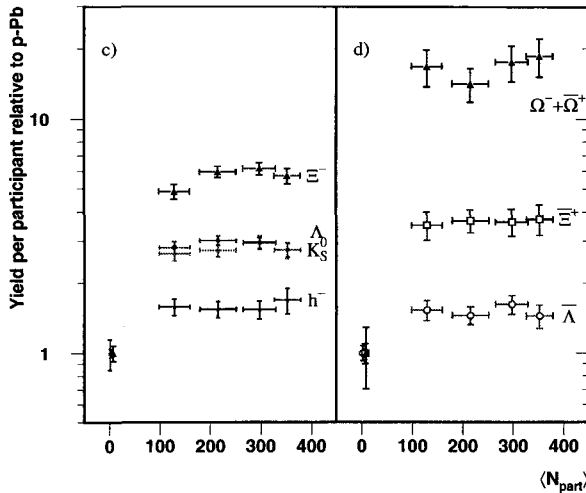


Figure 5. Yields of hyperons measured by the experiment WA97 in Pb-Pb collisions at  $\sqrt{s_{NN}} = 17.2$  GeV (from ref.<sup>11</sup>).

simulations carried out in microscopic transport models: they show that differences between hadronisation and post-freeze-out abundances of long-lived (with respect to the system's lifetime) particles are anyhow less than 30%<sup>8</sup>. Yet, this does not mean that HIC and EC are not different process. Indeed, in the former, equilibrium is achieved *early* on possibly *large* fireball volumes, whereas in the latter equilibrium is a *late* pre-hadronisation feature over small colour singlet clusters (mini-QGP droplets). Another apparent distinctive feature is the different strangeness suppression, which will be discussed in the next subsection.

### 3.2 Strangeness enhancement

That QGP formation should lead to an enhancement of strange particle production is a rather old idea put forward by Rafelski and Muller<sup>12</sup>. The argument was based on a faster time scale for strange quark pair creation via gluon collisions in an equilibrating QGP, due to a smaller strange quark mass. The enhancement was predicted to be more dramatic for multiply strange hadrons. Following this idea, an experiment devoted to the identification and measurement of strange hyperons has been set up at CERN on the SPS lead beam, WA97 and its successor NA57. This experiment has actually found a clear

hierarchical enhancement of strange hyperons production with respect to pp and pA collisions (see Fig. 5). The enhancement pattern has been also found by extracting the ratio  $\lambda_S$  between the number of newly produced  $s\bar{s}$  pairs and  $u\bar{u}$ ,  $d\bar{d}$  pairs by means of the statistical-thermal analyses<sup>13</sup> (see Fig. 6). This ratio is almost as twice as high in high energy HIC with respect to a fairly constant  $\approx 0.22$  value in EC.

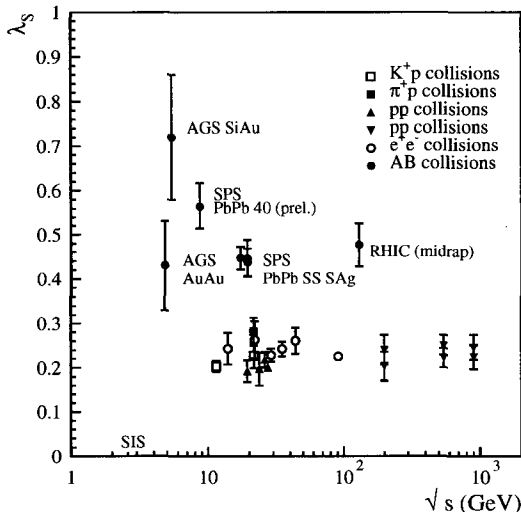


Figure 6. Ratio  $\lambda_S = 2\langle s\bar{s} \rangle / (\langle u\bar{u} \rangle + \langle d\bar{d} \rangle)$  between newly produced quark pairs in elementary and heavy ion collisions as a function of centre-of-mass energy (from ref.<sup>6</sup>).

Still, the interpretation of this result is not settled. Much of the observed increase in strange quark production with respect to EC can be attributed to the increased system size in a pure hadronic framework<sup>14,15</sup>. In fact, the effect of zero-strangeness constraint in small EC systems reduces the available phase space and, as a consequence, the average multiplicities of strange particles (*canonical suppression*). As volume increases, this effect slowly disappears. Furthermore, this suppression is more severe for multiply strange hadrons, in full agreement with the hierarchical enhancement pattern observed by WA97. On the other hand, in order to reproduce full-phase space multiplicities, a strangeness suppression parameter  $\gamma_S$  (see Eq. (3)) must be introduced and this turns out to be higher in HIC ( $\approx 0.7 - 0.8$ ) with respect to pp ( $\approx 0.5$ ). The

main point here is that  $\gamma_S$  must be powered to the number of valence quarks and this goes beyond a pure hadronic scheme. It has been proposed that  $\gamma_S$  can be dropped ( $\gamma_S = 1$ ) by simply assuming that the volume within which strangeness exactly vanishes is consistently lower than the overall volume (i.e. the sum of fireball volumes)<sup>15</sup>. This assumption would entail a canonical suppression for open strange particles such that the agreement with the data would be restored; a pure hadronic scheme would be thereby recovered. On the other hand, the mechanism of canonical suppression does not affect the yield of hidden strangeness particles, such as  $\phi$  meson, which do not carry any charge, still do need a suppression by  $\gamma_S^2$  to be in agreement with the data. Therefore, in the opinion of the author, resorting to the quark degrees of freedom to explain the actual pattern of strangeness production in EC and HIC is unavoidable. Thus, the observed differences between the two system might be the key to unveil the presence of a deconfined quark phase in HIC.

Analyses of hadronic multiplicities and ratios of them over a limited rapidity region<sup>16</sup> have found  $\gamma_S \simeq 1$ , particularly at RHIC ( $\Delta y = 1$ ). The difference between strange quark yield in full phase space and at midrapidity has been found at SPS as well<sup>6</sup>. It is still matter of debate whether this finding indicates the presence of a fully chemically equilibrated hadron gas in the central region, or it is rather an artefact of the kinematical cut.

What reinforces strangeness enhancement as a candidate QGP signature is the inability of microscopic transport models based on “conventional” hadronic physics to account for it. None of the mostly used models can attain the observed level of strange quark production unless forcing it by hand from the beginning<sup>8</sup>. Even though strangeness would be disproved as a QGP signature, the data has definitely demonstrated that HIC cannot be considered in this regard as an incoherent superposition of  $NN$  collisions and that there must be non-trivial communication between different subregions.

### 3.3 Flow and Kinetic Freeze-out

Flow implies a hydrodynamical collective expansion of the system which is sustained by the onset of pressure and pressure gradients in a single collision event. Thence, flow is an event-by-event phenomenon and involves the existence of matter cells moving with a collective velocity  $\beta(\mathbf{x})$ .

The so-called *radial flow* refers to its component in the transverse plane (with respect to the beam axis) and it has been studied by the inclusive  $p_T$  distributions of various particle species, which are frozen at the kinetic freeze-out. It must be emphasized that, although leading to the same  $p_T$  broadening effect on single-particle inclusive distribution as jet emission, flow

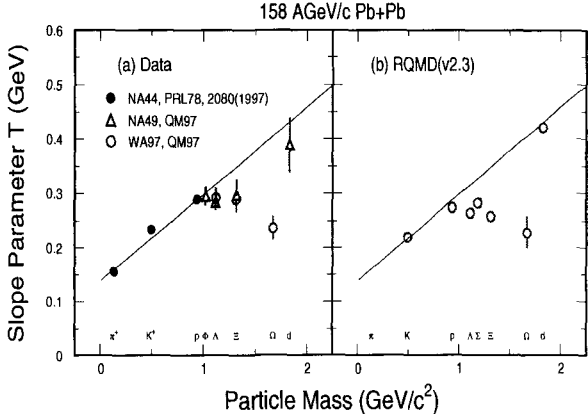


Figure 7. Slope parameter  $T_{slope}$  fitted with  $p_T$  spectra (left) of several particle species and predicted by a hadronic transport model (right) (from ref.<sup>18</sup>).

is a completely different physical phenomenon because, as has been mentioned, it implies a *collective* broadening of all particles in a single event instead of the occasional emission of a bunch of particles at very high  $p_T$ . Radial flow is measured by fitting inclusive  $p_T$  spectra of identified particles to the predicted shape in a transversely boosted thermal system:

$$\frac{d^2 N}{dm_T dy} = m_T^2 \cosh y \exp(-m_T \cosh y) I_0 \left( \frac{u_T p_T}{T} \right) \quad (4)$$

where  $m_T = \sqrt{p_T^2 + m^2}$ ,  $u_T = \beta_T \gamma_T$ . This formula can be applied to final (weakly decaying) measured hadrons provided that kinetic freeze-out occurs considerably later than chemical freeze-out, so that both primary hadrons and products from strong decays have enough time to re-thermalize. At low  $p_T$ , the above formula can be approximated with the no-flow one by replacing  $T$  with  $T_{app} = T + m\beta_T^2/2$ . In practice, the transverse spectra are fitted to a simpler formula,  $A m_T^\alpha \exp(-m_T/T_{slope})$  and  $T_{slope}$  quoted. In fact, it is very hard to disentangle temperature from flow velocity by fitting  $p_T$  spectra only, as they are strongly correlated.

The dependence of  $T_{slope}$  upon the particle mass is shown in Fig. 7 for Pb-Pb collisions at top SPS energy. The expected linear rise with the mass is broken by heavy weakly decaying particles. This finding is in agreement with hadronic transport models which predict an earlier decoupling of those particles due to their lower elastic cross-section with surrounding hadrons.

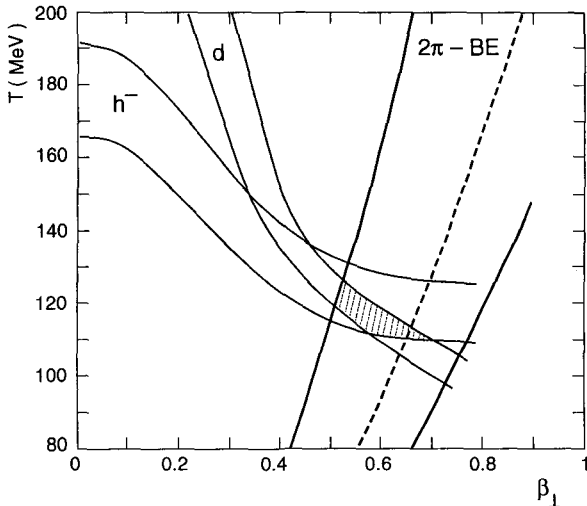
This is an evidence that kinetic freeze-out occurs later for light stable (with respect to weak interactions) particles than for heavy ones.

Another kind of flow which has drawn the attention of heavy ion physicists is the so-called *elliptic flow*. This phenomenon consists in an azimuthal (i.e. in the transverse plane with respect to the beam axis) anisotropy of particle emission in peripheral heavy ion collisions, when the impact parameter is comparable to nucleus size. In a simple geometrical model, the overlapping region of the two colliding nuclei in the transverse plane turns out to be almond-shaped. The anisotropy of this shape induces larger pressure gradients in the direction along the line connecting nuclei's centres than in its perpendicular direction. Thus, an enhanced flow along this direction is expected and, by this mechanism, an initial spacial anisotropy is turned into a momentum distribution anisotropy, a clear demonstration of the peculiar ability of this system to build up collective behaviours. Besides the impact parameter, the amount of elliptic flow also depends on how fast thermal equilibration at parton level occurs. Indeed, the maximal response to the anisotropy can be calculated with hydrodynamical models assuming thermal equilibrium from a given time  $\tau_0$  onwards. The comparison between actual RHIC data and hydrodynamical calculations in semi-peripheral collisions indicates an early thermalization time ( $\approx 0.5 \text{ fm}/c$ ) and energy densities well above the critical one<sup>17</sup>. This means that QGP would have been formed in Au-Au collisions at RHIC.

### 3.4 Bose-Einstein Correlations

Due to quantum statistics, the presence of identical bosons in the same phase space cell is favoured with respect to distinguishable particles. Therefore, the spectrum of the difference between momenta of identical boson pairs in the same event can be used to determine the size of the homogeneous emitting sources, at the kinetic freeze-out. This technique has been introduced first in astrophysics by Hanbury Brown and Twiss to determine the size of distant stars. It has been borrowed in high energy physics in the early '60s and extensively used ever since. The actually used parametrizations of the source are nowadays more complex than earligh ones and refined analyses in HIC allow to determine both longitudinal and transverse size of the source as well as its lifetime. Overall, the radii measured in Pb-Pb collisions by using charged pions ( $\approx 5 - 6 \text{ fm}$ ) are definitely larger than those in EC ( $\approx 1 \text{ fm}$ ), confirming the expected formation of large homogeneous thermalized regions over many hadronic volumes.

Another very interesting feature of Bose-Einstein correlations is the de-



$$T = 120 \pm 12 \text{ MeV}$$

$$\beta_{\perp} = 0.55 \pm 0.12$$

Figure 8. Kinetic freeze-out temperature and radial flow velocity determined by the combined analysis of source size and transverse momentum spectrum slopes (from ref.<sup>20</sup>).

pendence of the transverse radius of the source on the radial flow velocity, which, in a hydrodynamical model can be calculated as<sup>19</sup>:

$$r_{\perp}(m_T) \simeq \frac{R}{\sqrt{1 + 5m_T\beta_T^2/T}} \quad (5)$$

This dependence has been studied in detail and the behaviour predicted by above formula confirmed. The analysis of the data then gives information on the ratio  $\beta_T^2/T$  and, thereby, an independent relationship between  $T$  and  $\beta_T$  besides that provided by the inclusive single-particle  $p_T$  spectra. Moreover, this relationship yields a parabolic constraint in the  $(\beta_T, T)$  plane which is very different in shape from that relevant to the  $p_T$  spectra. By locating the intersection between the two  $1\sigma$  bands in the  $(\beta_T, T)$  plane, the kinetic freeze-out temperature and radial flow velocity can be determined. This is shown in Fig. 8 for Pb-Pb collisions at top SPS energy; this method yields a temperature around 120 MeV, 40 MeV lower than the chemical freeze-out

temperature, and a flow velocity about 0.55. The same analysis at RHIC is not available yet.

## 4 Conclusions

There is a great deal of theoretical and experimental ongoing work in this field, aimed at understanding the best signatures of the QGP formation and measuring them. The lack of a well established theoretical description based on QCD first principles makes the use of models necessary, especially when dealing with soft observables. This is thus a very good opportunity to study strong interactions in the soft regime independently of QGP discovery. In this respect, though a conclusive evidence is still missing, there are now many clues in favour of QGP: strangeness enhancement, early thermalization as suggested by the elliptic flow analysis and the onset of peculiar collective phenomena. Investigations will certainly continue and be refined both at low energy (an experimental programme to scan the few GeV  $\sqrt{s_{NN}}$  region not covered by AGS and SPS, is envisaged at SIS) and at high energy with the forthcoming data from RHIC and later at LHC.

## References

1. see for instance: F Karsch in Proc. of *QCD@work*, AIP Conf. Proc. 602 (2001) 323, hep-lat 0109017 and references therein.
2. U Heinz in Proc. of *QCD@work*, AIP Conf. Proc. 602 (2001) 281, hep-ph 0109006.
3. F Becattini *et al*, *Phys. Rev. C* **64**, 024901 (2001).
4. F Becattini, G Passaleva, *Eur. Phys. J. C* **23**, 551 (2002).
5. F Becattini, to appear in Proc. of *Statistical QCD*.
6. F Becattini, hep-ph 0202071, to appear in Proc. of *Strange Quarks in Matter 2001*, *J. Phys. G*.
7. F Becattini, *Z. Phys. C* **69**, 485 (1996); F Becattini in Proc. of *Universality features of multihadron production and the leading effect*, p. 74, hep-ph 9701275; F Becattini and U Heinz, *Z. Phys. C* **76**, 269 (1997).
8. U Heinz, *Nucl. Phys. A* **661**, 140 (1999) and references therein.
9. R Stock, *Phys. Lett. B* **456**, 277 (1999).
10. R Hagedorn, *Nuovo Cimento Suppl.* **3**, 147 (1965).
11. F Antinori *et al*, *Phys. Lett. B* **449**, 401 (1999).
12. J Rafelski, B Muller, *Phys. Rev. Lett.* **48**, 1066 (1982).
13. F Becattini, M Gazdzicki, J Sollfrank, *Eur. Phys. J. C* **5**, 143 (1998).
14. J Sollfrank *et al*, *Nucl. Phys. A* **638**, 399c (1998).

15. S Hamieh *et al*, *Phys. Lett. B* **486**, 61 (2000).
16. P Braun Munzinger *et al* *Phys. Lett. B* **518**, 41 (2001).
17. P Kolb, J Sollfrank and U Heinz, *Phys. Rev. C* **62**, 054909 (2000).
18. R Stock, *Nucl. Phys. A* **661**, 282 (1999)
19. S Chapman, J Nix, U Heinz, *Phys. Rev. C* **52**, 2694 (1995).
20. H Appelshäuser *et al*, *Eur. Phys. J. C* **2**, 661 (1998).

## HEAVY ION COLLISION PHENOMENOLOGY II - HARD PROBES -

M. NARDI

*Dipartimento di Fisica Teorica dell'Università di Torino and  
Istituto Nazionale di Fisica Nucleare, Sezione di Torino,  
via P.Giuria 1, I-10125 Torino, Italy*

This contribution is short discussion of hard probes in nuclear collisions, in particular of photon and dilepton production.

### 1 Introduction

The aim of ultrarelativistic heavy ion collisions is to produce and reveal a new phase of matter: the quark-gluon plasma (QGP), in which quarks and gluons are deconfined and weakly interacting, as predicted by QCD in the regime of asymptotic freedom.

Many signals have been proposed to probe the properties of this new phase. They are essentially divided into two classes: the “hard probes”, originated in the early stage of the collision, giving information about the QGP in a direct way, and the “soft probes”, generated after the decay of the plasma. The latter are discussed in the contribution of F. Becattini, in these proceedings.

The hard processes are not strongly affected by the surrounding hadronic matter. For example, photons and dilepton pairs produced in the QGP formed at the early stage of a nucleus-nucleus collision are easily emitted outside the plasma, carrying information about it. Other hard signals are jet quenching and  $J/\psi$  suppression : they can test the nature of the medium they traverse. The latter probes have been discussed by H. Satz in these proceedings, therefore this contribution will be mainly focused on photon and dilepton production.

### 2 Direct Photons

During the QGP phase, the photon production occurs mostly through quark-antiquark annihilation ( $q\bar{q} \rightarrow g\gamma$ ) and by absorption of a gluon by a quark followed by the emission of a photon ( $qg \rightarrow q\gamma$ ,  $\bar{q}g \rightarrow \bar{q}\gamma$ ). These processes are shown in Fig. (1) (the process  $q\bar{q} \rightarrow \gamma\gamma$  is purely electromagnetic, therefore it is much weaker than the process involving a gluon).

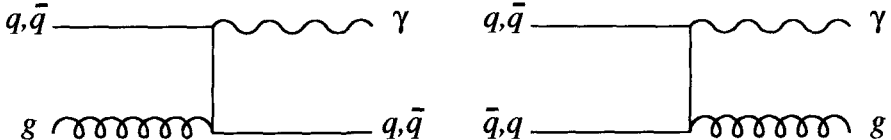


Figure 1. Lowest order diagrams for the photon production in the QGP phase; left diagram: gluon absorption by a quark or antiquark (“Compton” scattering); right diagram: quark-antiquark annihilation

The emitted photon has, in the strongly interacting medium, a long mean free path, therefore it easily escapes and carries information on the thermodynamical state of the medium at the moment of its emission.

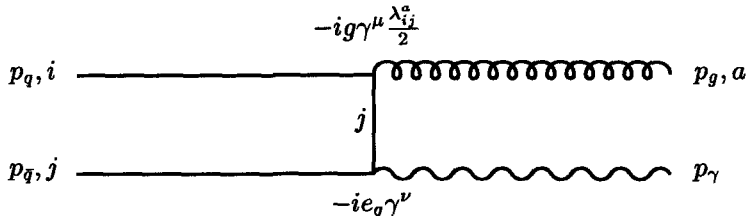


Figure 2. Lowest order diagram for the  $q\bar{q}$  annihilation. The labels indicate the particle momenta and colour state (indices  $i, j = 1, 2, 3$  for the  $q, \bar{q}$ , index  $a = 1, \dots, 8$  for the gluon);  $g$  is the strong coupling constant ( $g^2 = 4\pi\alpha_s$ ),  $e_q$  is the quark (antiquark) electric charge.

## 2.1 Thermal Rate from the QGP

The photon production rate in the deconfined phase can be obtained from the matrix elements of these basic processes, using the distribution functions of the participating partons. In the case of quark-antiquark annihilation, the rate can be written as (the particle momenta are indicated in Fig. (2)) :

$$\frac{dN_{ann}^\gamma}{d^4x d^3p_\gamma} = \frac{1}{(2\pi)^3 2E_\gamma} \int \frac{d^3p_q}{(2\pi)^3 2E_q} \frac{d^3p_{\bar{q}}}{(2\pi)^3 2E_{\bar{q}}} \frac{d^3p_g}{(2\pi)^3 2E_g} n_q(E_q) n_{\bar{q}}(E_{\bar{q}}) [1 + n_g(E_g)] \sum \langle |\mathcal{M}|^2 \rangle (2\pi)^4 \delta^{(4)}(P_q + P_{\bar{q}} - P_g - P_\gamma). \quad (1)$$

In Eq. (1),  $P_\gamma = (E_\gamma, \vec{p}_\gamma)$  is the 4-momentum of the produced photon, the momenta of the other particles being indicated in a similar way.  $\sum \langle |\mathcal{M}|^2 \rangle$

is the modulus square of the matrix element of the process, averaged over the initial spin states and summed over the final ones. The rate is given by a convolution with the distribution functions  $n_\alpha(E_\alpha)$  for the various species. In an equilibrated ideal gas at temperature  $T$ ,  $n_\alpha(E_\alpha)$  is the Bose-Einstein or the Fermi-Dirac distribution for gluons or quarks (antiquarks) respectively. The factor  $[1 + n_g(E_g)]$  describes the Bose enhancement of the gluon in the final state. Note that a similar factor is missing for the photon: it is assumed that, due to its weaker coupling with the medium ( $\gamma$  has only electromagnetic interaction, whereas the gluon interacts strongly) the photon decouples before reaching thermodynamical equilibrium.

At the lowest order, the cross-section can be calculated in a straightforward way and turns out to be :

$$\frac{d\sigma}{dt}(q\bar{q} \rightarrow \gamma g) = 4 \left( \frac{e_q}{e} \right)^2 \frac{8\pi\alpha_s\alpha}{s(s-4m_q^2)} \left\{ \left( \frac{m_q^2}{t-m_q^2} + \frac{m_q^2}{u-m_q^2} \right)^2 + \left( \frac{m_q^2}{t-m_q^2} + \frac{m_q^2}{u-m_q^2} \right) - \frac{1}{4} \left( \frac{t-m_q^2}{u-m_q^2} + \frac{u-m_q^2}{t-m_q^2} \right) \right\}, \quad (2)$$

where  $m_q$  is the quark mass in the plasma<sup>1</sup>, and the Mandelstam variables  $s = (P_q + P_{\bar{q}})^2$ ,  $t = (P_q - P_\gamma)^2$ ,  $u = (P_{\bar{q}} - P_\gamma)^2$  have been used. The multiplicative factor 4 in Eq. (2) comes from the sum over the colour states of  $q$ ,  $\bar{q}$  and  $g$ .

In Eq. (2), the denominators can be rewritten as:

$$\begin{aligned} t - m_q^2 &= -2 P_\gamma \cdot P_q = -2 E_\gamma (E_q - |\vec{p}_q| \cos \theta_{q\gamma}) \\ u - m_q^2 &= -2 P_\gamma \cdot P_{\bar{q}} = -2 E_\gamma (E_{\bar{q}} - |\vec{p}_{\bar{q}}| \cos \theta_{\bar{q}\gamma}); \end{aligned} \quad (3)$$

From Eq. (2) and (3) one easily sees that the distribution of the emitted photons is peaked for  $\theta_{q\gamma} = 0$  and  $\theta_{\bar{q}\gamma} = 0$ , i.e. in the directions of the incoming quark or antiquark.

In the high energy limit, where the quark mass can be neglected,  $\theta_{q\gamma} = 0$  implies  $E_\gamma = E_q$ , or  $P_\gamma \simeq P_q$ . Similarly, if the photon is emitted along the antiquark direction ( $\theta_{\bar{q}\gamma} = 0$ ), one finds  $P_\gamma \simeq P_{\bar{q}}$ .

These results lead to the following conclusions: the photon produced in the quark-antiquark annihilation carries approximately the same energy and momentum of one of the two incoming particles. Consequently, also the emitted gluon carries (approximately) the same energy and momentum of the other particle. Therefore, an analysis of the direct photons can bring informations on the properties, i.e. energy and momentum distribution, of the deconfined medium.

Analogous considerations hold for the “Compton scattering” in Fig. (1). Instead of Eq. (1) we have ( $P_{q_1}$  and  $P_{q_2}$  are, respectively, the momenta of the incoming and outgoing quark or antiquark) :

$$\frac{dN_C^\gamma}{d^4x \, d^3p_\gamma} = \frac{1}{(2\pi)^3 2E_\gamma} \int \frac{d^3p_{q_1}}{(2\pi)^3 2E_{q_1}} \frac{d^3p_{q_2}}{(2\pi)^3 2E_{q_2}} \frac{d^3p_g}{(2\pi)^3 2E_g} n_q(E_{q_1}) n_g(E_g)$$

$$[1 - n_q(E_{q_2})] \sum \langle |\mathcal{M}|^2 \rangle (2\pi)^4 \delta^{(4)}(P_{q_1} + P_g - P_{q_2} - P_\gamma), \quad (4)$$

and the corresponding cross-section reads :

$$\frac{d\sigma}{dt}(qg \rightarrow q\gamma) = \left(\frac{e_q}{e}\right)^2 \frac{8\pi\alpha_s\alpha}{(s - m_q^2)^2} \left\{ \left( \frac{m_q^2}{s - m_q^2} + \frac{m_q^2}{u - m_q^2} \right)^2 + \right.$$

$$\left. + \left( \frac{m_q^2}{s - m_q^2} + \frac{m_q^2}{u - m_q^2} \right) - \frac{1}{4} \left( \frac{s - m_q^2}{u - m_q^2} + \frac{u - m_q^2}{s - m_q^2} \right) \right\}. \quad (5)$$

From Eq. (5) one can extract some information about the energy and momentum distribution of the emitted photon, analogously to what done from Eq. (2) : the produced photon carries approximately the same energy and momentum of the incident quark (or antiquark), while the initial gluon turns into the final  $q$  (or  $\bar{q}$ ) with approximately the same energy and momentum.

The complete calculation of the photon production rate is rather complicated. First of all, using only bare propagators and vertices for gauge theories (QED, QCD) at finite temperature, one finds IR divergences and gauge dependent results<sup>2,3</sup>. The reason for this unphysical behaviour is that perturbative QCD at finite temperature is incomplete, i.e., higher order diagrams contribute to lower order in the coupling constant<sup>4</sup>. This problem is solved by the “Hard Thermal Loop” (HTL) approximation<sup>5,6,7</sup>, which is equivalent to the high temperature limit. The HTL diagrams have internal loops with momenta (of the order  $T$ ) much larger than the ones of the external particles (of the order  $gT$ ,  $g \ll 1$ ), and can be resummed into effective propagators and vertices.

With the HTL technique, consistent results (i.e. gauge independent) can be obtained for physical quantities. In many cases, the IR singularities are removed to leading order (for other cases, where singularities still survive, an improved HTL resummation scheme has been proposed<sup>8</sup>); at the same time, important medium effects, such as effective parton masses, Debye screening and Landau damping, are properly taken into account.

The HTL theory has been calculated, so far, up to 2-loop diagrams. Recent studies have also investigated the 3-loop contributions, and the extensions

to finite baryon density and to a non-equilibrated medium.

The HTL resummation technique has been applied to other observables of the QGP: parton energy loss, thermalization time of quarks and gluons, dilepton production rates.

## *2.2 Thermal Rate from the Hadron Gas and Prompt Photons*

Photons are not only emitted by the deconfined medium, but will be produced during the subsequent phases of the evolution of the system. The QGP evolves, cools down and eventually decays in an interacting, hadronic gas, where reactions such as  $\rho\pi^\pm \rightarrow \gamma\pi^\pm$ ,  $\pi^+\pi^- \rightarrow \gamma\gamma$  and many others, take place. After the freeze-out, when all interactions stop, a new source of photon will be the hadronic decays. In addition to the photons coming from the final state, there are the “prompt” photons, i.e. the ones produced in the primary nucleon-nucleon collisions, before the formation of the deconfined medium. Prompt photons and photons originated from hadronic interactions and decays constitute a huge background (the ratio signal to background is approximately 0.2), therefore their contribution must be evaluated with high accuracy, in order to identify the real QGP radiation.

In contrast to the QGP, for which there is a well defined theory, the QCD, the hadronic interaction phase can be studied only with effective theories. There are many examples of such theories in the literature : they differ for the number and/or species of hadrons forming the final gas, for the initial conditions, for the relative abundances of hadronic species, for the effective Lagrangians used to describe interactions between particles. In general, a few free parameters are tuned to reproduce hadron masses and widths, then numerical calculations predict the number and the energy distribution of the photon in final state.

Many models consider also the role of medium effects on particle properties, like change of mass or width of vector mesons which can have significant consequences on the photon production<sup>9,10,11,12</sup>.

All these effects give rise to predictions for the photon spectrum in the final state that differ by factors 2 or 3. In addition to the uncertainty in the hadronic production mechanism of photons, there is the evolution of the system: the hadron gas is not equilibrated, it expands and cools down. Therefore the spectrum of emitted photon changes with time. To get a realistic answer from the calculation, one has to convolute the production rates with the space-time evolution of the system, described by hydrodynamic expansion<sup>13</sup>. The assumption and approximations of the hydrodynamical models are another source of uncertainties in evaluating the contribution to the photon spectrum

from the hadronic medium.

All these ambiguities in the theoretical prediction of photon production constitute a very serious problem. It is even possible, in principle, to explain the photon production without introducing a phase transition, i.e. with normal hadronic reactions alone. The crucial test to discriminate between different models and interpretations would be to compare the theoretical predictions to experimental results taken at different energies and/or different interacting nuclei (including proton-nucleus collisions). A successful model should reproduce, with a single set of parameters, all experimental data. The rich program of RHIC and LHC accelerators will put severe constraints to the existing models.

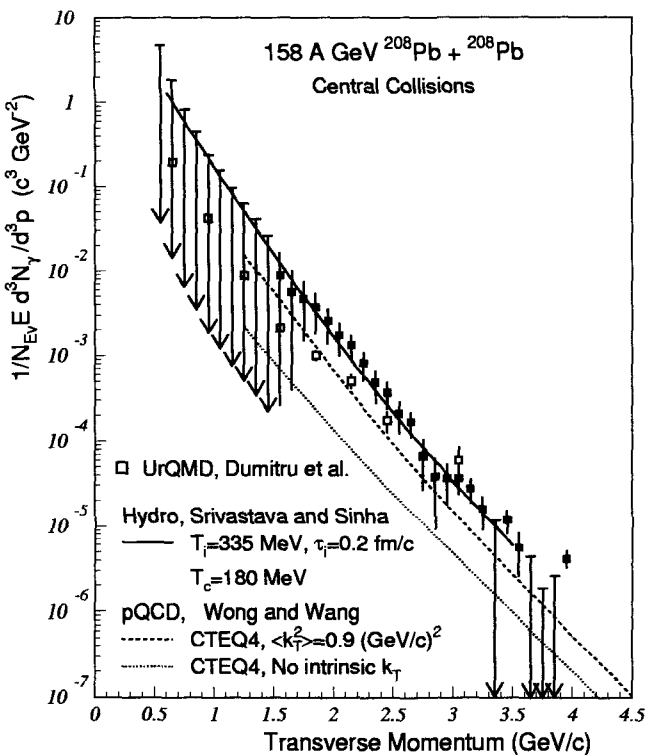


Figure 3. The invariant direct photon multiplicity for central Pb-Pb collisions at SPS (WA98 Collab.), compared to some theoretical predictions (from <sup>15</sup>).

### 2.3 Comparison with experiment

At the SPS, measurement of the direct photon production has been performed, for instance, by the WA80 Collaboration with  $^{16}O$  and  $^{32}S$  beams<sup>14</sup>. No evidence for direct photon production (i.e. excess over hadronic sources) was found in  $O - Au$  and  $S - Au$  collisions. The WA98 Collaboration has collected data for  $Pb - Pb$  collisions at  $\sqrt{s_{NN}} = 17.3$  GeV<sup>15</sup>, showing a significant direct photon excess only in central collisions with respect to what was expected from ordinary hadronic matter alone (see Fig.(3)). However, the uncertainties in the theoretical prediction are such that no final conclusion can be extracted about the formation of deconfined matter.

The situation at RHIC and LHC is more promising: the QGP is expected to be formed at much higher temperature and energy density and with a longer life-time; the contribution to the total production of photons from the deconfined phase, therefore, will be more important than at SPS and it should be possible to distinguish between different scenarios.

## 3 Thermal dileptons

In the QGP phase, pairs of dileptons ( $\ell^+ \ell^-$ , where  $\ell$  denotes both an electron or a muon) are produced via the annihilation of a quark and an antiquark.

The produced leptons do not interact strongly with the free quarks in the deconfined phase; therefore, as in the case of the photons, they quickly decouple from the medium and carry informations about its temperature and momenta distribution.

The variables characterizing the dilepton pair are the total four-momentum  $q^\mu \equiv p_{\ell^+}^\mu + p_{\ell^-}^\mu$  and the invariant mass  $M^2 \equiv q_\mu q^\mu$ .

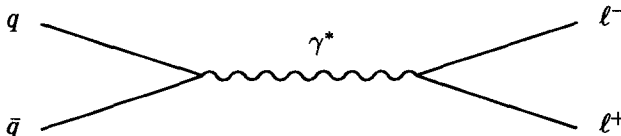


Figure 4. Lowest order diagram for dilepton production in the QGP phase

At sufficiently high densities and temperatures, in the regime of asymptotic freedom, the rate of dilepton production can be calculated with the perturbation theory. At the lowest order in the strong coupling constant, the

process is purely electromagnetic, as shown in Fig. (4), and the rate can be expressed as<sup>16</sup>

$$\frac{dN_{\ell\ell}}{d^4q} = \int \frac{d^3p_q}{(2\pi^3)^3} \frac{d^3p_{\bar{q}}}{(2\pi^3)^3} \sum_q v_{q\bar{q}} \sigma_{q\bar{q} \rightarrow \ell\ell}(M) f_q(P_q) f_{\bar{q}}(P_{\bar{q}}) \delta^{(4)}(q - P_q - P_{\bar{q}}), \quad (6)$$

where the cross-section (averaged over colour), for a given quark flavor  $q$ , is :

$$\begin{aligned} \sigma_{q\bar{q} \rightarrow \ell\ell}(M) = e_q^2 \frac{4\pi\alpha^2}{3M^2} & \left(1 - \frac{4m_q^2}{M^2}\right)^{-1/2} \left(1 - \frac{4m_\ell^2}{M^2}\right)^{1/2} \times \\ & \times \left(1 + 2\frac{m_q^2 + m_\ell^2}{M^2} + 4\frac{m_q^2 m_\ell^2}{M^4}\right). \end{aligned} \quad (7)$$

Here  $v_{q\bar{q}}$  is the relative velocity between quark and antiquark, and  $f_q$  ( $f_{\bar{q}}$ ) are the quark (antiquark) momentum distribution, including spin-color degeneracy factors (for an equilibrated plasma, the quark and antiquark momentum distributions have the Fermi-Dirac form).

Perturbative QCD corrections have been evaluated<sup>17</sup> and found to be appreciable for  $M$  smaller than 1 GeV, where the strong coupling constant  $\alpha_s$  is comparable with the electromagnetic one. Furthermore, since for the plasma phase at temperature slightly above  $T_c$ ,  $\alpha_s$  is large, non-perturbative effects can be important<sup>16,18</sup>.

Another contribution to the dilepton radiation comes from the chiral phase transition following the QGP phase: if the transition from the chirally symmetric plasma to the chirally broken phase is sufficiently fast, regions of misaligned condensate can be formed. The so called “Disoriented Chiral Condensate” (DCC), in which  $\langle \vec{\pi} \rangle = \langle \bar{q}\gamma_5 \vec{\tau} q \rangle \neq 0$  is realized instead of the standard ground state,  $\langle \sigma \rangle = \langle \bar{q}q \rangle \neq 0$ <sup>19</sup>. This phenomenon can be detected in event-by-event analysis of nuclear collisions through anomalous fluctuations in the number of pions in a rather narrow window of invariant mass ( $M \simeq 2m_\pi$ ).

### 3.1 Comparison with experiment

As for the case of photon production, to extract the effective dilepton radiation from the QGP it is necessary to subtract, from the experimental data, the contributions from other sources. First of all, the Drell-Yan pair production occurring at the very early stages of the nucleus-nucleus collision, as a consequence of the primary interactions of nucleons. A quark from a nucleon

of nucleus "A" and an antiquark from a nucleon of nucleus "B" annihilate and produce (via the process described, in the lowest order in perturbation theory, by Fig.(4)) a dilepton pair. The formula ruling this process is very similar to Eq. 6, the only difference being the momentum distribution functions: instead of free quarks and antiquarks, there are now partons confined in normal hadrons; the momentum distribution functions are, therefore, the ones extracted from deep inelastic scattering experiments (taking into account nuclear effects, like shadowing, EMC).

The Drell-Yan (DY) cross section is calculable from first principles, i.e. from perturbative QCD (including higher order corrections), and is in good agreement with experiment. The DY process is the only contribution to the dilepton production for  $M$  above the  $J/\psi$  and  $\psi'$  masses, in this region, therefore, it can be identified and extrapolated to lower invariant masses.

The contribution to the dilepton production originated from hadronic interactions in the final state and particle decays is important only for invariant masses well below the  $J/\psi$  peak. The cross-sections for these processes can be evaluated with effective theories, analogously to the photon production discussed in the previous section.

The measurement of dilepton spectra in heavy ion collisions has been performed at the SPS by three collaborations<sup>20,21</sup>: CERES/NA45 (low mass region), HELIOS-3 (up to the  $J/\psi$  mass) and NA50 (up to very high masses).

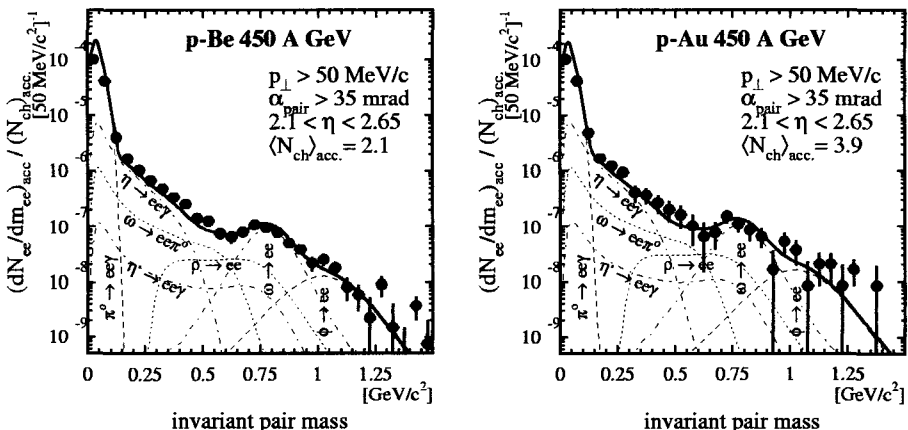


Figure 5. Dilepton invariant mass spectrum of proton-nucleus at SPS energy, measured by CERES Collab.<sup>22</sup> compared to the superposition of all hadronic sources.

At RHIC energies, similar measurements will be done by the PHENIX collaboration. CERES and HELIOS-3 found that the low-mass dilepton production in proton-nucleus collisions can be understood as final state hadron decays. Fig.(5) shows CERES results for  $p - Be$  and  $p_A u$  collisions at the highest SPS energy. The invariant mass distribution of dilepton originated by various particle decays are evaluated, the normalization is fitted to the observed multiplicity and the sum of all channels is compared to the experimental data: the agreement is indeed very good.

This is not the case for nucleus-nucleus collisions, where the theoretical predictions strongly underestimate the observed spectra in the region below the  $\rho$  peak (Fig(6)). On the other hand, in a deconfined scenario, with chiral symmetry restoration, the observed excess can be explained by a decreasing of the  $\rho$  mass at finite temperature and density<sup>24</sup>.

Unfortunately, not everything is completely under control yet, in particular, off-equilibrium effects in the final hadronic gas can be important, therefore no final conclusions about the excess of the low-mass dilepton can be obtained.

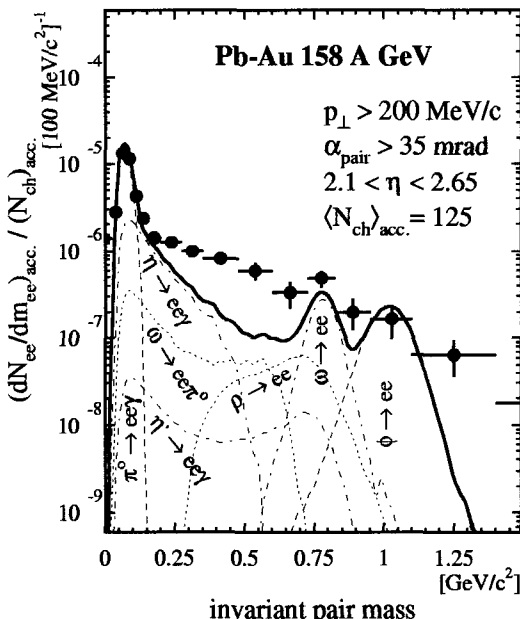


Figure 6. Dilepton invariant mass spectrum of nucleus-nucleus collisions at SPS energy, measured by CERES Collab.<sup>23</sup>, compared to the superposition of all hadronic sources.

## 4 Conclusions

The data on thermal photons and dilepton production have raised great interest in the scientific community. Many models have been proposed but it is not possible, yet, to distinguish between different, and sometimes even opposite, scenarios. Very useful are the data of proton-nucleus experiments: these collisions, where the QGP is not expected to form, allow the determination of the behaviour of normal hadronic matter<sup>25</sup>, and constitute a good reference starting point for nucleus-nucleus collisions. In the future, new data from RHIC, at different energies and/or nuclei (including  $p - A$  collisions) will certainly help in discriminating between models and interpretations.

## References

1. K. Kajantie and P. V. Ruuskanen, *Phys. Lett. B* **121**, 352 (1983).
2. K. Kajantie and J. Kapusta, *Ann. Phys. (N.Y.)* **160**, 477 (1985).
3. J. C. Parikh, P. J. Siemens, J. A. Lopez, *Pramana* **32**, 555 (1989).
4. R. D. Pisarski, *Phys. Rev. Lett.* **63**, 1129 (1989).
5. E. Braaten and R. D. Pisarski, *Nucl. Phys. B* **337**, 569 (1990).
6. J. Frenkel and J.C. Taylor, *Nucl. Phys. B* **334**, 199 (1990)
7. J.P. Blaizot, E. Iancu, *Nucl. Phys. B* **390**, 589 (1993); *Phys. Rev. Lett.* **70**, 3376 (1993); *Nucl. Phys. B* **417**, 608 (1994); *Phys. Rev. D* **63**, 065003 (2001).
8. F. Flechsig and A. K. Rebhan, *Nucl. Phys. B* **464**, 279 (1996).
9. M. A. Halász, J. V. Steele, G. Li, G. E. Brown, *Phys. Rev. C* **58**, 365 (1998).
10. S. Sarkar, J. Alam, P. Roy, A. K. Dutt-Mazumder, B. Dutta-Roy, B. Sinha, *Nucl. Phys. A* **634**, 206 (1998).
11. C. Song and G. Fai, *Phys. Rev. C* **58**, 1689 (1998).
12. P. Roy, S. Sarkar, J. Alam, B. Sinha, *Nucl. Phys. A* **653**, 277 (1999).
13. T. Peitzmann, M. H. Thoma, *Phys. Rept.* **364**, 175 (2002).
14. WA80 Collab., *Phys. Rev. Lett.* **76**, 3506 (1996); *Z. Phys. C* **51**, 1 (1991).
15. WA98 Collab., *Phys. Rev. Lett.* **85**, 3595 (2000); nucl-ex/0006007.
16. R. Rapp, J. Wambach, *Adv. Nucl. Phys.* **25**, 1 (2000)
17. E. Braaten, R.D. Pisarski, T. C. Wang, *PRL* **64**, 2242 (1990)
18. R. Rapp, S. Schäfer, E.V. Shuryak, M. Velkovsky, *Annals Phys.* **280**, 35 (1999)
19. K. Rajagopal, F. Wilczek, *Nucl. Phys. B* **404**, 577 (1993)
20. A. Drees, *Nucl. Phys. A* **610**, 536 (1996)

21. L. Kluberg, *Nucl. Phys. A* **661**, 300 (1999)
22. G. Agakishiev et al., *Eur. Phys. J C* **4**, 231 (1998)
23. G. Agakishiev et al., *Nucl. Phys. A* **638**, 159 (1998)
24. G.E. Brown, M. Rho, *Phys. Rev. Lett.* **66**, 2720 (1991)
25. H. Satz, these proceedings.

# NON-CONVENTIONAL STATISTICAL EFFECTS IN RELATIVISTIC HEAVY-ION COLLISIONS

W.M. ALBERICO

*Dipartimento di Fisica, Università di Torino, Italy*  
*INFN - Sezione di Torino, Italy*

A. LAVAGNO<sup>1</sup> AND P. QUARATI<sup>2</sup>

*Dipartimento di Fisica, Politecnico di Torino, Italy*

<sup>1</sup>*INFN, Sezione di Torino, Italy*

<sup>2</sup>*INFN, Sezione di Cagliari, Italy*

We show that non-conventional statistical effects (due to the presence of long range forces, memory effects, correlations and fluctuations) can be very relevant in the interpretation of the experimental observables in relativistic heavy-ions collisions. Transverse mass spectrum, transverse momentum fluctuations and rapidity spectra are analysed in the framework of the non-extensive statistical mechanics.

## 1 Introduction and motivations

Most of the theoretical analyses related to observables in relativistic heavy-ion collisions involve (implicitly or explicitly) the validity of the standard Boltzmann-Gibbs statistical mechanics. In particular, if the thermal equilibrium is achieved, the Maxwell-Boltzmann (MB) distribution (Fermi-Dirac or Bose-Einstein distribution if quantum statistical effects are not negligible) is assumed to hold. When the system approaches equilibrium, the phase-space distribution should be derived as a stationary state of the dynamical kinetic evolution equation. It is well known that in the absence of non-Markovian memory effects, long-range interactions and local correlations, the MB distribution is obtained as a steady state solution of the kinetic Boltzmann equation. However, it is a rather common opinion that, because of the extreme conditions of density and temperature in ultrarelativistic heavy ion collisions, memory effects and long-range color interactions give rise to the presence of non-Markovian processes in the kinetic equation affecting the thermalization process toward equilibrium as well as the standard equilibrium distribution<sup>1,2,3,4</sup>.

The aim of the present contribution is to explore, from a phenomenological point of view, the relevance of the above mentioned statistical effects that can influence the dynamical evolution of the generated fireball toward the freeze-out stage and, as a consequence, the physical observables.

## 2 Generalized non-extensive statistics

A quite interesting generalization of the conventional Boltzmann–Gibbs statistics has been recently proposed by Tsallis<sup>5</sup> and proves to be able to overcome the shortcomings of the conventional statistical mechanics in many physical problems, where the presence of long-range interactions, long-range microscopic memory, or fractal space–time constraints hinders the usual statistical assumptions.

The Tsallis generalized thermostatistics is based upon the following generalization of the entropy<sup>5</sup>

$$S_q = \frac{1}{q-1} \sum_{i=1}^W p_i (1 - p_i^{q-1}), \quad (1)$$

where  $p_i$  is the probability of a given microstate among  $W$  different ones and  $q$  is a fixed real parameter. The new entropy has the usual properties of positivity, equiprobability, concavity and irreversibility, preserves the whole mathematical structure of thermodynamics and reduces to the conventional Boltzmann–Gibbs entropy  $S = -\sum_i p_i \log p_i$  in the limit  $q \rightarrow 1$ .

The single particle distribution function is obtained through the usual procedure of maximizing the Tsallis entropy under the constraints of keeping constant the average internal energy and the average number of particles. For a dilute gas of particles and/or for  $q \approx 1$  values, the average occupational number can be written in a simple analytical form

$$\langle n_i \rangle_q = \frac{1}{[1 + (q-1)\beta(E_i - \mu)]^{1/(q-1)} \pm 1}, \quad (2)$$

where the + sign is for fermions, the – for bosons and  $\beta = 1/T$ . In the limit  $q \rightarrow 1$  (extensive statistics), one recovers the conventional Fermi–Dirac and Bose–Einstein distribution. under the same conditions, but in the classical limit, one has the following generalized Maxwell–Boltzmann distribution<sup>5</sup>:

$$\langle n_i \rangle_q = [1 + (q-1)\beta(E_i - \mu)]^{1/(1-q)}. \quad (3)$$

When the entropic  $q$  parameter is smaller than 1, the distributions (2) and (3) have a natural high energy cut-off:  $E_i \leq 1/[\beta(1-q)] + \mu$ , which implies that the energy tail is depleted; when  $q$  is greater than 1, the cut-off is absent and the energy tail of the particle distribution (for fermions and bosons) is enhanced. Hence the nonextensive statistics entails a sensible difference of the particle distribution shape in the high energy region with respect to the standard statistics. This property plays an important rôle in the interpretation of the physical observables, as it will be shown in the following.

### 3 Transverse mass spectrum and momentum fluctuations

Let us consider the transverse momentum distribution of particles produced, e.g., in relativistic heavy ion collisions: it depends on the phase-space distribution and usually an exponential shape is employed to fit the experimental data. This shape is obtained by assuming a purely thermal source with a MB distribution. High energy deviations from the exponential shape are taken into account by introducing a dynamical effect due to collective transverse flow, also called blue-shift.

Let us consider a different point of view and argue that if long tail time memory and long-range interactions are present, the MB distribution must be replaced by the generalized distribution (3). Limiting ourselves to consider here only small deviations from standard statistics ( $q - 1 \approx 0$ ); then at first order in  $(q - 1)$  the transverse mass spectrum can be written as

$$\frac{dN}{m_\perp dm_\perp} = C m_\perp \left\{ K_1(z) + \frac{(q-1)}{8} z^2 [3 K_1(z) + K_3(z)] \right\}, \quad (4)$$

where  $K_i$  are the modified Bessel function at the  $i$ -order.

The above equation is able to reproduce very well the transverse momentum distribution of hadrons produced in S+S collisions (NA35 data<sup>6</sup>) providing we take  $q = 1.038$ <sup>7</sup>. Furthermore, it is easy to see that at first order in  $(q - 1)$  from Eq.(4), the generalized slope parameter takes the following form:

$$T_q = T + (q - 1) m_\perp. \quad (5)$$

Hence nonextensive statistics predicts, in a purely thermal source, a generalized  $q$ -blue shift factor at high  $m_\perp$ ; moreover this shift factor is not constant but increases (if  $q > 1$ ) with  $m_\perp = \sqrt{m^2 + p_\perp^2}$ , where  $m$  is the mass of the detected particle. Such a behavior has been observed in the experimental NA44 results<sup>8</sup>.

Another observable very sensitive to non-conventional statistical effects are the transverse momentum fluctuations. In fact, in the framework of non-extensive statistics, the particle fluctuation  $\langle \Delta n^2 \rangle_q = \langle n^2 \rangle_q - \langle n \rangle_q^2$  is deformed, with respect to the standard expression, as follows

$$\langle \Delta n^2 \rangle_q \equiv \frac{1}{\beta} \frac{\partial \langle n \rangle_q}{\partial \mu} = \frac{\langle n \rangle_q}{1 + (q-1)\beta(E-\mu)} (1 \mp \langle n \rangle_q), \quad (6)$$

where  $E$  is the relativistic energy  $E = \sqrt{m^2 + p^2}$ .

The fluctuations of an ideal gas of fermions (bosons), expressed by Eq.(6), are still suppressed (enhanced) by the factor  $1 \mp \langle n \rangle_q$  (as in the standard case)

but this effect is modulated by the factor  $[1 + (q - 1)\beta(E - \mu)]^{-1}$ . Therefore the fluctuations turn out to be increased for  $q < 1$  and are decreased for  $q > 1$ . Very good agreement with the experimental NA49 analysis<sup>9</sup> is obtained by taking  $q = 1.038$ <sup>4</sup>, notably the same value used in transverse momentum spectra.

#### 4 Anomalous diffusion in rapidity spectra

An important observable in relativistic heavy-ion collisions is the rapidity distribution of the detected particles. In particular, there is experimental and theoretical evidence that the broad rapidity distribution of net proton yield ( $p - \bar{p}$ ) in central heavy-ion collisions at SPS energies could be a signal of non-equilibrium properties of the system. We want to show now that the broad rapidity shape can be well reproduced in the framework of a non-linear relativistic Fokker-Planck dynamics which incorporates non-extensive statistics and anomalous diffusion.

A class of anomalous diffusions are currently described through the non-linear Fokker-Planck equation (NLFPE)

$$\frac{\partial}{\partial t}[f(y, t)]^\mu = \frac{\partial}{\partial y} \left[ J(y)[f(y, t)]^\mu + D \frac{\partial}{\partial y}[f(y, t)]^\nu \right], \quad (7)$$

where  $D$  and  $J$  are the diffusion and drift coefficients, respectively. Tsallis and Bukman<sup>10</sup> have shown that, for linear drift, the time dependent solution of the above equation is a Tsallis-like distribution with  $q = 1 + \mu - \nu$ . The norm of the distribution is conserved at all times only if  $\mu = 1$ , therefore we will limit the discussion to the case  $\nu = 2 - q$ .

Imposing the validity of the Einstein relation for Brownian particles, we can generalize to the relativistic case the standard expressions of diffusion and drift coefficients as follows

$$D = \alpha T, \quad J(y) = \alpha m_\perp \sinh(y) \equiv \alpha p_{||}, \quad (8)$$

where  $p_{||}$  is the longitudinal momentum and  $\alpha$  is a common constant. It is easy to see that the above coefficients give us the Boltzmann stationary distribution in the linear Fokker-Planck equation ( $q = \nu = 1$ ) (such a result cannot be obtained if one assumes a linear drift coefficient as in Ref.<sup>11</sup>) while the stationary solution of the NLFPE (7) with  $\nu = 2 - q$  is a Tsallis-like distribution with the relativistic energy  $E = m_\perp \cosh(y)$ :

$$f_q(y, m_\perp) = \left\{ 1 - (1 - q) \beta m_\perp \cosh(y) \right\}^{1/(1-q)} \quad (9)$$

Basic assumption of our analysis is that the rapidity distribution is not appreciably influenced by transverse dynamics, which is considered in thermal equilibrium. This hypothesis is well confirmed by the experimental data<sup>8,12</sup> and adopted in many theoretical works<sup>13</sup>. Therefore, the time dependent rapidity distribution can be obtained, first, by means of numerical integration of Eq.(7) with initial  $\delta$ -function condition depending on the value of the experimental projectile rapidities and, second, by integrating such a result over the transverse mass  $m_{\perp}$  (or transverse momentum) as follows

$$\frac{dN}{dy}(y, t) = c \int_m^{\infty} m_{\perp}^2 \cosh(y) f_q(y, m_{\perp}, t) dm_{\perp}, \quad (10)$$

where  $c$  is the normalization constant fixed by the total number of the particles. The calculated rapidity spectra will ultimately depend on the nonextensive parameter  $q$  only, since there exists only one “interaction time”  $\tau = \alpha t$  which reproduces the experimental distribution<sup>14</sup>.

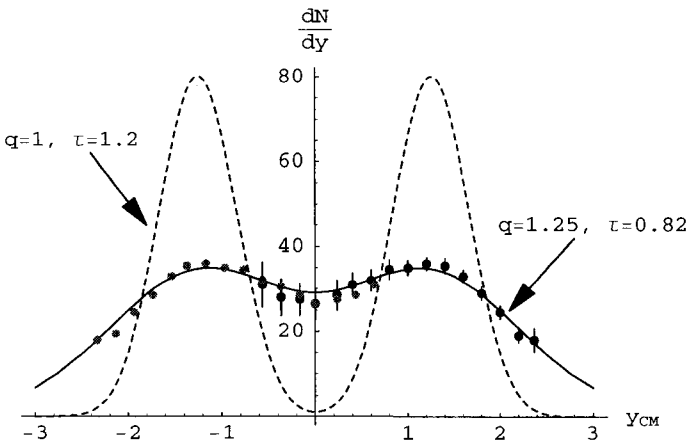


Figure 1. Rapidity spectra for net proton production ( $p - \bar{p}$ ) in central Pb+Pb collisions at 158A GeV/c (grey circles are data reflected about  $y_{cm} = 0$ ). Full line corresponds to our results by using a non-linear evolution equation ( $q = 1.25$ ), dashed line corresponds to the linear case ( $q = 1$ ).

In Fig.1 we show the calculated rapidity spectra of net proton compared with the experimental NA49 data from central Pb+Pb collisions at 158 GeV/c<sup>12</sup>. The obtained spectra are normalized to 164 protons and the beam rapidity is fixed to  $y_{cm} = 2.9$  (in the c.m. frame)<sup>12</sup>. The full line corresponds to the NLFPE solution (10) at  $\tau = 0.82$  and  $q = 1.25$ ; the dashed line corresponds to

the solution of the linear case ( $q = 1$ ) at  $\tau = 1.2$ . Only in the non-linear case ( $q \neq 1$ ) there exists a (finite) time for which the obtained rapidity spectra well reproduces the broad experimental shape. A value of  $q \neq 1$  implies anomalous superdiffusion in the rapidity space, i.e.,  $[y(t) - y_M(t)]^2$  scales like  $t^\alpha$  with  $\alpha > 1$ <sup>10</sup>.

## 5 Conclusions

The nonextensive statistics appears suitable to evaluate physical observables recently measured in heavy ion collision experiments. The physical motivation for the validity of a non-conventional statistical behavior can be related to the presence of memory effects and long range interactions at the early stage of the collisions, even if a microscopic justification of these effects is still lacking. A rigorous determination of the conditions that produce a nonextensive statistical regime should be based on microscopic calculations relative to the parton plasma originated during the high energy collisions. Non-perturbative QCD effects in the proximity of hadronic deconfinement could play a crucial role in the determination of the quantum kinetic evolution of the system toward the equilibrium<sup>3</sup>.

## References

1. T.S. Biró and C. Greiner, *Phys. Rev. Lett.* **79**, 3138 (1997).
  2. S. Schmidt et al, *Phys. Rev. D* **59**, 94005 (1999).
  3. D.V. Vinnik et al., *Eur. Phys. J. C* **22**, 341 (2001).
  4. W.M. Alberico, A. Lavagno, P. Quarati, *Eur. Phys. J. C* **12**, 499 (2000).
  5. C. Tsallis, *J. Stat. Phys.* **52**, 479 (1988).
- See also <http://tsallis.cat.cbpf.br/biblio.htm> for a regularly updated bibliography on the subject
6. T. Alber et al. (NA35 Collab.), *Eur. Phys. J. C* **2**, 643 (1998).
  7. W.M. Alberico, A. Lavagno, P. Quarati, *Nucl. Phys. A* **680**, 94 (2001).
  8. I.G. Bearden et al. (NA44 Collab.), *Phys. Rev. Lett.* **78**, 2080 (1997).
  9. A. Appelshäuser et al. (NA49 Collab.), *Phys. Lett. B* **467**, 21 (1999).
  10. C. Tsallis, D.J. Bukman, *Phys. Rev. E* **54**, R2197 (1996).
  11. G. Wolschin, *Eur. Phys. J. A* **5**, 85 (1999).
  12. H. Appelshäuser et al. (NA49 Collab.), *Phys. Rev. Lett.* **82**, 2471 (1999).
  13. P. Braun-Munzinger et al., *Phys. Lett. B* **344**, 43 (1995); *Phys. Lett. B* **356**, 1 (1996).
  14. A. Lavagno, *Physica A* **305**, 238 (2002).

# STRANGENESS PRODUCTION IN A CONSTITUENT QUARK MODEL

F.BECATTINI AND G.PETTINI\*

*Department of Physics, University of Florence and I.N.F.N., Florence, Italy  
E-mail: becattini@fi.infn.it, pettini@fi.infn.it*

We develop a model to calculate strangeness production in both elementary and heavy ion collisions, within the framework of a statistical approach to hadronisation. Calculations are based on the canonical partition function of the thermal Nambu-Jona-Lasinio model with exact conservation of flavor and color. It turns out that the growth of strange quarks production in heavy ion collisions is due to the initial excess of non-strange matter over antimatter, whereas a suppression occurs for elementary collisions, owing to the constraint of exact quantum charges conservation over small volumes.

## **1 The Statistical Model of Hadronisation (SHM) and the Wroblewski factor $\lambda_S$**

A statistical calculation of hadron multiplicities in high energy collisions has been developed in ref.<sup>1</sup>. The SHM relies on the assumption of equiprobability of multi-hadronic states originating from hadronising clusters, entailing that particle production in hadronisation of both elementary (EC) and heavy ion (HIC) collisions can be treated as an equilibrium process. The main advantage of the model is the low number of free parameters necessary to reproduce the observed hadron multiplicities. These are: the total volume  $V$  of the set of clusters, temperature  $T$ , and a phenomenological parameter  $\gamma_S$  reducing the production of strange particles with respect to a fully chemically equilibrated hadron gas. The exact conservation of initial electric, baryon and strange total quantum charges is enforced in the model. However, when dealing with HIC, the conservation of the initial baryon number can be imposed only on the average and the baryon chemical potential  $\mu_B$  has to be introduced. A remarkable outcome of the SHM is that the temperature fitted in any EC is almost constant ( $T \sim 160$  MeV), and very close to that obtained in HIC with small fitted  $\mu_B$ . Furthermore, for different HIC, to an increase of the fitted value of  $\mu_B$  corresponds a decrease of the value of  $T$ .

An interesting insight in strangeness production is obtained when studying the so-called Wroblewski factor, the ratio between newly produced valence strange and light quark pairs  $\lambda_S = 2\langle s\bar{s} \rangle / (\langle u\bar{u} \rangle + \langle d\bar{d} \rangle)$ , which is fairly constant in several EC, with  $\sqrt{s}$  spanning two orders of magnitude, whereas it is significantly higher and more variable in HIC<sup>2</sup> (see Fig. 1).

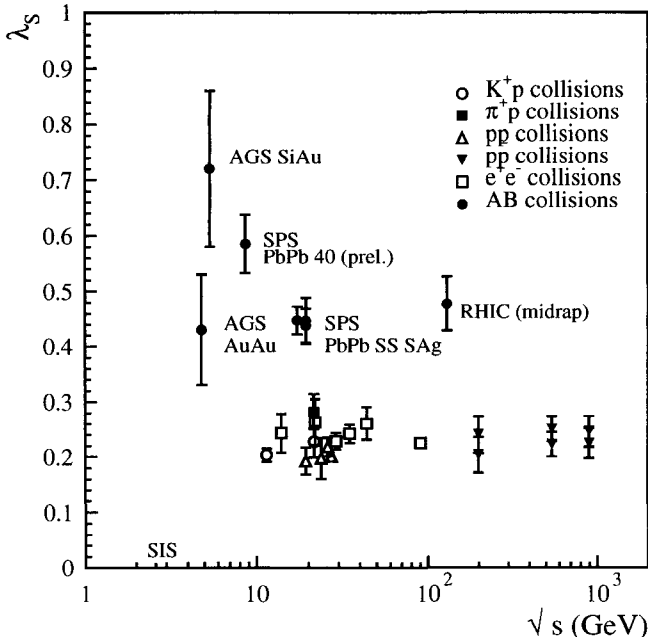


Figure 1.  $\lambda_S$  as a function of  $\sqrt{s}$  in several kinds of collisions (from ref. <sup>2</sup>).

The peculiar behaviour of  $\lambda_S$ , together with the apparent universality of the scale of temperature fitted within EC, suggest to look for a more fundamental description of strangeness production, by employing effective models (EM) having quarks as fundamental degrees of freedom.

## 2 Connection with effective models

In using EM, the same physical scheme of the SHM is kept. However, we now assume the formation of a set of hadronising clusters endowed with given  $U, D, S$  and color charges, in which every allowed quantum state is equally likely. The assumption of suitable maximum disorder fluctuations of cluster flavor charges is retained <sup>2</sup>, which allows to impose exact flavor conservation over the total volume  $V$ . Further conjectures are introduced:

1. Temperature  $T$  and baryon chemical potential  $\mu_B$ , fitted within the SHM, are interpreted as the critical values for deconfinement and (approximate)

## chiral symmetry restoration

2. The produced s quarks, or at least the ratio s/u, survive in the hadronic phase
3. Each single cluster is a color singlet

The first assumption is the strongest one, as it implies that hadronisation itself is assumed to be a critical process. The aforementioned constancy of fitted temperature for many collisions <sup>2</sup> and the consistency with other estimates, support this identification. Assumption (2) implies that full chemical equilibrium is assumed at constituent quark level. Thus, no parameter such as  $\gamma_S$  is now required to account for strangeness production. Conversely, assumption (3) introduces a further parameter, a characteristic cluster size  $V_c$  over which color is exactly conserved, which, together with the constancy of  $T$  and a weak dependence of  $\lambda_S$  itself on the total volume  $V$ , contributes in stabilizing  $\lambda_S$  for EC. On the other hand, a large  $V_c$  in HIC could be a signal for color deconfinement over large volumes.

The simplest effective model to start with is the thermal Nambu-Jona-Lasinio model <sup>3</sup>. It cannot account for deconfinement but it does embody chiral symmetry breaking and its restoration ( $\chi$ SR), which is expected to occur at the same critical point <sup>4</sup>. Although not renormalizable, the NJL model shares the main features with other effective models, referred in literature as *ladder-QCD* <sup>5</sup>. Actually the phase diagram for  $\chi$ SR exhibits a tricritical point in the chiral limit, separating second order from first order phase transitions. We are interested to include the current quark masses, in which case a smooth cross-over transition is expected for the light quarks in the second order region (in which we are interested in the present work). This implies a quasi-critical behavior of the light quark condensates and a smooth decrease of the strange one for higher temperatures. The same happens to the constituent quark masses which are the physical quantities, together with the UV cutoff  $\Lambda$  <sup>3</sup>, affecting the number of quarks (or antiquarks). Actually, the thermodynamics of the mean-field NJL model can be derived by a free Dirac Hamiltonian having constituent quark masses replacing the current ones. The dependence of quark multiplicities on  $V, V_c$  emerges when requiring exact conservation of quantum flavor and color charges by restricting the partition function to the allowed set of multi-particle states. This is accomplished by means of standard methods <sup>6</sup> and implies a five-dimensional integration over the group  $SU(3)_c \times U(1)_u \times U(1)_d \times U(1)_s$ . Calculations are shown in detail in ref. <sup>7</sup>.

### 3 Results

#### 3.1 Heavy Ions

For HIC , the fitted total volumes <sup>2</sup> are large enough to disregard the fluctuations of flavor quantum numbers. Then, if  $V_c$  is large enough, it can be explicitly checked that a grand-canonical calculation of quark multiplicities is reliable. This implies that  $\lambda_S$  can be obtained by the simple grand-canonical formula for a gas of free constituent quarks with an UV cutoff limiting the momentum integration <sup>3</sup>, and it is independent on  $V, V_c$ . Temperature  $T$  and chemical potentials  $\mu_i$  are taken coincident with those fitted within the SHM. A first comparison with the SHM predictions can be performed by considering the values of the constituent quark masses  $M_i$  for the strange quark ( $\mu_s = 0$ ) and for a light quark  $q$  ( $\mu_q \sim \mu_B/3$ ) with mass  $\tilde{m} = (m_u + m_d)/2$ , as free parameters to be determined imposing the SHM value of  $\lambda_S$  for a given process. A more complete analysis can be obtained by using the thermal NJL model in a predictive way. The coincidence of the cross-over point with the best fit of the SHM is possible by tuning the parameter  $T_0$ , defined in ref. <sup>3</sup>, which controls the strength of the six-fermion term and which physically represents the critical temperature for  $U(1)_A$  restoration. Then the cross-over line, obtained by studying the chiral light quark susceptibility can be compared with the fitted values of  $T$  and  $\mu_B$  in the SHM, as well as  $\lambda_S$  along the critical line. In this case the constituent masses  $M_i(T, \mu_i)$  are predicted by minimizing the NJL grand canonical potential. A good agreement is found with  $T_0 = 170$  MeV for various HIC.

However, as it turns out that  $M_s$  is almost independent on the choice of  $T_0$ , the model needs the specification of only one parameter, either  $T_0$  or  $M_q$ . This is shown in Fig. 2, which shows, on the other hand, that under the reasonable assumption that the light quark constituent mass has sensibly decreased at the cross-over point, the agreement with the SHM is guaranteed by  $M_s(T = 0) \sim 500$  MeV. The limit  $\Lambda \rightarrow \infty$  serves to show that the UV contribution is not expected to change this picture, even if the analysis in renormalizable models such as *ladder-QCD* <sup>5</sup> is necessary.

#### 3.2 Elementary Collisions

The location of the cross-over point for EC,  $T \sim 160$  MeV ( $\mu_B = 0$ ), as well as  $M_i$ , are obtained in the predictive NJL model with  $T_0 = 170$  MeV in the infinite volume limit. Consequently, quark multiplicities depend on the volume only through the explicit dependence of the canonical partition function on  $V, V_c$  <sup>7</sup>. This approximation already allows us to observe canonical

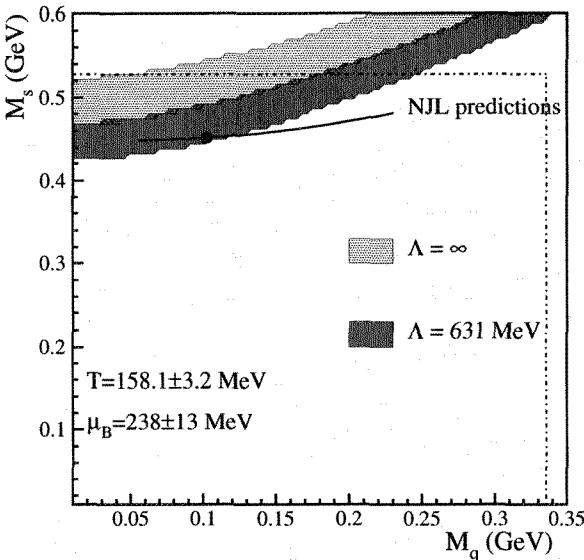


Figure 2. Constituent quark masses  $M_q, M_s$  determined by  $\lambda_S \simeq 0.45$  as fitted in Pb-Pb collisions at  $\sqrt{s}_{NN} = 17.4$  GeV. The hatched lighter region corresponds to the free constituent quark gas with  $\Lambda = 631$  MeV as in ref.<sup>3</sup> whereas the darker hatched region is for  $\Lambda = \infty$ . Together, we plot the predictions of the NJL model with  $T_0$  ranging from zero (no KMT term) to  $\infty$  from left to right (solid line). The black point is for  $T_0 = 170$  MeV. The dashed pointed horizontal and vertical lines correspond to the  $T = \mu_B = 0$  constituent masses values for the strange quark and for the light quark  $q$  respectively.

suppression. We find consistency with our physical picture, as far as processes with zero initial electric charge are concerned, whereas for pp collisions the Pauli exclusion principle and canonical suppression balance each other and  $\lambda_S$  remains constant around  $\sim 0.3$ . In Fig. 3 we plot the predictions of the model compared to the SHM expectations for  $e^+e^-$  collisions.

#### 4 Conclusions

We have studied strangeness production within a statistical model of hadronisation by using an effective model with constituent quarks. The study supports the idea that the SHM analysis may help in effective models building for the QCD phase transition, whereas EM may give a natural explanation of strangeness suppression in EC, assuming full chemical equilibrium, as due to the absence of baryon chemical potential and to canonical suppression work-

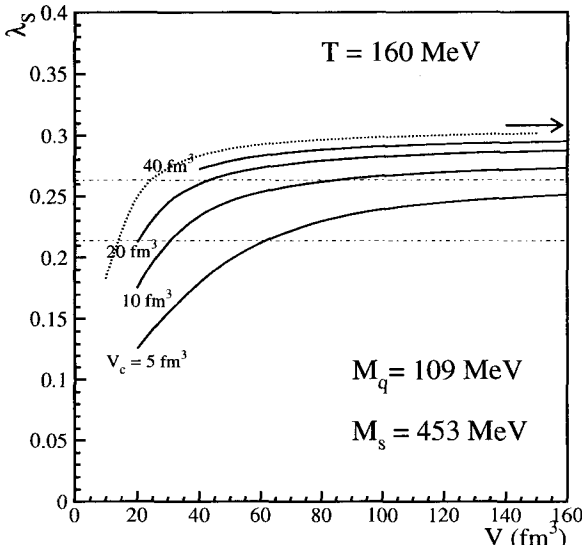


Figure 3. Calculated  $\lambda_S$  in  $e^+e^-$  collisions at  $T=160$  MeV within the NJL model<sup>3</sup> with  $T_0 = 170$  MeV, as a function of the total volume  $V$  for various single cluster volumes  $V_c$ . The dotted line is with  $V_c = V$  and the arrow indicates the grand-canonical limit. The horizontal bands are the ranges of fitted  $\lambda_S$  values in the SHM (see Fig. 1).

ing in small volumes. A significative discrepancy is found only in pp collisions, where further analysis is required.

## References

1. F. Becattini, Z. Phys. **C69** 485 (1996); F. Becattini and U. Heinz, Z. Phys. **C76** 269 (1997).
2. F. Becattini, in *Strange Quarks in Matter 2001*, hep-ph 0202071, to appear in J. Phys. G, and references therein.
3. T. Hatsuda and T. Kunihiro, Phys. Rep. **247**, 221 (1994).
4. F. Karsch and E. Laermann, Phys. Rev. **D59** 031501 (1999).
5. A. Barducci et al., Phys. Rev. **D41**, 1610 (1990); A. Barducci et al., Phys. Rev. **D49**, 426 (1994) and references therein.
6. K. Redlich and L. Turko, Z. Phys. **C5**, 201 (1980).
7. F. Becattini and G. Pettini in *QCD@Work*, AIP PROCEEDINGS, Vol. 62, 333 (2001); F. Becattini and G. Pettini, in preparation.

# DOUBLE PARTON COLLISIONS IN $NN$ AND $NA$ INTERACTIONS

ALESSIO DEL FABBRO AND DANIELE TRELEANI

*Dipartimento di Fisica Teorica, Università di Trieste,  
Strada Costiera 11, I-34014 Trieste  
and INFN, Sezione di Trieste via Valerio 2, I-34127 Trieste*

Multiple parton collisions play an increasingly important role in high energy hadronic and nuclear interactions. The rates of double parton scatterings in heavy quark production at LHC are estimated while a few interesting features, peculiar of hadron-nucleus interactions, are outlined.

As a consequence of the large flux in the small  $x$  region, an increasing number of partons become active for hard collision processes at high energies. Hard cross sections therefore grow with energy, which implies that when the c.m. energy is large enough unitarization effects will show up also in the kinematical domain where perturbation theory is applicable. One may get in touch with the problem looking at the cross section to produce large  $p_t$  jets, integrated on the exchanged momentum with the cutoff  $p_{cut}$ . When  $p_{cut}$  is moved towards relatively small values, the integrated cross section, being divergent for  $p_{cut} \rightarrow 0$ , becomes very large already well inside the perturbative regime<sup>1</sup>.

The unitarization of the hard cross section introduces multiple hard collisions in the interaction process. In fact, when the incoming partons flux is very large there is a finite probability of producing events where, in a given hadronic interaction, different pairs of partons interact independently with momentum exchange above  $p_{cut}$ , generating states with many jets at a relatively large  $p_t$ <sup>2</sup>. In the integrated inclusive cross section of jet production, those events count with the multiplicity factor of the partonic collisions and, as a consequence, when multiple parton collisions are introduced, the inclusive cross section is no more bounded from above. In the kinematical regime where the inclusive cross sections of jet production is comparable to the total inelastic cross section, the average number of partonic collisions in a typical inelastic event is close to one and the probability of multiple parton interactions is sizable. The simplest case of multiple parton interaction is the double parton collision. In the process two different pairs of partons interact independently at different points in transverse space, so that the transverse momenta are balanced

separately in the two partonic collisions. The cross section is:

$$\sigma_D = \frac{1}{2} \int \Gamma_A(x_1, x_2; b) \hat{\sigma}(x_1, x'_1) \hat{\sigma}(x_2, x'_2) \Gamma_B(x'_1, x'_2; b) dx_1 dx'_1 dx_2 dx'_2 d^2 b \quad (1)$$

The non perturbative inputs to the double parton collision process are the two-body parton distribution  $\Gamma(x_1, x_2; b)$  which depend on the two fractional momenta  $x_1$  and  $x_2$  of the two partons and on their distance in transverse space  $b$ . If the two partons are not correlated in  $x$  and if the dependence on  $b$  can be factorized one may write

$$\Gamma(x_1, x_2; b) = G(x_1)G(x_2)F(b) \quad (2)$$

and the expression of  $\sigma_D$  (in the case of two indistinguishable parton interactions) is:

$$\sigma_D(p_t^{cut}) = \frac{[\sigma_S(p_t^{cut})]^2}{2\sigma_{eff}} \quad (3)$$

where  $\sigma_S$  has the usual single scattering expression of perturbative QCD, i.e. the convolution of the parton distributions with the partonic cross section:

$$\sigma_S = \int_{p_t > p_{cut}} G_A(x_1) \hat{\sigma}(x_1, x'_1) G_B(x'_1) dx_1 dx'_1 \quad (4)$$

$p_t^{cut}$  is the lower integration threshold and  $\sigma_{eff}$  a scale factor with dimensions of a cross section:

$$\frac{1}{\sigma_{eff}} = \int d^2 b F^2(b) \quad (5)$$

where  $F(b)$  is the density of parton pairs as a function of their relative transverse distance  $b$ . Notice that the scale factor  $\sigma_{eff}$  represents a new information on the hadron which cannot be obtained when testing the structure with an elementary probe.

The qualitative features of the process are readily obtained from Eq.(3) as a consequence of the proportionality of  $\sigma_D$  with  $\sigma_S^2$ : a rapid decrease for  $p_t \rightarrow \infty$  and a rapid growth for  $p_t \rightarrow 0$ , a fast increase with  $s$  at a fixed value of  $p_t$ . Since multiple parton collisions increase with  $s$  as a power of  $\sigma_S$ , the ratio multiple/single is a growing function of energy.

Multiple parton collisions are relevant in jets production, where the integrated cross section can easily exceed the unitarity limit, at large energies and keeping fixed the cutoff  $p_t^{cut}$ . Comparing the leading  $(2 \rightarrow 4)$  with the power suppressed  $(2 \rightarrow 2)^2$  double parton interaction at LHC energy, one obtains that double parton collisions will dominate the leading QCD  $(2 \rightarrow 4)$  parton process, in jets production, for approximately  $p_t \leq 20 GeV$  and  $|y| < 3^3$ .

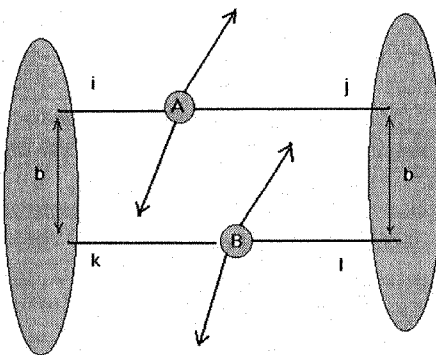


Figure 1. Double parton scattering

Double parton collisions have been measured at Fermilab by CDF looking at final states with three mini-jets and one photon<sup>4</sup>. The observation of the process is consistent with the simplest factorization hypothesis above. Output of the experiment is the scale factor  $\sigma_{eff}$ . The measured value is:

$$\sigma_{eff} = 14.5 \pm 1.7^{+1.7}_{-2.3} mb$$

One should expect different kinds of partons to have a different distribution in transverse space inside the hadron. A simplest generalization of Eq.(3), for two parton processes  $A$  and  $B$ , is<sup>5</sup>:

$$\sigma_D(A, B) = \frac{m}{2} \sum_{ijkl} \Theta_{kl}^{ij} \sigma_{ij}(A) \sigma_{kl}(B) \quad (6)$$

$\sigma_{ij}(A)$  is the hadronic inclusive cross section where the two partons  $i$  and  $j$  undergo the hard interaction  $A$ , while the partons  $k$  and  $l$  undergo the hard interaction  $B$  with cross section  $\sigma_{kl}(B)$ .  $m = 1$  when the two parton processes  $A$  and  $B$  are identical, while  $m = 2$  if they are distinguishable.

$$\Theta_{kl}^{ij} = \int d^2 b F_k^i(b) F_l^j(b) \quad (7)$$

are geometrical coefficients, with dimensions an inverse cross section. The function  $F_k^i(b)$  represents the density of the pair of partons  $k, i$  in a hadron as a function of the relative transverse distance  $b$ , normalized to one. Hence, by selecting final states as  $jjjj$ ,  $b\bar{b}b\bar{b}$  or  $c\bar{c}c\bar{c}$  one will measure  $\Theta_{gg}^{gg}$ , while final states with a prompt photon, as  $\gamma jjj$ ,  $\gamma jb\bar{b}$  or  $\gamma jc\bar{c}$  will allow one to obtain

$\Theta_{gg}^{gg}$ . The scale factor  $\Theta_{gg}^{gg}$  may be measured by looking at double parton collisions with a Drell-Yan pair accompanied by two minijets or by a pair of heavy quarks. Two equal sign  $W$  bosons will allow one to have information on the correlation in transverse space of valence quarks.

All final states produced by double parton collisions can be produced also by the more conventional leading QCD mechanism, where the hard process is initiated by two partons. A channel where one expects a sizable effect of multiple parton collisions is  $b$  production, whose inclusive cross section is estimated to be about 1mb at the LHC. To have an indication on the rates of the two contributions we have compared the leading ( $2 \rightarrow 4$ ) process with the power suppressed ( $2 \rightarrow 2$ )<sup>2</sup> double parton collision for  $b\bar{b}b\bar{b}$  production inside the ALICE detector. As a scale factor we have used the value of  $\sigma_{eff}$  measured by CDF. The elementary parton interactions have been evaluated at the lowest order in perturbative QCD by MadGraph<sup>6</sup> and we have used the CTEQ5 parton distributions<sup>7</sup>. To keep into account higher order corrections, we have multiplied the results by a  $k$ -factor of 5.5, which has been assumed to be the same in the  $2 \rightarrow 2$  and in the  $2 \rightarrow 4$  processes (notice that in a ( $2 \rightarrow 2$ )<sup>2</sup> interaction the  $k$ -factor appears at the second power). The value of the  $k$ -factor has been obtained using the results on heavy quark production in the  $k_t$ -factorization approach<sup>9</sup>. The dashed lines in the figures represent the leading QCD  $2 \rightarrow 4$  contribution, while the continuous lines the double parton scattering. In the low  $p_t^{min}$  region double parton scatterings dominate over the leading QCD  $2 \rightarrow 4$  by a large factor. Preliminary estimates indicate that the effect of multiple parton interactions is even more pronounced when considering  $c\bar{c}$  pairs production.

A convenient approach is to study multiparton interactions in hadron-nucleus collisions, given the substantial enhancement of the process due to the increased flux of incoming partons. A further advantage with hadron-nucleus collisions is that one may vary the rate of the multiparton interactions by choosing nuclear targets with different atomic masses, while keeping fixed the c.m. energy and the cuts in the produced final state. In proton-nucleus collisions one may identify two different contributions to the cross section, corresponding to the situations where one or two target nucleons are involved in the collision. The cross sections are<sup>8</sup>:

$$\begin{aligned}\sigma_1^D &= \sigma_D \int d^2B T(B) = A\sigma_D \\ \sigma_2^D &= \frac{1}{2} \int G_N(x_1, x_2) \hat{\sigma}(x_1, x'_1) \hat{\sigma}(x_2, x'_2) G_N(x'_1) G_N(x'_2) \prod_i dx_i dx'_i \int d^2B T^2(B)\end{aligned}\quad (8)$$

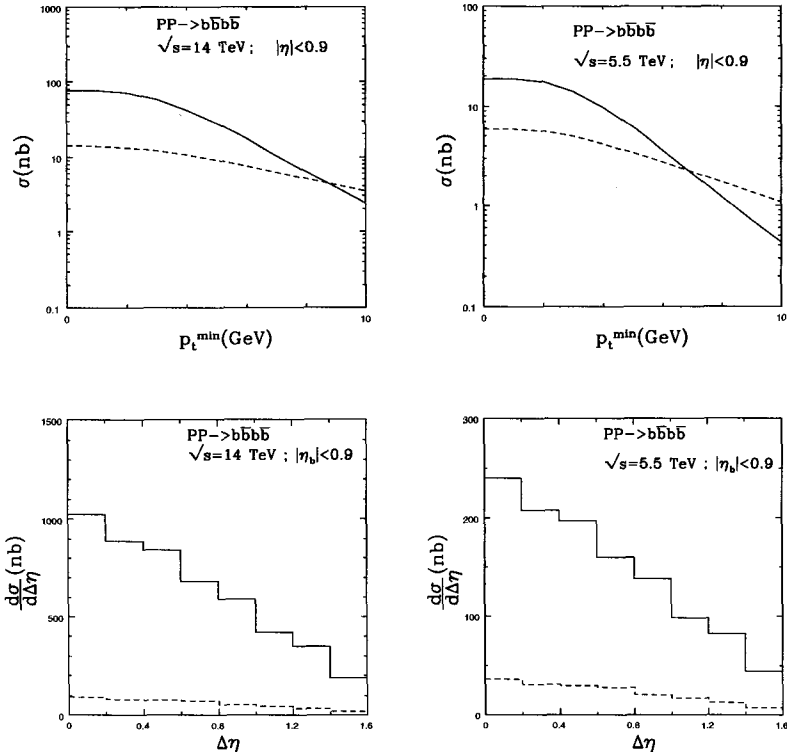


Figure 2. Upper figures: cross sections, for producing two pairs  $b\bar{b}$  with  $|\eta| \leq .9$  and with c.m. energies of 14 TeV and 5.5 TeV, as a function of  $p_t^{\min}$ , the smallest among all the transverse momenta of the produced quarks. Lower figures: pseudorapidity difference distributions for two  $b$ -quarks with  $|\eta| \leq .9$  and with c.m. energies of 14 TeV and 5.5 TeV. The continuous lines are the double parton scattering ( $2 \rightarrow 2$ )<sup>2</sup>, the dashed lines are the leading QCD  $2 \rightarrow 4$ .

Since the nuclear density does not change within a transverse scale  $\langle b \rangle \approx R_N \ll R_A$ , one may neglecting the variation of  $\Gamma_A(x'_1, x'_2; b)$  in a integration domain in  $b$  of the order of the hadron dimension. The cross section  $\sigma_2^D$  becomes therefore a function of the dimensionless quantity  $G_N(x_1, x_2) = \int \Gamma_N(x_1, x_2; b) d^2b$ . Remarkably, as a consequence of the large nuclear size,  $\sigma_2^D$  does not depend on the transverse correlation.

The dependence on  $A$  of  $\sigma_1^D$  and  $\sigma_2^D$  is different:  $\sigma_1^D \simeq A$  and  $\sigma_2^D \simeq A^{4/3}$ ,

which allows one to separate the two contributions. Notice that the dependence on  $A$  of  $\sigma_1^D$  is the same of the  $2 \rightarrow 4$  partons process, which constitutes a background to the double scattering term and which could be therefore disentangled from the  $(2 \rightarrow 2)^2$  process by means of the  $A$  dependence. The  $\sigma_1^D$  term has the same dependence on  $A$  of all process which can be treated in impulse approximation at partonic level, which allows one to separate  $\sigma_1^D$  and  $\sigma_2^D$  also in a kinematical regime where non additive effects to the nuclear parton distributions play an important role. Notice that, while non additive effects to the nuclear parton distributions may reduce the cross section by a factor  $\simeq .7$  at small  $x$ , the enhancement with  $A$  of  $\sigma_2^D$  is a much larger effect. The contribution of  $\sigma_2^D$  may in fact constitute 70% of the whole double parton scattering cross section, in a collision with a heavy nucleus.

In conclusion multiple parton collisions are enhanced in hadronic and nuclear interactions at high energies. The non-perturbative inputs to the multiple parton collisions, the multiparton distributions, are related directly to the multi-parton correlations in the hadron structure. By observing different double parton collision processes one will be able to measure the correlations of different kinds of parton pairs. Correlations depend both on the longitudinal and on the transverse degrees of freedom, the two effects being disentangled (in a model independent way) using hadron-nucleus collisions.

Finally a main reason of interest on the whole matter is that, by measuring multiparton correlations, one will learn about the three dimensional structure of the proton, the acquired information regarding the typical transverse distances of different pairs of partons at different values of  $x$ .

## References

1. A. Capella, J. Tran Thanh Van and J. Kwiecinski, Phys. Rev. Lett. **58**, 2015 (1987).
2. N. Paver and D. Treleani, Nuovo Cim. A **70**, 215 (1982).
3. S. Catani *et al.*, arXiv:hep-ph/0005025.
4. F. Abe *et al.* [CDF Collaboration], Phys. Rev. D **56**, 3811 (1997).
5. A. Del Fabbro and D. Treleani, Phys. Rev. D **63**, 057901 (2001).
6. T. Stelzer and W. F. Long, Comput. Phys. Commun. **81**, 357 (1994).
7. H. L. Lai *et al.* [CTEQ Collaboration], Eur. Phys. J. C **12** (2000) 375.
8. M. Strikman and D. Treleani, Phys. Rev. Lett. **88**, 031801 (2002).
9. Y. M. Shabelski and A. G. Shuvaev, arXiv:hep-ph/0107106.

# SEQUENTIAL QUARKONIUM SUPPRESSION

S. FORTUNATO

*Fakultät für Physik, Universität Bielefeld, D-33501, Bielefeld (Germany)*

The behaviour of quarkonium states in a strongly interacting medium can be studied through non-relativistic potential theory in a static picture, by using the heavy-quark potential provided by lattice QCD calculations. That leads to a sequential suppression pattern: higher excited states may decay into open charm/beauty even below the deconfinement temperature, due to in-medium modifications of the open charm/beauty threshold, whereas tightly bound states, like the  $J/\Psi$  or  $\Upsilon$ , can be dissolved only in a deconfined medium, due to colour screening.

## 1 Introduction

The suppression of  $J/\Psi$  in high energy heavy ion collisions was proposed by Matsui and Satz as a signature for the transition from hadronic matter to quark-gluon plasma (QGP)<sup>1</sup>. Since then the investigation of quarkonium states at high temperatures became a fruitful topic, especially after the experimental findings on the suppression of charmonium states of the NA50 collaboration at CERN SPS.

In the original paper<sup>1</sup>, it was shown that a bound  $c\bar{c}$  state cannot exist if the temperature is in the range 130-200 MeV, which is a temperature at which most likely hadronic matter has already melt in a QGP. The result was obtained by reducing the effects of the medium to a modification of the interaction between the quarks of the  $c\bar{c}$  pair; the charmonium spectrum is then obtained by solving the Schrödinger equation

$$\left[ 2m_c + \frac{1}{m_c} \nabla^2 + V_1(r) \right] \Phi_i^c = M_i^c \Phi_i^c, \quad (1)$$

where  $m_c$  ( $\approx 1.3$  GeV) is the mass of the charm quark,  $V_1(r)$  is the potential describing the interaction, which varies with temperature, and  $M_i^c$  the energy of the state. If the temperature is high enough, equation (1) does not admit bound state solutions.

The application of non-relativistic potential theory is justified by the large mass of the charm quark, which is much bigger than the kinetic energy due to the motion of the charm quark (antiquark) in the bound system. Indeed, in the absence of a medium, both charmonium and bottomonium spectra are quite well described by solving the Schrödinger equation (1), if one uses the

Cornell potential

$$V_1(r) = \sigma r - \frac{\alpha}{r}, \quad (2)$$

where  $\sigma$  is the string tension and the  $1/r$  term contains both Coulombic and transverse string effects <sup>2,3,4</sup>.

In the presence of a medium, one tried initially to model the interaction on the basis of a screened form of the Cornell potential <sup>5,6</sup>. The temperature dependence of the parameters was obtained by comparison with lattice results on  $SU(3)$  pure gauge theory. But such predictions cannot be satisfactory from a quantitative point of view. It is clear that, in order to extract realistic results for the dissociation temperatures of the various quarkonium states, one needs to adopt the heavy quark potential of full QCD. Recent lattice data allowed to obtain good estimates of the heavy quark potential <sup>7,8</sup>.

Besides, from lattice results of QCD at finite temperature, one can investigate the evolution of string breaking in the confined phase. This is very important in studies of quarkonium dissociation, since some higher excited states have quite a small binding energy, so that it could be possible that they get dissociated below the deconfinement temperature  $T_c$ . In this case a charmonium state, for instance, would decay into an open charm  $D\bar{D}$  pair. In order for this decay to be possible, the mass of the charmonium state must be bigger than the mass of the  $D\bar{D}$  pair. This can occur if the mass of the open charm meson decreases with temperature faster than the charmonium mass. Lattice studies of the heavy quark potential in the confined phase determine the temperature dependence of the string breaking threshold <sup>7,9</sup>. We stress the importance of this fact: the Schrödinger equation focuses on the  $c\bar{c}$  system and knows nothing about confinement, i.e. the possibility of string breaking which leads to the creation of a new quark-antiquark pair which combines with  $c\bar{c}$  into  $D\bar{D}$ .

The considerations above are the basis of recent work <sup>10,11</sup> of Digal, Petreczky and Satz (DPS), which we present in this contribution. Because of the different suppression mechanisms at work below and above the deconfinement temperature  $T_c$ , we will expose their results in two separate sections.

## 2 Quarkonium Dissociation Below $T_c$ : String Breaking

In finite temperature lattice QCD, the heavy quark potential  $V(T, r)$  at temperature  $T$  and distance  $r$  is obtained from Polyakov loop correlators

$$-T \ln \langle L(0)L^+(r) \rangle = V(T, r) + C. \quad (3)$$

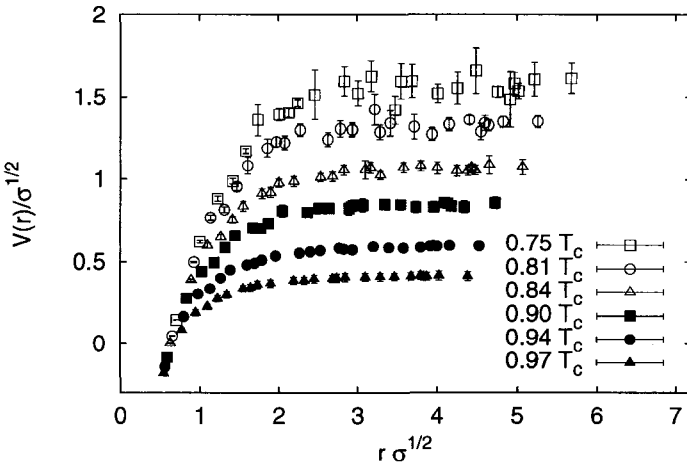


Figure 1. The heavy quark potential at different temperatures, normalized to the Cornell potential at short distance.

The first member of equation (3) represents indeed the free energy of the gauge system if we put in it a static quark and an antiquark at a distance  $r$  from each other. Therefore, the constant  $C$  is temperature-dependent, since it contains the entropy term  $-TS$ . In Fig. (1) some representative curves of the potential in units of  $\sqrt{\sigma}$  are shown: they were obtained from Monte Carlo simulations of three flavour QCD<sup>7</sup>.

The constant  $C$  was fixed here by requiring that at very short distances,  $r \ll T^{-1}$ , the potential maintains the zero-temperature form (2), since the effects of the medium should become negligible. From Fig. (1) one notices that all curves reach a plateau starting from some value  $r_0$  of the distance which is, in general, temperature-dependent:  $r_0$  is the distance at which the string breaks. The plateau value of the potential  $E_s$  is the energy needed to break the string between the heavy quarks. One can then determine how  $E_s$  varies with temperature, which is nothing but the variation of the mass of the open charm (beauty) meson. To express such values in conventional energy units, one fits the plateau values extracted from the curves of Fig. (1) to the zero-temperature values of the open-charm (beauty) threshold, which are known from experiments (3.729 and 10.559 GeV, respectively).

What remains to be done is to evaluate the quarkonium spectrum. For this purpose, it is necessary to have a parametrization of the short-distance

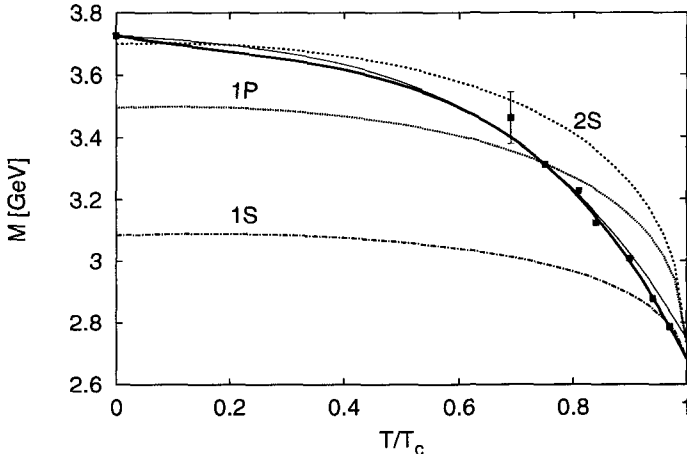


Figure 2. The open charm threshold and the masses of different charmonium states versus temperature.

interaction, which allows to account for the possibility to obtain states whose mass is higher than the string breaking threshold. For this reason, one cannot use directly the potential of Fig. (1): DPS made use of the following form for the potential

$$V_{string}(r, T) = -(e - \frac{1}{6} \arctan(2rT)) \frac{1}{r} + (\sigma(T) - \frac{\pi T^2}{3} - \frac{2T^2}{3} \arctan \frac{1}{rT}) r + \frac{1}{2} \ln(1 + 4r^2 T^2), \quad (4)$$

which describes quite well the temperature dependence of the heavy quark potential in  $SU(3)$  pure gauge theory for suitably chosen  $\sigma(T)$ <sup>8</sup>. The resulting charmonium spectrum obtained by solving the Schrödinger equation (1) with  $V_{string}(r, T)$  is presented as a function of temperature in Fig. (2), where we can also see the variation of the open charm threshold. It is clear from the plot that both the  $2S(\Psi')$  and the  $1P(\chi_c)$  states decay in the confined phase. For the  $J/\Psi$  it is hard to draw a conclusion: the lines seem to join slightly below  $T_c$ , but that could be just due to the inevitable approximation with which the lines were derived. For bottomonium one proceeds in a perfectly analogous way, and one obtains that, except the strongly bound states  $1S$ ,  $1P$  and  $2S$ , for which we cannot say with certainty what happens, all other states decay in open beauty below  $T_c$ . We will see that these results are compatible with those obtained above  $T_c$ .

### 3 Quarkonium Dissociation Above $T_c$ : Colour Screening

In the deconfined phase, the presence of many free colour charges leads to a screening of the interaction between the heavy quarks of the quarkonium state. The interaction is usually rather well expressed through a Debye-screened form of the Coulomb potential

$$V_D(T, r) = \frac{\alpha(T)}{r} \exp\{-\mu(T)r\}, \quad (5)$$

analogously to what happens in an electric plasma. If we want to derive the potential directly from lattice QCD data we meet a difficulty. What one extracts through relation (3) is the so-called color averaged potential  $V_{AVG}$ , whereas in potential models it is assumed that quarkonium is dominantly a singlet  $Q\bar{Q}$  state, so that the interaction should be expressed through the color singlet potential  $V_1$ . Existing lattice data allow to determine only  $V_{AVG}$ , so that, in order to determine  $V_1$ , it is necessary to use the following relation

$$\exp(-V_{AVG}(r, T)/T) = \frac{1}{9} \exp(-V_1(r, T)/T) + \frac{8}{9} \exp(-V_8(r, T)/T), \quad (6)$$

where  $V_8(r, T)$  is the color octet potential. Since we just know  $V_{AVG}$  but we do not know either  $V_1$  or  $V_8$ , one must introduce some additional condition in order to determine  $V_1$ . DPS assumed that  $V_1$  and  $V_8$  are both of the form (5), and that the ratio  $V_1/V_8$  is the simple color factor  $-8$  in the high temperature regime<sup>a</sup> (which they defined as  $T \geq 1.45 T_c$ ), compatibly with leading order perturbation theory results, and some function  $c(T)$  of the temperature for  $T_c < T < 1.45 T_c$ , as suggested by lattice results on  $SU(3)$  pure gauge theory<sup>12</sup>.

In this way, DPS could determine the color singlet potential above  $T_c$  by means of fits of the three flavour QCD lattice data<sup>7</sup>. These data also show that the potential becomes flat starting from some distance  $r_0$ , which varies with temperature, exactly as we saw in the confined phase. In this case, however, this phenomenon indicates that there are no interactions if the heavy quark-antiquark separation gets larger than  $r_0$ , which sets a natural limit to the radius of eventual bound states of the heavy quark pair. By solving the Schrödinger equation with the singlet potential determined as described above, one finds the dissociation temperatures of charmonium and bottomonium states by comparing the radii of the bound states with the limit radius  $r_0$ . Fig. (3) shows the variation of the quarkonium radii and  $r_0$  with temperature. We see that both the  $J/\Psi$  and the  $\Upsilon$  ( $1S$ ) melt in the

---

<sup>a</sup>The minus sign is due to the fact that  $V_8$  is repulsive, at least in perturbation theory.

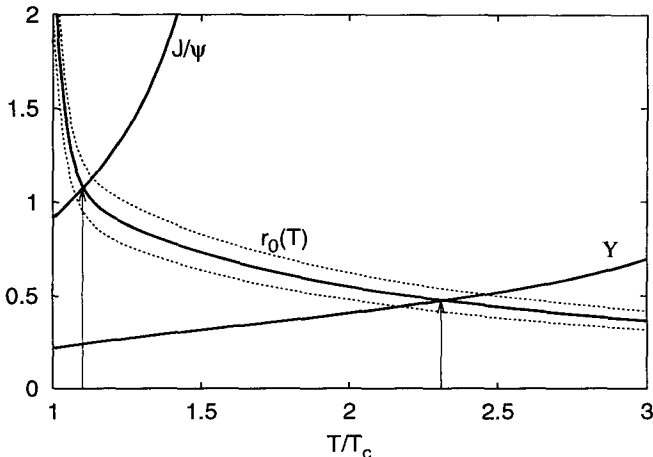


Figure 3. The radii (in fm) of  $J/\psi$  and  $\Upsilon$  states as function of  $T/T_c$ , compared to  $r_0(T)$ .

deconfined phase, which consistently complements the results of the analysis of the previous section. In Table 1 we list the dissociation temperatures of all charmonium and bottomonium states.

Table 1. Dissociation temperatures of charmonium and bottomonium states.

$q\bar{q}$	$J/\Psi$	$\chi_c$	$\psi'$	$\Upsilon(1S)$	$\chi_b(1P)$	$\Upsilon(2S)$	$\chi_b(2P)$	$\Upsilon(3S)$
$T/T_c$	1.10	0.74	0.2	2.31	1.13	1.10	0.83	0.75

#### 4 Conclusions

The work of DPS presented here is an interesting attempt to derive the quarkonium suppression pattern directly from the "real" QCD interaction at work in the heavy quark-antiquark system. The results can be however considerably improved by determining the color singlet potential directly from lattice data, instead of extrapolating it. In this case one should as well investigate the quark mass dependence of the potential, which could be important near the critical temperature. Finally, in a hot deconfined medium the interaction of a quarkonium state with partonic constituents (e.g. gluon scattering) can

also lead to its dissociation; this mechanism (thermal activation) should also be taken into account.

### Acknowledgments

I would like to thank H. Satz, S. Digal and P. Petreczky for the detailed explanations of their work. I gratefully acknowledge the financial support of the TMR network ERBFMRX-CT-970122 and the DFG Forschergruppe FOR 339/1-2.

### References

1. T. Matsui and H. Satz, Phys. Lett. **B178**, 416 (1986).
2. E. Eichten et al., Phys. Rev. **D17**, 3090 (1978) and Phys. Rev. **D21**, 203 (1980).
3. S. Jacobs et al., Phys. Rev. **D33**, 3338 (1986).
4. E. Eichten and C. Quigg, Phys. Rev. **D52**, 1726 (1995).
5. F. Karsch et al., Z. Phys. **C37**, 617 (1988).
6. F. Karsch and H. Satz, Z. Phys. **C51**, 209 (1991).
7. F. Karsch et al., Nucl. Phys. **B605**, 579 (2001).
8. O. Kaczmarek et al., Phys. Rev. **D62**, 034021 (2000).
9. C. DeTar et al., Phys. Rev. **D59**, 03150 (1999).
10. S. Digal et al., Phys. Lett. **B514**, 57 (2001).
11. S. Digal et al., Phys. Rev. **D64**, 094015 (2001).
12. N. Attig et al., Phys. Lett. **B209**, 65 (1988).

# INCLUSIVE DISTRIBUTIONS AND COLLECTIVE PHENOMENA IN HEAVY ION COLLISIONS

ROBERTO UGOCCIONI

*Dipartimento di Fisica Teorica and I.N.F.N. - sezione di Torino  
via P. Giuria 1, 10125 Torino, Italy*

Recent results on charged particle pseudo-rapidity densities from RHIC are analysed in the framework of the Dual String Model, in particular when including string fusion.

The dependence of measurable quantities like charged particle density, transverse energy and  $J/\psi$  production rate on the number  $N_{\text{part}}$  of participant nucleons in high energy heavy ion collisions is extremely important both for a better understanding of the initial conditions in the evolution of newly created dense matter and because it provides the information for discriminating among different models.<sup>1,2,3,4</sup> In this contribution I analyse such quantities in the framework of the Dual String Model (DSM).

As a start, nucleus-nucleus collisions are built as resulting from superposition of nucleon-nucleon collisions, in the way it is done in the Glauber model approach and its generalisations: in the DSM, i.e., the Dual Parton Model<sup>5</sup> with the inclusion of strings,<sup>6</sup> the valence quarks of the nucleon produce particles, via strings, only once —this is the wounded nucleon model case— and production is proportional to the number  $N_A$  of participant nucleons (Fig. 1a). As the energy and  $N_A$  increase, the role of sea quarks and gluons increases: they interact and produce, again via strings, particles, and the number of collisions  $\nu$  becomes the relevant parameter (Fig. 1b). One should notice that the diagram of Fig. 1b may be interpreted as multiple inelastic scattering, occurring either internally within a given nucleon-nucleon collision or externally involving interactions with different nucleons.

Following Ref. <sup>7</sup>, and taking into account the above basic properties, one can now write an expression for the particle pseudo-rapidity density,

$$\left. \frac{dN}{dy} \right|_{N_A N_A} = N_A [2 + 2(k - 1)\alpha] h + (\nu_{N_A} - N_A) 2k\alpha h, \quad (1)$$

where  $h$  is the height of the valence-valence rapidity plateau,  $\alpha$  is the relative weight of the sea-sea (including gluons) plateau and  $k$  is the average number of string pairs per collision. Elementary multi-scattering arguments<sup>7</sup> give  $\nu_{N_A} = N_A^{4/3}$ . However, as mentioned above, the diagram corresponding to sea-sea

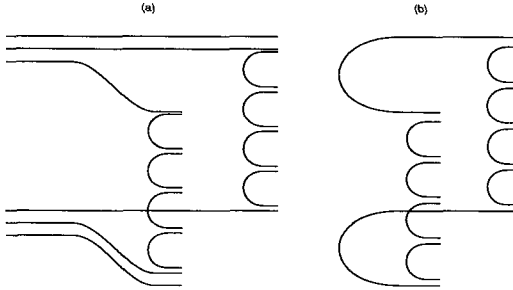


Figure 1. Two strings are produced by each collisions of valence partons (a) and sea partons (b). Notice how the nucleon is broken up in (a), so that further interactions are of the type illustrated by (b).

scattering can be iterated with  $k \geq 1$  being, in general, a function of energy. The number of nucleon-nucleon collisions is, of course,  $N_A + (\nu_{N_A} - N_A) = \nu_{N_A}$ , and the number of strings is  $N_s = N_A [2 + 2(k - 1)] + (\nu_{N_A} - N_A)2k = 2k\nu_{N_A}$ . The first term on the right-hand side of Eq. (1) is just a sum over nucleon-nucleon scattering contributions (including internal parton multiple scattering) and one can thus write

$$\frac{dN}{dy} \Big|_{N_A N_A} = \frac{dN}{dy} \Big|_{pp} N_A + (\nu_{N_A} - N_A)2k\alpha h. \quad (2)$$

If external multiple scattering is absent, by putting  $\nu_{N_A} = N_A$ , one obtains the wounded nucleon model limit; if  $k \gg 1$  we obtain the limit in which multiple scattering dominates. Assuming that  $h$  and  $\alpha$  are energy independent (constant plateaus), the energy dependence of  $dN/dy|_{pp}$ , obtained from a parametrisation of experimental data,<sup>4</sup> fixes the energy dependence of  $k$ , giving  $\alpha = 0.05$  and  $h = 0.75$ .

In the DSM, strings may interact by fusing<sup>12,13</sup> in the transverse plane of interaction thus modifying the number and the distributions of produced particles: in particular, due to the vector nature of the colour charge, a cluster of  $m$  strings will emit fewer particles than  $m$  separate strings.<sup>14</sup>

The number of strings coming from nucleon multiple scattering —the second term in Eq. (1)—is  $N_A(N_A^{1/3} - 1)2k$  and they occupy the transverse interaction area  $S_{N_A}$ , which, for central collisions, is approximately given by  $S_{N_A} \simeq \pi \left(1.14N_A^{1/3}\right)^2$ , such that the dimensionless transverse density

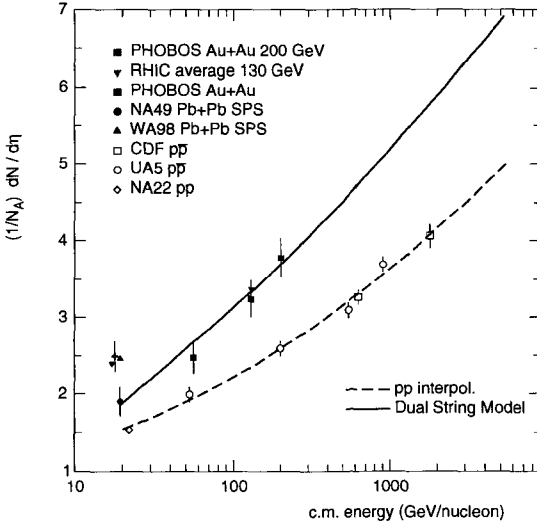


Figure 2. Pseudo-rapidity density normalised per participant pair as a function of c.m. energy. The solid line is the result of the Dual String Model with fusion, Eq. (4), based on the interpolation of  $pp$  and  $p\bar{p}$  data<sup>8,9,10,11</sup> given by the dashed line (which represents also the pure wounded nucleon model limit). AA points are taken from Ref. <sup>1,2,3,20</sup>

parameter  $\eta$  is

$$\eta = \left( \frac{r_s}{1.14} \right)^2 2kN_A^{1/3}(N_A^{1/3} - 1), \quad (3)$$

where  $r_s \simeq 0.2$  fm is the string transverse section radius. Note that  $\eta$  increases with  $N_A$  and, via  $k$ , also with  $\sqrt{s}$ .

When fusion occurs, Eq. (2) becomes<sup>4</sup>

$$\frac{1}{N_A} \frac{dN}{dy} \Big|_{N_A N_A} = \frac{dN}{dy} \Big|_{pp} + F(\eta)(N_A^{1/3} - 1)2k\alpha h, \quad (4)$$

where  $F(\eta)$  is the particle production reduction factor,<sup>15</sup>

$$F(\eta) \simeq \sqrt{\frac{1 - e^{-\eta}}{\eta}}. \quad (5)$$

In Fig. 2, the quantity in Eq. 4 is presented as function of the c.m. energy  $\sqrt{s}$  (solid line). It is very interesting to notice that at low energy there is a discrepancy between recent measurements<sup>20</sup> and earlier ones:<sup>1</sup> the almost flat

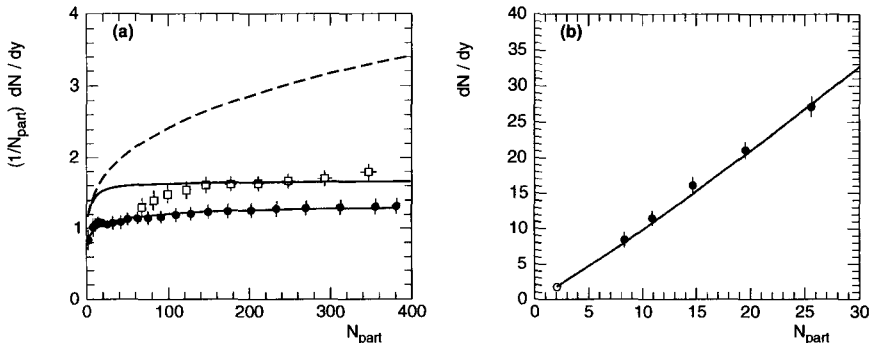


Figure 3. (a) Charged particle density per participant nucleon versus the number of participants at  $17.3A \text{ GeV}$   $\text{Pb}+\text{Pb}$  (filled circles)<sup>2</sup> and at  $130A \text{ GeV}$   $\text{Au}+\text{Au}$  (open squares);<sup>21</sup> the solid lines show results from Eq. (4) at the two energies, respectively; the dashed line shows the result at  $130A \text{ GeV}$  without string fusion, see Eq. (2). (b) absolute charged particle density versus the number of participants; the open circle refers to  $pp$  collisions.<sup>17</sup>

behaviour below  $100 \text{ GeV}/\text{nucleon}$ , if confirmed, is puzzling and not predicted by any model. The overall growth measured at RHIC in  $\text{Au}+\text{Au}$  collisions is not far from that measured at SppS in  $p\bar{p}$  collisions.

It can also easily be shown<sup>16</sup> that the DSM with fusion predicts saturation of the particle rapidity densities per participant pair of nucleons as  $N_A$  increases. This prediction is compared to experimental data in figure 3.

Furthermore, it is to be noted that the predictions for particle densities in central  $\text{Pb}+\text{Pb}$  collisions of the DSM without fusion and of the DSM with fusion are very different at  $\sqrt{s} = 200A \text{ GeV}$  (RHIC) —respectively 1500 and 700— and at  $\sqrt{s} = 5.5A \text{ TeV}$  (LHC) —respectively 4400 and 1400.

Of course this model is essentially soft. The parameters of the elementary collision densities,  $h$  and  $\alpha$ , were assumed constant, all the energy dependence being attributed to the parameter  $k$ , the average number of string pairs per elementary collision. If  $h$  and  $\alpha$  are allowed to grow with energy, as a result, for instance, of semi-hard effects, the parameter  $k$  may then have a slower increase than the one obtained here.

Finally, one should consider the idea that string fusion eventually leads to a situation of percolation<sup>12,13</sup> with the formation of extended regions of colour freedom, with the features of the expected Quark-Gluon Plasma. Indeed the parameter  $\eta$  at the CERN-SPS has the value  $\eta \approx 1.8$ , larger than the

critical density ( $\eta_c \approx 1.12 \div 1.17$ ) which means that percolation transition is already taking place at  $\sqrt{s} = 20$  AGeV, even allowing for non-uniform matter distribution in the nucleus ( $\eta_c \approx 1.5$ );<sup>18</sup> this result is valid even with  $k = 1$ . The observed anomalous  $J/\psi$  suppression<sup>19</sup> may then be a signature of the percolation transition to the Quark-Gluon Plasma.<sup>12,13</sup>

Indeed, in our simple approach,<sup>13</sup>  $J/\psi$  and Drell-Yan production are treated as rare events: this implies that their ratio is given by the product of two functions, one describing absorption of  $J/\psi$  (which is assumed as usual to be exponential in the amount of matter longitudinally traversed), the other describing  $J/\psi$  ( $c\bar{c}$ ) suppression due to Debye screening. If one takes the drastic position that the latter is 100% effective if there is percolation, and ineffective otherwise, then screening is described by the probability of non-percolation, which can be parametrised as

$$P_{\text{non-perc}}(\eta) = \left[ 1 + \exp\left(\frac{\eta - \eta_c}{a_c}\right) \right]^{-1}, \quad (6)$$

with  $a_c$  a parameter linked to the finite size of the nuclear system. Thus the onset of the phase transition is characterised by a change in the curvature of the  $J/\psi$  over D.Y. ratio from positive (during absorption) to negative. This however is only a qualitative description: a quantitative one should probably take into account more details of the process (e.g., geometry varying with impact parameter, resonances, ...).

In conclusion, the DSM is a model with two components, the valence-valence component and the sea-sea component, the sea-sea component increasing its importance with energy and number of participants. This is somewhat similar to the HIJING<sup>22</sup> Monte Carlo model, with soft and hard components. On the other hand, with fusion the DSM behaves, for large  $N_A$ , similarly to the EKRT<sup>23</sup> model, but with strict saturation of the particle density per participant nucleon. However, in the original EKRT model the saturation criterion in the transverse plane is stronger than in case of fusion of strings. Here, saturation in the interaction area is asymptotic (when  $\eta \rightarrow \infty$ ) while in the EKRT model it occurs at finite density. This causes the decrease of the particle density with  $N_A$  in the EKRT original model. It should furthermore be mentioned that the fusion/percolation idea appears necessary also in the quark-gluon model approach.<sup>24</sup>

Probably different explanations, such as the ones based on string fusion, parton saturation, parton shadowing, are in some sense dual and refer to the same underlying physics.<sup>7</sup> What is becoming clear is that saturation of particle density puts strong constraints in models, and limits the rise of the (pseudo-)rapidity plateau at RHIC and eventually at LHC.

## References

1. B.B. Back et al., PHOBOS Collaboration, Phys. Rev. Lett. **85**, 3100 (2000).
2. M.M. Aggarwal et al., WA98 Collaboration, Eur. Phys. J. C **18**, 651 (2001).
3. X.-N. Wang and M. Gyulassy, Phys. Rev. Lett. **86**, 3496 (2001).
4. J. Dias de Deus and R. Ugoccioni, Phys. Lett. B **491**, 253 (2000).
5. A. Capella et al., Physics Reports **236**, 225 (1994).
6. N.S. Amelin, M.A. Braun and C. Pajares, Phys. Lett. B **306**, 312 (1993); N.S. Amelin, M.A. Braun and C. Pajares, Z. Phys. C **63**, 507 (1994).
7. N. Armesto and C. Pajares, Int. J. Mod. Phys. A **15**, 2019 (2000).
8. M. Adamus et al., NA22 Collaboration, Z. Phys. C **37**, 215 (1988).
9. G.J. Alner et al., UA5 Collaboration, Physics Reports **154**, 247 (1987).
10. R.E. Ansorge et al., UA5 Collaboration, Z. Phys. C **43**, 357 (1989).
11. F. Abe et al., CDF Collaboration, Phys. Rev. D **41**, 2330 (1990).
12. N. Armesto et al., Phys. Rev. Lett. **77**, 3736 (1996); M. Nardi and H. Satz, Phys. Lett. B **442**, 14 (1998).
13. J. Dias de Deus, R. Ugoccioni and A. Rodrigues, Eur. Phys. J. C **16**, 537 (2000).
14. T.S. Biro, H.B. Nielsen and J. Knoll, Nucl. Phys. B **245**, 449 (1984).
15. M.A. Braun and C. Pajares, Eur. Phys. J. C **16**, 349 (2000).
16. J. Dias de Deus and R. Ugoccioni, Phys. Lett. B **494**, 53 (2000).
17. C. De Marzo et al., Phys. Rev. D **26**, 1019 (1982).
18. A. Rodrigues, R. Ugoccioni and J. Dias de Deus, Phys. Lett. B **458**, 402 (1999).
19. M.C. Abreu et al., NA50 Collaboration, Phys. Lett. B **477**, 28 (2000).
20. Talk given by NA50 Collaboration at the 4th International Conference on Physics and Astrophysics of Quark-Gluon Plasma 26-30 Nov. 2001, Jaipur (India).
21. B.B. Back et al., PHOBOS Collaboration, Phys. Rev. C **65**, 031901 (2002).
22. X.-N. Wang and M. Gyulassy, Phys. Rev. D **44**, 2501 (1991).
23. K.J. Eskola et al., Nucl. Phys. B **570**, 379 (2000); K.J. Eskola, K. Kajantie and K. Tuominen, preprint JYFL-3700 and HIP-2000-45/TH (hep-ph/0009246), Univ. of Jyväskylä and Univ. of Helsinki.
24. J. Dias de Deus, Yu.M. Shabelski and R. Ugoccioni, preprint DFTT 24/2001 and FISIST/12-2001/CENTRA (hep-ph/0108253), Università di Torino and IST/CENTRA (2001).

This page is intentionally left blank

## MANY BODY THEORIES AND THE NUCLEAR EQUATION OF STATE

*A firm understanding of ordinary hadronic matter and of its properties at high densities and temperatures is preliminarily required in order to disentangle evidence for a deconfined Quark Gluon Plasma.*

*The random matrix theory is introduced by De Pace and Molinari as a useful method for averaging randomness in nuclear physics: it allows to realize a new unified approach to the continuum spectrum (optical model) and to the bound states (shell model) of a nucleus. The relevance of this stochastic model in connection with the spectrum of the Dirac operator is elucidated, pointing to future, possibly interesting applications to QCD.*

*The main focus of this chapter is centered on the nuclear and/or neutron matter Equation of State (EOS). This issue is developed with various techniques (variational, perturbative) and models. On several occasions the results are discussed in connection with neutron stars (cold, dense hadronic matter) and other objects of astrophysical interests.*

*The Auxiliary Field Diffusion Monte Carlo technique, recently developed by Fantoni and collaborators to perform quantum simulations of medium size nuclear systems, has significantly improved the possibility of performing “ab initio” calculations on nuclear and neutron matter.*

*A thorough analysis of the constraints set by nuclear and neutron stars data on the EOS at  $T = 0$  is presented by Benhar, together with some new insights from the study of gravitational waves emitted by neutron stars.*

*In the contributions by Di Toro et al. and by Zuo et al., the symmetry energy and the magnetic susceptibility of nuclear matter are related, within different frameworks (Quantum Hadrodynamics, Relativistic Random Phase Approximation, Brueckner-Hartree-Fock) to the relevant spin-isospin dependence of the nucleon-nucleon interaction. The density dependence of these properties is carefully investigated.*

*The influence of a sizable strange quark component in the neutron star EOS is considered, using various nuclear and quark models, both (by Baldo) in connection with the microscopic Bethe-Brueckner-Goldstone theory, extended up to the three hole-line diagrams contribution, and (by Drago and Lavagno) in a specific study of the critical density, which separates hadronic matter from a mixed phase of quarks and hadrons.*

*Finally Terranova and collaborators propose a dynamical model to describe, within a semiclassical approximation, relativistic heavy ion collisions starting from quark degrees of freedom, including color.*

This page is intentionally left blank

# RANDOMNESS IN NUCLEI AND IN THE QUARK-GLUON PLASMA

A. DE PACE AND A. MOLINARI

*Dipartimento di Fisica Teorica dell'Università di Torino and  
Istituto Nazionale di Fisica Nucleare, Sezione di Torino,  
via P.Giuria 1, I-10125 Torino, Italy*

The issue of averaging randomness is addressed, mostly in nuclear physics, but shortly also in QCD. The Feshbach approach, so successful in dealing with the continuum spectrum of the atomic nuclei (*optical model*), is extended to encompass bound states as well (*shell model*). Its relationship with the random-matrix theory is discussed and the bearing of the latter on QCD, especially in connection with the spectrum of the Dirac operator, is briefly touched upon. Finally the question of whether Feshbach's theory can cope with the averaging required by QCD is considered.

## 1 The random-matrix theory and nuclear applications

The random-matrix theory (RMT) is built out of any stochastic modelling of the matrix representation of a Hamiltonian. It was introduced half-a-century ago by Wigner, who considered an ensemble of Hamiltonians, different but sharing some symmetry, having independent random variables as elements and searched for those properties common to (nearly) all the members of the ensemble. For this purpose he introduced the probability of the occurrence of a given matrix  $H$  in the ensemble by multiplying a weighting function  $P_{N\beta}(H)$ , —  $N$  being the Hilbert space dimension and  $\beta$  an index specifying the symmetry of the ensemble, — for the differentials of all the elements of the matrix representing  $H$ .

Wigner focused on matrices with random elements having a gaussian distribution (Gaussian statistical hypothesis). The weighting function of a Hamiltonian with  $N$  quantum states is then

$$P_{N\beta}(H) = e^{-\beta N \text{tr} H^2 / \lambda^2}, \quad (1)$$

$\lambda$  being some  $N$ -independent constant.

Concerning the symmetry, in the framework of the quantum Gaussian random-matrix theory (GRMT) one can define three different ensembles:

- i) the ensemble of the real symmetric matrices, describing time-reversal and rotationally invariant systems, referred to as GOE (Gaussian orthogonal ensemble) and corresponding to  $\beta = 1$ ;

- ii) the ensemble of Hermitian matrices, describing systems violating time-reversal invariance, as, e. g., a nucleus in an external magnetic field, referred to as GUE (Gaussian unitary ensemble) and characterized by  $\beta = 2$ ;
- iii) the ensemble of the matrices that are linear combinations of the  $2 \times 2$  unit matrix and the Pauli matrices, namely

$$H_{nm} = H_{nm}^{(0)} \mathbf{1}_2 - i \sum_{j=1}^3 H_{nm}^{(j)} \sigma_j, \quad (2)$$

where  $H_{nm}^{(0)}$  and  $H_{nm}^{(j)}$  are real matrices, symmetric and antisymmetric, respectively. The matrices (2) describe systems with half-integer spin, time-reversal, but not rotationally, invariant and the associated ensemble is referred to as GSE (Gaussian symplectic ensemble), which corresponds to the choice  $\beta = 4$ .

The elements of the matrices belonging to the ensembles GOE, GUE and GSE are real, complex and quaternion numbers, respectively.

How to derive predictions on observables and how to compare these with the data in the GRMT framework are questions recently reviewed by Weidenmueller *et al.*<sup>1</sup> These authors emphasize that predictions having universal validity, i. e. unrelated to the specific nature of the system under investigation, concern the fluctuations around mean values. Typical in this connection is the energy spectrum of a complex system with its mean level spacing  $\Delta(\epsilon)$  and the related fluctuations: In the GRMT the latter are universal, the energies of the individual systems are not.

More generally, are the local correlations among the eigenvalues (and the eigenvectors as well) that are accounted for by the GRMT, using  $\Delta(\epsilon)$  as an input to fix the parameter  $N/\lambda^2$  in (1). As it is well-known, an amazing example in this connection is offered by the short-range fluctuations in the spectra of the atomic nuclei near the neutron emission threshold ( $\sim 8$  MeV). Indeed, given  $s = S/\Delta(\epsilon)$  where  $S$  denotes the actual level spacing, the data of the nearest neighbour spacing distributions of the nuclear levels,  $p(s)$ , are strikingly in accord with the GRMT predictions as shown in Fig. 1.

It is of importance to realize that the strong repulsion displayed by the nuclear levels, when their excitation energy is sufficiently large and their distance sufficiently small, in the GRMT is engrained in Eq. (1). Indeed, if the eigenvalues  $E_1, E_2, \dots, E_N$  and the eigenvectors of the matrices of the ensemble are chosen as new independent variables, then (1) factorizes in two terms:

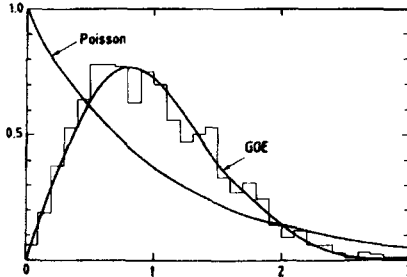


Figure 1. Nearest-neighbor spacing distribution versus the variable  $s$  defined in the text. The GRMT prediction (denoted GOE) is compared to the data (histogram). Also shown the result obtained with a Poisson distribution. (Taken from Ref.<sup>1</sup>).

One only eigenvalue, the other only eigenvector dependent. The former reads

$$P_{N\beta}(E_1..E_N) = \prod_{m>n} |E_m - E_n|^\beta \prod_{l=1}^N dE_l \quad (3)$$

and clearly displays the levels repulsion in the Vandermonde determinant that multiplies  $dE_1..dE_N$ .

Actually, there is still a long way to go from (3) to  $p(s)$ . It is remarkable that Wigner was able to cross it with his famous ansatz

$$p(s) = ase^{-bs^2}, \quad (4)$$

which turned out to be very close to the exact predictions of the GRMT.<sup>2</sup> Note that the gaussian fall-off of (4) is not related to the gaussian nature of the ensemble, but directly arises from the Vandermonde determinant in (3).

Applications of GRMT to QCD will be just touched upon in Sec. 3.

## 2 Feshbach's theory

Feshbach's approach assumes the existence of randomness in complex systems whose internal structure is revealed by their excitation spectrum. On the other hand, in this view there are no systems completely ruled by randomness. The latter is defined through the relation

$$\langle \sigma(A)\sigma(B) \rangle = \langle \sigma(A) \rangle \langle \sigma(B) \rangle, \quad (5)$$

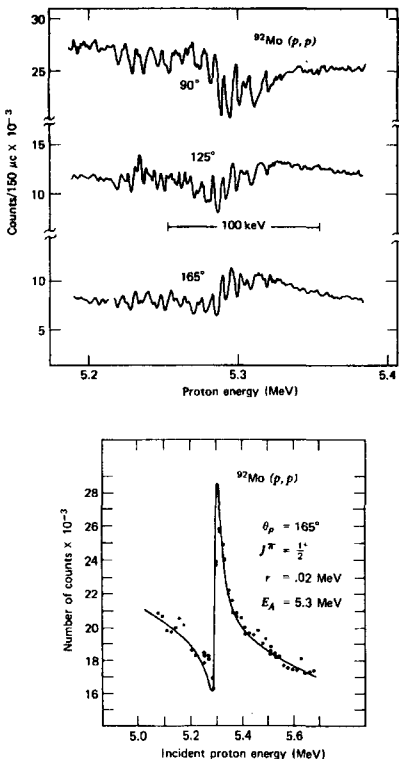


Figure 2. (a) Elastic scattering of protons by  $^{92}\text{Mo}$  for energies close to the  $s$ -wave isobar analog resonance; (b) what one obtains by averaging the data of (a). (Taken from Ref. <sup>4</sup>).

$\sigma$  being some physical observable of the system, dependent upon a parameter: The system is chaotic if the value of  $\sigma$  in correspondence of the value  $A$  for the parameter is independent of the value  $\sigma$  assumes for any other value of the parameter, say  $B$ .

Feshbach's <sup>3</sup> view is that systems totally ruled by randomness do not exist or, equivalently, that coherent combinations of  $\sigma$  can always be found such to allow the existence of correlations where now, in contrast with the discussion of Sec. 1, the correlations are *dynamical*, not *statistical*, they relate to *order*, not to *disorder*.

The question then arises: How these dynamical correlations can be unraveled? The answer is: With appropriate averaging procedures. Before formally

defining the average, it is illuminating to experience how it works in a specific example: The elastic scattering of protons from the nucleus  $^{92}\text{Mo}$  at various scattering angles and in the energy range of a few MeV. In Fig. 2a we show the data obtained with a poor energy resolution: They indeed appear to display the features of a random process (note that the values  $A$  and  $B$  of a generic parameter in (5) here correspond to specific values of the energy). But in Fig. 2b the same data (at  $\theta = 165^\circ$ ) are shown as obtained with a high energy resolution. What appears is astonishing: A perfect resonance typical of a highly correlated scattering process.

The Heisenberg uncertainty principle  $\Delta E \Delta t \geq \hbar/2$ , provides the key to understand. Poor energy resolution means large  $\Delta E$ , hence small  $\Delta t$  or short time for the system to interact: The data appear random. On the other hand, small  $\Delta E$  entails large  $\Delta t$ , hence a long time for the system to average out the fluctuations: The results are then those of Fig. 2b.

The necessity of averaging procedures to properly deal with randomness is thus clear. This program has been carried out by Feshbach<sup>5</sup> in his unified theory of nuclear reactions. We here extend his formalism to the bound states of many-body systems, focusing on the ground state, to complete Feshbach's program and to illustrate how it works. For this purpose we start by partitioning the Hilbert space associated to a many-body system in the  $P$  and  $Q$  sectors, respectively.

## 2.1 Theoretical framework

As it is well-known, the splitting of the Hilbert space induced by the projection operators  $P$  and  $Q$  transforms the Schrödinger equation

$$H\psi = E\psi \quad (6)$$

into the pair of coupled equations

$$(E - H_{PP})(P\psi) = H_{PQ}(Q\psi) \quad (7)$$

$$(E - H_{QQ})(Q\psi) = H_{QP}(P\psi), \quad (8)$$

the meaning of the symbols being obvious. From the above the equation obeyed solely by  $(P\psi)$  is derived. It reads

$$\mathcal{H}(P\psi) = E(P\psi), \quad (9)$$

the  $P$ -space Hamiltonian being

$$\mathcal{H} = H_{PP} + H_{PQ} \frac{1}{\left(\frac{1}{e_Q}\right)^{-1} + W_{QQ}} H_{QP}, \quad (10)$$

with

$$e_Q = E - H_{QQ} - W_{QQ} \quad (11)$$

$$W_{QQ} = H_{QP} \frac{1}{E - H_{PP}} H_{PQ}. \quad (12)$$

It is of significance that although Eq. (9) is not an eigenvalue equation, since the energy  $E$  also appears in the denominator of its right hand side, yet its solutions only occur for those values of  $E$  which are eigenvalues of (6) as well; in other words, a one-to-one correspondence between the values of  $E$  allowed by (6) and (9) exists (see later for a further discussion of this point). However, the solutions of (9) in correspondence to the various values of  $E$  are *not* orthogonal.

Now, we assume the quantum deterministic aspect of nuclear dynamics to be embodied in the  $P$ -space, the chaotic one in the  $Q$ -space. Hence, the strategy of averaging over the latter follows, although, admittedly, some fuzziness does affect this partitioning. To set up the averaging procedure we start by the recognition that the wave functions in the  $Q$ -space are rapidly varying functions of the energy  $E$ , viewed as a parameter classifying their ensemble.

Accordingly, we average over this ensemble following the prescription

$$\langle f(E) \rangle = \int_{-\infty}^{\infty} dE \rho(E, \bar{E}_0, \epsilon) f(E), \quad (13)$$

$f$  being a generic function to be averaged over the variable  $E$  with the distribution  $\rho(E, \bar{E}_0, \epsilon)$ . The latter depends, beyond  $E$ , also upon the value  $\bar{E}_0$  around which the average, — taken over a range of  $E$  essentially set by  $\epsilon$ , — is performed. A distribution convenient for our purposes is

$$\rho(E, \bar{E}_0, \epsilon) = \frac{1}{2\pi i} \frac{e^{iE\eta}}{E - (\bar{E}_0 - \epsilon) - i\eta}, \quad (14)$$

which is indeed correctly normalized being

$$\int_{-\infty}^{\infty} dE \rho(E, \bar{E}_0, \epsilon) = 1 \quad (15)$$

(one should let  $\eta \rightarrow 0^+$  after the integration has been performed). Note that Eq. (14) extends in some sense the Lorentz distribution of the optical model<sup>5</sup> to the situation of a zero width state. Hence the present formalism is especially suited to deal with ground states, which are of course stable: We shall accordingly focus mainly on the latter in the following.

Now, in the  $Q$ -space the wave functions are found to be<sup>6,7,8</sup>

$$(Q\psi) = \frac{1}{e_Q} H_{QP} \psi_0, \quad (16)$$

$\psi_0$  being an auxiliary function that in the end disappears from the formalism. By averaging Eq. (16) according to the prescriptions (13) and (14), one then finds that the averaged wave function of the nuclear ground state in the  $P$ -space (here denoted by the angle brackets) obeys the equation

$$\bar{\mathcal{H}}\langle P\psi \rangle = \bar{E}_0\langle P\psi \rangle. \quad (17)$$

In (17)  $\bar{E}_0$  is the mean field energy and

$$\bar{\mathcal{H}} = H_{PP} + H_{PQ} \frac{1}{\left\langle \frac{1}{e_Q} \right\rangle^{-1} + W_{QQ}(E = \bar{E}_0)} H_{QP} \quad (18)$$

is the mean field Hamiltonian. This can be further elaborated since the singularities of the operator  $1/e_Q$  lie in the  $\text{Im}E < 0$  half-plane<sup>9</sup>. Accordingly, one gets

$$\begin{aligned} \left\langle \frac{1}{e_Q} \right\rangle &= \frac{1}{2\pi i} \int_{-\infty}^{\infty} dE \frac{e^{iE\eta}}{E - (\bar{E}_0 - \epsilon) - i\eta} \frac{1}{E - H_{QQ} - W_{QQ}(E)} \\ &= \frac{1}{\bar{E}_0 - \epsilon - H_{QQ} - W_{QQ}(E = \bar{E}_0 - \epsilon)} \approx \frac{1}{\bar{E}_0 - \epsilon - H_{QQ} - W_{QQ}(E = \bar{E}_0)}, \end{aligned} \quad (19)$$

the last passage holding if the energy dependence of the operator  $W_{QQ}$  is mild and if the parameter  $\epsilon$  is not too large (it should be not too small either, otherwise the energy averaging procedure becomes meaningless).

The insertion of (19) into (18) leads then to the following useful alternative expression for the mean field Hamiltonian

$$\bar{\mathcal{H}} = H_{PP} + V_{PQ}V_{QP} \frac{1}{\bar{E}_0 - \epsilon - E}, \quad (20)$$

where the energy dependent operators

$$V_{PQ} = H_{PQ} \sqrt{\frac{\bar{E}_0 - \epsilon - E}{\bar{E}_0 - \epsilon - H_{QQ}}} \quad (21)$$

and

$$V_{QP} = \sqrt{\frac{\bar{E}_0 - \epsilon - E}{\bar{E}_0 - \epsilon - H_{QQ}}} H_{QP}, \quad (22)$$

represent the residual effective NN interaction. The usefulness of the Eqs. (20), (21) and (22) was realized in Ref. <sup>10</sup>, where it was noticed that with their help

the pair of equations (2.1) can be recast, as far as  $(P\psi)$  is concerned, into the form

$$(E - \bar{\mathcal{H}})(P\psi) = V_{PQ}(Q\psi) \quad (23)$$

$$(E - H_{QQ})(Q\psi) = V_{QP}(P\psi), \quad (24)$$

which is suitable for expressing the mean field fluctuations (the “error”).

Indeed, by exploiting the spectral decomposition of the operator  $(E - \bar{\mathcal{H}})^{-1}$  in terms of the eigenfunctions  $\phi_n$  of the mean field Hamiltonian  $\bar{\mathcal{H}}$ ,<sup>a</sup> one gets from Eq. (23)

$$\begin{aligned} |P\psi\rangle &= \sum_n \frac{|\phi_n\rangle}{E - \bar{E}_n} \langle \phi_n | V_{PQ} | Q\psi \rangle \\ &= |\phi_0\rangle \frac{\langle \phi_0 | V_{PQ} | Q\psi \rangle}{E - \bar{E}_0} + \left( \frac{1}{E - \bar{\mathcal{H}}} \right)' V_{PQ} | Q\psi \rangle, \end{aligned} \quad (25)$$

which, upon left multiplication by  $\langle \phi_0 |$ , yields

$$\langle \phi_0 | P\psi \rangle = \frac{\langle \phi_0 | V_{PQ} | Q\psi \rangle}{E - \bar{E}_0}. \quad (26)$$

In the second term on the right hand side of Eq. (25), the prime stands for the omission of the  $n = 0$  term in the spectral decomposition.

Next, the insertion of Eq. (25) into (24) leads to

$$|Q\psi\rangle = \frac{1}{E - h_{QQ}} V_{QP} |\phi_0\rangle \langle \phi_0 | P\psi \rangle, \quad (27)$$

where the operator

$$h_{QQ} = H_{QQ} + V_{QP} \left( \frac{1}{E - \bar{\mathcal{H}}} \right)' V_{PQ} \quad (28)$$

has been introduced. Finally, by combining (26) and (27), one arrives at the equation

$$E - \bar{E}_0 = \langle \phi_0 | V_{PQ} \frac{1}{E - h_{QQ}} V_{QP} | \phi_0 \rangle, \quad (29)$$

which is the basis for computing the mean field energy error (or the fluctuations of the energy associated with randomness).

Although Eq. (29) is valid for any choice of the projectors  $P$  and  $Q$ , its use is in fact appropriate when the  $P$ -space is one-dimensional, as it was indeed

---

<sup>a</sup>We omit here the difficult proof concerning the normalization and orthogonalization of the eigenfunctions  $|\phi_n\rangle$  of  $\bar{\mathcal{H}}$ .

the case in Ref.<sup>8</sup>, where this choice was made for sake of simplicity. For a two-dimensional  $P$ -space, as we shall later see, one should rather single out two, rather than one, terms in the spectral decomposition of the operator  $(E - \bar{\mathcal{H}})^{-1}$  on the right hand side of Eq. (25).

We refer the reader to Refs.<sup>6,7,8</sup> for a discussion on how the average of the square of Eq. (29) is actually computed (the average of (29) of course should vanish) and on how the complexity expansion is organized. Here, we confine ourselves to the leading term of this fast converging expansion.

## 2.2 Energy averaging

To understand better the significance of the energy averaging distribution (14) we show how it works in the simple cases of a bi-dimensional (A) and of a tri-dimensional (B) Hilbert space.

### A. Bi-dimensional Hilbert space

Let  $|\chi_1\rangle$  and  $|\chi_2\rangle$  be the two normalized states spanning the space. Here the only possible choice for the projectors clearly is

$$P \equiv |\chi_1\rangle\langle\chi_1| \quad \text{and} \quad Q \equiv |\chi_2\rangle\langle\chi_2|. \quad (30)$$

Then, by expanding the operator  $1/(E - H_{QQ})$ , Eq. (9) can be recast as follows

$$\left[ E - |\chi_1\rangle a_{11}\langle\chi_1| - |\chi_1\rangle a_{12}\langle\chi_2| \frac{1}{E} \sum_{n=0}^{\infty} \left( \frac{a_{22}}{E} \right)^n (|\chi_2\rangle\langle\chi_2|)^n |\chi_2\rangle a_{12}^* \langle\chi_1| \right] |P\psi\rangle = 0, \quad (31)$$

which, upon multiplying from the left by  $\langle\chi_1|$  and exploiting the idempotency of  $|\chi_2\rangle\langle\chi_2|$ , simplifies to

$$\left[ E - a_{11} - \frac{|a_{12}|^2}{E - a_{22}} \right] \langle\chi_1| P\psi\rangle = 0, \quad (32)$$

where the shorthand notations

$$a_{11} = \langle\chi_1|H|\chi_1\rangle, \quad a_{22} = \langle\chi_2|H|\chi_2\rangle \quad \text{and} \quad a_{12} = \langle\chi_1|H|\chi_2\rangle \quad (33)$$

have been introduced. This equation is trivially solved yielding the eigenvalues

$$E_{\pm} = \frac{1}{2} \left[ a_{11} + a_{22} \pm \sqrt{(a_{11} - a_{22})^2 + 4|a_{12}|^2} \right], \quad (34)$$

which coincide with those of  $H$ . It helps notice that the eigenvalues (34) are also found as intersections of the hyperbola

$$E = a_{11} + \frac{|a_{12}|^2}{\omega - a_{22}} \quad (35)$$

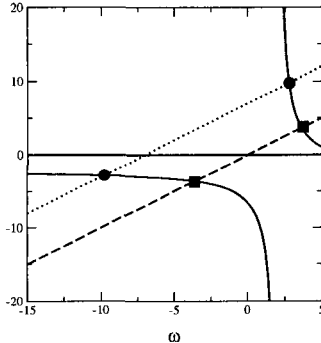


Figure 3. The eigenvalues of a bi-dimensional Hilbert space. The matrix elements of the Hamiltonian are taken to be  $a_{11} = -2$ ,  $a_{22} = 2$  and  $a_{12} = 3$ , in arbitrary units. The exact eigenvalues (squares) and the ones of the energy averaged Hamiltonian  $\bar{H}$  (circles) are shown. They correspond to the intersections with the straight line  $E = \omega + \epsilon$ : The former with  $\epsilon = 0$ , the latter with  $\epsilon = 7$ . The stability of the lowest eigenvalue and the upward shift of the highest one are clearly apparent.

with the straight line  $E = \omega$ .

Also the energy averaged Hamiltonian (20) can be expressed in the basis spanned by  $\chi_1$  and  $\chi_2$  and one gets the mean field equation

$$\left[ \bar{E} - a_{11} - \frac{|a_{12}|^2}{\bar{E} - \epsilon - a_{22}} \right] \langle \chi_1 | \langle P\psi \rangle \rangle = 0. \quad (36)$$

The latter is again trivially solved yielding

$$\bar{E}_{\pm} = \frac{1}{2} \left[ a_{11} + a_{22} + \epsilon \pm \sqrt{(a_{11} - a_{22} - \epsilon)^2 + 4|a_{12}|^2} \right], \quad (37)$$

which now corresponds to the intersections of the hyperbola (35) (with  $\bar{E}$  replacing  $E$ ) with the new straight line  $\bar{E} = \omega + \epsilon$ .

From Fig. 3, where the solutions  $E_{\pm}$  and  $\bar{E}_{\pm}$  are graphically displayed, it clearly appears that, while  $\bar{E}_- \cong E_-$ , the solution  $\bar{E}_+$  is much larger than  $E_+$ , the more so the greater  $\epsilon$  is. It is thus clear that the averaging distribution (14), while mildly affecting the eigenvalue of  $H$  lying in the  $P$ -space, drives away the one lying in the  $Q$ -space.

## B. Tri-dimensional Hilbert space

The space is spanned by the normalized states  $|\chi_1\rangle$ ,  $|\chi_2\rangle$  and  $|\chi_3\rangle$ . Now, two choices are possible for the projectors, namely

$$P \equiv |\chi_1\rangle\langle\chi_1| + |\chi_2\rangle\langle\chi_2| \quad (38)$$

$$Q \equiv |\chi_3\rangle\langle\chi_3| \quad (39)$$

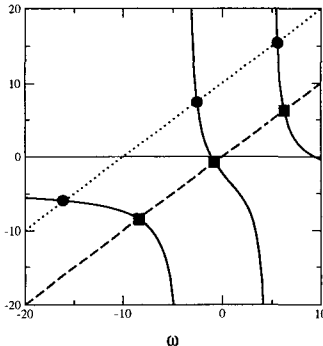


Figure 4. The eigenvalues of a tri-dimensional Hilbert space: The case of a one-dimensional  $P$ -space. The following matrix elements of the Hamiltonian are taken:  $a_{11} = -4$ ,  $a_{22} = -2$ ,  $a_{33} = 3$ ,  $a_{12} = 2$ ,  $a_{13} = -5$  and  $a_{23} = 3.5$ , in arbitrary units. The exact eigenvalues (squares) and the ones of the energy averaged Hamiltonian  $\bar{\mathcal{H}}$  (circles) are shown. They correspond to the intersections with the straight line  $E = \omega + \epsilon$ : The former with  $\epsilon = 0$ , the latter with  $\epsilon = 10$ . The stability of the  $P$ -space eigenvalue and the upward shift of those belonging to the  $Q$ -space are clearly apparent.

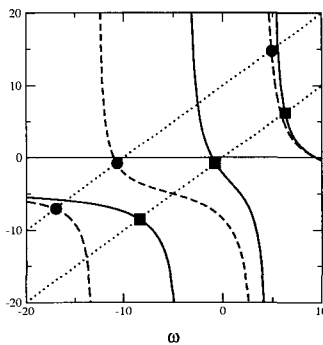


Figure 5. The eigenvalues of a tri-dimensional Hilbert space: The case of a bi-dimensional  $P$ -space. The matrix elements of the Hamiltonian are taken as in Fig. 4. The exact eigenvalues (squares) correspond to the intersections of the straight line  $E = \omega$  with the continuous curve. The eigenvalues of the energy averaged Hamiltonian  $\bar{\mathcal{H}}$  correspond to the intersections of the straight line  $\bar{E} = \omega + \epsilon$ , with  $\epsilon = 10$ , with the dashed curves. Note the dependence upon  $\epsilon$ . The stability of the  $P$ -space eigenvalue and the upward shift of the one belonging to the  $Q$ -space are again clearly apparent.

and

$$P \equiv |\chi_1\rangle\langle\chi_1| \quad (40)$$

$$Q \equiv |\chi_2\rangle\langle\chi_2| + |\chi_3\rangle\langle\chi_3|. \quad (41)$$

In both cases, Eq. (9) can be recast as follows

$$(E - a_{11})(E - a_{22})(E - a_{33}) - |a_{12}|^2(E - a_{33}) - |a_{13}|^2(E - a_{22}) - |a_{23}|^2(E - a_{11}) = 0, \quad (42)$$

which is the cubic equation yielding the exact eigenvalues. Note that Eq. (42) is easily obtained with the choice (2.2), because in this case the operator  $(E - H_{QQ})^{-1}$  is expanded in terms of the idempotent operator  $|\chi_3\rangle\langle\chi_3|$ . Not so with the choice (2.2), because now  $(E - H_{QQ})^{-1}$  should be expanded in terms of the operator (41), *which is not idempotent*. Actually, the larger the powers of the latter are, the more cumbersome they become. Yet, also in this case it can be proved that Eq. (42) holds valid.

Let us now examine the solutions of Eq. (20): As in the previous bi-dimensional case it is convenient to display the solutions graphically. For the partition (2.2), one finds that they are given by the intersections of the  $\epsilon$ -independent curve

$$\bar{E} = a_{11} + \frac{|a_{12}|^2(\omega - a_{33})}{\mathcal{D}_1(\omega)} + \frac{|a_{13}|^2(\omega - a_{22})}{\mathcal{D}(\omega)} + \frac{a_{12}a_{13}^*a_{23}}{\mathcal{D}(\omega)} + \frac{a_{12}^*a_{13}a_{23}^*}{\mathcal{D}(\omega)}, \quad (43)$$

where

$$\mathcal{D}(\omega) = (\omega - a_{22})(\omega - a_{33}) - |a_{23}|^2, \quad (44)$$

with the straight line  $\bar{E} = \omega + \epsilon$ , as displayed in Fig. 4, where the case  $\epsilon = 0$ , — which clearly provides the exact eigenvalues  $E_i$  of the Schrödinger equation, — is also shown. From the figure, it transparently appears that  $\bar{E}_0 \cong E_0$ , whereas  $\bar{E}_1 \gg E_1$  and  $\bar{E}_2 \gg E_2$ , the latter inequalities being stronger when the parameter  $\epsilon$  is large.

In the case of the partition (2.2), the solutions are given by the intersections of the curve obtained replacing  $a_{22} \rightarrow a_{22} - \epsilon$  in Eqs. (43) and (44) with the straight line  $\bar{E} = \omega + \epsilon$ , as displayed in Fig. 5. We face here a new situation, since now not only the straight line, but also Eqs. (43) and (44) are  $\epsilon$ -dependent. Yet, one again sees that for  $\epsilon = 0$  one recovers the eigenvalues  $E_i$ , whereas when  $\epsilon \neq 0$  the intercepts occur for  $\bar{E}_0 \cong E_0$  and  $\bar{E}_1 \cong E_1$ , but for  $\bar{E}_2 \gg E_2$ . Hence, we conclude that the action of the averaging distribution (14) affects very little the eigenvalues belonging to the  $P$ -space, while pushing off the ones in the  $Q$ -space by an amount proportional to  $\epsilon$ .

### 2.3 The $P$ -space

Having defined the energy averaging procedure, to get further it is necessary to define the operators  $P$  and  $Q$ . For this purpose the natural candidates as building blocks of the  $P$  operator appear to be the eigenstates  $|\phi_n\rangle$  of the mean field Hamiltonian (20), defined by the equation

$$\bar{\mathcal{H}}|\phi_n\rangle = \bar{E}_n|\phi_n\rangle. \quad (45)$$

Their finding requires, however, the solution of a difficult self-consistency problem. Hence, we make the simpler choice of viewing as building blocks of  $P$  the Hartree-Fock (HF) variational solutions, which are, e. g., trivial in nuclear matter, the system we shall consider.

For sake of illustration we start with a one-dimensional  $P$ -space by setting

$$P = |\chi_{\text{HF}}\rangle\langle\chi_{\text{HF}}|, \quad (46)$$

$|\chi_{\text{HF}}\rangle$  being the HF ground state wave function of nuclear matter (the Fermi sphere). Then, on the basis of (46), one derives the mean field equation

$$\bar{E}_0 = E_{\text{HF}} + \frac{\beta^2}{\bar{E}_0 - \epsilon - E}, \quad (47)$$

which relates the mean field ( $\bar{E}_0$ ), the HF ( $E_{\text{HF}}$ ) and the true ( $E$ ) energies *per particle*, and the equation for the statistical fluctuation of the energy

$$E - \bar{E}_0 = \pm \frac{1}{E - \bar{\epsilon}_2} \sqrt{\frac{2}{N_2}} \beta^2, \quad (48)$$

where

$$\beta^2 = \sum_{2p-2h} |\langle\psi_{2p-2h}|V|\chi_{\text{HF}}\rangle|^2, \quad (49)$$

the bras  $\langle\psi_{2p-2h}|$  representing the two-particle–two-holes (2p-2h) states of nuclear matter, whose average energy *per particle* is  $\bar{\epsilon}_2$ . Thus all the quantities appearing in Eqs. (47) and (48) are *per particle*, including the parameter  $\epsilon$  and the residual effective interaction  $V$  (which are accordingly divided by the nuclear mass number  $A$ ).

Note also that Eq. (48) gives the “fluctuations” of the mean field energy in the first order of the complexity expansion, which is based on an organization of the  $Q$ -space in blocks of excited states of increasing complexity (see Fig. 6): Here, the contribution to the error only arises from the sector of the  $Q$ -space set up with the 2p-2h excitations. Moreover, although the states of the  $Q$ -space obey well-defined, coupled differential equations (see Ref. <sup>7</sup>), we describe

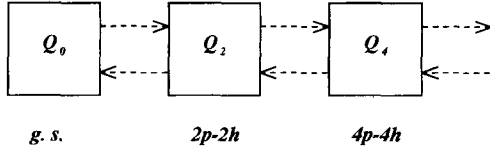


Figure 6. The partition of the Hilbert space of nuclear matter in sets of increasing complexity. The first box on the left defines the  $P$ -space, the second one embodies the simplest states in the  $Q$ -space and so on.

them with the HF multi-particle–multi-hole solutions, an approximation not impairing the orthogonality constraint  $P \cdot Q = 0$ .

The sum in Eq. (49) is performed over the ensemble of the 2p-2h excited states lying in an appropriate energy range (in Refs. <sup>7,8</sup> taken to be fixed essentially by the parameter  $\epsilon$ ), whose number  $\mathcal{N}_2$  can be computed using the Ericson’s formula<sup>11</sup> for the density of the spin  $J$   $N$ -particle– $N$ -hole nuclear states, namely

$$\rho_{ph}^{(N)}(\mathcal{E}, J) = \frac{g(g\mathcal{E})^{N-1}}{p!h!(N-1)!} \frac{2J+1}{\sqrt{8\pi}\sigma^3 N^{3/2}} \exp[-(2J+1)^2/(8N\sigma^2)], \quad (50)$$

where

$$g = \frac{3}{2} \frac{A}{\epsilon_F} \quad \text{and} \quad \sigma^2 = \mathcal{F} \sqrt{\frac{\mathcal{E}}{a} \frac{1}{\hbar^2}}, \quad (51)$$

$\mathcal{F}$  being the nuclear moment of inertia,  $\epsilon_F$  the Fermi energy,  $a = A/8$  MeV<sup>-1</sup> and  $\mathcal{E}$  the excitation energy of the system.

Now, Eqs. (47) and (48), owing to the double sign appearing in the latter, set up two systems, each one including two equations, in two unknowns. Two options are then possible in selecting the latter: One can choose either the ground state mean field and true energies per particle, i. e.  $\bar{E}_0$  and  $E$ , — assuming the matrix elements of the residual effective interaction to be known, — or  $\bar{E}_0$  and  $\beta^2$ , when  $E$  is experimentally known, — which is indeed the case in nuclear matter.

We take the latter choice, requiring in addition the coincidence of the two  $\bar{E}_0$  obtained by solving the two systems separately. Actually, and notably, both systems lead to the same formal expression for the mean field energy per particle, namely

$$\bar{E}_0 = \frac{1}{2} \left\{ (E_{HF} + E + \epsilon) - \sqrt{(E_{HF} - E - \epsilon)^2 + 4\beta^2} \right\}, \quad (52)$$

which holds valid for  $\epsilon < E_{\text{HF}} - E$ , the right hand side of this inequality being positive because of the variational principle. The above, when  $\beta^2 \rightarrow 0$ , yields

$$\bar{E}_0 = E + \epsilon, \quad (53)$$

in accord with (21) and (22), but also with (48), which, for  $V \rightarrow 0$ , gives  $\bar{E}_0 = E$ : Indeed, when the residual effective interaction vanishes no fluctuations can occur and hence the parameter  $\epsilon$  should vanish as well.

On the other hand, the two systems yield two different expressions for the sum of the matrix elements of the residual effective interaction squared, namely

$$\begin{aligned} \beta_l^2 = \sqrt{\mathcal{N}_2/2} \frac{E_l - \bar{\epsilon}_2}{2} & \left\{ \left[ E_l(1 + \sqrt{\mathcal{N}_2/2}) - (\epsilon + \sqrt{\mathcal{N}_2/2}\bar{\epsilon}_2) - E_{\text{HF}} \right] \right. \\ & \left. + \sqrt{\left[ E_l(1 + \sqrt{\mathcal{N}_2/2}) - (\epsilon + \sqrt{\mathcal{N}_2/2}\bar{\epsilon}_2) - E_{\text{HF}} \right]^2 + 4\epsilon(E_l - E_{\text{HF}})} \right\} \end{aligned} \quad (54)$$

and

$$\begin{aligned} \beta_u^2 = \sqrt{\mathcal{N}_2/2} \frac{E_u - \bar{\epsilon}_2}{2} & \left\{ \left[ E_u(-1 + \sqrt{\mathcal{N}_2/2}) - (-\epsilon + \sqrt{\mathcal{N}_2/2}\bar{\epsilon}_2) + E_{\text{HF}} \right] \right. \\ & \left. + \sqrt{\left[ E_u(-1 + \sqrt{\mathcal{N}_2/2}) - (-\epsilon + \sqrt{\mathcal{N}_2/2}\bar{\epsilon}_2) + E_{\text{HF}} \right]^2 + 4\epsilon(E_u - E_{\text{HF}})} \right\}, \end{aligned} \quad (55)$$

both of which vanish in the limit  $\epsilon \rightarrow 0$ , in accord with the previous discussion.

Formula (54), solution of the first system of equations (the one with the “+” sign on the right hand side of (48)), yields the value of the *energy dependent* quantity (49) (here denoted by  $\beta_l^2$ ) on the lower border of the energy band expressing the fluctuations of the ground state energy  $E$  (and thus encompassing  $\bar{E}_0$ ). Formula (55), solution of the second system of equations (the one with the minus sign on the right hand side of (48)), provides instead (49) (here denoted by  $\beta_u^2$ ) on the upper border of the band (remember that  $E - \bar{\epsilon}_2 < 0$ ).

Of course, of the energy per particle  $E$  we only know the experimental value, not the values on the borders of the band: As a consequence, we can only surmise the width  $W$  of the latter, thus providing two different inputs for the energy  $E$  appearing on the right hand side of (2.3), namely  $E_u = E + W/2$  and  $E_l = E - W/2$ . However, we can explore whether, for a given  $W$ , a value for the parameter  $\epsilon$  can be found (not too large, not too small) such to have the two mean field energies per particle to coincide. If this search succeeds, then an orientation on  $W$  (or, equivalently, on the size of the fluctuations of the ground state energy) can be gained.

Note that the framework above outlined holds because the same quantity  $\beta^2$  appears in both (47) and (48). This occurrence stems from an approximation whose validity is discussed in Ref.<sup>8</sup>.

We now extend the formalism by letting the projector  $P$  to encompass, beyond the ground state, the 2p-2h excitations of the HF variational scheme as well. Thus, instead of Eq. (46), we write

$$P = |\chi_{\text{HF}}\rangle\langle\chi_{\text{HF}}| + \sum_{\beta} |\chi_{\text{HF}}^{2\beta}\rangle\langle\chi_{\text{HF}}^{2\beta}|, \quad (56)$$

where the sum is meant to be extended to the whole set of 2p-2h HF excitations  $|\chi_{\text{HF}}^{2\beta}\rangle$ .

With the choice (56) the mean field Hamiltonian (20) is then defined and one can compute the mean field ground state energy per particle,  $\bar{E}_0 = \langle\phi_0|\bar{\mathcal{H}}|\phi_0\rangle$ , using for the ket  $|\phi_0\rangle$  the expression

$$|\phi_0\rangle = s_0|\chi_{\text{HF}}\rangle + \sum_{\gamma} s_2^{\gamma}|\chi_{\text{HF}}^{2\gamma}\rangle, \quad (57)$$

and accounting for the influence of the  $Q$ -space on the ground state mean energy per particle in first order of the complexity expansion, i. e. by setting

$$Q = \sum_{\gamma} |\chi_{\text{HF}}^{4\gamma}\rangle\langle\chi_{\text{HF}}^{4\gamma}|, \quad (58)$$

the sum running over the whole set of the HF 4p-4h excitations. In (57)  $s_0$  and  $s_2^{\gamma}$  are complex coefficients, fixed, in principle, by Eq. (45) and satisfying the normalization condition

$$|s_0|^2 + \sum_{\gamma} |s_2^{\gamma}|^2 = 1. \quad (59)$$

After straightforward, but lengthy, algebra using (57) and (58) one arrives at the following new mean field equation

$$\begin{aligned} \bar{E}_0 = & |s_0|^2 E_{\text{HF}} + \sum_{\gamma} |s_2^{\gamma}|^2 \langle\chi_{\text{HF}}^{2\gamma}|H|\chi_{\text{HF}}^{2\gamma}\rangle + 2s_0^* \sum_{\gamma} s_2^{\gamma} \langle\chi_{\text{HF}}|\mathcal{V}|\chi_{\text{HF}}^{2\gamma}\rangle + \\ & + \frac{1}{\bar{E}_0 - \epsilon - E} \sum_{\beta\gamma} |s_2^{\gamma}|^2 \langle\chi_{\text{HF}}^{4\beta}|V|\chi_{\text{HF}}^{2\gamma}\rangle|^2, \end{aligned} \quad (60)$$

$\mathcal{V}$  being the bare NN potential.

Notably, Eq. (60) turns out to formally coincide with (47). Indeed, the first three terms on the right hand side of Eq. (60) just yield the mean value of the original bare Hamiltonian  $H$  in the state (57). In the thermodynamic limit of nuclear matter out of these pieces only the HF energy survives. Indeed, the

correction to the HF energy per particle due to a finite number of particle-hole excitations vanishes in the thermodynamic limit. In other words, the 2p-2h admixture into (57) *does not change* the expectation value of the Hamiltonian.

Hence, defining

$$\zeta^2 = \sum_{\beta\gamma} |s_2^\gamma|^2 |\langle \chi_{\text{HF}}^{4\beta} | V | \chi_{\text{HF}}^{2\gamma} \rangle|^2, \quad (61)$$

(60) can be recast into the form

$$\bar{E}_0 = E_{\text{HF}} + \frac{\zeta^2}{\bar{E}_0 - \epsilon - E}, \quad (62)$$

whose similarity with Eq. (47) is transparent.

The same will take place for *any* admixture of  $Np-Nh$  HF excited states in  $|\chi_{\text{HF}}\rangle$ : Hence, in our framework different choices of the projection operator  $P$  lead to the same structure for the mean field equation for nuclear matter. This invariance does not hold in finite nuclei.

The only, of course important, difference between (49) and (61) relates to the residual interaction  $V$ , which in (61) induces transitions from 2p-2h to 4p-4h states, rather than from the Fermi sphere to the 2p-2h states.

Concerning the statistical fluctuation equation one can again use (29), with the state  $|\phi_0\rangle$  given now by Eq. (57). Then invoking *the randomness of the phases of the Q-space wave functions (RPA)* and proceeding exactly as done in Refs. 7,8, one deduces the new fluctuation equation

$$E - \bar{E}_0 = \pm \frac{1}{E - \bar{\epsilon}_4} \sqrt{\frac{2}{N_4}} \zeta^2, \quad (63)$$

where  $\bar{\epsilon}_4$  denotes the average energy per particle of the 4p-4h HF states. In (63),  $N_4$  represents the number of 4p-4h excitations contributing to the sum over the index  $\beta$  in (61).

Hence, the “formal invariance”, with respect to the choice for the projector  $P$ , holds for both the equations at the core of our statistical approach to nuclear matter in first order of the complexity expansion.

Indeed, the inclusion of  $Np-Nh$  states (with  $N > 2$ ) into the  $P$ -space would merely imply the replacement, in (63), of  $N_4$  with  $N_{N+2}$  and, at the same time, to have  $\zeta^2$  defined in terms of the matrix elements of  $V$  between  $Np-Nh$  and  $(N+2)p-(N+2)h$  states. In addition, one should of course insert in the energy denominator the average energy per particle of the  $(N+2)p-(N+2)h$  HF states.

Therefore, the extension of the  $P$ -space rapidly leads to the vanishing of the fluctuations, owing to the very fast increase of the number  $N_N$ .

However, as already mentioned, Eq. (29) *is not* in general a good starting point to derive the fluctuation equation. Indeed, it selects out only *one term* in the spectral decomposition of the operator  $1/(E - \bar{\mathcal{H}})$ , which is appropriate for a one-dimensional  $P$ -space only. Hence, in place of (25), we rather write

$$|P\psi\rangle = |\phi_0\rangle \frac{\langle\phi_0|V_{PQ}|Q\psi\rangle}{E - \bar{E}_0} + |\phi_2\rangle \frac{\langle\phi_2|V_{PQ}|Q\psi\rangle}{E - \bar{E}_2} + \left(\frac{1}{E - \bar{\mathcal{H}}}\right)^{''} V_{PQ}|Q\psi\rangle, \quad (64)$$

with an obvious meaning of the double primed operator in the last term on the right hand side. Clearly, Eq. (64) does not follows directly from (56), but it assumes that in the spectral decomposition of the  $(E - \bar{\mathcal{H}})^{-1}$  operator only one prominent (collective) state  $|\phi_2\rangle$  enters beyond the ground state  $|\phi_0\rangle$ .

Sticking to this model, instead of Eq. (27), we likewise write

$$|Q\psi\rangle = \frac{1}{E - h_{QQ}^{(2)}} V_{QP} \{|\phi_0\rangle\langle\phi_0|P\psi\rangle + |\phi_2\rangle\langle\phi_2|P\psi\rangle\}, \quad (65)$$

being

$$h_{QQ}^{(2)} = H_{QQ} + V_{QP} \left(\frac{1}{E - \bar{\mathcal{H}}}\right)^{''} V_{PQ}. \quad (66)$$

Then, by left multiplying (64) (with  $E = E_0$ ) by  $\langle\phi_0|$  and using (65), we obtain

$$E_0 - \bar{E}_0 = \langle\phi_0|V_{PQ} \frac{1}{E_0 - h_{QQ}^{(2)}} V_{QP}|\phi_0\rangle + \langle\phi_0|V_{PQ} \frac{1}{E_0 - h_{QQ}^{(2)}} V_{QP}|\phi_2\rangle \frac{\langle\phi_2|P\psi\rangle}{\langle\phi_0|P\psi\rangle}, \quad (67)$$

which generalizes Eq. (29).

In a perfectly analogous fashion, by left multiplying (64) (with  $E = E_2$ ) by  $\langle\phi_2|$  and using (65), we obtain

$$E_2 - \bar{E}_2 = \langle\phi_2|V_{PQ} \frac{1}{E_2 - h_{QQ}^{(2)}} V_{QP}|\phi_2\rangle + \langle\phi_2|V_{PQ} \frac{1}{E_2 - h_{QQ}^{(2)}} V_{QP}|\phi_0\rangle \frac{\langle\phi_0|P\psi\rangle}{\langle\phi_2|P\psi\rangle}. \quad (68)$$

In the above,  $E_0$  and  $E_2$  stand for the first two exact eigenvalues of the Schroedinger equation;  $\bar{E}_0$  and  $\bar{E}_2$  for the corresponding quantities associated with Eq. (45). Eq. (68) shows that, in the present framework, all the energies of the  $P$ -space fluctuate.

Now, the energy averaging of (67) and (68) vanishes by definition, but the energy averaging of their square, which yields the “error”, does not. Hence, proceeding along the lines of Refs. <sup>7,8</sup>, we subtract on the right hand side of both equations their average values, square the expressions thus obtained and

make use of RPA, keeping of our expansion in the complexity of the  $Q$ -space states the first term only. Next, we exploit the structure of  $|\phi_2\rangle$ , which, like  $|\phi_0\rangle$ , must be normalized, orthogonal to  $|\phi_0\rangle$  and of the form

$$|\phi_2\rangle = \sum_{\beta} c_2^{\beta} |\chi_{\text{HF}}^{2\beta}\rangle + c_0 |\chi_{\text{HF}}\rangle. \quad (69)$$

Finally, we arrive at the equation

$$E_0 - \bar{E}_0 = \pm \frac{1}{E_0 - \bar{\epsilon}_4} \sqrt{\frac{2}{N_4}} (\zeta^2 + r\xi^2), \quad (70)$$

where, in addition to (61), the further definition

$$\xi^2 = \sum_{\beta\gamma} s_2^{\gamma*} c_2^{\gamma} |\langle \chi_{\text{HF}}^{4\beta} | V | \chi_{\text{HF}}^{2\gamma} \rangle|^2 \quad (71)$$

has been introduced; moreover, we have set

$$r \equiv \frac{\langle \phi_2 | P\psi \rangle}{\langle \phi_0 | P\psi \rangle}. \quad (72)$$

Likewise, for the energy of the 2p-2h state of the  $P$ -space one obtains the fluctuation equation

$$E_2 - \bar{E}_2 = \pm \frac{1}{E_2 - \bar{\epsilon}_4} \sqrt{\frac{2}{N_4}} (\eta^2 + \frac{\xi^2}{r}), \quad (73)$$

where, naturally,

$$\eta^2 = \sum_{\beta\gamma} |c_2^{\gamma}|^2 |\langle \chi_{\text{HF}}^{4\beta} | V | \chi_{\text{HF}}^{2\gamma} \rangle|^2. \quad (74)$$

We thus see that the statistical fluctuation equations (70) and (73) are actually coupled through the term (71).

Concerning the mean field equations, clearly with the projector (56) an equation should exist also for the energy of the 2p-2h state. It can be derived by computing  $\bar{E}_2 = \langle \phi_2 | \bar{\mathcal{H}} | \phi_2 \rangle$  and, notably, it turns out to read

$$\bar{E}_2 = E_{\text{HF}}^{(2)} + \frac{\eta^2}{\bar{E}_2 - \epsilon - E_2}, \quad (75)$$

$E_{\text{HF}}^{(2)}$  representing the HF energy per particle of the system in the 2p-2h excited state. Since we split  $E_{\text{HF}}^{(2)}$  into a part associated with the HF ground state and a part associated with the 2p-2h *excitation energies*, both per particle, and since the latter vanishes in the thermodynamic limit, — as previously

noted in commenting Eq. (60), then  $E_{\text{HF}}^{(2)} = E_{\text{HF}}$ , a relation we expect to be approximately fulfilled also in a heavy nucleus.

We conclude from the above analysis that our approach leads to a set of mean field equations, one for each of the states lying in the  $P$ -space: These equations, unlike the fluctuation ones, are not coupled.

## 2.4 Normalization and fluctuation of the $P$ -space ground state wave function

In the present framework the ground state spectroscopic factor  $S$  is the square root of the norm of  $|P\psi\rangle$ , the system's ground state wave function projection in  $P$ -space. To find it we exploit the completeness of the normalized eigenstates of  $\hat{\mathcal{H}}$ . Hence we write

$$S^2 \equiv \langle P\psi | P\psi \rangle = \sum_{n=0}^M \langle P\psi | \phi_n \rangle \langle \phi_n | P\psi \rangle = 1 - \langle Q\psi | Q\psi \rangle. \quad (76)$$

Now, confining ourselves to set  $M = 1$ , then the Eq. (27) for  $|Q\psi\rangle$  is warranted and we rewrite (76) as follows

$$S^2 = 1 - \langle \phi_0 | V_{PQ} \frac{1}{(E_0 - h_{QQ})^2} V_{QP} | \phi_0 \rangle |\langle \phi_0 | P\psi \rangle|^2. \quad (77)$$

Moreover, when  $M = 1$  then

$$S^2 = |\langle \phi_0 | P\psi \rangle|^2. \quad (78)$$

Hence, by exploiting (29), Eq. (77) can be recast into the form<sup>7,8</sup>

$$S^2 = 1 + S^2 \left[ \frac{d}{dE_0} (E_0 - \bar{E}_0) + \frac{E_0 - \bar{E}_0}{\bar{E}_0 - \epsilon - E_0} \right]. \quad (79)$$

Finally, employing (52) the expression

$$S^2 = \left[ \frac{3}{2} + \frac{1}{2} \frac{E_{\text{HF}} - E_0 - \epsilon - 2d\beta^2/dE_0}{\sqrt{(E_{\text{HF}} - E_0 - \epsilon)^2 + 4\beta^2}} + \frac{\epsilon}{\bar{E}_0 - \epsilon - E_0} \right]^{-1} \quad (80)$$

follows<sup>7,8</sup>, where the energy derivative of the sum of the square moduls of the vacuum-2p-2h matrix elements of the effective interaction appears (its explicit expression is given in Ref. <sup>8</sup>). Note that (80) goes to one as  $\beta^2 \rightarrow 0$ , as it should.

If, however, the expression for the  $Q$ -space wave function appropriate for a two-dimensional  $P$ -space, namely (65), is used, then (see Ref. <sup>12</sup> for details)

one ends up with the expression

$$S^2 = \frac{1 - \left[ \frac{d(\bar{E}_2 - \bar{E}_0)}{d\bar{E}_0} + \frac{\bar{E}_2 - \bar{E}_0}{\bar{E}_0 - \epsilon - E_0} \right] |\langle \phi_2 | P\psi \rangle|^2}{1 + \frac{\epsilon}{\bar{E}_0 - \epsilon - E_0} + \frac{d\bar{E}_0}{dE_0}}, \quad (81)$$

which reduces to (79), as it should, if  $\langle \phi_2 | P\psi \rangle \rightarrow 0$ , i. e. for a one-dimensional  $P$ -space. In deducing (81) the approximation

$$\frac{1}{E_0 - h_{QQ}^{(2)}} \approx \frac{1}{E_2 - h_{QQ}^{(2)}} \quad (82)$$

has been made.

Since, from Eq. (72),

$$|\langle \phi_2 | P\psi \rangle|^2 = \frac{r^2}{1+r^2} S^2, \quad (83)$$

then Eq. (81) can be recast as follows

$$S^2 = \left\{ 1 + \frac{1}{\bar{E}_0 - \epsilon - E_0} \left[ \epsilon + \frac{r^2}{1+r^2} (\bar{E}_2 - \bar{E}_0) \right] + \frac{1}{1+r^2} \left( \frac{d\bar{E}_0}{dE_0} + r^2 \frac{d\bar{E}_2}{dE_0} \right) \right\}^{-1}, \quad (84)$$

which again reduces to (79) as  $r \rightarrow 0$ .

We now address the problem of the fluctuation of  $|P\psi\rangle$ . For this scope, we focus on the ground state and, by combining Eqs. (17), (23) and (24), we obtain

$$(E - \bar{\mathcal{H}})[|P\psi\rangle - |\langle P\psi \rangle\rangle] + (E - \bar{E}_0)|\langle P\psi \rangle\rangle = V_{PQ}|Q\psi\rangle \quad (85)$$

(the angle brackets meaning energy averaging).

Then, if use is made of the expression (27) for  $|Q\psi\rangle$  and of the spectral decomposition of the operator  $(E - \bar{\mathcal{H}})^{-1}$ , one gets

$$\begin{aligned} |P\psi\rangle - |\langle P\psi \rangle\rangle &= \sum' |\phi_n\rangle \frac{1}{E - \bar{E}_n} \langle \phi_n | V_{PQ} \frac{1}{E - h_{QQ}} V_{QP} |\phi_0\rangle \langle \phi_0 | P\psi \rangle \\ &\quad + \frac{1}{E - \bar{E}_0} |\phi_0\rangle \langle \phi_0 | V_{PQ} \frac{1}{E - h_{QQ}} V_{QP} |\phi_0\rangle \langle \phi_0 | P\psi \rangle \\ &\quad - (E - \bar{E}_0) \sum_n \frac{1}{E - \bar{E}_n} |\phi_n\rangle \langle \phi_n | \langle P\psi \rangle. \end{aligned} \quad (86)$$

Now, since  $|\langle P\psi \rangle\rangle \propto |\phi_0\rangle$ , from the above finally it follows

$$|P\psi\rangle - |\langle P\psi \rangle\rangle = (1 - |\phi_0\rangle \langle \phi_0|)^{-1} \left( \frac{1}{E - \bar{\mathcal{H}}} \right)' V_{PQ} \frac{1}{E - h_{QQ}} V_{QP} |\phi_0\rangle \langle \phi_0 | P\psi \rangle$$

$$= \langle \phi_0 | P\psi \rangle \left( \frac{1}{E_0 - \bar{\mathcal{H}}} \right)' V_{PQ} \frac{1}{E_0 - h_{QQ}} V_{QP} |\phi_0\rangle, \quad (87)$$

which *vanishes when  $P$  is given by (46)*, since clearly  $|P\psi\rangle$  does not fluctuate in a one-dimensional  $P$ -space.

If, on the other hand,  $P$  is given by Eq. (56), then the above can be computed in first order of the complexity expansion, using (57) for  $|\phi_0\rangle$ , (69) for  $|\phi_2\rangle$  and (58) for  $Q$ . One ends up with the expression (we set  $E = E_0$  to conform to previous notations)

$$[|P\psi\rangle - |\langle P\psi \rangle\rangle]_1 = \langle \phi_0 | P\psi \rangle \frac{|\phi_2\rangle}{E_0 - \bar{E}_2} \sum_{\beta\beta'\gamma} \langle \chi_{\text{HF}}^{2\beta} | V | \chi_{\text{HF}}^{4\gamma} \rangle \frac{c_{2\beta}^* s_{2\beta'}}{E_0 - \epsilon_{\text{HF}}^{4\gamma}} \langle \chi_{\text{HF}}^{4\gamma} | V | \chi_{\text{HF}}^{2\beta'} \rangle, \quad (88)$$

which can be further simplified invoking the randomness of the phases of the wave functions in the  $Q$ -space and again introducing the average energy per particle  $\bar{\epsilon}_4$  for the 4p-4h HF excited states. Then, with the help of Eq. (71), the formula

$$[|P\psi\rangle - |\langle P\psi \rangle\rangle]_1 = \frac{\langle \phi_0 | P\psi \rangle}{(E_0 - \bar{E}_2)(E_0 - \bar{\epsilon}_4)} |\phi_2\rangle \xi^2 \quad (89)$$

is derived. It gives the fluctuations of the wave function in first order of the complexity expansion.

Notice that in (89) the scalar product  $\langle \phi_0 | P\psi \rangle$ , unlike in Refs. <sup>7,8</sup>, does not coincide with the spectroscopic factor  $S$ , as defined in (76), since Eq. (89) refers to a  $P$ -space with dimensions larger than one. Rather, it measures the amount of the true ground state wave function of the system embodied in the mean field state  $|\phi_0\rangle$ .

The relevance of Eq. (89) lies in the possibility it offers to assess the “error” affecting the ground state expectation value of operators associated to physical observables like, e. g., the magnetic moments of nuclei.

### 3 A glance at QCD

Lately the existence of randomness has been unraveled also at the scale of quarks, namely at the level of the physics ruled by QCD. Here the RMT has achieved outstanding successes in connection with the low-lying eigenvalues of the Dirac operator for massless fermions:

$$iD = i\partial + g \sum_a \frac{\lambda^a}{2} A^a, \quad (90)$$

where  $g$  is the coupling constant, the matrices  $\lambda^a$  the generators of the gauge group and the  $A^a$  the gauge fields. Indeed, the spectrum of (90),

$$iD\phi_n = \lambda_n \phi_n, \quad (91)$$

has been computed for a SU(2) gauge theory (and for others as well) and from the  $\lambda_n$ 's the nearest-neighbor spacing distribution  $P(s)$  has been deduced. In turn, this has been compared to the prediction of the chRMT (chiral random matrix theory): An impressive agreement has been found,<sup>13</sup> pointing to the universality of the fluctuations of the eigenvalues of the Dirac operator.

The focus on the  $\lambda_n$ 's also stems from the anticommutator

$$\{iD, \gamma_5\} = 0, \quad (92)$$

whose vanishing in the chiral limit implies for the eigenvalues of (91) the occurrence in symmetrical pairs ( $\pm \lambda_n$ ) around  $\lambda = 0$ . As a consequence the  $\lambda_n$ 's tend to accumulate around the origin and their average density

$$\rho(\lambda) = \langle \sum_n \delta(\lambda - \lambda_n) \rangle, \quad (93)$$

the average being taken on all the configurations of the gauge field, on the one hand displays the level repulsion already encountered at the level of the physics of the nucleus, — thus signalling universality, — and on the other plays a central role in the physics of the quark-gluon plasma.

In fact, the density of the smallest eigenvalues of the Dirac operator is directly related to the chiral condensate according to Banks–Casher formula<sup>14</sup>:

$$\langle \bar{q}q \rangle = -\pi \rho(0)/V, \quad (94)$$

$V$  being the space-time volume. It is fascinating that such a fundamental aspect of nature as the breaking of the chiral symmetry appears to be ruled by chaos.

In conclusion, we feel that RMT, in both its normal and chiral versions, is invaluable in disentangling the stochastic content of nuclear physics and QCD. In the former case, in the Feshbach's approach, stochasticity should be averaged out, thus leading to an effective Hamiltonian that has been proved most successful in interpreting the data. We argue that the same path might be worth following also in QCD.

## Acknowledgments

We would like to express our gratitude to H. Weidenmueller for many enlightening discussions and to W. M. Alberico for the kind invitation to this workshop.

## References

1. T. Guhr, A. Mueller, and H. Weidenmueller, *Phys. Rep.* **299**, 189 (1998).
2. M. C. Gutzwiller, *Chaos in classical and quantum mechanics* (Springer, New York, 1990) p. 265.
3. H. Feshbach, Lectio Magistralis in occasion of the *Laurea honoris causa* at the University of Torino, in: *L'Ateneo*, November 2000, p. 5.
4. A. de Shalit and H. Feshbach, *Theoretical Nuclear Physics: Nuclear Structure* (J. Wiley & Sons, New York, 1974) p. 100.
5. H. Feshbach, *Theoretical Nuclear Physics: Nuclear Reactions* (J. Wiley & Sons, New York, 1992).
6. H. Feshbach, *Phys. Rep.* **264**, 137 (1996).
7. R. Caracciolo, A. De Pace, H. Feshbach, and A. Molinari, *Ann. Phys.* (N.Y.) **262**, 105 (1998).
8. A. De Pace, H. Feshbach, and A. Molinari, *Ann. Phys.* (N.Y.) **278**, 109 (1999).
9. G. E. Brown, *Unified Theory of Nuclear Models and Forces* (North-Holland, Amsterdam, 1967) p. 30.
10. M. Kawai, A.K. Kerman and K.W. McVoy, *Ann. Phys.* (N.Y.) **75**, 156 (1973).
11. T. E. O. Ericson, *Phil. Mag. Suppl.* **9**, 425 (1960).
12. A. De Pace and A. Molinari, *Ann. Phys.* (N.Y.) **296**, 263 (2002).
13. M. A. Halasz, T. Kalkreuter, and J. J. Verbaarschot, *Nucl. Phys.* **B53** (Proc. Suppl.), 266 (1997).
14. T. Banks and A. Casher, *Nucl. Phys.* **B169**, 103 (1980).

# QUANTUM MONTE CARLO FOR NUCLEAR ASTROPHYSICS

STEFANO FANTONI

*International School for Advanced Studies, SISSA,  
Via Beirut 2/4, I-34014 Trieste, Italy  
International Centre for Theoretical Physics, ICTP,  
Strada Costiera 32, I-34014 Trieste, Italy  
E-mail: fantoni@sissa.it*

ANTONIO SARSA

*International School for Advanced Studies, SISSA,  
Via Beirut 2/4, I-34014 Trieste, Italy  
E-mail: sarsa@sissa.it*

KEVIN E. SCHMIDT

*Department of Physics and Astronomy, Arizona State University,  
Tempe, AZ 85287 U.S.A.  
E-mail: schmidt@asu.edu*

We briefly review the Auxiliary Field Diffusion Monte Carlo (AFDMC) method, recently developed to perform quantum simulations of medium size nucleon systems. This quantum Monte Carlo method generalizes the well established Diffusion Monte Carlo method, largely used in condensed matter, and includes auxiliary fields of the Hubbard–Stratonovich type to linearize the spin–isospin dependence of the NN interaction. The AFDMC method has significantly improved the possibility of performing *ab initio* calculations on nuclear and neutron matter, as well as on medium–heavy nuclei. The results of recent calculations of the equation of state and the compressibility of a neutron matter model, characterized by the Argonne  $v_8'$  two-nucleon potential plus the Urbana IX three-nucleon force, are presented and discussed. Other properties of astrophysical interest such as the spin susceptibility of neutron matter and the symmetry energy are also discussed. Of particular interest for the mean free path of a neutrino in hadronic matter is the finding that NN correlations reduce by about a factor 3 the spin susceptibility of neutron matter.

## 1 Introduction

Short range NN correlations and their interplay with the Pauli and the long range correlations have significant and observable effects on both the single particle properties and the collective behaviors of nuclei and bulk nuclear matter<sup>1</sup>. A well established feature, amongst several others, is the depletion of the single particle occupancy  $n(\epsilon)$  for states below the Fermi energy  $\epsilon_F$ ,

with the consequent appearance of single particle states above the Fermi sea ( $n(\epsilon > \epsilon_F) \neq 0$ )<sup>2,3</sup>. In fact excitations at  $\sim 300\text{MeV}$  are still relevant to fulfill fundamental sum rules, like for instance,  $n(k) = \langle a_k^\dagger a_k \rangle = \int dE P_h(k, E)$ , where  $P_h(k, E)$  is the nuclear matter hole spectral function<sup>3</sup>.

As a consequence, highly sophisticated many-body techniques, similar to those used in condensed matter physics, are required for a quantitative understanding of the structural and dynamical properties of nuclei starting from the fundamental NN interaction. This is particularly true for the case of dense hadronic matter, at  $\rho > \rho_0$ , where  $\rho_0 = 0.16\text{fm}^{-3}$  is the equilibrium density, which cannot be realistically described without taking NN correlations into account.

Nuclear matter at high density and low temperature is the basic environment of fundamental astrophysical phenomena<sup>4</sup>. Things like the equation of state of nuclear matter, or the mean free path of neutrinos, which are fundamental information to understand the formation process of a proto-neutron star, cannot be understood within a Fermi gas model.

During the last few years important developments have been done in quantum Monte Carlo methods for nucleon systems. Accurate evaluations of the energy per particle and other important quantities such as the Landau parameters or the related ones, the compressibility  $\mathcal{K}$ , the effective mass  $m^*$  or the spin susceptibility  $\chi^{5,6,7,8}$  are today attainable from numerical simulations. In this paper we will briefly report on one of the most promising of such developments to deal with bulk nuclear matter and medium-heavy nuclei.

In the last two decades a great deal of work has been done to prove that a nonrelativistic Hamiltonian of the form

$$\begin{aligned} H &= T + V_2 + V_3 \\ &= -\frac{\hbar^2}{2m} \sum_{i=1,N} \nabla_i^2 + \sum_{i < j} v_{ij} + \sum_{i < j < k} V_{ijk} , \end{aligned} \quad (1)$$

where  $v_{ij}$  and  $V_{ijk}$  are two- and three-nucleon potentials, provides a realistic description of light nuclei, with mass number  $A \leq 8$ . *Modern two-body potentials*<sup>9,10,11</sup> all fit the Nijmegen data<sup>12</sup> below 350 MeV with a  $\chi^2/N_{data} \sim 1$ . They seem to be equivalent in describing most of the properties of both nuclear matter<sup>13</sup> and light nuclei. These potentials are characterized by a strong repulsion at short distances, and, in addition, by a strong spin-isospin dependence. It follows that the induced NN correlations are also spin-isospin dependent. This *spin problem* has inhibited the use of quantum Monte Carlo methods until very recently, except for light nuclei.

A widely used form of the two-nucleon potential  $V_2$  is that of the Urbana/Argonne potentials, given by

$$v_l = \sum_{i < j} v_{ij} = \sum_{i < j} \sum_{p=1}^l v_p(r_{ij}) O^{(p)}(i, j) , \quad (2)$$

where the number of operators  $O^{(p)}(ij)$ ,  $l$ , characterizes the rank of the potential. The most important of such operators are the first eight:

$$O^{p=1,8}(i, j) = \left( 1, \vec{\sigma}_i \cdot \vec{\sigma}_j, S_{ij}, \vec{L}_{ij} \cdot \vec{S}_{ij} \right) \otimes (1, \vec{\tau}_i \cdot \vec{\tau}_j) , \quad (3)$$

where  $S_{ij} = 3(\hat{r}_{ij} \cdot \vec{\sigma}_i)(\hat{r}_{ij} \cdot \vec{\sigma}_j) - \vec{\sigma}_i \cdot \vec{\sigma}_j$  is the two-nucleon tensor operator, and  $\vec{L}_{ij}$  and  $\vec{S}_{ij}$  are the relative angular momentum and the total spin.

The Argonne  $v_{18}$  potential (A18) consists of  $l = 18$  components<sup>10</sup>. Besides the 8 components, given in Eq. (3), it includes six other charge independent terms  $(L^2, L^2 \vec{\sigma}_i \cdot \vec{\sigma}_j, (\vec{L} \cdot \vec{S})^2) \otimes (1, \vec{\tau}_i \cdot \vec{\tau}_j)$ , as well as four other charge-symmetry-breaking and charge-dependent components. It fits both  $pp$  and  $np$  scattering data up to 350 MeV with a  $\chi^2 \sim 1$  per degree of freedom. However, the  $v_8$  spin-isospin structure is already sufficiently rich to provide a realistic NN interaction. The so called Argonne  $v'_8$  potential<sup>14</sup> (A8') is one such potentials<sup>14,15</sup>. It has been used in most of the calculations discussed in this contribution.

In contrast with the two-body force, the problem of finding three-body potentials whose validity can be extended beyond stable nuclei is much more open. Although phenomenological potentials have been found which reproduce the ground state and the low lying states energies of light nuclei<sup>16,14,17</sup>, it is uncertain whether they provide a realistic description of nuclear matter, particularly at densities higher than  $\rho_0$ . The Urbana IX potential<sup>16</sup> is one example. It has been used in a number of calculations performed with Correlated Basis Function (CBF) theory<sup>18</sup> as well as with the Green's Function Monte Carlo (GFMC) method<sup>16,14,17</sup>.

A first class of Quantum Monte Carlo methods for nuclear systems is based on an extension of GFMC, in which all the spin-isospin components are summed on explicitly<sup>19,20,21</sup>. The exponential growth of the number of such components with  $A$ , limits the application of this method to systems of up to  $\approx 10$  nucleons<sup>17</sup>.

The AFDMC method<sup>22</sup> circumvents this problem. It is based on sampling the spin-isospin states rather than performing a complete sum. In this approach the scalar parts of the Hamiltonian are propagated as in standard

Diffusion Monte Carlo (DMC)<sup>19</sup>. Auxiliary fields are introduced to replace the spin dependent interaction. The method consists of a Monte Carlo sampling of the auxiliary fields and then propagating the spin variables at the sampled values of the auxiliary fields. This propagation results in a rotation of each particle's spinors. The fermion sign problem is taken care of by applying a path-constraint approximation analogous to the fixed-node approximation. The AFDMC method for the spin-isospin calculations is essentially an application of the method of Zhang et al.<sup>23</sup> used in condensed matter lattice systems to the spin-isospin states of nucleon systems.

The AFDMC method has already demonstrated that energies per particle can be calculated with high statistical accuracy for a neutron drop with  $A = 7, 8$  for neutron matter, simulated with up to 66 neutrons in a periodic box<sup>24,25,26,27</sup>, and for a nuclear matter with up to 76 nucleons<sup>28</sup>.

We briefly describe in the next section the DMC method, which is on the basis of AFDMC. Section 3 is devoted to the AFDMC method, its differences with DMC and the way the spin-isospin variables are sampled. Results obtained for the equation of state and the spin susceptibility of neutron matter, and the asymmetry energy of nuclear matter are presented and discussed in the last Section.

## 2 The Diffusion Monte Carlo method

Diffusion Monte Carlo refers to a form of Green's function Monte Carlo where the imaginary time Schrödinger equation is solved.<sup>19</sup> In position space, the differential equation for a central potential and  $A$  particles is a diffusion equation in  $3A$  dimensions. That is

$$[H - E_T]|\psi(\tau)\rangle = -\frac{\partial}{\partial \tau}|\psi(\tau)\rangle, \quad (4)$$

has the form

$$\left[ -\frac{\hbar^2}{2m} \nabla^2 + V(R) - E_T + \frac{\partial}{\partial \tau} \right] \psi(R, \tau) = 0. \quad (5)$$

Here  $E_T$  is a constant trial energy that simply shifts the spectrum of  $H$  by a constant but does not change its eigenstates.  $\hbar^2/2m$  is the diffusion constant,  $V(R) - E_T$  acts like a creation or absorption term depending on whether it is negative or positive, and  $R$  and  $\nabla$  here refer to all  $3A$  coordinates.

A formal solution of the diffusion equation is

$$|\psi(\tau)\rangle = e^{-(H-E_T)\tau}|\psi(0)\rangle. \quad (6)$$

We can expand  $|\psi(0)\rangle$  in the complete set of normalized eigenstates of  $H$ ,

$$\begin{aligned} H|\phi_n\rangle &= E_n|\phi_n\rangle \\ |\psi(0)\rangle &= \sum_{n=0}^{\infty} c_n|\phi_n\rangle \end{aligned} \quad (7)$$

with

$$c_n = \langle\phi_n|\psi(0)\rangle. \quad (8)$$

The formal solution becomes

$$|\psi(\tau)\rangle = e^{-(E_0-E_T)\tau} \left[ c_0|\phi_0\rangle + \sum_{n=1}^{\infty} c_n e^{-(E_n-E_0)\tau}|\phi_n\rangle \right], \quad (9)$$

and since  $E_n > E_0$  for  $n > 0$ , the result converges exponentially in  $\tau$  to the ground state (or the lowest energy state contained in the original  $\psi(0)$ ). Eq. 9 shows that selecting  $E_T$  near  $E_0$  will keep the normalization of  $|\psi(\tau)\rangle$  from changing rapidly with  $\tau$ . The exponential change in the normalization can be used to calculate the ground state energy and is called the growth energy.

While it is possible to completely eliminate the time step errors by Monte Carlo sampling of all the terms in a convergent series for the propagator<sup>29</sup>, often the expansion of the propagator is simply truncated and the time step is either chosen sufficiently small or Richardson extrapolation is used to remove the errors from an approximate propagator. One way to derive the short time approximation for the propagator of diffusion Monte Carlo is to use the Trotter expansion to write

$$e^{-(T+V-E_T)\tau} = e^{E_T\tau} e^{-\frac{V}{2}\tau} e^{-T\tau} e^{-\frac{V}{2}\tau} + O(\tau^3). \quad (10)$$

For small  $\tau$ , the  $O(\tau^3)$  term can be dropped. The kinetic energy term is diagonal in momentum space while the potential operators are diagonal in position space. We can therefore write

$$\begin{aligned} \langle R|e^{-(T+V-E_T)\tau}|R'\rangle &= e^{E_T\tau} \langle R|e^{-\frac{V}{2}\tau} e^{-T\tau} e^{-\frac{V}{2}\tau}|R'\rangle + O(\tau^3) \\ &= \sum_P \langle R|P\rangle e^{-\frac{P^2}{2m}\tau} \langle P|R'\rangle e^{-\frac{1}{2}[V(R)+V(R')]\tau} e^{E_T\tau} + O(\tau^3). \end{aligned} \quad (11)$$

The matrix elements between  $P$  and  $R$  are plane waves, and doing the integral simply gives the free-particle propagator multiplied by exponential terms in the potential at the end points,

$$\langle R|e^{-(H-E_T)\tau}|R'\rangle = \left( \frac{m}{2\pi\hbar^2\tau} \right)^{3A/2} e^{-\frac{m(R-R')^2}{2\hbar^2\tau}} e^{-\frac{1}{2}[V(R)+V(R')]\tau} e^{E_T\tau} + O(\tau^3). \quad (12)$$

Dropping the  $O(\tau^3)$  term gives a simple short time approximation to the propagator

$$G_{\text{st}}(R, R', \tau) = \left( \frac{m}{2\pi\hbar^2\tau} \right)^{3A/2} e^{-\frac{m(R-R')^2}{2\hbar^2\tau}} e^{-\frac{1}{2}[V(R)+V(R')] \tau} e^{E_T \tau}. \quad (13)$$

The position space short-time solution to the imaginary time Schrödinger equation is then

$$\psi(R, \tau + \Delta\tau) = \int dR' G_{\text{st}}(R, R', \Delta\tau) \psi(R', \tau). \quad (14)$$

A simple Monte Carlo solution begins by sampling a set of walker positions  $R_i$  from a probability distribution proportional to  $\psi(R', \tau)$ . This can be thought of as replacing  $\psi(R', \tau)$  by a sum of delta functions. The integration over  $R'$  is then trivial and we have

$$\psi(R, \tau + \Delta\tau) = \sum_i G_{\text{st}}(R, R_i, \Delta\tau). \quad (15)$$

To obtain samples from this new  $\psi$ , the normalized gaussian in  $G_{\text{st}}$  is sampled. The result is a delta function multiplied by a constant given by the exponential of the difference of the trial energy and the average of the potential energy at the two end points all multiplied by the time step  $\Delta\tau$ . Various methods can be used to deal with the fluctuating weight. Perhaps the simplest is to convert it statistically into an integer by assigning a weight  $\text{int}(w+\xi)$  where  $w$  is the original weight and  $\xi$  is a uniform random number on  $(0, 1)$ . If the trial energy  $E_T$  is selected to be close to the ground-state energy, the population of walkers will remain roughly constant.

A problem with this simplest method is that it can have large fluctuations in the population. For example walkers that move into regions where the potential is attractive will multiply while those moving into regions where the potential is repulsive will tend to die off. Instead of first moving and then discovering the consequences, a better algorithm preferentially samples regions that correspond to large weights and tends to sample infrequently regions where the weights are small.

Importance sampling is a standard way to implement this preferential sampling. It is straightforward to show that in general the expected weight for a walker is the solution of the adjoint equation run backward in time. For our case, this is the same solution as our original equation, and the expected weight is the value of the ground-state wave function. A reasonable trial ground-state wave function, typically found from a variational calculation, can therefore be used as an importance function. We can trivially write our

propagation equation as

$$\psi_T(R)\psi(R, \tau + \Delta\tau) = \int dR' \left[ \frac{\Psi_T(R)}{\Psi_T(R')} G_{\text{st}}(R, R', \Delta\tau) \right] \psi_T(R')\psi(R', \tau), \quad (16)$$

where we now solve for  $\psi_T(R)\psi(R, \tau)$  and use the kernel in brackets as the propagator. To sample this propagator, we can realize that since  $\Delta\tau$  is small,  $R$  and  $R'$  will not be far apart. We can expand

$$\frac{\Psi_T(R)}{\Psi_T(R')} = \exp \left( \frac{\nabla'\psi_T(R')}{\psi_T(R')} (R - R') + \dots \right). \quad (17)$$

If this linear term as well as the second derivative terms are included in the exponent, we can first notice that the terms that are odd in  $(R - R')$  will vanish under the integral. Completing the square leads to sampling a drifted gaussian, given by

$$\left( \frac{m}{2\pi\hbar^2\tau} \right)^{3A/2} e^{-\frac{m(R-R'-\nabla' \ln[\psi_T(R')])\frac{\hbar^2}{m}\tau)^2}{2\hbar^2\tau}}. \quad (18)$$

Typical calculations sample from this drifted gaussian and then compute the weight either by including the higher order terms in the expansion of the trial function or by simpling dividing the correct importance sampled Green's function by the sampled distribution. When higher order terms are included, it is easy to show that the weight in the short time approximation is proportional to  $\exp(-\frac{1}{2}[E_L(R) + E_L(R')]\tau + E_T\tau)$  where

$$E_L(R) = \frac{H\Psi_T(R)}{\Psi_T(R)} \quad (19)$$

is the local energy. If the trial function were the exact ground-state, the weights would be independent of position, and if  $E_T = E_0$  the weights are always 1. This corresponds to the perfect importance sampling limit.

Some versions of diffusion Monte Carlo include a Metropolis step to enforce detailed balance (which is analogous to having a time reversible propagator for real time dynamics). This however, also includes an unphysical delta function component in the propagator, and we have not used such a Metropolis step here. Both the lack of detailed balance and the delta function counterbalance vanish in the short time limit.

In the AFDMC method standard diffusion Monte Carlo is used for the spatial sampling. The difference is that the  $e^{-V\tau}$  terms must be dealt with in a numerically efficient way.

### 3 The AFDMC method

The method generalizes the DMC method discussed in the previous section to treat spin-isospin dependent hamiltonians. The first consequence of this dependence is that the orbitals in the Slater Determinant must include the spinor components (two for neutron matter and four for nuclear matter). The second one is the presence of the spin-isospin dependent part of the interaction,  $V_2^{SD} + V_3^{SD}$ , in the propagator of eq. (13). The AFDMC method is based on sampling the spin states of the nucleons instead of suming over all of them as in previous applications of GFMC method on nuclear problems. Direct sampling of the spin-isospin states produced when operated on by the imaginary time propagator  $\exp(-(V_2^{SD} + V_3^{SD})\Delta t)$  in the usual spin up/down basis gives high variance.

One efficient way to deal with the sampling of the spin states is to break up the spin dependent operators into terms that give a single new product spin state when they operate on a product spin state. By sampling these terms we effectively sample the spin-isospin sums. In addition, we want our propagation to be local in both space and spin. More explicitly, as  $\Delta t \rightarrow 0$  we want our propagator to go smoothly to the identity and the walker to remain the same as  $\Delta t \rightarrow 0$ .

To get that, the spin part of the propagator (for the sake of simplicity we will consider here neutron systems only, omitting the isospin idependence of the interaction) should be written in the form of a sum of terms like

$$\prod_{i=1}^A [a_i(R) + \vec{b}_i(R) \cdot \vec{\sigma}_i], \quad (20)$$

and  $a_i(R) + \vec{b}_i(R) \cdot \vec{\sigma}_i$ , operating on  $\Psi(R, S, \tau)$ , acts as a rotation operator in the spin space of particle  $i$ .

While this method introduces unwanted components that have to be averaged out, it avoids the “all or nothing” sampling that occurs in the  $z$  component basis.

#### 3.1 The Auxiliary Field Breakup.

Let us consider the  $v_6$  two-body interaction (2). This can be written as

$$\sum_{i < j} \left[ \sum_{p=1}^3 v_p^{PNM}(r_{ij}) O^{(p)}(i, j) \right] = V_2^{SI} + V_2^{SD}$$

$$= V_2^{SI} + \frac{1}{2} \sum_{i,\alpha,j,\beta} \sigma_{i,\alpha} A_{i,\alpha,j,\beta} \sigma_{j,\beta} \quad (21)$$

where

$$A_{i,\alpha,j,\beta} = 3 v_3^{PNM}(r_{ij}) \hat{r}_{ij}^\alpha \hat{r}_{ij}^\beta + (v_3^{PNM}(r_{ij}) - v_3^{PNM}(r_{ij})) \delta_{\alpha\beta} . \quad (22)$$

The  $A_{i,\alpha,j,\beta}$  matrix is taken to be zero when  $i = j$  and it is real and symmetric. It therefore has real eigenvalues and eigenvectors. The eigenvectors and eigenvalues are defined by

$$\sum_{j,\beta} A_{i,\alpha,j,\beta} \psi_n^\beta(j) = \lambda_n \psi_n^\alpha(i) . \quad (23)$$

The matrices can be written in terms of their eigenvectors and eigenvalues to give the spin-dependent part of the potential

$$\begin{aligned} V_2^{SD} &= \frac{1}{2} \sum_{i,j,n} \vec{\sigma}_i \cdot \vec{\psi}_n(i) \lambda_n \vec{\psi}_n(j) \cdot \vec{\sigma}_j \\ &= \frac{1}{2} \sum_{n=1}^{3A} (O_n)^2 \lambda_n , \end{aligned} \quad (24)$$

with

$$O_n = \sum_i \vec{\sigma}_i \cdot \vec{\psi}_n(i) . \quad (25)$$

The Hubbard-Stratonovich transformation is then used to write the spin part of the propagator in the form of Eq. (20). It is given by

$$e^{-\frac{1}{2} \lambda_n O_n^2 \Delta t} = \left( \frac{\Delta t |\lambda_n|}{2\pi} \right)^{\frac{1}{2}} \int_{-\infty}^{\infty} dx e^{-\frac{1}{2} \Delta t |\lambda_n| x^2 - \Delta t s \lambda_n O_n x} \quad (26)$$

where  $s$  is 1 for  $\lambda < 0$ , and  $s$  is  $i$  for  $\lambda > 0$ .

Our  $O_n$  don't commute, so we need to keep the time steps small so that the commutator terms can be ignored. Each of the  $O_n$  is a sum of 1-body operators as required above. A number of  $3A$  auxiliary field variables is required for the  $\sigma$  terms. Therefore, each time step requires the diagonalization of a  $3A$  by  $3A$  matrix. We sample a value of  $x$  for each of the  $3A$  auxiliary field variables. Once these values are known, the propagation reduces to a rotation in the spin space, and, therefore, to multiplying the current spinor value for each particle by the set of matrices given by the transformation

above. For a given eigenvalue  $\lambda_n \leq 0$  in eq. (24) the spin states of particle  $k$ ,  $\eta'_k = a'_k | \uparrow \rangle + b'_k | \downarrow \rangle$  will be rotated to the new one  $\eta_k$  having the following components

$$\begin{pmatrix} a_k \\ b_k \end{pmatrix} = \begin{pmatrix} \cosh(A_n) + \sinh(A_n)\psi_n^z(k) & \sinh(A_n)(\psi_n^x(k) - i\psi_n^y(k)) \\ \sinh(A_n)(\psi_n^x(k) + i\psi_n^y(k)) & \cosh(A_n) - \sinh(A_n)\psi_n^z(k) \end{pmatrix} \begin{pmatrix} a'_k \\ b'_k \end{pmatrix}, \quad (27)$$

where

$$A_n = \Delta t |\lambda_n| x_n \sqrt{[(\psi_n^x(k))^2 + (\psi_n^y(k))^2 + (\psi_n^z(k))^2]}, \quad (28)$$

and  $x_n$  is the sampled Hubbard–Stratonovich value. For positive values of  $\lambda_n$ , one has a similar set of equations, in which  $\sinh(A_n)$  is substituted with  $i \sin(-A_n)$ .

The auxiliary field break up for the spin–orbit interaction and the three–body potential can be found in ref. <sup>30,27</sup>.

### 3.2 Trial wave function and Path Constraint

The various AFDMC calculations performed to date have always been using a simple trial function given by a Slater determinant of one-body space-spin orbitals multiplied by a central Jastrow correlation,

$$|\Psi_T\rangle = \left[ \prod_{i < j} f(r_{ij}) \right] A \left[ \prod_i |\phi_i, s_i\rangle \right]. \quad (29)$$

The overlap of a walker with this wave function is the determinant of the space-spin orbitals, evaluated at the walker position and spinor for each particle, and multiplied by a central Jastrow product.

For unpolarized neutron matter in a box of side  $L$ , the orbitals are plane waves that fit in the box times up and down spinors. The usual closed shells are 2, 14, 38, 54, 66, ... particles.

As in standard fermion DMC, the AFDMC method has the usual sign problem. In this case the overlap of our walkers with the trial function will be complex so the usual fermion sign problem has become a phase problem. To deal with this problem, the path of the walkers is constrained to regions where the real part of the overlap with our trial function is positive. For spin independent potentials this reduces to the fixed-node approximation. It is straightforward to show that if the sign of the real part is that of the correct

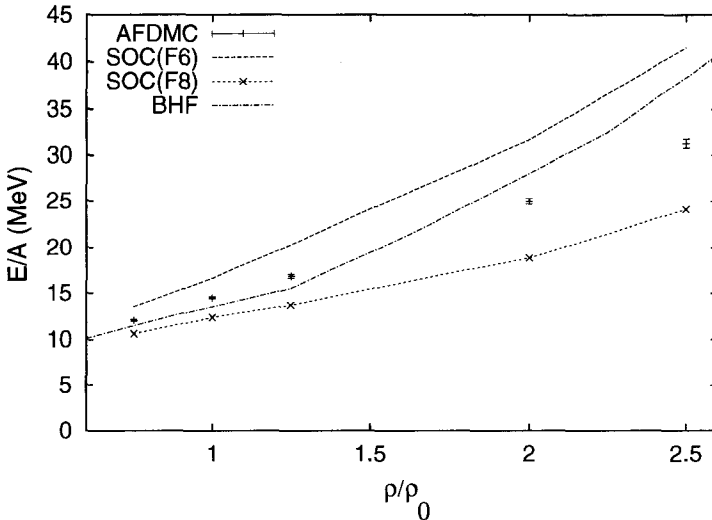


Figure 1. EOS of neutron matter with the  $A8'$  interaction. The FHNC/SOC variational results obtained with correlation functions of type  $F6$  or  $F8$  are compared with the BHF results <sup>31</sup> and AFDMC results obtained with 66 neutrons <sup>27</sup>. The interaction is  $A8'$  for SOC(F6), SOC(F8) and AFDMC, and  $A18$  for BHF.

ground state, we will get the correct answer and small deviations give second order corrections to the energy. It has not been possible to prove that this constraint always gives an upper bound to the ground state energy although it appears to do so for the calculations that have been done to date.

## 4 Results

In this section we present and discuss some of the most recent AFDMC applications to nuclear and neutron matter. The main focus is to show the potentialities of this novel quantum Monte Carlo method to study dense and cold hadronic matter. Comparisons with corresponding results obtained with other advanced many-body techniques, like CBF or those based on Brueckner Hartree–Fock (BHF) theory are also critically discussed.

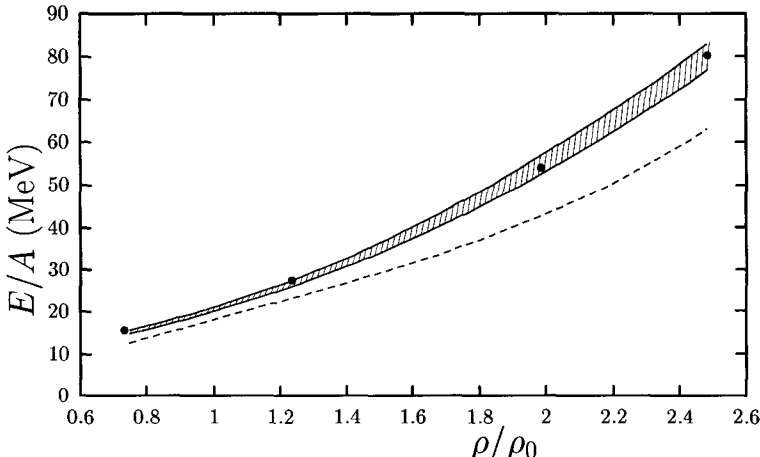


Figure 2. EOS of neutron matter with AU8' interaction. The AFDMC(66) equation of state<sup>26,27</sup> (dots) is compared with CBF theory<sup>32</sup> results for the same interaction model (shaded area: the highest values correspond to the variational estimates) and with the EOS results<sup>33</sup> for the AU18 interaction by using FHNC/SOC theory (dashes). The statistical errors of the AFDMC estimates are smaller than the symbols.

#### 4.1 Equation of state of neutron matter

The EOS of neutron matter has been the object of several calculations, performed with a variety of model hamiltonians and by using different many-body techniques. However, limiting the attention to not too high densities, say  $\rho < 2 - 3\rho_0$ , where non relativistic theory is expected to work, it is possible to select a few realistic *ab initio* calculations. Amongst them, particular attention should be shown to those performed with modern nuclear interactions, using CBF or BHF theory. Even restricting ourselves to these calculations shows non negligible differences which need to be resolved in the next few years.

The main sources of the existing discrepancies are the following: (i) very little is known about the nature of three-body force at  $\rho > \rho_0$ ; (ii) the solution of the many-body Schrödinger equation with CBF or BHF theory implies a hierarchy of integro-differential equations which is necessarily truncated. Next order terms with respect to the present calculations are practically impossible, so that their reliability is difficult to ascertain. AFDMC calculations of neutron matter have been performed for the cases of the A8' and A6' (A8' without the spin-orbit components) two-nucleon interaction with and with-

out the Urbana IX three-body force<sup>26,27</sup>. Up to 66 neutrons in a periodic box have been considered in the simulations. Finite size corrections for the 66 neutron simulations are very small.

Fig. 1 displays the EOS of neutron matter for the case of the AU8' two-body force. The quantum simulation results obtained within AFDMC are compared with FHNC/SOC variational results for the same interaction and with BHF results for the A18 force<sup>31</sup>. The SOC results shown in the figure have been performed by using a correlation operator  $\hat{F}_l(ij) = \sum_{p=1}^l f_p(r_{ij}) O^{(p)}(i,j)$  which either has  $l = 6$  or that includes the spin-orbit component ( $l = 8$ ) also. The BHF calculations include three hole line terms. One can see that SOC(F6) and SOC(F8) lead to quite different equations of state, particularly at high density. Whether this discrepancy is due to the intrinsic SOC approximation in treating spin-orbit correlations<sup>a</sup> or to the inadequacy of the F6 ansatz for a  $v_8$  interaction is not known. The AFDMC results are much closer to SOC(F6) than to SOC(F8)<sup>b</sup>. In both AFDMC and SOC(F6) the contribution to the energy per particle from the spin-orbit component of the interaction is very small.

On the other hand AFDMC reasonably agrees with BHF in the whole range of the density values displayed in the figure. Transient estimates to go beyond the path constrained approximation in AFDMC indicate a lowering of  $\sim 1\text{MeV}$  at  $\rho = 2\rho_0$ <sup>27</sup>.

In Fig. 2 the AFDMC equation of state of neutron matter for the AU8' interaction is compared with that obtained with CBF theory and  $F_6$  correlations<sup>32</sup>. The equation of state obtained by Akmal et al.<sup>33</sup> with the AU18 potential by using FHNC/SOC and  $F_8$  correlations is also reported. One can see that the good agreement between AFDMC and CBF(F6) is maintained after the introduction of three-body force. It is also clear from the figure that three-body force give a repulsive contribution to the EOS which increases very rapidly with the density. At twice the nuclear matter equilibrium density its contribution amounts to  $\sim 26\text{MeV}$ , namely  $\sim 50\%$  of the total energy per particle.

The compressibility  $\mathcal{K} = [\rho^3 \partial^2 E(\rho)/\partial \rho^2 + 2\rho^2 \partial E(\rho)/\partial \rho]^{-1}$  can be directly estimated from the equation of state. For a Fermi gas the compressibility is  $\mathcal{K}_0/A = 9\pi^2 m/(k_f^5 \hbar^2)$ . The AFDMC results for  $\mathcal{K}/\mathcal{K}_0$  are shown in Fig. 3. They are compared with the corresponding CBF estimates<sup>32</sup> and

<sup>a</sup>Spin-orbit correlations are included in SOC approximation at an effective two-body cluster order only.

<sup>b</sup>Second order perturbative corrections plus the contributions from the lowest order elementary diagrams slightly lower both the SOC(F6) and SOC(F8) results. For instance, at  $\rho = 2\rho_0 \Delta E \sim -2\text{MeV}$ .

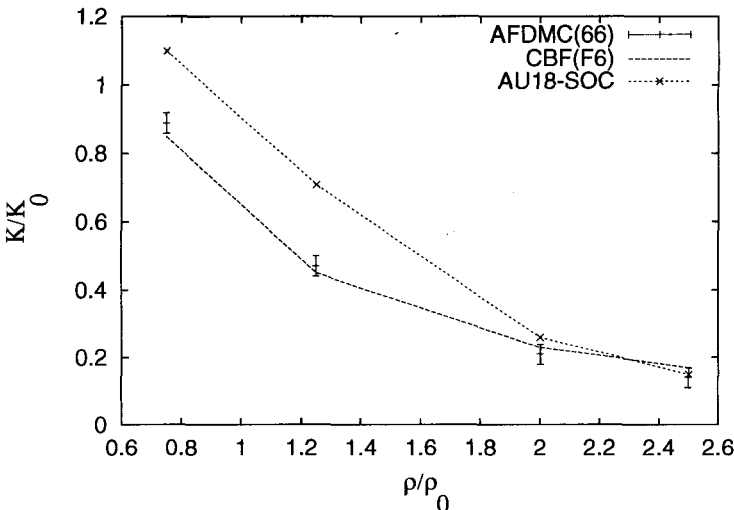


Figure 3. Neutron matter compressibility. The AFDMC results<sup>26</sup> are compared with the CBF results based on  $F_6$  correlations<sup>32</sup>, the BHF results for the Reid potential<sup>34</sup> and the variational FHNC/SOC results of Akmal et al.<sup>33</sup> for the *AU18* interaction.

other existing BHF calculations performed with the old Reid potential<sup>34</sup> and the FHNC/SOC calculations of ref.<sup>33</sup> with the *AU18* potential.

#### 4.2 Asymmetry energy of nuclear matter

AFDMC can be applied to nucleon systems having  $N \neq Z$ . Therefore it can be used to compute the dependence of the energy per particle on the asymmetry parameter  $\alpha = (N - Z)/(N + Z)$  for realistic nuclear forces, which is important in the description of beta stable matter to study the evolution of proto-neutron stars.

Fig. 4 shows the results of an AFDMC calculations<sup>28</sup> performed by using the spin-isospin central two-body potential MS3 as NN interaction<sup>35,28</sup>, at equilibrium nuclear matter density  $\rho_0$ . The quantum simulations have been performed for (i) symmetrical nuclear matter with 28 and 76 nucleons in a periodic box; (ii) pure neutron matter with  $N = 14, 38, 66$  and (iii)  $N \neq Z$  matter, with  $(N, Z) = (14, 2), (38, 14)$ . The AFDMC energies for symmetrical nuclear matter ( $\alpha = 0$ ) and pure neutron matter ( $\alpha = 1$ ) are below the corresponding FHNC/SOC variational estimates by  $1.5 MeV$  and  $1.3 MeV$

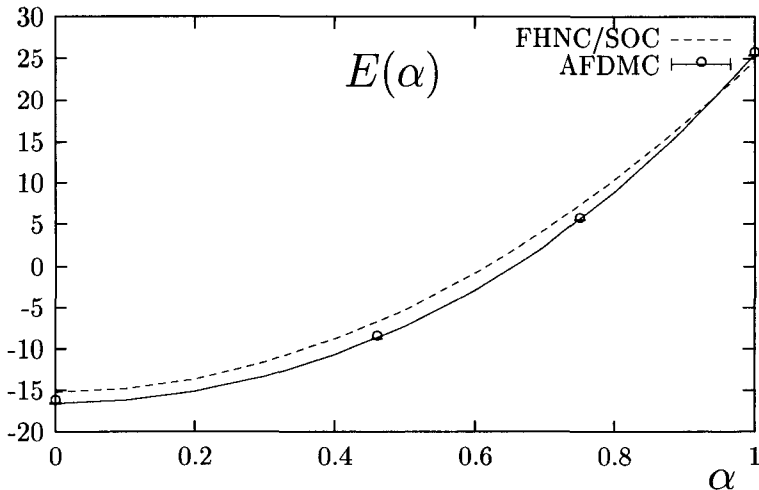


Figure 4. AFDMC and FHNC/SOC energy per particle of nuclear matter for several values of the asymmetry parameter<sup>28</sup>. The lines correspond to polynomial fits of the calculated energies.

respectively. Finite size corrections have been estimated by using PBFHNC calculations<sup>36,28</sup>.

The figure also reports the FHNC/SOC results for  $\alpha = 0$  and  $\alpha = 1$ . The dashed line corresponds to a quadratic fit for the above FNHC/SOC results giving a symmetry energy of 41.59 MeV.

The function  $E(\alpha)$  provided by the AFDMC results is not fully quadratic in  $\alpha$ , and corresponds to a symmetry energy of  $\sim 36.4$  MeV. However, considering the possibility that the nodal surface adopted for the neutron matter is better than that of nuclear matter, as well as the fact that the AFDMC energies for  $N \neq Z$  are not finite size corrected, one cannot expect an accuracy better than  $\sim 10\%$ .

AFDMC calculations of the asymmetry energy as a function of the density and the asymmetry parameter with modern NN potentials are in progress.

#### 4.3 Spin susceptibility of neutron matter

Parametric studies of core-collapse models seem to indicate that the outcome of stellar collapse is sensitive to modest changes in the neutrino opacity<sup>37</sup>. Tensor correlations are expected to play an important role on rates of neutrino processes<sup>4,5,6,7</sup>. Spin susceptibility, and more general spin and spin-isospin

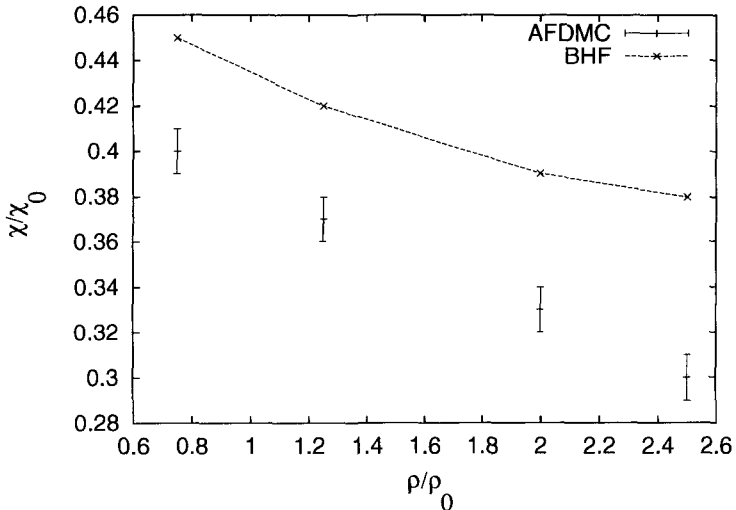


Figure 5. Spin susceptibility ratio  $\chi/\chi_F$  of neutron matter. The AFDMC results<sup>26</sup> for AU8' are compared with those extracted from the Landau parameters calculated with BHF<sup>34</sup>.

response of nuclear matter with various ratios of protons and neutrons is an important ingredient in neutral-current processes such as scattering of neutrinos, and emissionon of  $\nu\bar{\nu}$  pairs, as well as in the charged current  $\nu\bar{\nu}$  emissions in modified Urca process.

AFDMC can be applied to spin polarized matter. It can be used to compute the magnetic susceptibility  $\chi$  of nuclear matter with modern interactions. We report in this section the results of a recent calculation of  $\chi$  for pure neutron matter with AU6' and AU8' interactions<sup>26</sup>.

The Hamiltonian for the spin susceptibilty in a magnetic field ignoring any orbital effects is  $H_B = H - \mu \sum_i \vec{\sigma}_i \cdot \vec{B}$ , where  $\mu = 6.03 \times 10^{-18} \text{ MeV/Gauss}$  is the neutron magnetic moment. The susceptibility is defined as  $\chi = -\rho\mu^2 \partial^2 E(b)/\partial b^2$  at  $\vec{b} = \mu\vec{B} = 0$ .

The AFDMC method can compute the energy per particle for a given density  $\rho$  and a given polarization  $J_z = (N \uparrow - N \downarrow)/(N \uparrow + N \downarrow)$ . The results, normalized with the spin susceptibility of the Fermi free gas  $\chi_0 = \mu^2 m k_f / (\hbar^2 \pi^2)$ , are plotted in Fig. 5. They are also compared with the results extracted from the Landau parameters calculations by Backmann et al.<sup>34</sup> performed with BHF and the Reid potential. We have used the equation

$\chi/\chi_F \sim (1 + \frac{1}{3}F_1)/(1 + G_0)$  to relate  $\chi$  to the Landau parameters  $F_1$  and  $G_0$ <sup>c</sup>

Clearly, there is a strong effect of NN correlations reducing  $\chi$  by about a factor 3 at twice the equilibrium density of nuclear matter. The spin susceptibility remains rather small,  $\chi \sim 0.4\chi_F$ , at a low density value, such as  $\rho = 0.12 \text{ fm}^{-3}$ . This result confirms the importance of NN correlations on neutrino opacity<sup>6,4,38</sup>. The quenching of  $\chi$  is larger than that estimated by the BHF calculations of ref.<sup>34</sup>. Recent BHF calculations<sup>39</sup> of the spin susceptibility of neutron matter with A18 potential obtain results which are very close to the AFDMC results displayed in the figure.

## Acknowledgements

Portions of this work were supported by MURST-National Research Projects and CINECA computing center.

## References

1. V.R. Pandharipande, I. Sick, Peter K.A. deWitt Huberts, *Rev. Mod. Phys.* **69**, 981 (1997).
2. S. Fantoni, V.R. Pandharipande, *Nucl. Phys. A* **427**, 473 (1984).
3. O. Benhar, A. Fabrocini and S. Fantoni, *Nucl. Phys. A* **505**, 267 (1989); *Phys. Rev. C* **41**, R24 (1989).
4. G. G. Raffelt, *Stars as Laboratories for Fundamental Physics* (The University of Chicago Press, Chicago & London 1996).
5. R.F. Sawyer, *Phys. Rev. D* **11**, 2740 (1975); *Phys. Rev. C* **40**, 865 (1989).
6. N. Iwamoto and C.J. Pethick, *Phys. Rev. D* **25**, 313 (1982).
7. S. Reddy, M. Prakash, J.M. Lattimer and J.A. Pons, *Phys. Rev.* **59** 2888 (1999).
8. G. Baym and C.J. Pethick, *Landau Fermi-Liquid theory: concepts and applications* (Wiley, New York 1991).
9. V.G.J. Stoks, R.A.M. Klomp, C.P.F. Terheggen, and J. de Swart, *Phys. Rev. C* **49**, 2950 (1994).
10. R.B. Wiringa, V.G.J. Stoks and R.Schiavilla, *Phys. Rev. C* **51**, 38 (1995).
11. R. Machleidt, F. Sammarruca, and Y. Song, *Phys. Rev. C* **53**, R1483 (1996).

---

<sup>c</sup>Notice that the above equation is strictly valid for the case of central interactions. There are modifications due to the tensor force<sup>38</sup>

12. V.G.J. Stocks, R.A.M. Klomp, M.C.M. Rentmeester, and J. de Swart, *Phys. Rev. C* **48**, 792 (1993).
13. L. Engvik, M. Hjorth-Jensen, R. Machleidt, H. Müther and A. Polls, *Nucl. Phys A* **627**, 85 (1997).
14. B.S. Pudliner, V.R. Pandharipande, J. Carlson, S.C. Pieper, R.B. Wiringa, *Phys. Rev. C* **56**, 1720 (1997).
15. A. Fabrocini, F. Arias de Saavedra and C. Co' *Phys. Rev. C* **61**, 044302 (2000).
16. B.S. Pudliner, V.R. Pandharipande, J. Carlson and R.B. Wiringa, *Phys. Rev. Lett.* **74**, 4396 (1995).
17. S.C. Pieper, V.R. Pandharipande, R.B. Wiringa and J. Carlson, *Phys. Rev. C* **64**, 014001 (2001).
18. S. Fantoni and A. Fabrocini, in *Microscopic quantum many-body theories and their applications*, Lecture Notes in Physics Vol. 510 ed. J. Navarro and A. Polls (Springer-Verlag, Berlin, 1998).
19. K.E. Schmidt and M.H. Kalos, in *Monte Carlo Methods in Statistical Physics*, Vol. II (Springer-Verlag, Berlin, 1984).
20. J. Lomnitz-Adler and V.R. Pandharipande, *Nucl. Phys. A* **361**, 399 (1981).
21. J. Carlson, *Phys. Rev. C* **36**, 2026 (1987); **38**, 1879 (1988).
22. K.E. Schmidt and S. Fantoni, *Phys. Lett. B* **446**, 99 (1999).
23. S. Zhang, J. Carlson, and J. Gubernatis, *Phys. Rev. Lett.* **74**, 3652 (1995); *Phys. Rev. B* **55**, 7464 (1997).
24. S. Fantoni, A. Sarsa and K.E. Schmidt, *Prog. Part. Nucl. Phys.* **44**, 63 (2000).
25. K.E. Schmidt, A. Sarsa and S. Fantoni, *Int. J. Mod. Phys. B* **15**, 1510 (2001).
26. S. Fantoni, A. Sarsa and K.E. Schmidt, *Phys. Rev. Lett.* **87**, 181101 (2001).
27. A. Sarsa, S. Fantoni and K.E. Schmidt, in preparation.
28. S. Fantoni, A. Sarsa and K.E. Schmidt, in *Advances in Quantum Many-Body Theories* Vol. 5, ed R.F. Bishop, K.A. Gernoth and N.R. Walet, (World-Scientific, Singapore 2001).
29. M.H. Kalos, D. Levesque and L. Verlet, *Phys. Rev. A* **9**, 2178 (1974).
30. K.E. Schmidt, A. Sarsa and S. Fantoni, in *Quantum Monte Carlo: Recent Advances and Common Problems in Condensed Matter and Field Theory*, ed M.P. Lombardo, E. Campostrini and F. Pederiva, (ETS, Pisa 2001).
31. M. Baldo, G. Giansiracusa, U. Lombardo and H.Q. Song, *Phys. Lett. B* **473**, 1 (2000).
32. A. Fabrocini, private communication.

33. A. Akmal, V.R. Pandharipande and D.G. Ravenhall, *Phys. Rev. C* **58**, 1804 (1998).
34. S.O. Bäckmann and C.G. Källman, *Phys. Lett. B* **43**, 263 (1973).
35. I.A. Afnan and Y.C. Tang *Phys. Rev.* **175**, 1337 (1968).
36. S. Fantoni and K.E. Schmidt, *Nucl. Phys. A* **690**, 456 (2001).
37. H.T. Janka, *Astr. Astroph.* **368**, 527 (2001).
38. E. Olsson and C.J. Pethick, arXiv:astro-ph/0203011 (2002).
39. I. Vidaña, A. Polls and A. Ramos, *Phys. Rev. C* **65** 035804 (2002).

# IS THE EQUATION OF STATE OF STRONGLY INTERACTING MATTER OBSERVABLE ?

OMAR BENHAR

*INFN, Sezione di Roma*

*Dipartimento di Fisica, Università "La Sapienza"*

*I-00161 Roma, Italy*

*E-mail: benhar@roma1.infn.it*

I review the available empirical information on the equation of state of cold strongly interacting matter, as well as the prospects for obtaining new insights from the experimental study of gravitational waves emitted by neutron stars.

## 1 Introduction

The equation of state (EOS) is a nontrivial relation linking the thermodynamic variables specifying the state of a physical system<sup>1</sup>. The best known example of EOS is Boyle's *ideal gas law*, stating that the pressure of a collection of  $N$  noninteracting, pointlike classical particles, enclosed in a volume  $\Omega$ , grows linearly with the temperature  $T$  and the average particle density  $n = N/\Omega$ .

The ideal gas law provides a good description of very dilute systems. In general, the EOS can be written as an expansion of the pressure,  $P$ , in powers of the density (we use units such that Boltzmann's constant is  $K_B = 1$ ):

$$P = nT [1 + nB(T) + n^2C(T) + \dots] . \quad (1)$$

The coefficients appearing in the above series, that goes under the name of *virial expansion*, are functions of temperature only. They describe the deviations from the ideal gas law and can be calculated in terms of the underlying elementary interaction. Therefore, the EOS carries a great deal of dynamical information, and its knowledge makes it possible to establish a link between measurable *macroscopic* quantities, such as pressure or temperature, and the forces acting between the constituents of the system at *microscopic* level.

This point is best illustrated by the van der Waals EOS, which describes a collection of particles interacting through a potential featuring a strong repulsive core followed by a weaker attractive tail (see fig.1). At  $|U_0|/T \ll 1$ ,  $U_0$  being the strength of the attractive part of the potential, the van der Waals EOS takes the simple form

$$P = \frac{nT}{1 - nb} - an^2 , \quad (2)$$

and the two quantities  $a$  and  $b$ , taking into account interaction effects, can be directly related to the potential  $v(r)$  through

$$a = \pi \int_{2r_0}^{\infty} |v(r)|^2 r^2 dr , \quad b = \frac{16}{3} \pi r_0^3 , \quad (3)$$

where  $2r_0$  denotes the radius of the repulsive core (see fig.1).

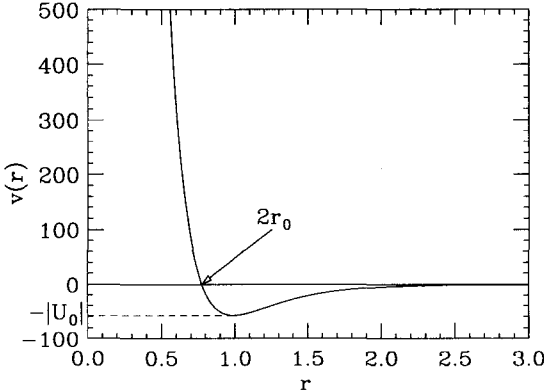


Figure 1. Behavior of the potential describing the interactions between constituents of a van der Waals fluid (the interparticle distance  $r$  and  $v(r)$  are both given in arbitrary units).

In spite of its simplicity, the van der Waals EOS describes most of the features of both the gas and liquid phases of the system, as well as the nature of the phase transition.

The EOS of strongly interacting matter reflects the complexity of the underlying dynamics, that makes the phase diagram extremely rich. As an example, fig.2 shows the phase diagram of charge neutral strongly interacting matter in  $\beta$ -equilibrium<sup>2</sup>.

In this talk, I will review the available empirical information on the EOS of strongly interacting matter at  $T \sim 0$ , and the extent to which this information can be used to constrain theoretical models. The knowledge coming from nuclear systematics and neutron stars data is summarized in Sections 2 and 3, respectively. Section 4 provides a short overview of the theoretical models of neutron star matter at supranuclear density, while Section 5 is devoted to the prospects for obtaining new insights from the experimental study of gravitational waves emitted by neutron stars. Finally, Section 6 summarizes the main results and states the conclusions.

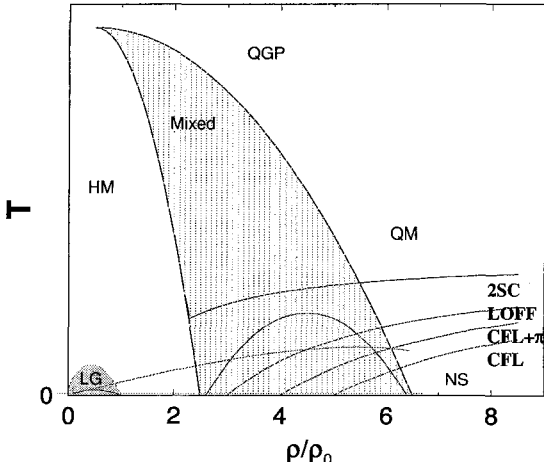


Figure 2. Temperature *vs* baryon density phase diagram of charge neutral strongly interacting matter in  $\beta$ -equilibrium. Hatched areas correspond to mixed phases of hadronic matter (HM) and quark matter (QM/QGP), as well as the nuclear liquid-gas (from ref.<sup>2</sup>).

## 2 Constraints on the EOS at $T=0$ from nuclear data

Under standard terrestrial conditions, strongly interacting matter is observed in form of rather small, cold chunks: the atomic nuclei.

Nuclei are self-bound systems consisting of  $Z$  protons and  $(A - Z)$  neutrons. Their smallness is a consequence of the electrostatic repulsion between protons, limiting  $A$  to  $\sim 200$ , while the fact that they can be described as cold objects follows from the observation that thermal energies are negligible in comparison to the large proton and neutron Fermi energies.

The body of data on nuclear masses provides a constraint on the density dependence of the energy per particle  $e = E/A$  at zero temperature, related to the EOS through

$$P(n, T = 0) = - \left( \frac{\partial E}{\partial \Omega} \right)_{T=0} = n^2 \left( \frac{de}{dn} \right)_{T=0}. \quad (4)$$

The  $A$ -dependence of the nuclear binding energy (i.e. the difference between the measured nuclear mass and the sum of the constituent masses) is well described by the semiempirical formula

$$B(Z, A) = a_V A + a_s A^{2/3} + a_c \frac{Z^2}{A^{1/3}} + a_A \frac{(A - 2Z)^2}{4A} - \lambda a_p \frac{1}{A^{1/2}}, \quad (5)$$

whose terms account for nuclear interactions, taking place both in the interior of the nucleus and on its surface, electrostatic interactions between protons, isospin asymmetry and shell effects.

The coefficient of the term linear in  $A$  yields the binding energy of *symmetric nuclear matter*, an ideal uniform system consisting of equal number of protons and neutrons coupled by strong interactions only. The equilibrium density of such a system,  $n_0$ , can be inferred exploiting saturation of nuclear densities, i.e. the fact that the central density of atomic nuclei, measured by elastic electron-nucleus scattering, does not depend upon  $A$  for large  $A$ .

The empirical equilibrium properties of nuclear matter are

$$e_0 = e(n = n_0, T = 0) = -16 \text{ MeV}/A , \quad n_0 \sim .16 \text{ fm}^{-3} . \quad (6)$$

In the vicinity of the equilibrium density  $e(n, T = 0)$  can be expanded according to (as we will only discuss the EOS at  $T = 0$ , the dependence upon  $T$  will be omitted hereafter)

$$e(n) \approx e_0 + \frac{1}{2} \frac{K}{9} \frac{(n - n_0)^2}{n_0^2} , \quad (7)$$

where

$$K = 9 n_0^2 \left( \frac{\partial^2 e}{\partial n^2} \right)_{n=n_0} = 9 \left( \frac{\partial P}{\partial n} \right)_{n=n_0} \quad (8)$$

is the (in)compressibility module, that can be extracted from the measured excitation energies of nuclear vibrational states. Empirical values range from  $K \sim 200$  MeV (corresponding to more compressible nuclear matter, i.e. to a *soft* EOS) to  $K \sim 300$  MeV (corresponding to a *stiff* EOS)<sup>3</sup>.

It has to be emphasized that the quadratic extrapolation of Eq.(7) cannot be expected to work far from equilibrium density. In fact, assuming a parabolic behavior of  $e(n)$  at large  $n$  ( $>> n_0$ ) leads to predict a speed of sound in matter,  $v_s$ , larger than the speed of light, i.e.

$$\left( \frac{v_s}{c} \right) = \frac{1}{n} \left( \frac{\partial P}{\partial e} \right) > 1 , \quad (9)$$

regardless of the value of  $K$ .

Eq.(9) shows that causality requires

$$\left( \frac{\partial P}{\partial \epsilon} \right) < 1 , \quad (10)$$

where  $\epsilon = E/\Omega$  is the energy-density. For a noninteracting Fermi gas  $\epsilon \propto n^{4/3}$ , implying (the equal sign corresponds to massless fermions)

$$P \leq \frac{\epsilon}{3}, \quad \left(\frac{v_s}{c}\right) \leq \frac{1}{3}. \quad (11)$$

In presence of interactions the above limits can be easily exceeded. For example, modeling the repulsion between nucleons in terms of a rigid core leads to predict infinite pressure at finite density.

The stiffest EOS compatible with causality is  $P = \epsilon$ , corresponding to  $(v_s/c) = 1$ . Back in the early 60's Zel'dovich was able to show that the  $v_s = c$  limit, corresponding to  $\epsilon \propto n^2$ , is indeed attained in a simple semirealistic theory, in which nucleons are assumed to interact through exchange of a vector meson <sup>4</sup>.

### 3 Constraints on the EOS at $T=0$ from neutron stars data

At very large  $A$  ( $\sim 10^{57}$ ), gravity becomes strong enough to balance the repulsive interactions between nucleons, and nuclear matter can occupy macroscopic regions of space. This is the situation occurring in the interior of neutron stars, compact astrophysical objects (typical values of mass and radius are  $\sim 1.4 M_\odot$  and  $\sim 10$  Km, respectively) whose central density largely exceeds  $n_0$ . The structure of a neutron star is schematically represented in

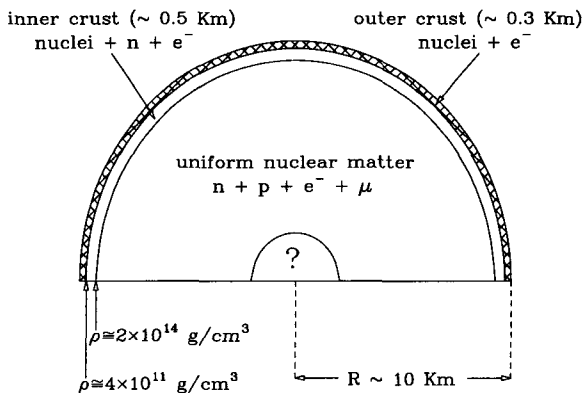


Figure 3. Cross section of a neutron star. Note that the equilibrium density of nuclear matter corresponds to  $\sim 2.7 \times 10^{14}$  g/cm<sup>3</sup>.

fig.3. Note that the inner and outer crusts contain a comparatively small

amount of matter, most of the star mass being concentrated in the region of supranuclear densities ( $n > n_0$ ). In addition, as all relevant Fermi energies are much larger than the typical temperature ( $\lesssim 10^9$  K  $\sim 100$  KeV), neutron stars can be regarded as cold object. The main features of the theoretical models of neutron star matter will be summarized in Section 4.

Given the EOS describibg matter in the interior of a neutron star, its mass and radius can be obtained from the Tolman-Oppenheimer-Volkov (TOV) equations

$$\frac{dP(r)}{dr} = -G \frac{[\epsilon(r) + P(r)/c^2] [M(r) + 4\pi r^2 P(r)/c^2]}{r^2 [1 - 2GM(r)/rc^2]} . \quad (12)$$

$$M(r) = 4\pi \int_0^r r'^2 dr' \epsilon(r') , \quad (13)$$

In the above equations, combining hydrostatic equilibrium with Einstein's equations of general relativity for a nonrotating star,  $P$  and  $\epsilon$  denote pressure and energy-density, respectively, and  $G$  is the gravitational constant.

For any value of the central energy-density  $\epsilon_c = \epsilon(r = 0)$  Eq.(12) can be integrated outward until the star radius  $R$ , defined by the condition  $P(R) = 0$ , is reached. The star mass  $M(R)$  can then be obtained from Eq.(13).

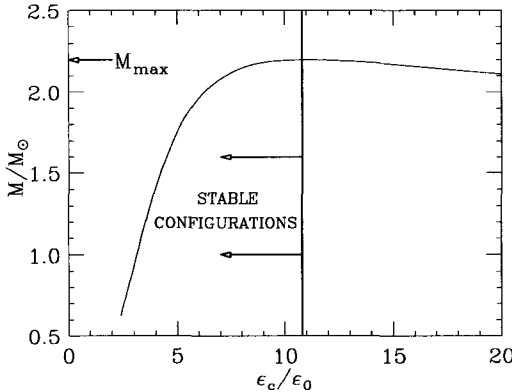


Figure 4. Typical dependence of the neutron star mass (in units of the solar mass  $M_\odot$ ) upon the energy-density at the center of the star (in units of the energy-density of symmetric nuclear matter at equilibrium).

Fig.4 shows the typical behavior of the neutron star mass as a function

of the central energy-density. Denoting by  $\bar{\epsilon}$  the central energy-density corresponding to the maximum mass, all stable configurations have  $\epsilon_c < \bar{\epsilon}_c$ .

The value of the maximum mass is mostly determined by the *stiffness* of the EOS, more incompressible neutron star matter (i.e. *stiffer* EOS) corresponding to larger  $M_{max}$ . Therefore, in principle measurements of neutron star masses may provide information on the behavior of the EOS at  $n > n_0$ .

The most precise experimental data, obtained from studies of the timing of radio pulsars, yield the average value<sup>5</sup>

$$M = 1.35 \pm 0.04 M_\odot , \quad (14)$$

thus constraining any realistic model of EOS to support a stable star with mass  $\sim 1.4 M_\odot$ .

Neutron star masses can also be obtained from the analysis of binary systems containing an X-ray pulsar. A recent determination of the mass of the Vela X-1 pulsar yields  $M = 1.86 \pm 0.33 M_\odot$ <sup>6</sup>, suggesting the possibility of a mass well above the canonical value of Eq.(14). If confirmed, the existence of a neutron star with  $M > 1.8 M_\odot$  would provide a very stringent constraint, ruling out theoretical models that predict very soft EOS.

#### 4 Theoretical models of neutron star matter at supranuclear density.

Theoretical models of neutron star matter are based on different approaches, involving different degrees of freedom, which are expected to be applicable in different density regimes.

In the range  $n_0 \lesssim n \lesssim 4n_0$  matter in the interior of the star is believed to take the form of a cold uniform fluid, that can be described in terms of hadronic degrees of freedom, within the framework of either nonrelativistic many-body theory<sup>7</sup> or relativistic mean-field approaches<sup>8</sup>.

At  $n$  just above  $n_0$  neutrons dominate, with a small fraction of protons and leptons in equilibrium with respect to the weak interaction processes ( $\ell$  denotes either an electron or a muon)

$$n \rightarrow p + \ell + \bar{\nu}_\ell , \quad p + \ell \rightarrow n + \nu_\ell . \quad (15)$$

For any baryon density  $n$ , minimization of the total energy-density with the constraints of baryon number conservation and charge neutrality fixes the relative abundances of neutrons, protons and leptons. Note that, as the proton fraction is small, typically  $< 10\%$ , theoretical calculations of the EOS involve the study of strongly *asymmetric* nuclear matter, whose energy is most sensitive to the isospin asymmetry term in Eq.(5). The importance of isospin

asymmetry is illustrated in fig.5, showing the calculated density dependence of the energy per particle of symmetric nuclear matter ( $(Z/A) = 1/2$ ) and pure neutron matter ( $(Z/A) = 0$ ). It clearly appears that unlike symmetric nuclear matter, whose energy exhibits a minimum, pure neutron matter is not self-bound at any density.

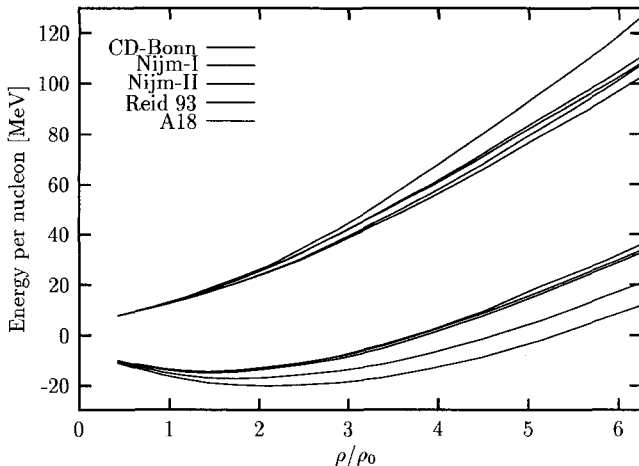


Figure 5. Typical density dependence of the energy per nucleon of pure neutron matter (upper curves) and symmetric nuclear matter (lower curves), obtained from nonrelativistic nuclear many-body approaches<sup>7</sup>. The density is given in units of the equilibrium density of symmetric nuclear matter.

As the density increases, different forms of matter, containing hadrons other than protons and neutrons, can become energetically favored. For example, the weak interaction process



leading to the appearance of a strange baryon, sets in as soon as the sum of the electron and neutron chemical potentials exceeds  $M_{\Sigma^-}$  (typically at  $n \gtrsim 2n_0$ ). At larger density the production of  $\Lambda^0$ 's is also energetically allowed.

For any fixed baryon density, the relative abundances of the different hadronic and leptonic species are dictated by the requirements of equilibrium with respect to weak interactions, conservation of baryon number and charge neutrality. Fig.6 shows the particle fractions resulting from the nonrelativistic many-body approach of ref.<sup>9</sup>.

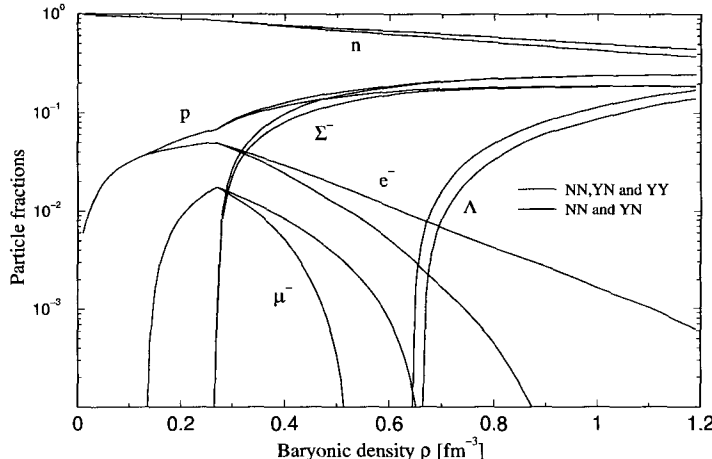


Figure 6. Relative abundances of hadrons and leptons in a hadronic model of neutron star matter (taken from ref.<sup>9</sup>).

The transition from nucleon matter to hadronic matter is associated with a softening of the EOS, as it basically amounts to replacing particles carrying large Fermi energies with more dilute, and therefore less energetic, strange baryons. Hence, using the EOS of hadronic matter as an input for the solution of the TOV equations leads to predict a value of the maximum mass significantly lower than that obtained using nucleon matter.

At very large density ( $n > 4n_0$ ) a new transition, to a phase in which quarks are no longer clustered into nucleons or hadrons, is eventually expected to take place. In most theoretical studies of neutron stars structure, the EOS of quark matter has been estimated using the simple MIT *bag model* (for a recent review see ref.<sup>10</sup>).

The bag model assumes that quarks be confined to a finite region of space (the bag), whose volume is limited by a pressure  $B$  (the bag constant). Its simplest implementation includes only massless and noninteracting  $u$  and  $d$  quarks. Equilibrium with respect to the process ( $\ell$  denotes either an electron or a muon)

$$d \rightarrow u + \ell + \bar{\nu}_\ell , \quad (17)$$

requires that the  $u$  and  $d$  chemical potentials satisfy (note that, as the mean free path of neutrinos in dense nucleon matter largely exceeds their typical

radius, neutron stars can be regarded as transparent to neutrinos)

$$\mu_d = \mu_u + \mu_\ell , \quad \mu_e = \mu_\mu , \quad (18)$$

whereas the constraint of charge neutrality implies

$$\frac{2}{3}n_u = \frac{1}{3}n_d + n_e + n_\mu , \quad (19)$$

where  $n_q$  ( $q = u, d$ ) and  $n_\ell$  ( $\ell = e, \mu$ ) denote the quark and lepton densities, respectively.

The energy-density reads

$$\epsilon = \frac{E}{\Omega} = B + \frac{3}{4\pi^2} \sum_q p_{F_q}^4 , \quad (20)$$

and the quark Fermi momenta are related to the total baryon density  $n$  through

$$p_{F_q} = (\pi^2 f_q n)^{(1/3)} , \quad (21)$$

$f_q$  being the number of quarks of flavor  $q$  per baryon. Finally, the pressure can be readily obtained from

$$P = - \left( \frac{\partial E}{\partial \Omega} \right) = -B + \frac{1}{4\pi^2} \sum_q p_{F_q}^4 . \quad (22)$$

More realistic models include a massive strange quark and allow for one-gluon exchange interactions between quarks of the same flavor. At fixed baryon density the quark and lepton fractional densities are determined by the requirements of chemical equilibrium, charge neutrality and baryon number conservation. Fig.7 shows the results obtained including massless  $u$  and  $d$  quarks and strange quarks of mass  $m_s = 150$  MeV, neglecting all interactions and setting the value of the bag constant to  $B = 208$  MeV/fm<sup>3</sup>.

In the  $n \rightarrow \infty$  limit, the energy per baryon of nucleon matter,  $e_{NM}$ , grows linearly with baryon density, whereas in quark matter  $e_{QM} \sim n^{1/3}$ . Hence, a transition from nucleon to quark matter is expected to take place in the inner region of neutron stars, provided the central density is large enough.

In the simplest implementation, the phase transition is assumed to take place at constant pressure and chemical potential, so that matter density exhibits a discontinuity at the boundary between the two phases. According to this picture the star consists of a core of quark matter surrounded by nucleon matter.

The calculations of ref.<sup>11</sup>, based on nonrelativistic many-body theory for the description of nucleon matter and the bag model for the description of

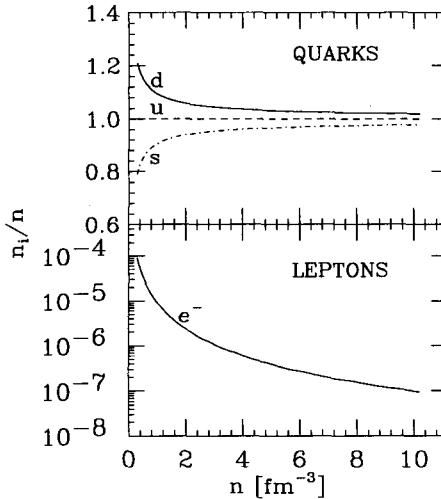


Figure 7. Relative abundances of quarks and leptons in  $\beta$ -stable matter consisting of massless  $u$  and  $d$  quarks and strange quarks with mass  $m_s = 150$  MeV. All interactions between quarks are neglected and the bag constant is set to  $B = 208$  MeV/fm $^3$ .

quark matter, predict a transition region  $5.4 < (n/n_0) < 9.8$  for  $B = 200$  MeV/fm $^3$  and  $4.9 < (n/n_0) < 7.5$  for  $B = 122$  MeV/fm $^3$ .

The transition to quark matter makes the EOS softer, thus lowering the value of the maximum neutron star mass. The authors of ref.<sup>11</sup> report a reduction  $\Delta M_{max}$  of  $\sim 10\%$  and  $\sim 20\%$  for  $B = 200$  and  $122$  MeV/fm $^3$ , respectively.

## 5 Will detection of gravitational provide new insight ?

As the pattern of nonradial oscillations of neutron stars depends upon the EOS describing matter in the interior of the star, detection of gravitational wave emission associated with the excitation of these modes can in principle provide additional constraints on theoretical models of the EOS.

For example, the complex oscillation frequencies of the axial (i.e. odd parity) modes of a nonrotating star are eigenvalues of a Schrödinger-like equation whose potential  $V_\ell(r)$  explicitly depend upon the EOS according to<sup>12</sup>

$$V_\ell(r) = \frac{e^{2\nu(r)}}{r^3} \left\{ \ell(\ell+1)r + r^3 [\epsilon(r) - P(r)] - 6M(r) \right\}, \quad (23)$$

where

$$\frac{d\nu}{dr} = -\frac{1}{[\epsilon(r) + P(r)]} \frac{dP}{dr}. \quad (24)$$

Using realistic EOS one obtains strongly damped eigenmodes, called *w-modes*, whose frequencies exhibit the behavior displayed in fig.8.

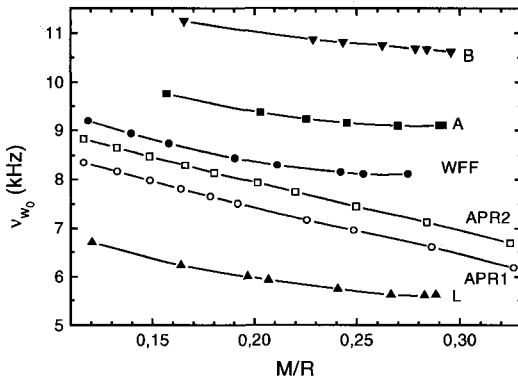


Figure 8. Frequencies of the first axial w-mode of a nonrotating neutron star, plotted as a function of the star compactness ( $M/R$ ). The different curves correspond to different models of EOS (taken from ref.<sup>12</sup>).

The pattern of frequencies strictly reflects the stiffness of the different EOS in the relevant density region (typically  $1 < (n/n_0) < 5$ , softer EOS corresponding to higher frequencies. For example, the curve labelled B has been obtained from a model including nucleons, nucleon excitations and strange baryons, predicting a very soft EOS and a maximum mass of  $1.42 M_\odot$ .

It is interesting to note that the dependence upon the ratio ( $M/R$ ) is rather weak, so that detection of a given frequency may allow one to discriminate between different models of EOS (e.g. between model B, corresponding to hadronic matter and model WFF, corresponding to nucleon matter) regardless of the compactness of the star.

A different class of nonradial oscillations, the *g-modes*, are associated with the occurrence of a density discontinuity in the interior of the star. Early studies of these modes focused on discontinuities that are known to be produced by the changes of chemical composition in the low density region of the crust, corresponding to a fractional distance from the surface ( $d/R$ )  $\lesssim 10\%$ .

As pointed out in Section 4, a different discontinuity may be produced by the transition from nucleon to quark matter, which is expected to take place at much larger density and involve a much larger density jump.

It has to be emphasized that, as nucleon and quark matter need not to be considered independently charge neutral, in general the deconfinement transition may involve the occurrence of a mixed phase (e.g. bubbles of quark matter in nucleon matter at lower density or *viceversa* at larger density) extending over a sizable region of space, rather than a sharp separation between the two phases<sup>10</sup>. Whether the mixed phase is energetically favored depends upon the balance between the gain in volume energy and the loss associated with Coulomb and surface energy<sup>13</sup>. If Coulomb and surface energies prevail, a density discontinuity is expected to occur.

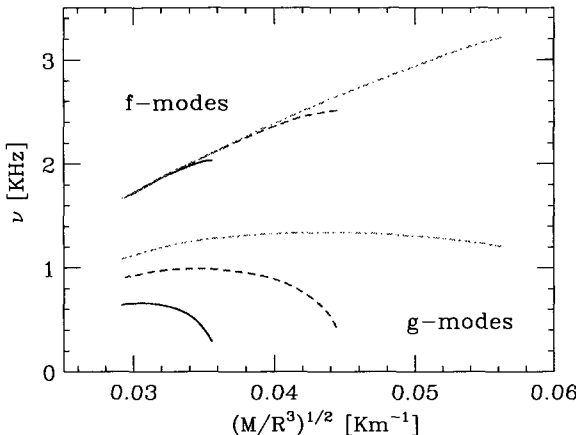


Figure 9. Frequencies of the f- and g-mode of a neutron star of mass  $M = 1.4M_{\odot}$  as a function of the average density. Solid, dashed and dot-dash lines correspond to density jumps of 10 %, 20 % and 30 %, respectively. All stellar models have polytropic exponent  $\Gamma = 2$  (see Eq.(25))<sup>14</sup>

The authors of ref.<sup>14</sup> have recently carried out an exploratory calculation of the frequencies of both the fundamental f-mode and the g-mode of a nonrotating neutron star, using a simple polytropic EOS with a density discontinuity  $\Delta n$  located at density  $n = n_D$ :

$$P(n) = \begin{cases} K \left(1 + \frac{\Delta n}{n_D}\right)^{\Gamma} n^{\Gamma} & n < n_D \\ Kn^{\Gamma} & n > n_D + \Delta n \end{cases} \quad (25)$$

The results of ref.<sup>14</sup> are summarized in fig.9, showing the f- and g-mode frequencies as a function of the average density of the star, whose mass is kept fixed at the canonical value of  $1.4 M_{\odot}$ . It clearly appears that, while the f-mode frequency exhibits a nearly linear growth, largely unaffected by the abrupt structural change associated with the phase transition, the frequencies of the g-mode strongly depend upon the jump in density  $\Delta n$ . Hence, a simultaneous measurements of the frequencies of the two modes would provide information on both size and location of the discontinuity.

## 6 Conclusions

The extent to which the currently available empirical information constrains the EOS of cold  $\beta$ -stable strongly interacting matter is illustrated in fig.10.

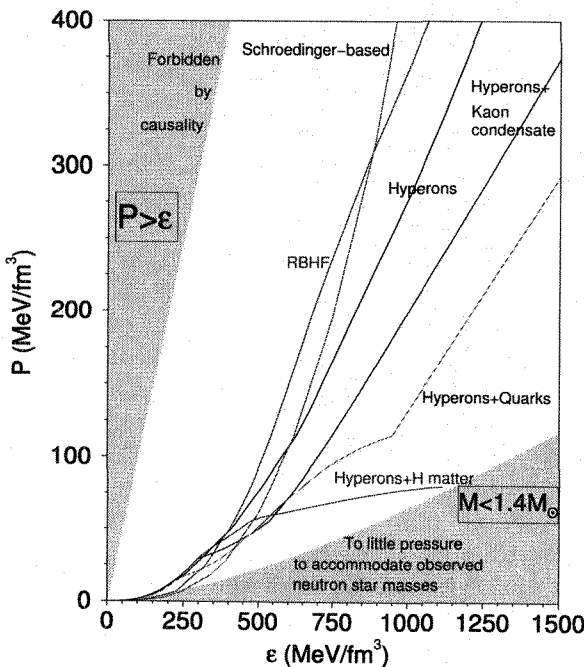


Figure 10. EOS of cold  $\beta$ -stable strongly interacting matter resulting from a variety of different theoretical approaches, based on both hadronic and quark degrees of freedom. The shaded areas show the region forbidden by causality and that corresponding to  $M_{max} < 1.4 M_{\odot}$  (taken from ref.<sup>15</sup>).

Although all EOS resulting from nonrelativistic approaches are known to be plagued by a noncausal behaviour at very large density, it appears that the constraint  $P > \epsilon$  is fulfilled by all EOS over a wide range of energy-density.

The requirement that the maximum mass be larger than  $1.4 M_{\odot}$  does not provide a stringent constraint either, as all reasonable models support a stable star with  $M = 1.4 M_{\odot}$ . However, as pointed out in Section 3, the situation may change should the mass of the Vela X-1 pulsar be confirmed to be larger than  $1.8 M_{\odot}$ . In this case the shaded region in the lower right corner of fig.10 would considerably extend upward, thus ruling out models that predict very soft EOS.

The observation of gravitational waves emitted by neutron stars may provide valuable new insight, allowing to further constrain theoretical models. Detection of gravitational radiation in the relevant few  $KHz$  frequency range may become possible with the recently proposed gravitational laser interferometric detector EURO<sup>16</sup>.

As far as theory is concerned, it has to be mentioned that the recent progress in Quantum Monte Carlo has made it possible to apply this approach to the study of the EOS of pure neutron matter<sup>17</sup>. The extension to the case of  $\beta$ -stable matter, that appears to be feasible, would be of great importance for the understanding of neutron star matter in the region of not too high density ( $n \lesssim 2n_0$ ), where the use of nucleonic degrees of freedom is likely to be reasonable.

At larger densities a transition to quark matter is expected to take place. A better theoretical description of this region will require a careful analysis of the nature of the phase transition as well as a more realistic description of the deconfined phase. In this context, a pivotal role is likely to be played by detailed quantitative studies of the possible occurrence of the color superconducting phase predicted by the fundamental theory of strong interactions<sup>18</sup>.

## References

1. K. Huang *Statistical Mechanics* (Wiley, New York, 1963).
2. H. Heiselberg, talk given at the Workshop on "Compact Stars in the QCD Phase Diagram", Copenhagen, August 15-18, 2001. astro-ph/0201465.
3. S. Shlomo and D.H. Youngblood, *Phys. Rev. C* **47**, 529 (1993).
4. Ya. B. Zel'dovich, *Sov. Phys. JETP* **14**, 1143 (1962).
5. S.E. Thorsett and D. Chakrabarty, *ApJ* **512**, 288 (1999).
6. M.H. van Kerkwijk, astro-ph/0110336.
7. H. Heiselberg and V.R. Pandharipande, *Ann. Rev. Nucl. Part. Sci.*, **50**, 481 (2000).

8. N.K. Glendenning, *Compact Stars* (Springer, New York, 1997).
9. I. Vidaña *et al*, *Phys. Rev. C* **62**, 035801 (2000).
10. H. Heiselberg and M. Hjorth-Jensen, *Phys. Rep.* **328**, 237 (2000).
11. A. Akmal, V.R. Pandharipande and D.G. Ravenhall, *Phys. Rev. C* **58**, 1804 (1998).
12. O. Benhar, E. Berti and V. Ferrari, *Mon. Not. R. Astron. Soc.* **310**, 797 (1999).
13. H. Heiselberg, C.J. Pethik and E.F. Staubö, *Phys. Rev. Lett.* **70**, 1355 (1993).
14. G. Miniutti, J.A. Pons, E. Berti, L. Gualtieri and V. Ferrari, paper in preparation.
15. F. Weber, *Pulsars as Astrophysical Laboratories for Nuclear and Particle Physics* (IoP Publishing, Bristol, 1999).
16. EURO: Europe's Third Generation Gravitational Wave Observatory. Proposal available at <http://carina.astro.cf.ac.uk/geo/euro/> (May, 2000).
17. K.E. Schmidt and S. Fantoni, *Phys. Lett.* **B446**, 99 (1999).
18. M.G. Alford, K. Rajagopal, S. Reddy and F. Wilczek, *Phys. Rev. D* **64**, 074017 (2000).

# ISOSPIN EFFECTS AT HIGH BARYON DENSITY

M. DI TORO, M. COLONNA AND V. GRECO

*Laboratori Nazionali del Sud, Via S.Sofia 44, I-95123 Catania, Italy, and*

*Dipartimento di Fisica e Astronomia, Univ. di Catania*

*E-mail: ditoro@lns.infn.it*

F.MATERA

*Dipartimento di Fisica, Univ. di Firenze and INFN, Sezione di Firenze, Via  
G.Sansone 1, I-50019, Sesto F.no (Firenze), Italy*

*E-mail: matera@fi.infn.it*

We study equilibrium and collective response properties of Asymmetric Nuclear Matter (*ANM*) within a Quantum-Hadro-Dynamics effective field picture of the hadronic sector. We focus our attention on the effects of the interplay between scalar and vector channel contributions. The introduction of an explicit coupling to the scalar-isovector channel of the nucleon-nucleon interaction is strongly supported. This coupling (to a  $\delta$ -meson-like effective field) leads to a larger repulsion of the symmetry term at high baryon density and to new features of the collective response. Interesting contributions are found on the propagation of isovector-like modes at normal density and on an expected smooth transition to isoscalar-like oscillations at high baryon density. Important "chemical" effects on the neutron-proton structure of the mode are shown. For dilute *ANM* we have the isospin distillation mechanism of the unstable isoscalar-like oscillations, while at high baryon density we predict an almost pure neutron wave structure of the propagating sounds. Using the same hadronic *EOS*'s we finally support, from collision simulations, the possibility of an "early" transition to a mixed hadron-deconfined phase in charge asymmetric heavy ion reactions at intermediate energies.

## 1 Introduction

The *QHD* effective field model represents a very succesfull attempt to describe, in a fully consistent relativistic picture, equilibrium and dynamical properties of nuclear systems at the hadronic level<sup>1,2,3</sup>. Very nice results have been obtained for the nuclear structure of finite nuclei<sup>4,5,6</sup>, for the *NM* Equation of State and liquid-gas phase transitions<sup>7</sup> and for the dynamics of nuclear collisions<sup>8,9</sup>. Relativistic Random-Phase-Approximation (*RRPA*) theories have been developed to study the nuclear collective response<sup>10,11,12,13,14,15</sup>.

In this paper we present a relativistic linear response theory with the aim of a trasparent connection between the collective dynamics and the coupling to various channels of the nucleon-nucleon interaction. In particular we will focus our attention on the dynamical response of asymmetric nuclear matter since one of the main points of our discussion is the relevance of the coupling

to a scalar isovector channel, the virtual  $\delta[a_0(980)]$  meson, not considered in the usual dynamical studies<sup>16</sup>.

Moreover the  $\delta$ -meson coupling leads to a fast increasing repulsion of the symmetry term at high baryon density. This is certainly of interest for astrophysics. Here we stress the possibility of a relatively early transition of a cold  $ANM$  to the mixed hadron-quark phase, at baryon densities of the order of  $2 \rho_0$ , see also<sup>17</sup>.

## 2 Kinetic Equations from a QHD effective theory

We start from the  $QHD$  effective field picture of the hadronic phase of nuclear matter<sup>1,2,3</sup>. In order to include the main dynamical degrees of freedom of the system we will consider the nucleons coupled to the isoscalar scalar  $\sigma$  and vector  $\omega$  mesons and to the isovector scalar  $\delta$  and vector  $\rho$  mesons.

The Lagrangian density for this model, including non-linear isoscalar/scalar  $\sigma$ -terms<sup>18</sup>, is given by:

$$\begin{aligned} \mathcal{L} = & \bar{\psi}[\gamma_\mu(i\partial^\mu - g_\omega V^\mu - g_\rho B^\mu \cdot \tau) - (M - g_\sigma \phi - g_\delta \tau \cdot \delta)]\psi + \\ & \frac{1}{2}(\partial_\mu \phi \partial^\mu \phi - m_s^2 \phi^2) - \frac{a}{3}\phi^3 - \frac{b}{4}\phi^4 - \frac{1}{4}W_{\mu\nu}W^{\mu\nu} + \frac{1}{2}m_v^2 V_\nu V^\nu + \\ & \frac{1}{2}(\partial_\mu \delta \cdot \partial^\mu \delta - m_\delta^2 \delta^2) - \frac{1}{4}\mathbf{G}_{\mu\nu} \cdot \mathbf{G}^{\mu\nu} + \frac{1}{2}m_\rho^2 B_\nu \cdot B^\nu \end{aligned} \quad (1)$$

where  $W^{\mu\nu}(x) = \partial^\mu V^\nu(x) - \partial^\nu V^\mu(x)$  and  $\mathbf{G}^{\mu\nu}(x) = \partial^\mu B^\nu(x) - \partial^\nu B^\mu(x)$ . Here  $\psi(x)$  is the nucleon fermionic field,  $\phi(x)$  and  $V^\nu(x)$  represent neutral scalar and vector boson fields, respectively.  $\delta(x)$  and  $B^\nu(x)$  are the charged scalar and vector fields and  $\tau$  denotes the isospin matrices.

From the Lagrangian Eq.(1) with the Euler procedure a set of coupled equations of motion for the meson and nucleon fields can be derived. The basic approximation in nuclear matter applications consists in neglecting all the terms containing derivatives of the meson fields, with respect to the mass contributions. Then the meson fields are simply connected to the operators of the nucleon scalar and current densities by the following equations:

$$\hat{\Phi}/f_\sigma + A\hat{\Phi}^2 + B\hat{\Phi}^3 = \bar{\psi}(x)\psi(x) \equiv \hat{\rho}_S \quad (2)$$

$$\begin{aligned} \hat{V}^\mu(x) &= f_\omega \bar{\psi}(x)\gamma^\mu \psi(x) \equiv f_\omega \hat{j}_\mu, \\ \hat{\mathbf{B}}^\mu(x) &= f_\rho \bar{\psi}(x)\gamma^\mu \tau \psi(x), \\ \hat{\delta}(x) &= f_\delta \bar{\psi}(x)\tau \psi(x) \end{aligned} \quad (3)$$

where  $\hat{\Phi} = g_\sigma \phi$ ,  $f_\sigma = (g_\sigma/m_\sigma)^2$ ,  $A = a/g_\sigma^3$ ,  $B = b/g_\sigma^4$ ,  $f_\omega = (g_\omega/m_\omega)^2$ ,  $f_\rho = (g_\rho/2m_\rho)^2$ ,  $f_\delta = (g_\delta/m_\delta)^2$ .

For the nucleon fields we get a Dirac-like equation. Indeed after substituting Eqs.(2,3) for the meson field operators, we obtain an equation which contains only nucleon field operators. All the equations can be consistently solved in a Mean Field Approximation (*RMF*), where most applications have been performed, in particular in the Hartree scheme<sup>3,5</sup>.

The inclusion of Fock terms is conceptually important<sup>19,20</sup> since it automatically leads to contributions to various channels, also in absence of explicit coupling terms. A thorough study of the Fock contributions in a *QHD* approach with non-linear self-interacting terms has been recently worked out<sup>21</sup>, in particular for asymmetric matter<sup>22</sup>.

We perform the many-body calculations in the quantum phase-space introducing the Wigner transform of the one-body density matrix for the fermion field<sup>23,24</sup>.

The one-particle Wigner function is defined as:

$$[\hat{F}(x, p)]_{\alpha\beta} = \frac{1}{(2\pi)^4} \int d^4 R e^{-ip\cdot R} \langle : \bar{\psi}_\beta(x + \frac{R}{2}) \psi_\alpha(x - \frac{R}{2}) : \rangle ,$$

where  $\alpha$  and  $\beta$  are double indices for spin and isospin. The brackets denote statistical averaging and the colons denote normal ordering. The Wigner function is a matrix in spin and isospin spaces; in the case of asymmetric NM it is useful to decompose it into neutron and proton components. Following the treatment of the Fock terms in non-linear *QHD* introduced in Ref.<sup>21,22</sup>, we obtain for the Wigner function the following kinetic equation ( $i = n, p$ ):

$$\begin{aligned} & \frac{i}{2} \partial_\mu \gamma^\mu \hat{F}^{(i)}(x, p) + \gamma^\mu p_{\mu i}^* \hat{F}^{(i)}(x, p) - M_i^* \hat{F}^{(i)}(x, p) + \\ & \frac{i}{2} \Delta \left[ \tilde{f}_\omega j_\mu(x) \gamma^\mu \pm \tilde{f}_\rho j_{3\mu}(x) \gamma^\mu - \tilde{f}_\sigma \rho_S(x) \mp \tilde{f}_\delta \rho_{S3}(x) \right] \hat{F}^{(i)}(x, p) = 0, \end{aligned} \quad (4)$$

where  $\Delta = \partial_x \cdot \partial_p$ , with  $\partial_x$  acting only on the first term of the products. Here  $\rho_{S3} = \rho_{Sp} - \rho_{Sn}$  and  $j_{3\mu}(x) = j_\mu^p(x) - j_\mu^n(x)$  are the isovector scalar density and the isovector baryon current, respectively. We have defined the kinetic momentum and effective masses, as:

$$\begin{aligned} p_{\mu i}^* &= p_\mu - \tilde{f}_\omega j_\mu(x) \pm \tilde{f}_\rho j_{3\mu}(x) \\ M_i^* &= M - \tilde{f}_\sigma \rho_S(x) \pm \tilde{f}_\delta \rho_{S3}(x) , \end{aligned} \quad (5)$$

with the effective coupling functions given by:

$$\begin{aligned} \tilde{f}_\sigma &= \frac{\Phi}{\rho_S} - \frac{1}{8} \frac{d\Phi(x)}{d\rho_S(x)} - \frac{1}{2\rho_S} Tr \hat{F}^2(x) \frac{d^2\Phi(x)}{d\rho_S^2(x)} + \frac{1}{2} f_\omega + \frac{3}{2} f_\rho - \frac{3}{8} f_\delta , \\ \tilde{f}_\omega &= \frac{1}{8} \frac{d\Phi(x)}{d\rho_S(x)} + \frac{5}{4} f_\omega + \frac{3}{4} f_\rho + \frac{3}{8} f_\delta , \end{aligned}$$

$$\begin{aligned}\tilde{f}_\delta &= -\frac{1}{8} \frac{d\Phi(x)}{d\rho_S(x)} + \frac{1}{2} f_\omega - \frac{1}{2} f_\rho + \frac{9}{8} f_\delta , \\ \tilde{f}_\rho &= \frac{1}{8} \frac{d\Phi(x)}{d\rho_S(x)} + \frac{1}{4} f_\omega + \frac{3}{4} f_\rho - \frac{1}{8} f_\delta ,\end{aligned}\tag{6}$$

where  $8 \operatorname{Tr} \hat{F}^2(x) = \rho_S^2 + j_\mu j^\mu + \rho_{S3}^2 + j_{3\mu} j^{3\mu}$ . We remind that we are dealing with a transport equation so the currents and densities, in general, are varying functions of the space-time, at variance with the case of nuclear matter at equilibrium.

The expression of Eq.(5) for the effective mass, embodies an isospin contribution from Fock terms also without a direct inclusion of the  $\delta$  meson in the Lagrangian. The usual *RMF* approximation (Hartree level) is covered by the Hartree-Fock results, one has only to change the coupling functions  $\tilde{f}_i$  ( $i = \sigma, \omega, \rho, \delta$ ), Eqs.(6), with the coupling constants  $f_i$ .

### 3 The symmetry term of the nuclear Equation of State

The energy density and pressure for symmetric and asymmetric nuclear matter and the  $n, p$  effective masses can be self-consistently calculated just in terms of the four boson coupling constants,  $f_i \equiv (\frac{g_i^2}{m_i^2})$ ,  $i = \sigma, \omega, \rho, \delta$ , and the two parameters of the  $\sigma$  self-interacting terms,  $A \equiv \frac{a}{g_\sigma^2}$  and  $B \equiv \frac{b}{g_\sigma^4}$ , see ref.<sup>21,22</sup>.

The isoscalar meson parameters are fixed from symmetric nuclear matter properties at  $T = 0$ : saturation density  $\rho_0 = 0.16 \text{ fm}^{-3}$ , binding energy  $E/A = -16 \text{ MeV}$ , nucleon effective mass  $M^* = 0.7 M_N$  ( $M_N = 939 \text{ MeV}$ ) and incompressibility  $K_V = 240 \text{ MeV}$  at  $\rho_0$ . The fitted  $f_\sigma, f_\omega, A, B$  parameters are reported in the Table. They have quite standard values for these minimal non-linear *RMF* models. *Set I* and *Set II* correspond to the best parameters within a non-linear Hartree calculation, respectively with the  $\rho$ -(*Set I*,  $NLH + \rho$ ) and with the  $\rho + \delta$  (*Set II*,  $NLH + (\rho + \delta)$ ) couplings in the isovector channel (see the discussion in ref.<sup>16</sup>). *NLHF* stands for the non-linear Hartree-Fock scheme described before.

In the Table we report also the *NL3* parametrization, widely used in nuclear structure calculations<sup>26</sup>. We remind that the *NL3*-saturation properties for symmetric matter are chosen as  $\rho_0 = 0.148 \text{ fm}^{-3}$ ,  $M^* = 0.6 M_N$ ,  $K_V = 271.8 \text{ MeV}$ . The symmetry parameter is  $a_4 = 37.4 \text{ MeV}$ .

The symmetry energy in *ANM* is defined from the expansion of the energy

parameter	Set I	Set II	NLHF	NL3
$f_\sigma (fm^2)$	11.27	same	9.15	15.73
$f_\omega (fm^2)$	6.48	same	3.22	10.53
$f_\rho (fm^2)$	1.0	2.8	1.9	1.34
$f_\delta (fm^2)$	0.00	2.0	1.4	0.00
$A (fm^{-1})$	0.022	same	0.098	-0.01
$B$	-0.0039	same	-0.021	-0.003

per nucleon  $E(\rho_B, \alpha)$  in terms of the asymmetry parameter  $\alpha$  defined as

$$\alpha \equiv -\frac{\rho_{B3}}{\rho_B} = \frac{\rho_{Bn} - \rho_{Bp}}{\rho_B} = \frac{N - Z}{A}.$$

We have

$$E(\rho_B, \alpha) \equiv \frac{\epsilon(\rho_B, \alpha)}{\rho_B} = E(\rho_B) + E_{sym}(\rho_B)\alpha^2 + O(\alpha^4) + \dots \quad (7)$$

and so in general

$$E_{sym} \equiv \frac{1}{2} \frac{\partial^2 E(\rho_B, \alpha)}{\partial \alpha^2} \Big|_{\alpha=0} = \frac{1}{2} \rho_B \frac{\partial^2 \epsilon}{\partial \rho_{B3}^2} \Big|_{\rho_{B3}=0} \quad (8)$$

In the Hartree case an explicit expression for the symmetry energy can be easily derived <sup>16</sup>

$$E_{sym}(\rho_B) = \frac{1}{6} \frac{k_F^2}{E_F^*} + \frac{1}{2} \left[ f_\rho - f_\delta \left( \frac{M^*}{E_F^*} \right)^2 \right] \rho_B \equiv E_{sym}^{kin} + E_{sym}^{pot} \quad (9)$$

where  $k_F$  is the nucleon Fermi momentum corresponding to  $\rho_B$ ,  $E_F^* \equiv \sqrt{(k_F^2 + M^{*2})}$  and  $M^*$  is the effective nucleon mass in symmetric  $NM$ ,  $M^* = M_N - g_\sigma \phi$ .

We see that, when the  $\delta$  is included, the observed  $a_4$  value actually assigns the combination  $[f_\rho - f_\delta(\frac{M}{E_F^*})^2]$  of the  $(\rho, \delta)$  coupling constants. If  $f_\delta \neq 0$  we have to increase the  $\rho$ -coupling (see Fig.1 of ref.<sup>7</sup>). In our calculations we use the value  $a_4 = 32 MeV$ .

The Set I corresponds to  $f_\delta = 0$ . In the Set II  $f_\delta$  is chosen as  $2.0 fm^2$ . Although this value is relatively well justified, <sup>16</sup>, we stress that aim of this work is just to show the main qualitative new dynamical effects of the  $\delta$ -meson coupling. In order to have the same  $a_4$  we must increase the  $\rho$ -coupling constant of a factor three, up to  $f_\rho = 2.8 fm^2$ . Now the symmetry energy at saturation density is actually built from the balance of scalar (attractive) and vector (repulsive) contributions, with the scalar channel becoming weaker with increasing baryon density <sup>16</sup>. This is indeed the isovector counterpart of the

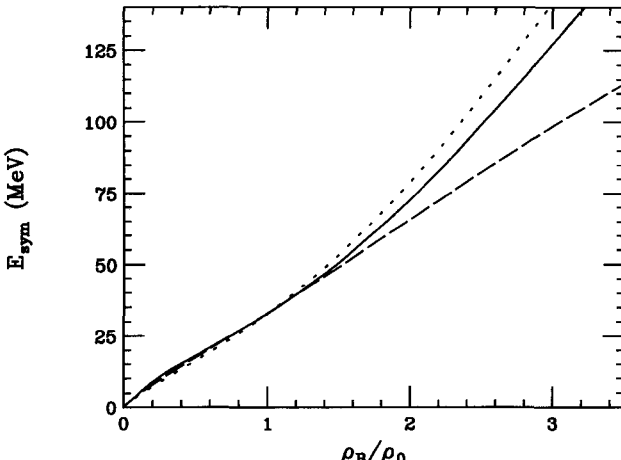


Figure 1. Total (kinetic+potential) symmetry energy as a function of the baryon density. Long dashed: Hartree ( $NLH + \rho$ ). Dotted: Hartree ( $NLH + \rho + \delta$ ). Solid: Hartree-Fock ( $NLHF$ ).

saturation mechanism occurring in the isoscalar channel for the symmetric nuclear matter. From such a scheme we get a further strong fundamental support for the introduction of the  $\delta$ -coupling in the symmetry energy evaluation.

Details of the calculation can be found in Refs. <sup>22,16</sup>, here we show only the result corresponding to the parametrizations (*Sets I, II* and *NLHF*) that we will use to investigate the dynamical response. In Fig.1 we report the symmetry energy as a function of the baryon density in the Hartree case ( $\rho$  and  $\rho + \delta$ ) and with the Fock terms [ $(\rho + \delta)$  case]. When the  $\delta$  “channel” is included the behaviour is stiffer for the relativistic mechanism discussed before, see also ref. <sup>16</sup>. This result will be used in the last section to enhance the possibility of an “earlier” transition to a mixed hadron-quark phase in asymmetric  $NM$ .

When the Fock terms are evaluated the new “effective” couplings Eqs.(6) naturally acquire a density dependence, see <sup>25</sup>. The decrease of the “effective”  $\rho$  coupling at high density accounts for the slight softening of the symmetry energy seen in Fig.1 (from the dotted to the solid line).

## 4 Linear Response Equations

In this section we study collective oscillations that propagate in cold nuclear matter due to the mean field dynamics. In some sense we follow a relativistic extension of the method introduced by Landau to study liquid- $^3He$ <sup>27,28,29</sup> and recently applied to investigate stable and unstable modes in nuclear matter<sup>30,31,32</sup>. The starting point is the kinetic transport equation Eq.(4). We look for solutions corresponding to small oscillations of  $\hat{F}(x, p)$  around the equilibrium value. Therefore we put

$$\hat{F}(x, p) = \hat{H}(p) + \hat{G}(x, p) \quad (10)$$

where  $\hat{H}(p)$  is the Wigner function at equilibrium and  $\hat{G}(x, p)$  represent its fluctuations.

The explicit expressions of the linearized kinetic equations, together with some of their properties, can be found in ref.<sup>25</sup>. We notice that the formalism developed in Hartree-Fock approximation allows to achieve a set of equations valid also for an approach to *QHD* based on a dependence on the scalar density of all couplings<sup>33</sup>. In particular in our case the coupling functions to the scalar-isoscalar channel depend on all the isoscalar and isovector densities and currents (for details, see<sup>21</sup>), then it is even more general.

Since the physics effects appear more transparent we will show here the Hartree results, keeping well in mind that the Fock contributions can be easily included<sup>25</sup>. We expect to have some extra contributions in the various interaction channels without qualitative modifications of the physical response.

The normal collective modes are plane waves, characterized by the wave vector ( $k^\mu = (k^0, 0, 0, |\mathbf{k}|)$ ). They correspond only to longitudinal waves and do not depend on  $k^0$  and  $|\mathbf{k}|$  separately, but only on the ratio

$$v_s = \frac{k^0}{|\mathbf{k}|} .$$

The sound velocities are given by values of  $v_s$  obtained from the dispersion relations,<sup>25</sup>. In correspondence the neutron/proton structure of the eigenvectors (normal modes) can be derived. It should be remarked that in asymmetric nuclear matter isoscalar and isovector components are mixed in the normal modes. This can be argued by the fact that in each of the linearized eqs. both proton/neutron densities and currents are appearing.

However we remind that one can still identify isovector-like excitations as the modes where neutrons and protons move out of phase, while isoscalar-like modes are characterized by neutrons and protons moving in phase<sup>31,35</sup>.

## 5 Collective Modes in Asymmetric Nuclear Matter

Let us start by considering isovector-like excitations. In Fig.2a we show the sound velocities in the Hartree approximation, as a function of the asymmetry parameter  $\alpha$  for different baryon densities. We actually plot the sound velocities in units of the neutron Fermi velocities. This is physically convenient: when the ratio is approaching 1.00 we can expect that this “zero” sound will not propagate due to the strong coupling to the “chaotic” single particle motions (“Landau damping”). This quantity then will also directly give a measure of the “robustness” of the collective mode we are considering.

Dotted lines refer to calculations including  $(\rho + \delta)$  mesons, long-dashed lines correspond to the case with only the  $\rho$  meson. Calculations are performed at  $\rho_B = \rho_0$  and  $\rho_B = 2\rho_0$ . We stress that the results of the two calculations differ already at zero asymmetry,  $\alpha = 0$ . At normal density ( $\rho_0$  curves), in spite of the fact that the symmetry energy coefficient,  $a_4 = E_{sym}(\rho_0)$ , is exactly the same in the two cases, significant differences are observed in the response of the system. From Fig.2(a) we can expect a reduction of the frequency for the bulk isovector dipole mode in stable nuclei when the scalar isovector channel ( $\delta$ -like) is present. Moreover we note that, in the  $NLH - \rho$  case, the excitation of isovector modes persists up to higher asymmetries at saturation density. These are non-trivial features, related to the different way scalar and vector fields are entering in the dynamical response of the nuclear system. Such behaviours are therefore present in both collective responses, isoscalar and isovector.

Differences are observed even at  $\rho_B = 2\rho_0$ , where however also the symmetry energy is different. A larger  $E_{sym}$  is obtained in the case including the  $\delta$  meson (see Fig.1) and this leads to a compensation of the effect observed at normal nuclear density. In particular, at higher asymmetries  $\alpha$  the collective excitation becomes more robust for  $NLH - (\rho + \delta)$ . Differences are observed also in the “chemical” structure of the mode, represented by the ratio  $\delta\rho_p/\delta\rho_n$ , plotted in Fig.2(b). The ratio of the out of phase  $n,p$  oscillations is not following the ratio of the  $n,p$  densities for a fixed asymmetry, given by the full circles in the figure. We systematically see a larger amplitude of the neutron oscillations. The effect is more pronounced when the  $\delta$  (scalar-isovector) channel is present (dotted lines).

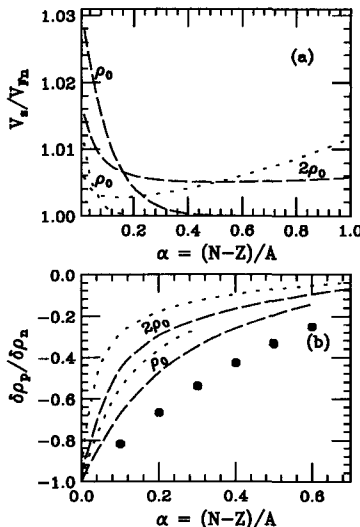


Figure 2. Isovector-like modes: (a) Ratio of zero sound velocities to the neutron Fermi velocity  $V_{F_n}$  as a function of the asymmetry parameter  $\alpha$  for two values of baryon density. Long dashed line:  $NLH - \rho$ ; Dotted line:  $NLH - (\delta + \rho)$ . (b) Corresponding ratios of proton and neutron amplitudes. All lines are labelled with the baryon density,  $\rho_0 = 0.16 \text{ fm}^{-3}$ . The full circles in panel (b) represent the trivial behaviour of  $-(\rho_p/\rho_n)$  vs.  $\alpha$ .

### *Disappearance of the Isovector Modes: Exotic High Baryon Density Sounds*

For asymmetric matter we have found that, in all the calculation schemes, with increasing baryon density the isovector modes disappear: we call such densities  $\rho_B^{cross}$ . E.g. from Fig.2(b) we see that the ratio  $\delta\rho_p/\delta\rho_n$  tends very quickly to zero with increasing baryon density, almost for all asymmetries. Around this transition density we expect to have an almost *pure neutron wave* propagation of the sound. Here we show the results of the  $NLH + \rho$  case, see Figs.3 and 4, but the effect is clearly present in all the models.

For symmetric matter we have a real crossing of the two phase velocities, isoscalar and isovector, as shown in Fig.3(a). Above  $\rho_B^{cross}$  the isoscalar mode is the most robust.

For asymmetric matter we observe a transition in the structure of the propagating normal mode, from isovector-like to isoscalar-like, Fig.3(b,c). Similar effects have been seen in a non-relativistic picture<sup>31</sup>.

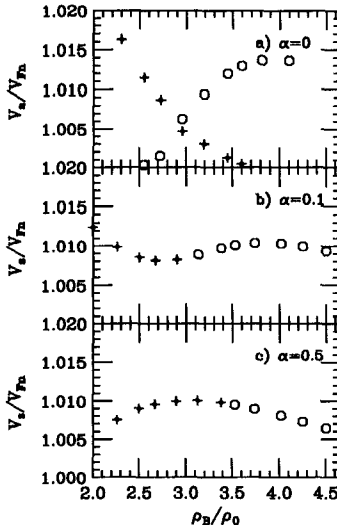


Figure 3. Sound phase velocities of the propagating collective mode vs. the baryon density ( $NLH + \rho$  case). Crosses: isovector-like. Open circles: isoscalar-like. (a): symmetric matter. (b): asymmetric matter,  $\alpha = 0.1$ . (c): asymmetric matter,  $\alpha = 0.5$ .

For a given asymmetry  $\alpha$  the value of  $\rho_B^{cross}$  is different for the three models considered, as can be argued by the behaviour of  $\delta\rho_p/\delta\rho_n$  at  $2\rho_0$  in Fig.2(b). E.g. for  $\alpha = 0.1$   $NLH - (\rho + \delta)$  has the lower value ( $\rho_B^{cross} \simeq 2.4\rho_0$ ), while  $NLH - \rho$  has the higher one ( $\rho_B^{cross} \simeq 3.0\rho_0$ ). This is again related to the reduction of the isovector restoring force when the scalar-isovector channel ( $\delta$ -like) is present, see previous section.

From Fig.4 we see that the proton component of the propagating sound is quite small in a relatively wide region around the "transition" baryon density, a feature becoming more relevant with increasing asymmetry, see the open circle line. This is quite interesting since it could open the possibility of an experimental observation of the *neutron wave effect*.

These *Exotic High Baryon Density Sounds* are clearly shown in Fig.5, where results on the isoscalar-like modes above  $\rho_B^{cross}$  are reported.

In particular note the "chemical composition" (Fig.5(b)). The black spots show the trivial behaviour of  $\rho_p/\rho_n$  vs.  $\alpha$ .

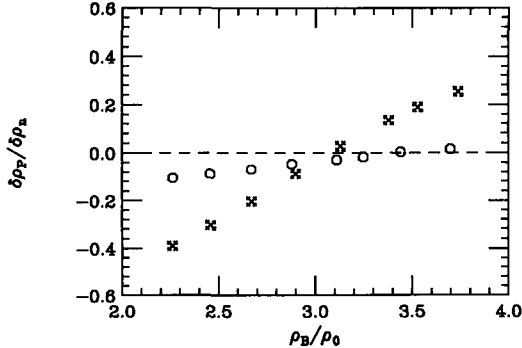


Figure 4. Ratio of protons and neutron amplitudes in the propagating mode, for different asymmetries, as a function of the baryon density around the  $\rho_B^{cross}$ . Crosses:  $\alpha = 0.1$ , Fig.3b. Open circles:  $\alpha = 0.5$ , Fig.3c.

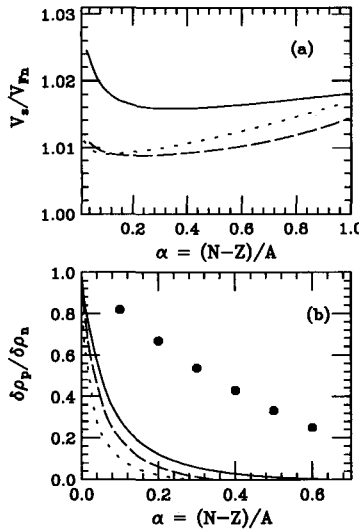


Figure 5. The same of Fig.2 for isoscalar-like modes, at  $\rho_B = 3.5\rho_0$ . Solid line: NLHF. Long Dashed line:  $NLH - \rho$ . Dotted line:  $NLH - (\rho + \delta)$ . The full circles in panel (b) represent the behaviour of  $\rho_p/\rho_n$  vs.  $\alpha$ .

## 6 Testing Deconfinement with Radioactive Beams?

It is relatively easy to show that at high baryon density and low temperature we can expect a transition from hadronic matter to deconfined quark matter.

The procedure is straightforward:

- Start from two "reasonable" model Equations of State (*EOS*), one for the hadronic phase, which can reproduce saturation properties, one for the quark phase, which can reproduce the hadron spectrum.
- Construct the phase separation boundary surface from the Gibbs phase rule<sup>27</sup>. See Ch.19 of the J.D.Walecka book<sup>36</sup> and ref.<sup>37</sup>.

For symmetric matter the baryon density  $\rho_{trans}$  corresponding to the transition to the coexistence region is relatively high, as expected, ranging from 4 to 8 times the saturation value  $\rho_0$ , depending on the stiffness of the hadronic *EOS* at high densities.

The new feature we would like to focus on in this report is the isospin dependence of such boundary location. We can foresee an interesting asymmetry effect, in the appealing direction of a decrease of  $\rho_{trans}$ , since the hadronic *EOS* becomes more repulsive. This has been actually seen in the calculations of ref.<sup>37</sup> (see the Fig.7): for a proton fraction  $Z/A = 0.3$  the boundary density is shifted to the left of about a 10%, from the  $4.0\rho_0$  of symmetric matter to a  $3.5\rho_0$ . The point we like to note is that this evaluation has been obtained in quite "adverse" conditions. The interaction symmetry part of the hadronic *EOS* is only coming from the charged vector  $\rho$ -meson coupling, which gives a linear increase of the symmetry energy with the baryon density, see the discussion in ref.<sup>16</sup>. The *EOS* of the quark phase is obtained within the *MIT* bag model with a very high pressure-of-vacuum parameter  $B^{1/4} = 190\text{MeV}$ , i.e. it is very repulsive.

We have repeated the study with new *EOS*'s in the two phases, with modifications, inspired by sensible physics arguments, which lead to a stiffer asymmetric matter and to a softer quark matter and therefore to an earlier transition, see also ref.<sup>17</sup> for more details.

For the hadronic phase we have enhanced the symmetry repulsion at high baryon density introducing also the coupling to the charged scalar  $\delta$ -meson. As remarked in ref.<sup>16</sup>, this is fully in agreement with the spirit of the effective field theories, and of course with the phenomenology of the free nucleon-nucleon interaction.

In the quark phase we use smaller values of the bag constant, in the range  $B^{1/4} \simeq 140 - 150\text{ MeV}$ , consistent with the Witten-Bodmer hypothesis<sup>38,39</sup>, which is considerably softening the quark *EOS*, allowing also the possibility of the existence of quark stars<sup>40,41</sup>.

The proton fraction  $Z/A$  dependence of the  $\rho_{trans}$  is reported in Fig.4 with the bag constant value  $B^{1/4} = 150\text{ MeV}$  for the quark phase and

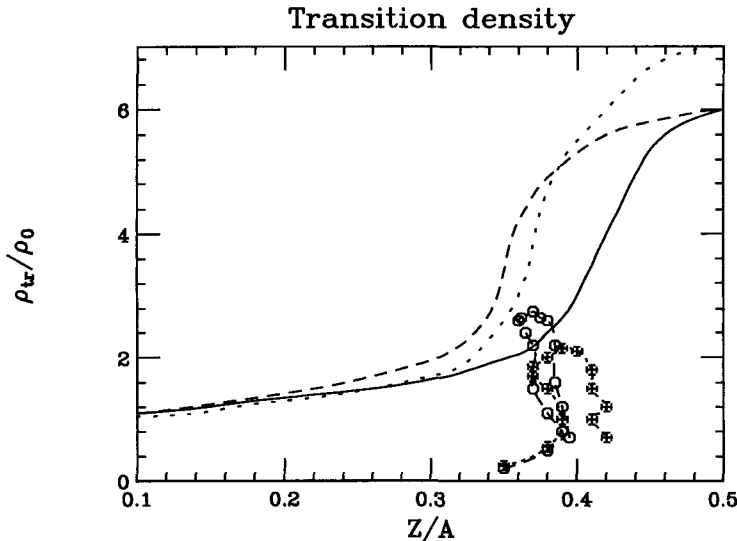


Figure 6. Variation of the transition density with proton fraction for various hadronic *EOS* (see text). The points represent the path followed in the interaction zone during a semi-central  $^{132}Sn + ^{132}Sn$  collision at 1AGeV (circles) and 300AMeV (crosses)

various choices for the hadronic *EOS*: *Dotted line* GM3 parametrization<sup>42</sup>; *Dashed line* NLH $\rho$  parametrization<sup>16</sup>; *Solid line* NLH( $\rho + \delta$ ) parametrization<sup>16</sup>. GM3 and NLH $\rho$  have the same source of the interaction symmetry term (only the  $\rho$ -meson) while NLH( $\rho + \delta$ ) has also the scalar charged meson contribution which gives an almost quadratic increase of the symmetry repulsion with baryon density.

The effects of the asymmetry appears now quite dramatic: we see a  $\rho_{trans}$  as low as  $2\rho_0$  for proton fractions between 0.3 and 0.4, conditions that with some confidence we could "locally" reach in a heavy ion collision at *intermediate* energy using exotic very asymmetric beams.

Using a Relativistic Transport Code, with the same effective interaction of the NLH( $\rho + \delta$ ) *EOS*, we have performed some simulations of the  $^{132}Sn + ^{132}Sn$  (average  $Z/A = 0.38$ ) collision at various energies, for a semicentral impact parameter,  $b = 6fm$ , just to optimize the neutron skin effect in order to get a large asymmetry in the interacting zone. In Fig.6 the paths in the  $(\rho, Z/A)$  plane followed in the c.m. region during the collision are reported, at two energies 300 AMeV (crosses) and 1 AGeV (circles). We see that already at 300 AMeV we are reaching the border of the mixed phase,

and we are well inside it at 1  $AGeV$ . We like to note that the results can be even more favorable just using an harder *EOS* for symmetric Nuclear Matter at high density. This is actually the case of ref.<sup>37</sup> where a smaller effective mass is used with an increase of the isoscalar vector coupling  $f_\omega$ . Now we start from a lower  $\rho_{trans}$  for symmetric matter  $Z/A = 0.5$ , around 4 times  $\rho_0$ .

### *A Softening of the Hadronic EOS?*

Our results seem to support the possibility of observing precursor signals of the phase transition to a deconfined matter in violent collision (central and semicentral) of exotic (radioactive) heavy ions in the energy range of few hundred MeV per nucleon. A possible signature could be revealed through an earlier "softening" of the hadronic *EOS* for larger asymmetries, to see on the behaviour of the collective flows for particles with large transverse momentum.

In order to have an idea of where we are in the hadron sector, in Fig.7 we show our pressure plot ( $NLH(\rho + \delta)$ ) for  $Au$  systems ( $N/Z = 1.49$ ). The area inside the dotted line represents the constraints deduced by Pawel Danielewicz<sup>43</sup> from transverse and elliptic flows. The dashed line is the prediction of the *NL3* parametrization.

The constrained area can be further reduced from transverse momentum selections. A softening of the "EOS" around the baryon densities discussed here appears to be quite realistic.

## 7 Conclusions and Outlook

We have developed a linear response theory starting from a relativistic kinetic equations deduced within a Quantum-Hadro-Dynamics effective field picture of the hadronic phase of nuclear matter. In the asymmetric case we consider as the main dynamical degrees of freedom the nucleon fields coupled to the *isoscalar*, scalar  $\sigma$  and  $\omega$ , and to the *isovector*, scalar  $\delta$  and vector  $\rho$ , mesons.

Using the Landau procedure we derive the dispersion relations which give the sound phase velocity and the internal structure of the normal collective modes, stable and unstable. We have focussed our attention on the effect of the isovector mesons on the collective response of asymmetric (neutron-rich) matter. In order to better understand the dynamical role of the different mesons, the results are obtained in the Hartree approximation, which has a simpler and more transparent form. The contribution of Fock terms is also discussed.

We have singled out some qualitative new effects of the  $\delta$ -meson-like channel on the dynamical response of *ANM*. Essentially, our investigation indi-

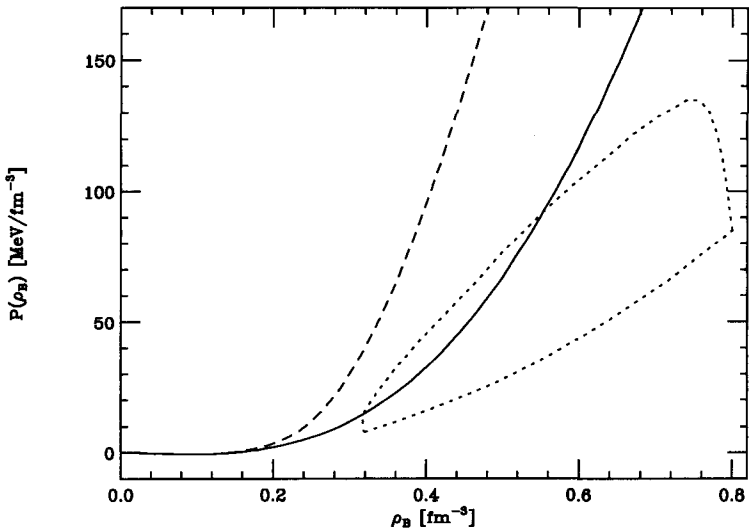


Figure 7. Pressure vs. baryon density for various interactions in the  $Au$  system. Solid line:  $NLH$  ( $\rho + \delta$ ). Dashed line:  $NL3$ . The dotted line limits the "flow constrained" area, see text.

cates that even if the symmetry energy is fixed, the dynamical response is affected by its internal structure, i.e. the presence or not of an isovector-scalar field. This is implemented by the explicit introduction of an effective  $\delta$ -meson and/or by the Fock term contributions. The interest comes from the fact that both mechanisms are absent in the usual relativistic  $RPA$  calculations for finite nuclei.

From the numerical results on the collective response of  $ANM$  some general features are qualitatively present in all the effective interactions in the isovector channel:

- In asymmetric matter we have a mixing of pure isoscalar and pure isovector oscillations which leads to *chemical* effect on the structure of the propagating collective mode: the ratio of the neutron/proton density oscillations  $\delta\rho_n/\delta\rho_p$  is different from the initial  $\rho_n/\rho_p$  of the matter at equilibrium. However we can still classify the nature of the excited collective motions as *isoscalar-like* (when neutron and protons are oscillating in phase) and *isovector-like* (out of phase). To note that similar effects can be obtained also using non-relativistic effective forces <sup>31,35</sup>.

- For a given asymmetry the isovector-like mode is the most robust at low baryon density, always showing a larger neutron component in the oscillations. With increasing baryon density we observe a smooth transition, at a  $\rho_B^{cross} \simeq 2 - 3\rho_0$ , to an isoscalar-like branch, still with a dominant  $\delta\rho_n$ . In the region of the transition we predict a propagation of almost *pure neutron waves*. For relatively large asymmetries ( $\alpha \equiv \frac{N-Z}{N+Z} = 0.5, N = 3Z$ ) this behaviour is present in a wide interval of densities around  $\rho_B^{cross}$ . All that seems to suggest the possibility of an experimental observation of related effects in intermediate energy heavy ion collisions with exotic beams. If the compressibility of nuclear matter is decreasing at high baryon density also these exotic isoscalar-like mode will disappear. This could be a nice signature of the softening of nuclear *EOS* at high densities.

Finally, in connection to the last point, we also suggest the possibility of a such *EOS* softening for asymmetric matter due to an "early" transition to a mixed hadron-quark phase at baryon densities of the order of  $2\rho_0$ , that can be reached in terrestrial labs. during the compression stage of heavy ion collisions at intermediate energies, see also ref. <sup>17</sup>.

### *Acknowledgements*

We warmly thank Hermann H. Wolter, Stephan Typel, Alessandro Drago and Andrea Lavagno for several pleasant and stimulating discussions.

### **References**

1. J.D.Walecka, Ann.Phys. (N.Y.) **83**, 491 (1974).
2. B. D. Serot and J. D. Walecka, in *Advances in Nuclear Physics*, edited by J. W. Negele and E. Vogt ( Plenum, New York, 1986 ) Vol. 16.
3. B. D. Serot and J. D. Walecka, Int. J. Mod. Phys. E **6**, 515 (1997).
4. M.M. Sharma, M.A. Nagarajan and P. Ring, Ann. Phys. (NY) **231**, 110 (1994) ,  
G.A. Lalazissis, M.M. Sharma, P. Ring and Y.K. Gambhir, Nucl. Phys. **A608**, 202 (1996).
5. P. Ring, Prog. Part. Nucl. Phys. **37**, 193 (1996).
6. S. Typel and H.H. Wolter, Nucl. Phys. **A656**, 331 (1999).
7. H.Müller and B.D.Serot, Phys.Rev. **C52**, 2072 (1995).
8. B. Blattel, V. Koch and U. Mosel, Rep. Prog. Phys. **56**, 1 (1993).
9. C.M. Ko and G.Q. Li, J. of Phys. **G22**, 1673 (1996).
10. A. Dellafiore and F. Matera, Phys. Rev. C **44**, 2456 (1991).

11. F. Matera and V. Yu. Denisov, Phys. Rev. C **49**, 2816 (1994).
12. D. Vretenar, G.A. Lalazissis, R. Behnsch, W. Poeschl and P. Ring, Nucl.Phys. **A621**, 853 (1997).
13. Z.Y. Ma , N. Van Giai, H. Toki and M. L'Huillier, Phys. Rev. C **55**, 2385 (1997).
14. Z.Y. Ma , N. Van Giai, A. Wandelt, D. Vretenar and P. Ring, Nucl. Phys. **A686**, 173 (2001) and ref.s there in.
15. C.J. Horowitz and K Wehrberger, Nucl. Phys. **A531** , 665 (1991).
16. B.Liu, V.Greco, V.Baran, M.Colonna and M.Di Toro, Phys.Rev. **C65**, 045201 (2002).
17. A.Drago and A.Lavagno, contribution to these Proceedings. Phys. Lett. **428B**, 1 (1998).
18. J. Boguta and C.E. Price, Nucl. Phys. **A505**, 123 (1989).
19. C.J. Horowitz and B.D. Serot, Nucl.Phys. **A399**, 529 (1983).
20. A. Bouyssy, J.F. Mathiot, Nguyen Van Giai, and S. Marcos, Phys. Rev. C**36**, 380 (1987).
21. V. Greco, F. Matera, M. Colonna, M. Di Toro and G. Fabbri, Phys. Rev. C **63**, 035202 (2001).
22. V.Greco, M.Colonna, M.DiToro, G.Fabbri and F.Matera, Phys.Rev. C**64**, 045203 (2001).
23. S.R.de Groot, W.A. van Lee and Ch.G. van Weert, *Relativistic Kinetic Theory*, North-Holland Amsterdam 1980.
24. R.Hakim, Nuovo Cimento **6**,1 (1978).
25. V.Greco, M.Colonna, M.Di Toro, F.Matera, *Collective Modes of Asymmetric Nuclear Matter in QHD*, arXiv: nucl-th/0205046, sub. Phys.Rev.C
26. G.A.Lalazissis, J.Konig and P.Ring, Phys.Rev. C**55**, 540 (1997).
27. L.D. Landau and E.M. Lifshitz, *Statistical Physics*, Pergamon Press,Oxford 1980, pag. 288.
28. A.A. Abrikosov and I.M. Khalatnikov, Rep. Prog. Phys. **22**, 329 (1959).
29. G. Baym and C. J. Pethick in *The physics of Liquid and Solid Helium* edited by K.H. Bennemann and J.B. Ketterson, Vol 2, (Wiley, New-York, 1978), p.1.
30. C.J. Pethick and D.G. Ravenhall, Ann. Phys. (N.Y.) **183**, 131 (1988).
31. M.Colonna, M.Di Toro and A.B.Larionov
32. V. Baran, M. Colonna,M. Di Toro and A. B. Larionov, Nucl. Phys. **A632**, 287 (1998) .
33. Ch. Fuchs, H. Lenske and H.H. Wolter, Phys. Rev. C**52**, 3043 (1995).
34. We remind that if  $\phi$  field has self-interaction terms instead of  $f_\sigma$  one has to put  $\frac{d\phi}{d\rho_S}$ .

35. V.Baran, M. Colonna, M. DiToro and V.Greco, Phys. Rev. Lett. **86**, 4492 (2001).
36. J.D.Walecka, *Theoretical Nuclear and Subnuclear Physics*, Oxford University Press 1995.
37. H.Mueller, Nucl. Phys. **A618**, 349 (1997).
38. A.R.Bodmer, Phys. Rev. **D4**, 1601 (1971).
39. E.Witten, Phys. Rev. **D30**, 272 (1984).
40. M.Dey, I.Bombaci, J.Dey and B.C.Samanta, Phys. Lett. **B438**, 123 (1998).
41. X.D.Li, I.Bombaci, M.Dey, J.Dey and E.P.J. van der Heuvel, Phys. Rev. Lett. **83**, 3771 (1999).
42. N.K.Glendenning and S.A.Moskowski, Phys. Rev. Lett., **67**, 2414 (1991).
43. P.Danielewicz, Nucl. Phys. **A685**, 368c (2001).

# SEMICLASSICAL DESCRIPTION OF THE QUARK GLUON PLASMA

S.TERRANOVA, A. BONASERA, M.COLONNA

*Laboratorio Nazionale del Sud, Istituto Nazionale di Fisica Nucleare, Via S. Sofia  
44, 95123 Catania, Italy.*  
*E-mail:* bonasera@lns.infn.it

T. MARUYAMA

*Advanced Science Research Center, Japan Atomic Energy Research Institute, Tokai,  
Ibaraki 319-1195, Japan*  
*E-mail:* maru@hadron02.tokai.jaeri.go.jp  
*E-mail:* chiba@hadron31.tokai.jaeri.go.jp

We propose the use of a dynamical model to describe relativistic heavy ion collisions starting from quark degrees of freedom with colors. As a preliminary step, we calculate the equation of state of a system interacting through a Coulomb and a linear term. The Fermionic nature of the system is enforced. An analytical estimate is discussed.

## 1 INTRODUCTION

It is surely one of the most challenging open problems to understand nuclear dynamics starting from the quark-gluon degrees of freedom.<sup>1</sup> This also includes the possibility of understanding the basic free nucleon-nucleon interaction from quark and gluon dynamics. Some kind of solution to this problem is becoming more and more needed with the new experiments done or planned using ultra-relativistic heavy ions (RHIC) at CERN and at RHIC. The search for a quark-gluon plasma (QGP) in such collisions is in fact one of the new and most exciting directions in physics at the border between nuclear and particle physics.<sup>2</sup> Quantum ChromoDynamics (QCD) because of its difficulties (numerical and conceptual), has been applied so far to some limited cases such as quark matter at zero baryon density ( $\rho_B$ ) and high temperature ( $T$ ).<sup>1,2</sup> Furthermore in RHIC dynamics plays surely an important role and accordingly the theory should be dynamical.

Recently,<sup>3</sup> we have proposed a dynamical approach based on Vlasov/molecular dynamics<sup>4,5</sup> to reproduce hadron masses and the properties of nuclear matter at finite  $\rho_B$ . Some works in the same spirit are discussed in Refs.<sup>6,7</sup> Our approach needs as inputs the interaction potential among quarks, which was borrowed from phenomenology i.e. the Richardson's potential<sup>8</sup> and the quark masses which were fitted to reproduce known meson masses such as the  $\pi$ , the  $\phi$ , the  $\eta_c$  etc. When the particles are embedded in a dense medium such as

in nuclear matter (NM) the potential becomes screened in a similar fashion as ions and electrons in condensed matter do, i.e. Debye screening (DS).<sup>2,5</sup> This is explicitly obtained by introducing the color degrees of freedom.

In order to understand some basics properties of the plasma consider a neutral plasma made of several charges  $q_i$  and at average density  $\rho_{q_i 0}$  such that<sup>9,10</sup>:

$$\sum_i q_i \rho_{q_i 0} = 0, \quad (1)$$

where  $i$  denotes the kind of quarks. Note that the charges of quarks obey SU(3) algebra. Thus  $q_i$  is not a scalar quantity but is represented by a vector with 8 components. So is the potential  $\phi$  which we discuss later. It is clear that if the plasma would be homogeneously distributed, because of the neutrality condition, the total field would be exactly zero. However, the plasma rearranges in such a way to have opposite charges distributed around a given charge. Thus such a cloud of quarks will screen the original charge (Debye screening). Because of these correlations among opposite charges the potential energy  $E_{\text{cor}}$  will not be zero and in particular will depend on the density. Clearly, knowing the potential  $\phi$ , we can easily calculate the correlation energy<sup>9</sup>:

$$E_{\text{cor}} = \frac{V}{2} \sum_i q_i \rho_{q_i 0} \phi. \quad (2)$$

$V$  is the volume where the quarks are located and the sum runs over all the quarks. Let us estimate the field in a TF approximation. The Fermi energy for quarks located at a position  $r$  of certain density is:

$$E_F(r) = \sqrt{P_F^2(r) + m^2} + q\phi(r), \quad (3)$$

where  $m$  is the quark mass and  $q$  its charge. Assuming that all kinds of quarks have the same numbers  $\rho_{q_1 0} = \rho_{q_2 0} = \dots$ , the quark density is given by

$$\rho_q = g_q \rho_{q_i}, \quad (4)$$

$$\rho_{q_i} = \frac{1}{6\pi^2} P_F^3(r) = \frac{1}{6\pi^2} E_F^3 \left[ \left( 1 - \frac{q\phi(r)}{E_F} \right)^2 - (m/E_F)^2 \right]^{3/2}, \quad (5)$$

where  $g_q = N_c \times N_f \times N_s$ , i.e. the product of the number of colors, flavors and spin<sup>1,2</sup>. Here we assume  $N_c = 3$ ,  $N_f = N_s = 2$ . The last equality is in a form that can be expanded in the quantity  $q\phi/E_F$  which we assume to be small. Thus

$$\rho_{q_i} \approx \frac{1}{6\pi^2} E_{F0}^3 \left[ \left( 1 - \frac{m^2}{E_{F0}^2} \right)^{3/2} - 3 \left( 1 - \frac{m^2}{E_{F0}^2} \right)^{1/2} \left( \frac{q_i \phi}{E_{F0}} \right) \right], \quad (6)$$

where  $E_{F0}$  is the Fermi energy calculated at large distances where the field  $\phi(r) \rightarrow 0$ , cfr. Eq. (3), and  $\rho_{q0} = \frac{g_q}{6\pi^2} P_{F0}^3$ , i.e. we require that all the  $r$ -dependence is contained in the field and the density reduces to the free one for large distances from a given quark.

Inserting the last equation into the Poisson equation for the field we get:

$$\nabla^2 \phi = - \sum_i q_i \rho_{qi} \approx - \sum_i q_i \frac{1}{6\pi^2} E_{F0}^3 \left[ \left( 1 - \frac{m^2}{E_{F0}^2} \right)^{3/2} - 3 \left( 1 - \frac{m^2}{E_{F0}^2} \right)^{1/2} \left( \frac{q_i \phi}{E_{F0}} \right) \right] \quad (7)$$

Notice that in the last equality the term proportional to odd power of the charge cancel because of the neutrality condition Eq. (1) and the assumption that all the all kinds of quarks have same numbers. Thus the Poisson equation reduces to:

$$\nabla^2 \phi - \chi^2 \phi = 0, \quad (8)$$

where the Debye inverse radius is given by

$$\chi^2 = 3 \frac{g_q q_i^2}{6\pi^2} P_{F0} \sqrt{P_{F0}^2 + m^2}, \quad (9)$$

and  $P_{F0}$  is the Fermi momentum far away from the charge where  $\phi(r) \rightarrow 0$ . The Poisson equation can be solved to give:

$$\phi(r) = \frac{q_i}{4\pi} \frac{e^{-\chi r}}{r}. \quad (10)$$

This is simply the screened Coulomb potential as expected. If we expand the last equation for small  $r$  we get:

$$\phi(r) \approx \frac{q_i}{4\pi} (1/r - \chi + \dots). \quad (11)$$

The omitted terms go to zero for  $r \rightarrow 0$ . The first term is clearly the field created by the quark  $i$  which is surrounded by the quark cloud. The second term is the contribution of the cloud at the point where the  $i$  quark is located. This term is the contribution we are looking for to the correlation energy, Eq. (2). Knowing that  $\frac{q^2}{4\pi} = \frac{2}{3} \alpha_s^2$ , we get:

$$E_{\text{cor}}^{\text{Coul}} = - \frac{V}{2} \frac{2}{3} \sum_i \rho_{q,0} \chi \alpha_s. \quad (12)$$

The field that we have derived so far does not contain the confinement property of the quarks. In fact in the limit of zero density the field reduces to

a Coulomb one. It is an experimental fact that quarks in isolation do not exist. If two quarks are pulled apart the field between them increases approximately linearly with distance. If such a distance is larger than a given value a  $q\bar{q}$  pair is created<sup>2</sup>, which in turn makes some further screening. In order to consider this fact we repeat the above steps which gave the correlation energy in the Coulomb case but in one dimension. Assuming that the linear density is given by

$$\rho_l = (\rho_q)^{1/3}, \quad (13)$$

we can use the expansion as in Eqs. (5,6). Inserting this expansion in the Poisson equation in one dimension gives a linear field:

$$\phi_l = -\frac{q_i}{\chi_l} e^{-\chi_l r}, \quad (14)$$

where  $q^2 = \frac{2}{3}K$  and the string tension  $K \approx 1$  GeV/fm is the analogous of the strong coupling constant in one dimension and the linear Debye inverse radius is given by:

$$\chi_l^2 = \frac{4}{3} \left( \frac{g_q}{6\pi^2} \right)^{1/3} K \frac{\sqrt{P_{F0}^2 + m^2}}{P_{F0}}. \quad (15)$$

Notice the analogy of the linear screening to the Coulomb one, Eq. (9). Expanding the field for small  $r$  gives:

$$\phi_l \approx -\frac{q_i}{\chi_l} (1 - \chi_l r + \dots). \quad (16)$$

The second term is the linear potential created by the charge while the first term is the only surviving in the limit  $r \rightarrow 0$  and gives the contribution to the correlation energy:

$$E_{\text{cor}}^{\text{lin}} = -\frac{V}{2} \frac{2}{3} \sum_i \frac{K}{\chi_l} \rho_{q,i}. \quad (17)$$

From the knowledge of the correlation energies we can obtain the energy per particle :

$$E/A = E_{\text{kin}}/A + E_{\text{cor}}^{\text{Coul}}/A + E_{\text{cor}}^{\text{lin}}/A, \quad (18)$$

where  $A = 3Q$  is the number of baryons. Within the same Fermi gas approximation the kinetic term is given by:

$$E_{\text{kin}}/A = \frac{9 N_f}{2 P_F^3} \left[ \frac{P_F}{8} \sqrt{P_F^2 + m^2} (2P_F^2 + m^2) - \frac{m^4}{8} \ln \frac{P_F + \sqrt{P_F^2 + m^2}}{m} \right] - m_{\text{nucleon}}, \quad (19)$$

where we have subtracted the nucleon mass. In Fig. 1a we plot  $E/A$  versus

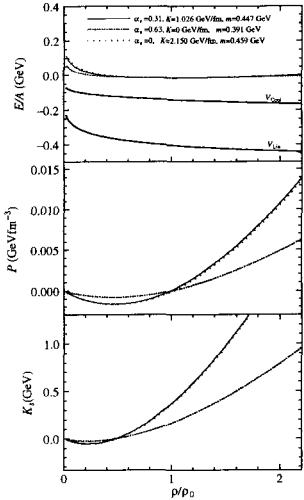


Figure 1: Energy per nucleon (top) and energy density of the quarks (bottom) vs. baryon density.

density. Here we have fixed the quark mass to 447 MeV in order to have a binding energy of roughly  $-16$  MeV at  $0.15 \text{ fm}^{-3}$  density. The parameters entering the potential term are  $K = 1.026 \text{ GeV/fm}$  and  $\alpha_s = 0.31$  (full line)<sup>1,2</sup>. For the same set of parameters we have plotted the linear and Coulomb contribution as well. Notice that the minimum at  $\rho_0$  depends critically on the finite quark mass value. If we decrease the quark mass, the minimum shifts to lower densities until eventually it disappears. It is very easy to verify that in the limit of zero quark mass, equation (18) does not have a minimum. For illustration we have discussed two other cases when the strong coupling constant is zero,  $m = 459 \text{ MeV}$ ,  $K = 2.15 \text{ GeV/fm}$  (dotted line) or the string tension is zero,  $m = 391$  and  $\alpha_s = 0.63$  (dashed line). Even though the three sets of parameters give a similar curve, since we have fitted the energy at  $\rho_0$ , the values of the last two parameter sets are unreasonably large while there is little difference in the quark mass value. Recall that in the constituent quark model the u,d quark masses are 310 MeV when fitting the meson masses and 363 MeV when fitting the baryons<sup>1</sup>. The larger value found here should not surprise in view of the approximations made. Clearly important physics is hidden in the quark masses.

Knowing the energy per particle we can easily calculate the pressure as:

$$P = \rho^2 \frac{\delta E/A}{\delta \rho}, \quad (20)$$

which is displayed in Fig. 1b. Notice that the pressure is negative for all the parameter sets at low densities signaling a liquid gas phase transition. The compressibility

$$K_s = 9 \frac{\rho}{\rho_0} \frac{\delta P}{\delta \rho} \quad (21)$$

is plotted in Fig. 1c. This quantity is negative at low densities and at  $\rho_0$ ,  $K_s \approx 350$  MeV while for the  $K = 0$  GeV/fm case, it is 166 MeV which is a rather small value. Recall that from monopole resonances in nuclei we know that  $K = 250 \sim 300$  MeV<sup>11</sup>.

## 2 THE BALESU LENARD VLASOV EQUATION

The exact (classical) one-body distribution function  $f_1(\mathbf{r}, \mathbf{p}, t)$  satisfies the equation (BBGKY hierarchy):<sup>5</sup>

$$\partial_t f_1 + \frac{\mathbf{p}}{E} \cdot \nabla_r f_1 = \int d^3 r_2 d^3 p_2 \nabla_r V(\mathbf{r}, \mathbf{r}_2) \nabla_p f_2(\mathbf{r}, \mathbf{r}_2, \mathbf{p}, \mathbf{p}_2, t), \quad (22)$$

where  $E = \sqrt{p^2 + m_i^2}$  is the energy and  $m_i = 10$  MeV is the (u,d) quark mass. Here we assume the potential to be dependent on the relative coordinates only. A generalization to include a momentum dependent part is straightforward.  $f_2$  is the two-body distribution function, which in the classical limit reads:

$$f_2(\mathbf{r}, \mathbf{r}_2, \mathbf{p}, \mathbf{p}_2, t) = \sum_{\alpha \neq \beta}^Q \delta(\mathbf{r} - \mathbf{r}_\alpha) \delta(\mathbf{p} - \mathbf{p}_\alpha) \times \delta(\mathbf{r}_2 - \mathbf{r}_\beta) \delta(\mathbf{p}_2 - \mathbf{p}_\beta). \quad (23)$$

where  $Q = q + \bar{q}$  is the total number of quarks and anti quarks . Inserting this equation into Eq. (1) gives:

$$\partial_t f_1 + \frac{\mathbf{p}}{E} \cdot \nabla_r f_1 - \nabla_r U \cdot \nabla_p f_1 = 0, \quad (24)$$

where  $U = \sum_j V(\mathbf{r}, \mathbf{r}_j)$  is the exact potential. Let us now define  $f_1$  and  $U$  as sums of an ensemble averaged quantity plus the deviation from this average:

$$f_1 = \bar{f}_1 + \delta f_1; U = \bar{U} + \delta U. \quad (25)$$

Substituting these equations in Eq. (3) and ensemble averaging gives:

$$\partial_t \bar{f}_1 + \frac{\mathbf{P}}{E} \cdot \nabla_r \bar{f}_1 - \nabla_r \bar{U} \cdot \nabla_p \bar{f}_1 = \langle \nabla_r \delta U \nabla_p \delta f_1 \rangle, \quad (26)$$

where one recognizes in the lhs the Vlasov term and in the rhs the Balescu-Lenard collision term.<sup>5,12,13</sup> The mean-field is given by:

$$\bar{U}(\mathbf{r}) = \frac{1}{N_{\text{ev}}} \sum_{\text{ev}} \sum_j V(\mathbf{r}, \mathbf{r}_j). \quad (27)$$

In agreement to LQCD calculations<sup>1,8</sup> the interacting potential  $V(\mathbf{r})$  for quarks is ( $\hbar = 1$ ):

$$V(\mathbf{r}_{ij}) = 3 \sum_{a=1}^8 \frac{\lambda_i^a}{2} \frac{\lambda_j^a}{2} \left[ \frac{8\pi}{33 - 2n_f} \Lambda (\Lambda r_{ij} - \frac{f(\Lambda r_{ij})}{\Lambda r_{ij}}) + \frac{8\pi}{9} \bar{\alpha} \frac{\langle \sigma_q \sigma_{\bar{q}} \rangle}{m_q m_{\bar{q}}} \delta(\mathbf{r}_{ij}) \right] \quad (28)$$

and<sup>8</sup>

$$f(t) = 1 - 4 \int \frac{dq}{q} \frac{e^{-qt}}{[ln(q^2 - 1)]^2 + \pi^2}. \quad (29)$$

We fix the number of flavors  $n_f = 2$  and the parameter  $\Lambda = 0.25$  GeV. In Eq. (28) we have added to the Richardson's potential the chromomagnetic term (ct), very important to reproduce the masses of the hadrons in vacuum. Since in this work we will be dealing with infinite matter, the ct can be neglected, we only notice that with the parameters choice discussed here, the hadron masses can be reproduced by suitably tuning the ct term.<sup>3</sup>

The  $\lambda^a$  are the Gell-Mann matrices. From lattice calculations we expect that there is no color transport for distances of the order of  $0.2 \sim 0.3$  fm, which are distances much shorter than the ones we will be dealing with in this paper. Thus we will use the  $\lambda_{3,8}$  only commuting diagonal Gell-Mann matrices (Abelian approximation).<sup>7</sup>

Numerically the BLV equation (5) is solved by using the test particles(tp) method<sup>4</sup>. Also, in order to preserve the Fermionic nature of the system, the occupation density is constrained to be less than one at all times<sup>14</sup>.

Here we discuss results on infinite matter by putting the quarks in a box with periodic boundary conditions. For this reason we use a cutoff on the potential at 3fm, i.e. for larger quarks distances the potential (and force) is zero. Infact we should have already from Debye screening that the potential becomes at short range. However the cutoff is imposed to avoid numerical fluctuation especially when using a small number of quarks and/or events (see

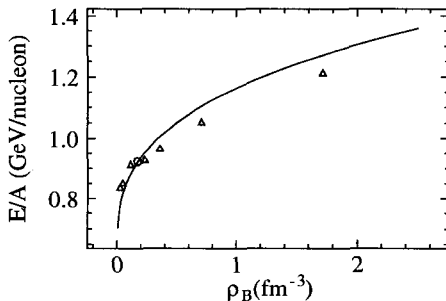


Figure 2: Energy per nucleon vs. baryon density.

below). Initially, we distribute randomly the tp in a box of side  $L$  in coordinate space and  $p_f$  in momentum space.  $p_f$  is the Fermi momentum estimated in a simple Fermi gas model by imposing that a cell in phase space of size  $h = 2\pi$  can accommodate at most two identical quarks of different spins, flavors and colors. In Fig. 2, we plot the total energy per nucleon vs. baryon density. In these preliminary calculations the linear term is turned off and the quarks masses ( $u,d$ ) are taken equal to 5 MeV. The numerical results (triangles) have been shifted up to the gs of infinite nuclear matter (circle). We could obtain a similar result using a larger quark mass. The analytical estimate based on eq(19) is also given (full line). The qualitative behavior is similar. We notice that for such small quark masses no minimum in energy is found.

### 3 Summary

In conclusion in this work we have discussed microscopic Vlasov/MD approaches to infinite matter at finite baryon density and zero temperature starting from quark degrees of freedom with colors. In order to fulfill the Pauli

principle a constraint has been enforced on the average one body distribution. Calculations including the linear term are in progress. We plan to use these results as the initial conditions for the nucleus ground state to simulate heavy ion collisions at ultra-relativistic energies with the Balescu Lenard collision term. The mean field and the collision term are calculated starting from the same elementary interactions. Collisions are connected to deviations from the average mean field. This gives also large fluctuations in the distribution function which results in new particles creation. Our approach can be very useful for the understanding of the quark gluon plasma formation and its signatures.

1. B. Povh, K. Rith, C. Scholz, F. Zetsche, *Particles and Nuclei: an introduction to the physical concepts*, Springer, Berlin, 1995.
2. C.Y. Wong, *Introduction to High-Energy Heavy ion Collisions*, World Scientific Co., Singapore,1994; L.P. Csernai *Introduction to Relativistic Heavy ion Collisions*, John Wiley and Sons, New York, 1994.
3. A. Bonasera nucl-th/9905025, nucl-th/9908036, Phys. Rev. C **60** (1999) 65212, Phys. Rev. C **62** (2000) 52202(R) and Nucl. Phys. A **681** (2000) 64c.
4. A. Bonasera, F. Gulminelli and J. Molitoris, Phys. Rep. **243** (1994) 1; G. Bertsch, S. Das Gupta, Phys. Rep. **160** (1988) 189; and references therein.
5. E.M. Lifshitz and L.P. Pitaevskii, *Physical Kinetics*, Pergamon Press 1991.
6. T. Vetter, T. Biro and U. Mosel, Nucl. Phys. A **581** (1995) 598; S. Loh, T. Biro, U. Mosel and M. Thoma, Phys. Lett. **B387** (1996) 685; S. Loh, C. Greiner, U. Mosel and M. Thoma, Nucl. Phys. A **619** (1997) 321; S. Loh, C. Greiner and U. Mosel, Phys. Lett. **B404** (1997) 238; C.T. Traxler, U. Mosel and T.S. Biro Phys. Rev. C **59** (1999) 1620.
7. M. Hofmann et al., Phys.Lett.**B478**(2000)161; T.Maruyama and T.Hatsuda Phys.Rev.**C61**(2000)062201(R).
8. J.L. Richardson, Phys. Lett. **B82** (1979) 272.
9. L. Landau and E. Lifshits, *Statistical Physics*, Pergamon, New York, 1980.
10. S.Terranova et al., submitted for publication.
11. P. Ring, P. Schuck, *The Nuclear Many-Body Problem*,Springer-Verlag, New York, 1980.
12. M. Belkacem, V. Latora and A. Bonasera, Phys. Lett. **B326** (1994)21.
13. D. F. Litim and C. Manuel, Phys. Rev. Lett. **82** (1999) 4981.
14. A. Bonasera, T. Maruyama, M. Papa, S. Chiba, arXiv:nucl-th/0110068; M. Papa, T. Maruyama and A. Bonasera, Phys. Rev. C **64** (2001) 024612.

# THE RELEVANCE OF THE DECONFINED PHASE FOR THE MASS OF NEUTRON STARS

M. BALDO

*Istituto Nazionale di Fisica Nucleare, Corso Italia 57, 95129 Catania*

The microscopic many-body theory of the Nuclear Equation of State is discussed in the framework of the Bethe-Brueckner-Goldstone method. The expansion is extended up to the three hole-line diagrams contribution. In order to study neutron stars static properties, the theory is extended to include strangeness, and the possible quark-gluon plasma component is described in the simplified MIT bag model. The results for the mass and radius of neutron stars are discussed. It is shown that the value of the neutron star maximum mass can be used as a direct test of the quark-gluon plasma Equation of State.

## 1 Introduction

It is commonly believed that macroscopic portions of (asymmetric) nuclear matter form the interior bulk part of neutron stars ( NS ), usually associated with pulsars. The internal structure of NS is therefore directly linked to the Equation of State (EOS) of infinite nuclear matter. An accurate prediction of the EOS is highly demanded for most studies of neutron stars and related astrophysical applications. Only indirect observations of NS structure are possible, but the astrophysics of neutron stars is rapidly developing, thanks to the observations coming from the new generation of artificial satellites. Then one can expect that it will be possible in the near future to confront the theoretical predictions with more and more stringent phenomenological data. At the hadron level, the main difficulty in the many-body theory of nuclear matter is the treatment of the strong repulsive core, which dominates the short range behaviour of the nucleon-nucleon (NN) interaction. One way of overcoming this difficulty is to introduce the two-body scattering G-matrix, which has a much smoother behaviour even for large repulsive core. It is possible to rearrange the perturbation expansion in terms of the reaction G-matrix, in place of the original bare NN interaction, and this procedure is systematically exploited in the Bethe-Brueckner-Goldstone (BBG) expansion<sup>1</sup>. In this work we present the latest results on the nuclear EOS based on BBG expansion and their extension to strange matter. In order to study the structure of neutron stars, quark matter is included in the framework of the MIT bag model. Predictions for the mass-radius relationship and the corresponding maximum mass are discussed and the relevance of the quark-gluon EOS is stressed.

## 2 The BBG expansion and the nuclear EOS

The BBG expansion for the ground state energy at a given density, i.e. the EOS at zero temperature, can be ordered according to the number of independent hole-lines appearing in the diagrams representing the different terms of the expansion. This grouping of diagrams generates the so-called hole-line expansion <sup>2</sup>. The diagrams with a given number  $n$  of hole-lines are expected to describe the main contribution to the  $n$ -particle correlations in the system. At the two hole-line level of approximation the corresponding summation of the ladder diagrams produces the Brueckner-Hartree-Fock (BHF) approximation, which incorporates the two particle correlations. The BHF approximation includes the self-consistent procedure of determining the single particle auxiliary potential, which is an essential ingredient of the method. Once the auxiliary self-consistent potential is introduced, the expansion is implemented by introducing the set of diagrams which include “potential insertions”. The summation of the ladder diagrams can be performed by solving the integral equation for the Brueckner G-matrix

$$\begin{aligned} \langle k_1 k_2 | G(\omega) | k_3 k_4 \rangle = & \langle k_1 k_2 | v | k_3 k_4 \rangle + \\ & + \sum_{k'_3 k'_4} \langle k_1 k_2 | v | k'_3 k'_4 \rangle \frac{(1 - \Theta_F(k'_3))(1 - \Theta_F(k'_4))}{\omega - e_{k'_3} - e_{k'_4}} \langle k'_3 k'_4 | G(\omega) | k_3 k_4 \rangle \end{aligned} \quad (1)$$

where  $\Theta_F(k) = 1$  for  $k < k_F$  and is zero otherwise, being  $k_F$  the Fermi momentum. The product  $Q(k, k') = (1 - \Theta_F(k))(1 - \Theta_F(k'))$ , appearing in the kernel of Eq. (1), enforces the scattered momenta to lie outside the Fermi sphere, and it is commonly referred as the “Pauli operator”. This G-matrix can be viewed as the in-medium scattering matrix between two nucleons. Indeed in the BBG expansion the original bare NN interaction is replaced by the G-matrix in all higher order terms. The effect of three-body correlations can be calculated by considering the three hole-line diagrams. They can be summed up by introducing a similar generalization of the scattering matrix for three particles. The three-body scattering problem for free particles has received a formal solution by Fadeev <sup>3</sup>. For identical particles the original three integral Fadeev equations reduce to one, because of symmetry. The analogous equation and scattering matrix in the case of nuclear matter has been introduced by Bethe <sup>4</sup>. The integral equation, the Bethe-Fadeev equation, reads

schematically

$$\begin{aligned}
 T^{(3)} &= G + G X \frac{Q_3}{e} T^{(3)} \\
 \langle k_1 k_2 k_3 | T^{(3)} | k'_1 k'_2 k'_3 \rangle &= \langle k_1 k_2 | G | k'_1 k'_2 \rangle \delta_K(k_3 - k'_3) + \\
 &\quad + \langle k_1 k_2 k_3 | G_{12} X \frac{Q_3}{e} T^{(3)} | k'_1 k'_2 k'_3 \rangle .
 \end{aligned} \tag{2}$$

The kernel contains the two-body scattering matrix  $G$  in place of the bare NN interaction, in line with the BBG scheme. The factor  $Q_3/e$  is the analogous of the similar factor appearing in the integral equation for the two-body scattering matrix  $G$ , see Eq. (1). Therefore, the projection operator  $Q_3$  imposes that all the three particle states lie above the Fermi energy, and the denominator  $e$  is the appropriate energy denominator, namely the energy of the three-particle intermediate state minus the entry energy  $\omega$ , in close analogy with Eq. (1). The real novelty with respect to the two-body case is the operator  $X$ . This operator interchanges particle 3 with particle 1 and with particle 2,  $X = P_{123} + P_{132}$ , where  $P$  indicates the operation of cyclic permutation of its indices. The reason for the appearance of the operator  $X$  is that no two successive  $G$  matrices can be present in the same pair of particle lines, since the  $G$  matrix already sums up all the two-body ladder processes. Higher order correlations can be introduced with the help of higher many-body scattering matrix, but we will see that this is not necessary. The results at the BHF level of approximation is reported in Fig. 1 in the case of symmetric nuclear matter (solid lines). The two EOS correspond to two different choices of the auxiliary potential, the standard and continuous choices. As one can see, the saturation curves are different for the two prescriptions. However, the apparent discrepancy of 4-5 MeV in the binding energies shown Fig. 1, is about 10% of the calculated potential energy per particle, which is about -40 MeV around saturation. This is the degree of convergence obtained at the Brueckner level. In view of these results it appears mandatory to consider the three hole-line diagrams. The value of their contribution can indeed provide a check of convergence and possibly an accurate EOS. The final EOS obtained by adding the three hole-line contribution is reported in Fig. 1, both for the gap choice (squares) and the continuous choice (stars). Two conclusions can be drawn from these results. i) The two saturation curves in the standard and continuous choices, with the inclusion of the three hole-line diagrams, tend now to collapse in a single EOS. This is a strong indication that a high degree of convergence has been reached. The saturation curves extend from low density to about five times saturation density, and it appears unlikely that the agreement between the two choices can be a fortuitous coincidence.

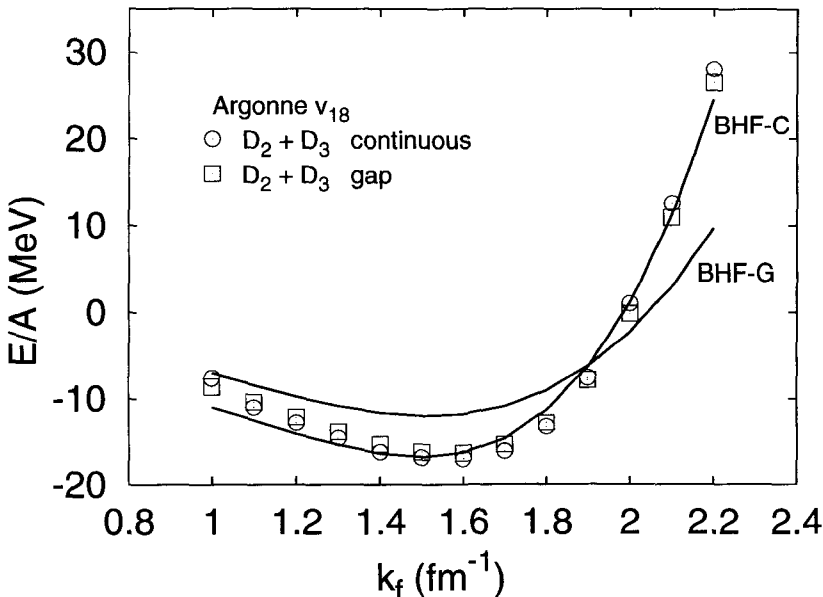


Figure 1. Nuclear matter saturation curve for the Argonne  $v_{18}$  NN potential. The solid lines indicate the results at the Brueckner (two hole-lines) level for the standard (BHF-G) and the continuous choices (BHF-C) respectively. The results obtained adding the three hole-line contribution are marked by the open squares (standard choice) and the open circles (continuous choice).

ii) The Brueckner EOS within the continuous choice turns out to be already close to the full EOS, i.e. in this case the three hole-line contribution is quite small. In first approximation one can adopt the BHF results with the continuous choice as the nuclear matter EOS. Indeed, this is a further indication of convergence. The phenomenological saturation point for symmetric nuclear matter is, however, not reproduced, which confirms the finding in ref. <sup>5</sup>. Usually this drawback is corrected by introducing three-body forces.

### 3 Neutron stars and the nuclear EOS

The study of neutron star interior requires a detailed knowledge of the EOS for densities much larger than saturation  $\rho_0$ . Whereas at densities  $\rho \approx \rho_0$  the matter consists mainly of nucleons and leptons, at higher densities sev-

eral species of particles may appear. Among these new particles are strange baryons, namely, the  $\Lambda$ ,  $\Sigma$  and  $\Xi$  hyperons. It is therefore mandatory to generalize the study of nuclear EOS with the inclusion of the possible hadrons, other than nucleons. Besides all that, a quark-gluon plasma can certainly appear at the center of massive NS. The possible appearance of the deconfined phase in the interior of NS poses a difficult theoretical challenge, but it also opens a window on the quark EOS, which can come from the comparison of theoretical predictions and phenomenological data on NS. We have extended the BHF procedure by including the possibility of hyperon formation<sup>6</sup> and ultimately also the presence of quark-gluon plasma component<sup>7</sup>. For the latter we used the simplified MIT bag model<sup>7</sup>. If the quark phase is allowed, a “mixed phase” will be in general present in some density region of the neutron star matter EOS. This is apparent in Fig. 2, where the mixed phase is indicated by the full dots. Above this area the matter is in the deconfined

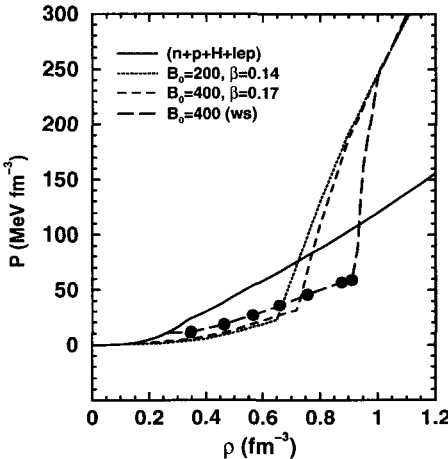


Figure 2. Neutron star matter EOS for different bag constant parametrizations. The full dots indicate the interval where the mixed phase is present (for a specific parametrization only). For detail see the text. The full line corresponds to the EOS with no quark phase.

phase, while below the area the matter is in the purely hadronic phase. The density dependent bag constant has been fixed in such a way that for symmetric nuclear matter the phase transition region is around a value of the energy density of about seven times the value at saturation. This value is taken near the value indicated by the CERN experiment<sup>8</sup>. Once the EOS is established, the NS density profile and corresponding mass and radius can be determined by solving the Tolman-Volkoff-Oppenheimer equations. The results for the

NS masses as a function of central density are summarized in Fig. 3. One

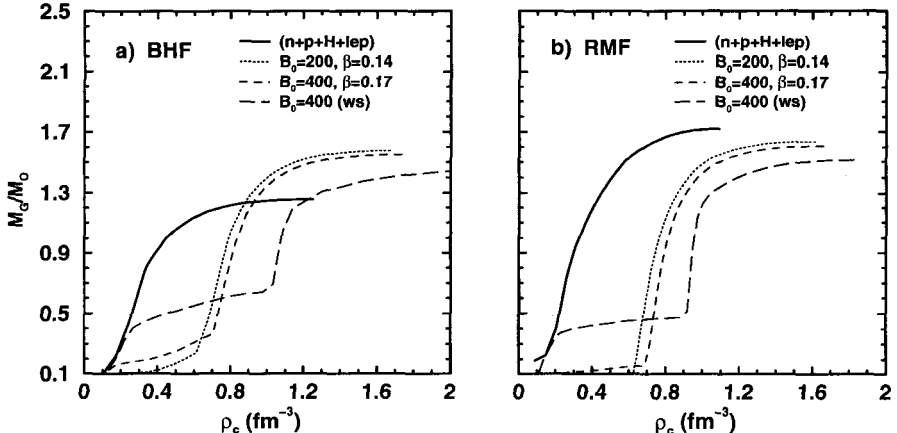


Figure 3. Neutron star mass as a function of the central baryon density for different parametrizations of the MIT bag model for the quark matter EOS.

can see (left panel) that the maximum mass is nearly independent on the parametrization of the bag constant and it is around 1.5-1.6 solar masses. For comparison on the right panel the results are reported for an hadron EOS based on relativistic mean field with the same value of the compressibility and symmetry energy at saturation. The maximum mass is very close to the one obtained with microscopic calculations. The density profiles for the different phases of nuclear matter are reported in Fig. 4 for a mass  $M = 1.4$  solar masses. One can see that a large fraction of the NS is in the quark phase, and this is the reason why the results for the mass are mainly determined by the quark EOS. This means that the maximum mass is a good test for the quark EOS. In particular a softer quark EOS is expected to produce a smaller maximum mass, possibly below the observational limit of 1.44 solar masses. On the contrary, a stiffer quark EOS would produce a larger maximum mass with even a larger region of quark phase inside the NS. Therefore, in any case the quark EOS dominates the bulk properties of NS.

## References

1. For a pedagogical introduction, see *Nuclear Methods and the Nuclear Equation of State*, Edited by M. Baldo, World Scientific, Singapore, International Review of Nuclear Physics Vol. 9, 1999.

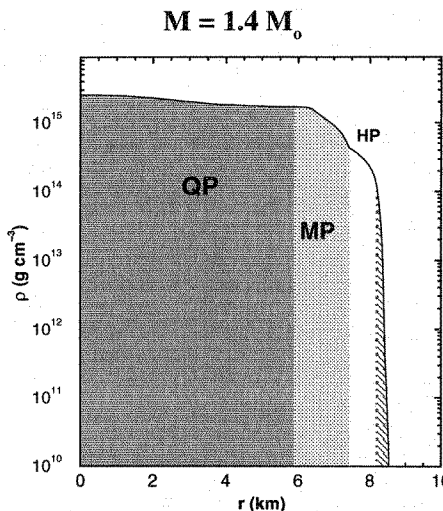


Figure 4. Energy density profiles for the different components of the inner part of a neutron star. Quark, mixed and pure hadronic phases are labelled QP, MP and HP, respectively. The thin shaded area indicates the crust region.

2. B.D. Day, *Brueckner-Bethe Calculations of Nuclear Matter*, Proceedings of the School E. Fermi, Varenna 1981, Course LXXIX, ed. A. Molinari, (Editrice Compositori, Bologna, 1983), p. 1-72; *Rev. Mod. Phys.* **39**, 719 (1967)
3. L.D. Faddeev, *Mathematical Aspects of the Three-Body Problem in Quantum Scattering Theory*, Davey, New York 1965.
4. R. Rajaraman and H. Bethe, *Rev. Mod. Phys.* **39**, 745 (1967).
5. B.D. Day *Phys. Rev.* **C24**, 1203 (1981); *Phys. Rev. Lett.* **47**, 226 (1981).
6. M. Baldo, G.F. Burgio and H.-J. Schulze, *Phys. Rev.* **C61**, 055801 (2000).
7. G.F. Burgio, M. Baldo, P.K. Sahu, A.B. Santra and H.-J. Schulze, *Phys. Lett.* **B526**, 19 (2002).
8. A. Chodos, R. L. Jaffe, K. Johnson, C. B. Thorn and V. F. Weisskopf, *Phys. Rev.* **D9**, 3471 (1974).
9. U. Heinz and M. Jacobs, *nucl-th/0002042*; U. Heinz, *hep-ph/0009170*.

# MIXED QUARK–HADRON PHASE IN NEUTRON-RICH MATTER

ALESSANDRO DRAGO

*Dip. di Fisica, Università di Ferrara and INFN, Sezione di Ferrara,  
44100 Ferrara, Italy*

ANDREA LAVAGNO

*Dip. di Fisica, Politecnico di Torino and INFN, Sezione di Torino,  
10100 Torino, Italy*

We explore the dependence of the critical density, separating hadronic matter from a mixed phase of quarks and hadrons, on the ratio  $Z/A$ . We use both the MIT bag model and the Color Dielectric Model to describe the quark dynamics, while for the hadronic phase we employ various relativistic equations of state. We find that, if the parameters of quark models are fixed so that the existence of quark stars is allowed, then the critical density drops dramatically in the range  $Z/A \sim 0.3\text{--}0.4$ . Moreover, for  $Z/A \sim 0.3$  the critical density is only slightly larger than the saturation density of symmetric nuclear-matter. This open the possibility to verify Witten-Bodmer hypothesis on absolute stability of quark matter using ground-based experiments in which neutron-rich nuclei are tested.

## 1 Introduction

Recently several analysis of observational data have emphasized the possible existence of compact stars having very small radii, of the order of 9 kilometers or less<sup>1,2</sup>. The most widely discussed possibility to explain the observed mass-radius relation is based on the existence of quark stars. Such compact objects consists of an approximately equal number of up, down and strange quarks having energy per baryon  $E/A$  smaller than that of iron ( $E_{Fe} \approx 930$  MeV), at zero temperature and pressure<sup>3</sup>. The existence of such an ultra-stable state of matter was postulated many years ago by Bodmer<sup>4</sup> and Witten<sup>5</sup>. Stars entirely composed of quark matter are self-bound<sup>6,7,8</sup> and can rotate with a period well below one millisecond<sup>9,10</sup>.

To satisfy the Witten-Bodmer hypothesis, strong constraints on quark model parameters have to be imposed. For instance, working with the MIT bag model, the so-called pressure-of-the-vacuum parameter  $B$  must have a very small value,  $B^{1/4} \sim 140\text{--}150$  MeV. In the following we assume the validity of Witten-Bodmer hypothesis and we explore possible signatures in ground experiments.

Assuming Witten-Bodmer hypothesis to be true, ordinary nuclear matter

would be metastable. In order not to contradict the obvious stability of normal nuclei, quark matter made of only two flavors must not be more stable than iron. As we shall see, slightly more strict boundaries on parameters' value can be imposed by requiring not only iron, but also neutron rich nuclei like e.g. lead, to be stable.

The critical density, separating nucleonic matter from a mixed-phase of quarks and nucleons, strongly depends on the  $Z/A$  ratio. For symmetric nuclear matter, having  $Z/A \sim 0.5$ , the critical density must be considerably larger than nuclear matter saturation density  $\rho_0$ . A critical density for symmetric nuclear matter of the order of several times  $\rho_0$  is also suggested by experiments with ultra-relativistic heavy ions. Concerning non-symmetric matter, general arguments based on Pauli principle suggest that the critical density decreases with  $Z/A$ . In the present contribution we will assume Witten-Bodmer hypothesis to be true and we will explore the consequences of this assumption on critical densities for strongly asymmetric matter. We want to study in particular the range  $Z/A \sim 0.3\text{--}0.4$ , which can be explored in radioactive nuclear beam facilities<sup>11</sup>.

## 2 Deconfinement critical density: models and results

The scenario we are going to explore corresponds to the situation realized in experiments at moderate energy, in which the temperature of the system is at maximum of the order of few tens MeV. In this situation, strange quarks cannot be produced and we need only to study the deconfinement transition from nucleonic matter into up and down quark matter. The phase transition is then described by imposing Gibbs equilibrium conditions<sup>12</sup>.

In our analysis we have explored various hadronic and quark models. Concerning the hadronic phase, we have used the relativistic non-linear Walecka-type models of Glendenning-Moszkowski (GM1, GM2, GM3)<sup>13</sup>. For the quark phase we have considered the MIT bag model at first order in the strong coupling constant  $\alpha_s$ <sup>3</sup> and the Color Dielectric Model (CDM)<sup>14,15</sup>. In the latter, quarks develop a density dependent constituent mass through their interaction with a scalar field representing a multi-gluon state.

In Fig. 1 we show the critical density  $\rho_{cr}$  separating nuclear matter from quark-nucleon mixed phase, as a function of the proton fraction  $Z/A$ . The figure has been obtained using three versions of the Glendenning-Moszkowski model for the hadronic phase<sup>13</sup> and the MIT bag model without gluons ( $\alpha_s = 0$ ). The most striking feature of the three figures is the sharp decrease of  $\rho_{cr}$  in the range  $Z/A \sim 0.3\text{--}0.4$ . The lower curves in each figure corresponds to parameters' values satisfying Witten-Bodmer hypothesis. In this latter

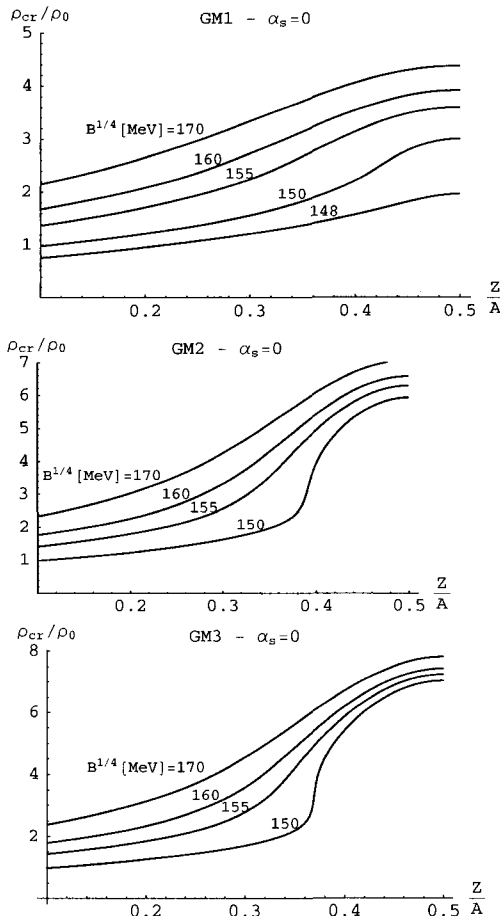


Figure 1. Critical density  $\rho_{cr}$  separating nuclear matter from quark-nucleon mixed phase, as a function of the proton fraction  $Z/A$ . Results obtained in the MIT bag model, with  $\alpha_s = 0$  and various values of the bag parameter  $B$ . GM1, GM2 and GM3 are three versions of the Glendenning-Moszkowski hadronic model.

case, and for  $Z/A \sim 0.3$ , the critical density is of the order of  $\rho_0$ . This opens the possibility to test the deconfinement transition in low energy experiments, such as the one performed in future RNB facilities.

The main features of Fig. 1 can be easily understood if one recalls that we are investigating situations in which the minimum of pure quark matter EOS is at an energy just above or just below the minimum of the hadronic matter EOS. The first scenario is the one in which the absolute minimum, for a given value of  $Z/A$ , corresponds to the quark matter EOS (this situation corresponds to very small values of the parameter  $B$ ). In this case, the deconfinement transition starts at very small densities, smaller than nuclear matter saturation density. The numerical determination of these densities is rather delicate and we limit ourself to indicate with vertical arrows in Fig. 1 the behavior of the critical density for a given value of  $B$ . If the value of  $B$  is further reduced, the vertical arrow shifts toward larger values of  $Z/A$  and therefore cannot correspond to a physically acceptable situation, since it would imply deconfinement at low densities even for almost symmetric nuclei. In particular we can exclude parameters' values for which the dramatic drop in the critical density takes place for  $Z/A \geq 0.4$ . In this way we define a *minimal* value of, e.g., parameter  $B$  of the MIT bag model.

The second situation is the one in which the minimum of the quark EOS lies slightly above the hadronic minimum. In this situation the deconfinement transition starts at a density slightly smaller than the one corresponding to the minimum of the quark EOS. The reason why the critical density cannot be further reduced is due to the fact that at even smaller densities the energy per particle in the quark phase rises dramatically both in the MIT bag model and in the CDM and therefore no mixing of the hadronic matter with the quark matter is possible at those densities. It is also important to notice that both in the MIT and in the CDM model, the position of the minimum of the energy per particle is near the value of nuclear matter saturation density when the energy of the minimum is near to the one obtained from the hadronic EOS<sup>16</sup>.

### 3 Discussion and conclusions

Concerning the practical feasibility of such experiments, the most promising nuclei are the ones near the r-process path, in particular for neutron numbers near the magic values  $N=82$  or  $126$ . In these regions, the proton fraction is as low as  $0.32\text{--}0.33$  and these nuclei could be studied in future experiments with neutron-rich beams.

Since the neutron-rich nuclei are presumably halo nuclei in which neutrons occupy an extended area around the core of the nucleus, the density of the neutron-rich area is very low, considerably lower than  $\rho_0$ . We cannot therefore expect to find a direct signal of deconfinement, but we can look for precursor

signals. In particular, we can expect that the formation of clusters containing six or nine quarks will be enhanced in proximity of the critical density. We can conceive at least two ways to detect this "anomalous" behavior of nucleons.

The first possibility is based on the measure of nuclear radii and neutron skins. It has been shown in Ref.<sup>17</sup> that a systematic experimental study of heavy unstable nuclei would enable us to determine the equation of state of asymmetric nuclear matter. A signal of deconfinement would correspond to an anomalous behavior of the extracted equation of state, as a function of  $Z/A$ . In particular, the enhanced formation of clusters of six or nine quarks would deeply modify three-body forces which are crucial in the calculation of the equation of state.

The second possibility is based on an analysis of the pre-equilibrium decay in heavy-ion collisions discussed in the review paper by Li, Ko and Bauer<sup>18</sup>. In particular, if peripheral scattering of two neutron rich nuclei is considered, very low values of  $Z/A$  can be dynamically tested. It has been shown that the ratio of pre-equilibrium neutrons to protons is essentially independent on the compressibility. By converse, the symmetry potential tends to make more neutrons than protons unbound. Moreover it makes neutrons more energetic than protons. It is relevant to notice that, to study the weak symmetry potential, relatively low beam energies are suited. Beam energies of the order of the Fermi energy or slightly larger should be the most appropriate<sup>19</sup>. A precursor deconfinement signal would appear again as an anomalous dependence of the symmetry energy on the proton fraction.

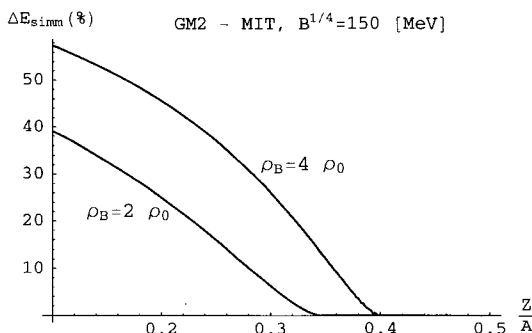


Figure 2. Symmetry energy deviation from hadronic matter at fixed hadronic density  $\rho_B$ .

Before concluding, let us clarify better what we do expect as an "anoma-

lous" behavior for the symmetry energy. In normal nucleonic matter the symmetry energy is well described by a quadratic expression as in

$$E_{sym} = a_{sym} \frac{(N - Z)^2}{A}. \quad (1)$$

In the presence of a phase transition, the energy is non-analytical at the critical density. The appearance of new degrees of freedom in the mixed phase reduces the energy of the system and therefore also  $E_{sym}$ . In Fig.2 we plot our evaluation of the symmetry energy deviation from hadronic matter at fixed hadronic density. A rather sudden deviation of  $E_{sym}$  from the quadratic expression (1) would therefore be a possible signal of deconfinement.

## References

1. X.D.Li et al., *Phys. Rev. Lett.* **83**, 3771 (1999).
2. M.Dey et al., *Phys. Lett. B* **438**, 123 (1998).
3. E. Farhi and R.L. Jaffe, *Phys. Rev. D* **30**, 2379 (1984).
4. A.R.Bodmer, *Phys. Rev. D* **4**, 1601 (1971).
5. E.Witten, *Phys. Rev. D* **30**, 272 (1984).
6. C. Alcock, E. Fahri, A. Olinto, *ApJ.* **310** 261 (1986).
7. P. Haensel, J.L. Zdunik, R. Schaeffer, *Astron. Astrophys.* **160**, 121 (1986).
8. A. Drago, A. Lavagno, *Phys. Lett. B* **511**, 229 (2001).
9. N.K. Glendenning, *Mod. Phys. Lett. A* **5**, 2197 (1990).
10. J. Madsen, *Phys. Rev. Lett.* **81** 3311 (1998); *Phys. Rev. Lett.* **85**, 10 (2000).
11. SPES Project Study, L.N.L. INFN (REP) 145/99.
12. N.K. Glendenning, *Phys. Rev. D* **46** 1274 (1992).
13. N.K.Glendenning and S.A.Moskowski, *Phys. Rev. Lett.* **67**, 2414 (1991).
14. H.J. Pirner, *Prog. Part. Nucl. Phys.* **29**, 33 (1992).
15. M.C. Birse, *Prog. Part. Nucl. Phys.* **25**, 1 (1990); J.A. McGoven, *Nucl. Phys. A* **533**, 553 (1991).
16. A. Drago, M. Fiolhais, U. Tambini, *Nucl. Phys. A* **588**, 801 (1995).
17. K. Oyamatsu et al., *Nucl. Phys. A* **634**, 3 (1998).
18. B.-A. Li, C.M. Ko, W. Bauer, *Int. J. Mod. Phys. E* **7**, 147 (1998).
19. B.-A. Li, C.M. Ko, *Phys. Rev. C* **57**, 2065 (1998).

# SPIN-POLARIZED STATES OF NUCLEAR MATTER

W. ZUO, U. LOMBARDO AND C. W. SHEN

*INFN-LNS, 44 Via S. Sofia, I-95123 Catania, Italy*

*Institute of Modern Physics, Lanzhou, China*

*Dipartimento di Fisica, 57 Corso Italia, I-95129 Catania, Italy*

*E-mail: umberto.lombardo@catania.infn.it*

The equations of state of spin-polarized nuclear matter and pure neutron matter are studied in the framework of the Brueckner-Hartree-Fock theory including a three-body force. The energy per nucleon  $E_A(\delta)$  calculated in the full range of spin polarization  $\delta = (\rho_\uparrow - \rho_\downarrow)/\rho$  for symmetric nuclear matter and pure neutron matter fulfills a parabolic law. In both cases the spin-symmetry energy is calculated as a function of the baryonic density along with the related quantities such as the magnetic susceptibility and the Landau parameter  $G_0$ . The main effect of the three-body force is to strongly reduce the degenerate Fermi gas magnetic susceptibility even more than the value with only two body force. The EOS is monotonically increasing with the density for all spin-aligned configurations studied here so that no any signature is found for a spontaneous transition to a ferromagnetic state.

## 1 Introduction

Studies of spin-polarized nuclear and neutron matter have been mainly focussed on the possible onset of a ferromagnetic transition in the neutron star core. This transition could explain in fact the high intensity magnetic fields ( $10^{12}$  gauss) estimated from the timing observations in pulsars and magnetars (for a review see Ref. [1]). Besides this exciting issue the motivation for such studies can be based on a more general context of nuclear physics.

First of all, from the change of the energy per nucleon with the spin polarization one may extract a theoretical prediction for the spin symmetry energy, whose empirical value is so far quite uncertain. The nuclear matter instability against spin fluctuations is driven by the Landau parameter  $G_0$  which is determined from the spin-symmetry energy. The value of this parameter is still a largely controversial topic and no agreement exists among the different approaches to the theory of nuclear matter<sup>2</sup>. Experimental information could come from spin giant resonances, which have not yet been clearly observed. Information could also come from heavy-ion collisions as soon as polarized heavy targets become available.

The second issue related to the study of spin-aligned states of nuclear matter is the propagation of neutrinos in neutron stars. It has been shown that the neutrino mean free path is strongly affected by the magnetic suscep-

tibility. The latter is sizeably suppressed by the strong correlations in nuclear matter and, as a consequence, the mean free path might change sizeably and, eventually drop to zero in the presence of a ferromagnetic transition<sup>3,4</sup>.

There is a guess that the ferromagnetic transition could be a relativistic effect due to  $\pi$ -exchange and in fact all calculations, based on the relativistic mean field approach, predict this transition to occur in dense matter<sup>5,6</sup>. On the other hand, non-relativistic approaches<sup>7,8,9,10</sup> do not support such a transition except Hartree-Fock calculations with phenomenological Skyrme-like forces (for a review see Ref. [4]). This aspect cannot be disconnected from the problem of the in-medium nucleon-nucleon (NN) force, which is poorly known in dense matter due to the lacking of empirical constraints far above the saturation density. However important relativistic effects can be incorporated into the effective interaction via the three-body force associated with a virtual nucleon-antinucleon excitation<sup>11</sup>. Moreover non-relativistic calculations including only two-body forces miss the empirical saturation point of nuclear matter<sup>12</sup>. So it seems worthwhile to investigate the spin-aligned states of nuclear and neutron matter in the non-relativistic Brueckner theory with three-body forces. They contain not only the above mentioned relativistic contributions but also nucleonic excitations which decisively enhance the agreement between theoretical and empirical saturation density<sup>13</sup>.

## 2 Formalism

The spin and isospin asymmetric nuclear matter (ANM) consists of spin-up neutrons ( $n \uparrow$ ), spin-down neutrons ( $n \downarrow$ ), spin-up protons ( $p \uparrow$ ) and spin-down protons ( $p \downarrow$ ) in different density states:  $\rho_{n\uparrow}$ ,  $\rho_{n\downarrow}$ ,  $\rho_{p\uparrow}$ , and  $\rho_{p\downarrow}$ , respectively. Therefore four parameters are required to specify a given configuration of spin and isospin ANM. The Fermi momenta of the four components are generally different from each other, and related to their respective densities by the following relation:  $\rho_\lambda = (k_F^\lambda)^3 / (6\pi^2)$ , where  $\lambda$  denotes the  $z$ -components of isospin and spin, i.e.,  $\lambda = (\tau_z, \sigma_z)$ . Instead of  $\rho_\lambda$ , one can use the following four parameters to identify a given spin and isospin state,

$$\beta = \frac{\rho_n - \rho_p}{\rho}, \quad \delta_n = \frac{\rho_{n\uparrow} - \rho_{n\downarrow}}{\rho_n}, \quad \delta_p = \frac{\rho_{p\uparrow} - \rho_{p\downarrow}}{\rho_p},$$

where  $\rho$ ,  $\rho_n$ , and  $\rho_p$  are total density, neutron density and proton density, respectively. The ratio  $\beta$  is the isospin asymmetry parameter and  $\delta_n$  and  $\delta_p$  are the spin asymmetry parameters for neutrons and protons, respectively.

The starting point of the Brueckner-Bethe-Goldstone (BBG) approach is the reaction  $G$ -matrix. The  $G$ -matrix incorporates strong short-range correla-

tions in nuclear medium by means of the infinite ladder diagram summation of the bare NN interaction. It satisfies the Bethe-Goldstone equation. The latter can be expressed for the spin-isospin ANM in the total angular-momentum basis as follows,

$$G_{LL'}^{TSJ,\lambda\lambda'}(\omega, P; q, q'; \rho, \beta, \delta_n, \delta_p) = v_{LL'}^{TSJ}(q, q') + \frac{2}{\pi} \sum_{L''} \int q''^2 dq'' v_{LL''}^{TSJ}(q, q'') \\ \times \frac{\langle Q^{\lambda\lambda'}(q'', P) \rangle}{\omega - e_{12}^{\lambda\lambda'}(q'', P) + i\eta} G_{L''L'}^{TSJ,\lambda,\lambda'}(\omega, P; q'', q'; \rho, \beta, \delta_n, \delta_p)$$

where  $v_{LL'}^{TSJ}(q, q')$  are the partial wave components of the NN interaction,  $\vec{P} = \vec{k}_1 + \vec{k}_2 = \vec{k}'_1 + \vec{k}'_2$  is the total momentum,  $\vec{q} = (\vec{k}_1 - \vec{k}_2)/2$  and  $\vec{q}' = (\vec{k}'_1 - \vec{k}'_2)/2$  the relative momenta of the two particles in their initial state and final state, respectively. The Pauli operator  $Q^{\lambda\lambda'}(\vec{q}'', \vec{P})$  and the energy denominator  $e_{12}^{\lambda\lambda'}(\vec{q}'', \vec{P}) = \epsilon^\lambda(k'_1) + \epsilon^{\lambda'}(k'_2)$  have been angle averaged in order to remove the coupling between different channels  $\alpha = \{JST\}$ . It is worth noticing that the different components of the  $G$ -matrix differ in general from each other due to the dependence of the Pauli operator and energy denominator on the spin-isospin configuration  $(\lambda, \lambda')$ . The single particle energy is given by  $\epsilon^\lambda(k) = \hbar^2 k^2 / 2m + U^\lambda(k)$ . The continuous choice for the auxiliary potential  $U^\lambda(k)$  is adopted in the present calculations since, on the one hand, it has been shown to provide a much faster convergence of the hole-line expansion than the gap choice <sup>15</sup>, on the other hand, it describes physically the single-particle potential felt by a nucleon in nuclear medium. In the continuous choice,  $U^\lambda(k)$  is the real part of the on-shell mass operator, i.e.,

$$U^\lambda(k) = \text{Re} \sum_{\vec{k}', \lambda'} n^{\lambda'}(k') \langle \vec{k}\lambda, \vec{k}'\lambda' | G[\omega = \epsilon^\lambda(k) + \epsilon^{\lambda'}(k'), P] | \vec{k}\lambda, \vec{k}'\lambda' \rangle_A,$$

where the subscript  $A$  denotes antisymmetrization. For spin and isospin ANM, it is convenient to split it into two contributions as  $U^\lambda = U^{\lambda\lambda} + U^{\lambda\lambda'}$ , ( $\lambda' \neq \lambda$ ). Each individual contribution is calculated by casting it into the partial wave expansion,

$$U^{\sigma_z \tau_z, \sigma'_z \tau'_z}(k) = \int_0^{k_F^{\sigma_z \tau_z}} d^3 k' \sum_{TSJ} \sum_{S_z T_z} \left[ C\left(\frac{1}{2} \sigma_z \frac{1}{2} \sigma'_z | SS_z \rangle\right) \right]^2 \left[ C\left(\frac{1}{2} \tau_z \frac{1}{2} \tau'_z | TT_z \rangle\right) \right]^2 \\ \times \sum_{LL'} \sum_{M_L} C(L' M_L S S_z | J M_L + S_z) C(L M_L S S_z | J M_L + S_z) \\ \times i^{L-L'} Y_{LM_L}^*(\hat{q}) Y_{LM_L}(\hat{q}) 2 G_{LL'}^{TSJ,\lambda\lambda'}(\omega, P; q, q; \rho, \beta, \delta_n, \delta_p).$$

The summation over partial wave states is physically constrained by the selection rule  $S + T + L = \text{odd}$  due to the Pauli principle and consequently

the antisymmetrization of the  $G$ -matrix simply implies multiplication by a factor of 2 for the allowed partial wave channels. For spin symmetric case ( $\delta_n = \delta_p = 0$ ), a spin-up neutron (proton) has the same Fermi momentum as a spin-down neutron (proton) and thus the single-particle potential felt by a nucleon does not depend on the direction of its spin. The summation on the spins of the two particles in the final state and the average of that in the initial state remove the non-diagonal contributions in angular-momentum from the single-particle potential. For spin-asymmetric but isospin-symmetric nuclear matter, we have  $\beta = 0$  and  $\delta_n = \delta_p = (\rho_\uparrow - \rho_\downarrow)/\rho = \delta$ . In this case, the single particle potential becomes,

$$\begin{aligned} U^{\sigma_z, \sigma'_z} &= \int_0^{k_F^{\sigma'_z}} d^3 k' \sum_{TSJ} \frac{2T+1}{2} \sum_{LL'} \sum_{S_z} i^{L-L'} \left[ C\left(\frac{1}{2}\sigma_z \frac{1}{2}\sigma'_z | SS_z \right) \right]^2 \\ &\times \sum_{M_L} C(L' M_L S_z | JM_L + S_z) C(L M_L S_z | JM_L + S_z) \\ &\times Y_{L'M_L}^*(\hat{q}) Y_{LM_L}(\hat{q}) 2G_{LL'}^{TSJ, \sigma_z \sigma'_z}(\omega, q, q; \rho, \delta). \end{aligned}$$

The present calculations will mainly consider this spin-polarized nuclear matter as well as the spin polarized neutron matter.

### 3 Results and conclusions

We performed some calculations within the BHF self-consistent approach above described. The Argonne  $V_{18}$  force is adopted as bare two-body interaction. This has been implemented by a microscopic three-body force, which is described in detail in Ref. [16] together with the average procedure to transform it into an effective two body force. In Fig. 1 the energy shift per nucleon  $E_A(\delta, \rho) - E_A(0, \rho)$  in symmetric nuclear matter is reported as a function of the square of spin polarization  $\delta^2$  for a set of densities. Due to the linear dependence on  $\delta^2$ , also reported in Refs. [9,10] one can write:

$$E_A(\delta, \rho) = E_A(0, \rho) + \mathcal{E}_{sym}(\rho)\delta^2,$$

i.e. the spin dependence of the energy per nucleon can be simply expressed in terms of spin-symmetry energy

$$\mathcal{E}_{sym}(\rho) = \frac{1}{2} \frac{\partial^2 E_A(\delta, \rho)}{\partial \delta^2}$$

in the density range here considered.

The  $\delta^2$ -law is mainly due to the BHF approximation (two-hole line terms only). The same behavior is in fact exhibited by the energy vs. isospin either <sup>14</sup>. The effects of three-hole line terms are rather small when adopting

### Spin-polarized symmetric nuclear matter

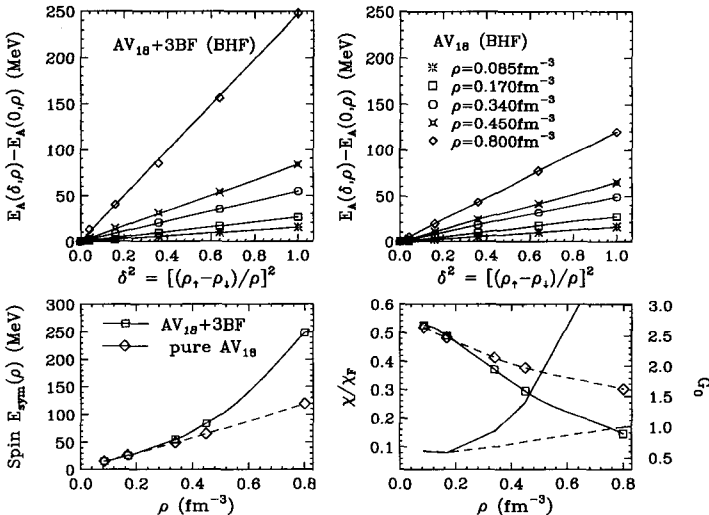


Figure 1. Up windows: The EOS of spin-asymmetric nuclear matter as a function of spin-asymmetry at five values of density, predicted by Brueckner Hartree-Fock calculations adopting pure AV<sub>18</sub> two-body force (right-up window) and AV<sub>18</sub> plus the TBF(left-up window). Right-Lower window: density dependence of spin-symmetry energy for both cases with the TBF (solid curve) and without the TBF(dash curve). Left-lower window: Magnetic susceptibility  $\chi/\chi_F$  (curves with symbol) and Landau parameter  $G_0$  (curves without symbol) as functions of density.

the continuous choice for the auxiliary potential <sup>15</sup>; this choice is also adopted for the present calculations. The slope of the energy shift is monotonically increasing with density so that no signature for a ferromagnetic phase transition in symmetric nuclear matter is expected. The effect of three-body force is to enhance this slope for densities above the saturation point. This effect is more clearly shown in the plot of  $\mathcal{E}_{sym}$  vs. density in Fig. 1.

The magnetic susceptibility has been also calculated from the spin-symmetry energy  $\chi = \bar{\mu}^2 \rho / (2\mathcal{E}_{sym})$ , where  $\bar{\mu}$  is the average of neutron and proton magnetic moments (in neutron matter  $\bar{\mu}$  is the exact neutron magnetic moment). Usually one calculates the ratio of  $\chi$  to  $\chi_F$ ,  $\chi_F$  being the magnetic susceptibility for a degenerate free Fermi gas. The effect of strong correlations in nuclear matter due to the two-body force is a reduction of  $\chi$  with respect to  $\chi_F$ . This reduction increases with density up to a factor of 0.3 at  $\rho = 0.8 \text{ fm}^{-3}$ . The above result is common to most Brueckner calculations <sup>8,9,10</sup>. More pronounced is the queching due to three-body force.

### Spin-polarized neutron matter

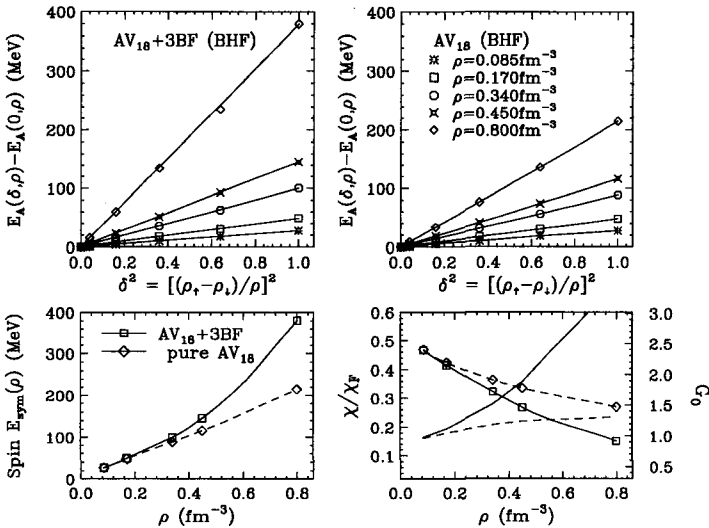


Figure 2. The same as Fig.1 for spin-polarized neutron matter.

Fig. 1 also shows the Landau parameter  $G_0$  describing the spin density fluctuations in the effective interaction.  $G_0$  is simply related to the spin-symmetry energy or, equally, to the magnetic susceptibility by the relation  $\chi/\chi_F = m^*/(1 + G_0)$ , where  $m^*$  is the effective mass. A magnetic instability would require  $G_0 < -1$  which is analogous to the condition  $F_0 < -1$  for the mechanical instability giving rise to the liquid-vapour phase transition. But, the value of  $G_0$  vs. density from the BHF calculations is always positive and monotonically increasing up to the highest density. The three-body force pushes up the curve of  $\chi$ . This result is in strong disagreement with the prediction with Skyrme forces. This is not a complete surprise since Skyrme forces are only well suited in the proximity of the empirical saturation point. Astonishing is the strong disagreement on this respect with the relativistic approaches because the three-body forces contain already important relativistic effects<sup>16</sup>. The accurate knowledge of  $G_0$  should lead to reliable predictions on the spin and spin-isospin giant modes as well as spin-spin part of the optical potential<sup>8</sup>.

The above calculations have been also repeated for the case of pure neutron matter and reported in Fig. 2. The same conclusions can be drawn as to the absence of the ferromagnetic phase transition and the quenching of the magnetic susceptibility caused by the strong correlations from the two- and

three-body forces. This quenching should have a strong influence on the neutrino propagation in dense matter such as supernovae and neutron stars. In the case of the transition to a ferromagnetic state it has been shown that the mean free path could drop to zero<sup>3</sup> that could have remarkable consequences as, for instance, on the neutron star cooling.

## References

1. A. Reisenegger, *Magnetic Fields across the Hertzsprung-Russell Diagram*, arXiv: astro-ph/0103010.
2. U. Lombardo, in “Nuclear Methods and the Nuclear Equation of State”, Ed. M. Baldo, World Scientific, Singapore, 1999, p.458 and references therein quoted.
3. J. Margueron, J. Navarro, N. van Giai and W. Jiang, Neutrino propagation in neutron matter and the nuclear equation of state, to appear in “The Nuclear Many-body Problem 2001”, NATO Science Series II (Kluwer Academic Publishers).
4. J. Margueron, PhD thesis (2001), Paris.
5. P. Bernardos, S. Marcos, R. Niembro and M. L. Quelle, Phys. Lett. B356 (1995) 175.
6. T. Maruyama and T. Tatsumi, Nucl. Phys. A693 (2001) 710.
7. P. Haensel, Phys. Rev. C11 (1975) 1822.
8. J. Cugnon, P. Deneye and A. Lejeune, Nucl. Phys. A485 (1988) 271.
9. I. Vidana, A. Polls and A. Ramos, Phys. Rev. C65 (2002) 035804.
10. I. Vidana and I. Bombaci, Equation of state and magnetic susceptibility of spin polarized isospin asymmetric nuclear matter, arXiv: nucl-th/0203061.
11. A. Lejeune, U. Lombardo and W. Zuo, Phys. Lett. 477 (2000) 45.
12. M. Baldo, in “Nuclear Methods and the Nuclear Equation of State”, Ed. M. Baldo, World Scientific, Singapore, 1999, p. 1 and references therein quoted.
13. W. Zuo, A. Lejeune, U. Lombardo and J. F. Mathiot, arXiv: nucl-th/0202077, to appear in Nucl. Phys. A.
14. W. Zuo, I. Bombaci and U. Lombardo, Phys Rev. C60 (1999) 024605.
15. H. Q. Song, M. Baldo, G. Giansiracusa and U. Lombardo, Phys. Rev. Lett. 81 (1998) 1584.
16. P. Grangé, A. Lejeune, M. Martzolff, and J.-F. Mathiot, Phys. Rev. C40 (1989) 1040.

## THE QCD PHASE DIAGRAM

*Nicola Cabibbo explained in his talk how the very idea of the Quark Plasma was conceived. This Chapter ideally follows up that work by introducing and exploiting the theoretical tools which are needed to study strong interactions in extreme conditions from first principles.*

*These theoretical approaches aim to provide a sound understanding of the conceptual arena in which experiments take place: they can confirm the existence of different phases, clarify their nature and interrelations, and suggest experimental probes.*

*Lattice QCD has provided so far a convincing evidence for quark and gluon liberation, and chiral symmetry restoration at high temperature. Exotic phases at high density have been discussed by Nardulli and Sannino, and new results for the LOFF phase and vector condensation have been presented by Mannarelli and Schäfer during the topical session. These predictions can be confronted by lattice studies of two color QCD, as discussed in the topical session. Theoretical studies also afford the possibility to embed QCD in a larger parameter space, as reviewed by Sannino.*

*Experimental signatures of the quark gluon plasma are associated either to chiral symmetry restoration and to confinement. Hence, understanding the interrelation between these two phenomena, discussed by Del Debbio and Meggiolaro, and by Cosmai and Papa in the topical session, is important both on theoretical and phenomenological grounds. The same is true for the fate of U(1) axial symmetry at the deconfinement transition, which has been assessed by Meggiolaro.*

*The search for the tricritical point discovered in the phase diagram – a genuine critical point amenable to an experimental observation – is another important theoretical/experimental question, which requires the extension of the current lattice techniques to finite baryon density. Possibilities for these calculations have been discussed by D'Elia in the topical session.*

*Last but not the least, the equation of state of strongly interacting matter – which is closely related with the phase structure of QCD – lies at the very heart of the phenomena we are considering. It is an ubiquitous subject much dealt with during this meeting: the lattice QCD approach provides us with the estimates for the critical energy densities which are so important for the experiments, as reviewed by Riccati and Satz in the introductory talks, and it is a long term, important goal to link these ab initio calculations with the more intuitive nuclear physics approach.*

This page is intentionally left blank

# AN INTRODUCTION TO QCD AT NON-ZERO TEMPERATURE AND DENSITY

MARIA-PAOLA LOMBARDO

*Istituto Nazionale di Fisica Nucleare – Sezione di Padova*

An overview aimed at non specialists who wish to follow the current literature: a brief outline of field theory thermodynamics is followed by a survey of the main theoretical idea and results on the QCD phase diagram. The lattice approach is then discussed, with emphasis on nonzero baryon density..

## 1 Introduction

QCD at nonzero temperature and density is a vast subject covered in many talks at this meeting: from the introductory lesson describing the very 'discovery' of quark gluon plasma <sup>1</sup>, to the subtle interrelations of gauge fields dynamics and charmonium suppresions <sup>2</sup>, from the detailed analysis of the exotic phases at large baryon density <sup>3</sup> to the fascinating aspects of the QCD phase diagram with many flavor <sup>4</sup>, and the time-honored theoretical subjects of the interplay between topology and confinement <sup>5</sup>, the rich aspects of the interrelations of chiral and axial symmetries <sup>6</sup>, and the many new results presented in the topical session on the QCD phases. These notes mostly aimed at the nonexpert might provide, besides some introductory material, a path among these many different and fascinating ideas.

The material is organised as follows: section 2 reviews the imaginary time formulation of field theory thermodynamics, and gives the functional integral representation of the partition function. The representation of  $\mathcal{Z}$  naturally leads to a theoretical suggestion: the concept of universality which is singled out in a small Section on its own, because it is so important. Section 4 discusses the QCD chiral transition, Section 5 the QCD deconfinement transition, and Section 6 how to put together the two, eventually describing the complex phenomenology of the real world high temperature QCD phase transition. The equation of state is briefly mentioned here. Section 6 introduces the method used to obtain all of the results of the previous Sections : the lattice regularisation. We shall see that introducing temperature is straightforward while a non zero density poses specific problems, and we will briefly review the main proposals to circumvent such problems, referring to <sup>7</sup> for details and recent results.

## 2 Formulation

Here we will concern ourselves with the path integral representation of the partition function. The basic property of equilibrium field theory is that one single function,  $\mathcal{Z}$ , the grand canonical partition function,

$$\mathcal{Z} = \mathcal{Z}(\mathcal{V}, \mathcal{T}, \mu) \quad (1)$$

determines completely the thermodynamic state of a system according to:

$$P = T \frac{\partial \ln \mathcal{Z}}{\partial V} \quad (2)$$

$$N = T \frac{\partial \ln \mathcal{Z}}{\partial \mu} \quad (3)$$

$$S = \frac{\partial T \ln \mathcal{Z}}{\partial T} \quad (4)$$

$$E = -PV + TS + \mu N \quad (5)$$

while physical observables  $\langle O \rangle$  can be computed as

$$\langle O \rangle = Tr O \hat{\rho} / \mathcal{Z} \quad (6)$$

Any of the excellent books on statistical field theory and thermodynamics can provide a more detailed discussion of these points. I would like to underscore, very shortly, that the problem is to learn how to represent  $\mathcal{Z}$  at non zero temperature and baryon density, and to design a calculational scheme.

### 2.1 $\mathcal{Z}$ at non-zero temperature and chemical potential

$\mathcal{Z}$  is the trace of the density matrix of the system  $\hat{\rho}$

$$\mathcal{Z} = Tr \hat{\rho} \quad (7)$$

$$\hat{\rho} = e^{(-H - \mu \hat{N})} / T \quad (8)$$

$H$  is the Hamiltonian,  $T$  is the temperature and  $\hat{N}$  is any conserved number operator.

### 2.2 Chemical potential, relativistic and non-relativistic

It is worth stressing the main differences between the non relativistic and relativistic meaning of a chemical potential  $\mu$ , eqs (5) and (8).

In a non relativistic setting, the chemical potential tells us the 'cost' of adding an extra particle to the system: we can have a different chemical potential for each 'type' of particle. The term which is added to the Hamiltonian is  $\mu_k N_k$ ,  $N_k$  being indeed the number of  $k$ -particles

In a relativistic setting, particles can be created and destroyed, thus losing their individuality, so to speak: it only makes sense to have a chemical potential coupled to the 0-th component of a conserved current.

In practice, we will mostly concern ourselves with the current  $J_\mu = \bar{\psi} \gamma_\mu \psi$ , i.e.  $J_0 = \bar{\psi} \gamma_0 \psi = \psi^\dagger \psi$  will be the density of fermion (baryon) number, or, more precisely, the difference between the number of fermions and antifermions:  $\int J_0 = N - \bar{N}$ . The chemical potential will then appear in the Lagrangian as a term  $\mu J_0$  and we recognize immediately that a change of sign for the chemical potential corresponds to an exchange particles–antiparticles.

Second difference between non-relativistic and relativistic approach concerns the magnitude itself of  $\mu$ , which in a relativistic theory contains the particle rest mass.

From a technical point of view, a finite density is easily handled in a non-relativistic setting. From a relativistic field theoretic perspective, there are important technical problems. We will discuss these problems later on, and we just anticipate here that the explicit breaking of the particle–antiparticle symmetry associated with a chemical potential induces the loss of positivity of the Action—the condition which makes possible lattice calculations.

### 2.3 Temperature

Consider the transition amplitude for returning to the original state  $\phi_a$  after a time  $t$

$$\langle \phi_a | e^{-iHt} | \phi_a \rangle = \int d\pi \int_{\phi(x,0)=\phi_a(x)}^{\phi(x,t)=\phi_a(x)} d\phi e^{i \int_0^t dt \int d^3x (\pi(\vec{x},t) \frac{\partial \phi(\vec{x},t)}{\partial t} - H(\pi, \phi))} \quad (9)$$

Compare now the above with expression (2) for  $\mathcal{Z}$ , and make the trace explicit:

$$\mathcal{Z} = Tr e^{-\beta(H - \mu \hat{N})} = \int d\phi_a \langle \phi_a | e^{-\beta(H - \mu N)} | \phi_a \rangle \quad (10)$$

We are naturally lead to the identification

$$\beta \equiv \frac{1}{T} \rightarrow it \quad (11)$$

We note – anticipating the discussions of Section below – that studying nonzero temperature on a lattice<sup>10</sup> is straightforward: one just takes advantage of the finite temporal extent of the lattice, while keeping the space directions much larger than any physical scale in the system.

By introducing the integral  $S(\phi, \psi)$  of the Lagrangian density (from now on we will always use  $1/T$  as the upper extremum for the time integration)

$$S(\phi, \psi) = \int_0^{1/T} dt \int d^3x \mathcal{L}(\phi, \psi) \quad (12)$$

$\mathcal{Z}$  is written as

$$\mathcal{Z} = \int d\phi d\psi e^{-S(\phi, \psi)} \quad (13)$$

The only missing ingredient are the boundary conditions for the fields: basically, they follow from the (anti)commuting properties of the (fermi)bose fields which imply

$$\hat{\phi}(\vec{x}, 0) = \hat{\phi}(\vec{x}, \beta) \quad (14)$$

for the bosons and

$$\hat{\psi}(\vec{x}, 0) = -\hat{\psi}(\vec{x}, \beta) \quad (15)$$

for the fermions.

Fermions and bosons obey antiperiodic and periodic boundary conditions, respectively, in the time direction.

The expression above, together with the boundary conditions just introduced, is the key to field thermodynamics.

### 3 Universality

It is intuitive that when the smallest significant length scale of the system  $l >> 1/T$  the system becomes effectively  $d$ -dimensional. Moreover, the description of the system can be effectively ‘coarse grained’, ignoring anything which happens on a scale smaller than  $l$ .

This can become true when the system is approaching a continuous transition: the correlation length of the system  $\xi$  is diverging. In such situation all the physics is dominated by long wavelength modes. Not only the system gets effectively reduced, but the coarse graining procedure becomes doable. As an effect of this procedure, systems which are very different one from another might well be described by the same model, provided that the long range physics is regulated by the same global symmetries: this is the idea of universality which provides the theoretical framework for the study of the QCD transition in two interesting (albeit non physical) cases which we review in the next two sections.

## 4 QCD chiral transition ( $m_q = 0$ )

Let us recall the symmetries of the QCD action with  $N_f$  flavors of massless quarks, coupled to a  $SU(N_c)$  color group:

$$SU(N_c)_C \times SU(N_f) \times SU(N_f) \times Z_A(N_f) \quad (16)$$

$SU(N_c)$  is the gauge color symmetry.  $SU(N_f) \times SU(N_f) \times Z_A(N_f)$  is the flavor chiral symmetry, after the breaking of the classical  $U_A(1)$  symmetry to the discrete  $Z_A(N_f)$ .

We want to study the realisation and pattern(s) of breaking of the chiral symmetries and we would like to know the interrelation of the above with the possibility of quark liberation predicted at high temperature and density.

In normal condition (zero temperature and density) the  $SU(N_f)_L \times SU(N_f)_R$  chiral symmetry is spontaneously broken to the diagonal  $SU(N_f)_{L+R}$ .

Let us note the isomorphy

$$SU(2) \times SU(2) \equiv O(4) \quad (17)$$

which shows that the symmetry is the same as the one of an O(4) ferromagnet. The relevant degrees of freedom are the three pions, and the sigma particle, and the effective potential is a function of  $\sigma^2 + |\pi|^2$  in the chiral space. Once a direction in the chiral sphere is selected (say in the  $\sigma$  direction) chiral symmetry is spontaneously broken in that direction, according to the equivalent patterns:

$$SU(2)_R \times SU(2)_L \rightarrow SU(2)_{L+R} \quad (18)$$

$$O(4) \rightarrow O(3) \quad (19)$$

Massless Goldstone particles (in this case, the three pions) appear in the direction orthogonal to the one selected by the spontaneous breaking.

### 4.1 Increasing $T$

Disorder increases with temperature. Then, one picture of the high  $T$  QCD transition can be drawn by using a ferromagnetic analogy of the chiral transition:  $\bar{\psi}\psi$  can be thought of as a spin field taking values in real space, but whose orientation is in the chiral sphere. Chiral symmetry breaking occurs when  $\langle \bar{\psi}\psi \rangle \neq 0$ , i.e. it corresponds to the ordered phase. By increasing  $T$ ,  $\langle \bar{\psi}\psi \rangle \rightarrow 0$ , and the O(4) symmetry should be restored.

Combining this symmetry analysis with the general idea of dimensional reduction, Pisarski and Wilczek <sup>11</sup> proposed that the high temperature transition in two flavor QCD should be in the universality class of the O(4) sigma

model in three dimensions. At high temperature when symmetry is restored there will be just one global minimum for zero value of the fields, and pion and sigma become eventually degenerate.

We have however to keep in mind possible sources of violation of this appealing scenario and, all in all, one has to resort to numerical simulations to measure the critical exponents, and verify or disprove the  $O(4)$  universality. In turn, this gives information on the issues raised for instance in as well as on the possible restoration of the axial anomaly, see the discussion in Meggiolaro's review.

In practice, one measures the chiral condensate as a function of the coupling parameter  $\beta$ , which in turns determines the temperature of the system. This gives the exponent  $\beta_{mag}$  according to

$$\langle \bar{\psi} \psi \rangle = B(\beta - \beta_c)^{\beta_{mag}} \quad (20)$$

The exponent  $\delta$  is extracted from the response at criticality:

$$\langle \bar{\psi} \psi \rangle = A m^{1/\delta}; \beta = \beta_c \quad (21)$$

The results for the critical exponents compare favourably with the  $O(4)$  results  $\beta_{mag} = .38(1)$ ,  $\delta = 4.8(2)$ , and definitively rule out mean fields exponents (which would have characterised a weak first order transition). However, the results can still be compatible with  $O(2)$  exponents, which would signal the persistence of some lattice artifact, and of course it is still possible that the final answer do not fit any of the above predictions, for instance one is just observing some crossover phenomenon.

In conclusion the symmetry analysis of the (two flavor) QCD transition gives a definite predictions for the value of the critical exponents, which is possibly (slightly) violated by the numerical results. The numerical relevance of this violation (i.e. possible systematic errors) as well as the its physical implications are an interesting open problem.

The contribution by E. Meggiolaro covers in more detail these points.

#### 4.2 Increasing density

Till two or three years ago, we thought that asymptotic freedom was the main physical agent behind the pattern of chiral symmetries at high density. Now it has been recognized that, at least at zero temperature, the main mechanisms are instability at the Fermi surface leading to color superconductivity<sup>9</sup>. The review by Nardulli and Sannino cover these points which, unfortunately, are not yet amenable to a lattice study. The lattice approach at nonzero density (see contribution by M. D'Elia) is still limited to rather high temperature, where color superconductivity is most likely lost anyway.

## 5 QCD deconfinement transition ( $m_q = \infty$ )

When  $m_q = \infty$  quarks are static and do not contribute to the dynamics: hence, the dynamic of the system is driven by gluons alone, i.e. we are dealing with a purely Yang-Mills model:

$$S = F_{\mu\nu}F^{\mu\nu} \quad (22)$$

In addition to the local gauge symmetry, the action enjoys the global symmetry associated with the center of the group,  $Z(N_c)$ . The order parameter is the Polyakov loop  $P$

$$P = e^{i \int_0^{1/T} A_0 dt} \quad (23)$$

In practice,  $P$  is the cost of a static source violating the  $Z(N_c)$  global symmetry.

The interquark potential  $V(R, T)$  ( $R$  is the distance,  $T$  is the temperature) is

$$e^{-V(R, T)/T} \propto < P(\vec{0})P^\dagger(\vec{R}) > \quad (24)$$

Confinement can then be read off the behaviour of the interquark potential at large distance. When  $V(R) \propto \sigma R$  it would cost an infinite amount of energy to pull two quarks infinitely apart. Above a certain critical temperature  $V(R)$  becomes constant at large distance: i.e. the string tension is zero, confinement is lost. The implication of this is that  $|P|^2 = V(\infty, T)$  is zero in the confining phase, different from zero otherwise.  $P$  plays then a double role, being the order parameter of the center symmetry, and an indicator of confinement. We learn that in Yang Mills models there is a natural connection between confinement and realisation of the  $Z(N_c)$  symmetry. Hence, the confinement / deconfinement transition in Yang Mills systems is amenable to a symmetry description. By applying now the same dimensional reduction argument as above, we conclude that the Universality class expected of the three color model is the same as the one of a three dimensional model with  $Z(3)$  global symmetry: Indeed, work by the Columbia, Tsukuba and APE group in the mid 80's found that the transition turns out to be 'almost' second order, i.e. very weakly first order, like the 3d three state Potts model.

The same reasoning tells us that the two color model is in the universality class of the three dimensional  $Z(2)$  (Ising) model. This prediction has been checked with a remarkable precision by Engels and collaborators<sup>12</sup>, and it is a spectacular confirmation of the general idea of universality and dimensional reduction.

## 6 Summary and Open Questions for the QCD High T Transition

What do we know about the real world: two (nearly) massless quark  $m_q \ll \Lambda_{QCD}$ , and one more heavy?

We can approach then the 'real' world from two sides, either decreasing the mass from infinity, or increasing the quark mass from zero.

### 6.1 Approaching the physical point from infinite mass

Remember that in the infinite mass limit QCD reduces to the pure gauge (Yang Mills) model. Yang Mills systems have a deconfining transition associated with the realisation of the global  $Z(N_c)$  symmetry. This places the system in the Ising 3d universality class for two colors, and makes the transition weakly first order (near second, infact) for three colors. General universality arguments are perfectly fulfilled by the deconfining transition.

The  $Z(N_c)$  symmetry is broken by the kinetic term of the action when the quarks are dynamic ( $m_q < \infty$ ) : this particular symmetry description of deconfinement only holds for infinite quark mass. When light quarks enter the game, the global  $Z(N_c)$  symmetry observed at infinite mass is lost, and the simple description of confinement in terms of such symmetry is not possible any more. It should however remain true that color forces at large distance should decrease with temperature: the main mechanism, already at work at  $T = 0$ , is the recombination of an (heavy) quark and antiquark with pairs generated by the vacuum:  $\bar{Q}Q \rightarrow \bar{q}Q + q\bar{Q}$ . At high temperature it becomes easier to produce light  $\bar{q}q$  pairs from the vacuum, hence it is easier to 'break' the color string between an (heavy) quark and antiquark  $\bar{Q}Q$ . In other words, we expect enhanced screening of the color forces, which should be sharp at the 'phase transition'. It is however worth mentioning that, even if the string 'breaks' bound states might well survive giving rise to a complicated, non-perturbative dynamics above the critical temperature. The physical scale of these phenomena is the larger physical scale in the system, i.e. the pion radius.

### 6.2 Approaching the physical point from zero mass

For zero bare mass the phase transition is chiral. For three colors, two flavors is second order with  $T_c \simeq 170 Mev$ . The prediction from dimensional reduction + universality - $O(4)$  exponents- is compatible with the data, but the agreement is not perfect.

If the agreement were confirmed, that would be an argument in favour of the non-restoration of the  $U_A(1)$  symmetry at the transition, which is also

suggested by the behaviour of the masses spectrum. Remember in fact that the chiral partner of the pion is the  $f_0$ , which is in turn degenerate with the scalar  $a_0$  with  $U_A(1)$  is realised. All in all,  $U_A(1)$  non-restoration across the chiral transition corresponds to  $m_\pi \simeq m_{f_0} \neq m_{a_0}$  which is the pattern observed in lattice calculations.

The transition with three (massless) flavour turns out to be first order. The question is then as to whether the strange quark should be considered ‘light’ or ‘heavy’. In general, the real world will be somewhere in between two and three light flavour, and to really investigate the nature of the physical phase transition in QCD one should work as close as possible to the realistic value of the quark masses.

### 6.3 What do we know on the real QCD phase diagram

Among the most prominent open questions, there is of course the behaviour of ‘real’ QCD, with two light flavour, and a third one of the order of  $\Lambda_{QCD}$ , so how and when exactly the  $N_f = 2$  scenario morphs with the  $N_f = 3$ ? Also, why is  $T_\chi$  much smaller than the pure gauge deconfining transition?

At a theoretical level the question is if it is possible to give an unified description of the two transitions, chiral and deconfining. This question is currently under active investigation: recent work suggests that a symmetry analysis of the deconfining transition can be extended also to theories with dynamical fermions. The physical argument is rooted in a duality transformation which allows the identification of magnetic monopoles as agent of deconfinement. The order parameter for deconfinement would be the monopole condensate<sup>5</sup>. An alternative approach uses percolation as the common agent driving chiral and confining transitions<sup>2</sup>.

One unifying description and perhaps the most dramatic evidence of a phase transition away from the ‘simple’ limits  $m_q = 0$  and  $m_q = \infty$  comes from the equation of state: for  $T \simeq 180\text{ MeV}$  we observe, from lattice calculations, a sharp increase of the internal energy: the behaviour of the internal energy is a direct probe of the number of degrees of freedom, and indicates quark and gluon liberation<sup>10</sup>.

Finally, the work<sup>13</sup> arrives at an interesting picture of the phase diagram of QCD by combining symmetry analysis and phenomenological consideration. Particularly interesting is the prediction of an endpoint of a first order line stemming from zero temperature chiral transition at finite density, which should be experimentally observable.

## 7 Methods for QCD at finite temperature and density

Here we will concern ourselves with computational schemes for QCD. The methods described here are those used to obtain the results reviewed above on the chiral transition, deconfinement and equation of state in QCD. We will give some details on these methods, we will explain why they are not immediately applicable at finite density and we will close up with a brief assessment of the current situation for finite density QCD.

The question is how to estimate the physical observables  $\langle O \rangle = Tr O \hat{\rho} / \mathcal{Z}$  starting from the representation of the partition function

$$\mathcal{Z}(\mu, T) = \int_0^{1/T} dt \int e^{-S_G + \bar{\psi}(\partial + m + \mu\gamma_0)\psi} d\bar{\psi} d\psi dU \quad (25)$$

The need for two integrations (over bosons and over fermions) lends itself naturally to two different paths: either integrate gluons first, or fermions.

In the first case (if gluons are integrated out first) we end up with a purely effective fermionic model:

$$\mathcal{Z}(T, \mu, \bar{\psi}, \psi, U) \simeq \mathcal{Z}(T, \mu, \bar{\psi}, \psi) \quad (26)$$

As the integration over gluons cannot be done exactly,<sup>a</sup>, such effective models are often built with the help of a symmetries' analysis for QCD. The gauge fields enter the game under the guise of coefficients for such models. Very important examples of this approach include instanton models, and four fermion models such as those discussed by Nardulli and Sannino at this meeting.

The other way takes advantage of the bilinear nature of  $S$  in the fermionic fields, yielding the exact expression:

$$\mathcal{Z}(T, \mu, U) = \int dU e^{-(S_g - \log(\det M))} \quad (27)$$

The above integral needs being regulated, and scheme for calculating it has to be devised. Both tasks are accomplished within the lattice approach.

### 7.1 Lattice field theory at $T, \mu \neq 0$

Temperature comes for free on a lattice: the lattice has a finite extent  $N_t a$ , hence temperature is given by  $T = 1/N_t a$ . The discretization can be carried

---

<sup>a</sup>There indeed a systematic approach to QCD based on the strong coupling expansion which makes these integrations easy, but this is not in the scope of this introduction

out in complete analogy to  $T = 0$ , and most of the techniques developed there (see e.g. the recent review for an introduction to lattice field theory at zero temperature) apply at finite temperature as well.

A finite density of baryons  $\mu_B J_0$ <sup>b</sup> poses instead specific problems.

How to discretize  $\mu\bar{\psi}\gamma_0\psi$

Recall first the 'natural' discretization of the matter fields  $\phi(x)$  and their derivatives  $\partial_\mu\phi(x)$  on a regular lattice with spacing  $a$ :

$$\phi_{LATT}(n_1, n_2, n_3, n_4) = \phi(n_1a, n_2a, n_3a, n_4a) \quad (28)$$

$$\Delta_\mu\phi_{LATT}(n_1, n_2, n_3, n_4) = (\phi(n_1a, (n_\mu + 1)a, n_3a, n_4a) - \quad (29)$$

$$\phi(n_1a, (n_\mu a, n_3a, n_4a))/2a \quad (30)$$

This, for instance, is the correct prescription for the chiral condensate:  $m\bar{\psi}\psi \rightarrow m\bar{\psi}_{LATT}\psi_{LATT}$  but not, as we will see in a moment, for the baryon density!  $\mu\bar{\psi}\gamma_0\psi \rightarrow \mu\bar{\psi}_{LATT}\gamma_0\psi_{LATT}$  is not the correct lattice form, i.e. *The naive discretization is not adequate for baryon density.*

Let us then consider free fermions in the continuum

$$S = \int_0^\beta \bar{\psi} \gamma_m u \partial_\mu \psi + m \bar{\psi} \psi + \mu \bar{\psi} \gamma_0 \psi$$

The internal energy  $\epsilon = \frac{1}{V} \frac{\partial}{\partial \beta} \ln Z = \frac{4}{(2\pi)^4} \int d^4 p \frac{(p_0 + i\mu)^2}{(p_0 + i\mu)^2 + p^2 + m^2}$ , after subtracting the vacuum energy, is finite at  $T = 0$ :  $\lim_{T \rightarrow 0} \epsilon = \frac{\mu^4}{4\pi^2}$  and gives the expect result

By use of the naive discretization,  $\epsilon$  would instead diverge in the continuum ( $a \rightarrow 0$ ):  $L = \bar{\psi}_x \gamma_\mu \psi_{x+\mu a} + m \bar{\psi}_x \psi_x + \mu \bar{\psi}_x \gamma_0 \psi_x \propto \frac{\mu^2}{a^2} \rightarrow_{a \rightarrow 0} \infty$

The solution :  $\mu$  is an external field

Note the analogy:  $\bar{\psi} \gamma_\mu A_\mu \psi \longleftrightarrow i \mu \bar{\psi} \gamma_0 \psi$ . It shows us that  $\mu$  looks like an external field in the time direction. But we know how to 'put' external field on a lattice: they live on the lattice links: for instance, in electrodynamics  $A \rightarrow \theta = e^{iA}$  (and, for the gauge fields, this implements in a natural and elegant way gauge invariance)

These considerations suggest how to put finite density on a lattice:

$$L(\mu) = \bar{\psi}_x \gamma_0 e^{\mu a} \psi_{x+\hat{0}} - \bar{\psi}_{x+\hat{0}} \gamma_0 e^{-\mu a} \psi_x \quad (31)$$

Indeed, this turns out to be the correct prescription: unphysical divergences disappear and the continuum limit is reproduced.

---

<sup>b</sup>Remember again that  $L(\mu) = L_0 + \mu J_0$ ,  $J_0 = \bar{\psi} \gamma_0 \psi$ , i.e.  $N - \bar{N} = \int J_0$

There is also a very expressive physical interpretation: as we can see, forward propagation is encouraged and backward propagation is suppressed: we are indeed inducing an asymmetry particles-antiparticles.

The 0-th component of the current  $j_0$  counts indeed the differences between backwards and forward propagation:

$$J_0 = -\partial_\mu L = \bar{\psi}_x \gamma_0 e^{\mu a} \psi_{x+\hat{a}} + \bar{\psi}_{x+\hat{a}} \gamma_0 e^{-\mu a} \psi_x \quad (32)$$

and reproduces the correct continuum limit.

#### Chemical potential and boundary conditions

By use of an unitary transformation of the fields it is possible to reexpress  $L$  as

$$L(\mu) = L(0) \quad (33)$$

with boundary conditions

$$\phi(x + N_T) = e^{\mu N_T} \phi(x) \quad (34)$$

$$\psi(x + N_T) = -e^{\mu N_T} \psi(x) \quad (35)$$

It is of some interest to consider the effect of the chemical potential on the baryonic propagators in the two cases – when the chemical potential is included into the Action, and when instead affects only the boundary conditions. In the first case, (at zero temperature, and ignoring feedbacks) a term  $\exp(-N_c \mu)$  multiplies the baryonic propagator: this produces an apparent decrease of the baryon mass

$$m_B = m_B - 3\mu \quad (36)$$

i.e. the baryon becomes massless at  $\mu = \mu_c = m_B/3$ . In the same situation, the chiral condensate remains constant till  $\mu_c$ , and then suddenly drops to zero. The behaviour of the chiral condensate would be suggestive of a strong first order transition, while the behaviour of the baryon mass would suggest a second order transition with  $\nu = 1$ !

In the other formulation (when chemical potential only affects the boundary conditions), at zero temperature the baryon mass is constant till  $\mu_c$ : this is consistent with the behaviour of the chiral condensate, and with the physical intuition that nothing should happen till the Fermi level is reached. Of course, nothing is wrong and the apparent contradiction is resolved by noticing that the apparent decrease of the baryon mass below  $\mu_c$  merely reflects the change of the reference energy. The relationships above provide a link between the two pictures.

QCD at nonzero T and  $\mu$  at a glance The continuum formulation:

$$\begin{aligned} L = L_{YM} + \bar{\psi}(i\gamma_\mu D_\mu + m)\psi \\ + \mu\bar{\psi}\gamma_0\psi \end{aligned} \tag{37}$$

$\mu$  is explicitly included via the coupling to  $\mu J_0$ , and the temperature is the reciprocal of the imaginary time.

On a lattice:

$$\begin{aligned} L = L_{YM} + \sum_{i=1}^3 \bar{\psi}_x U \gamma_i \psi_{x+i} - \bar{\psi}_{x+i} U^\dagger \gamma_i \psi_x \\ + m\bar{\psi}\psi + \bar{\psi}_x \gamma_0 e^{\mu a} U \psi_{x+\hat{0}} - \bar{\psi}_{x+\hat{0}} U^\dagger \gamma_0 e^{-\mu a} \psi_x \end{aligned}$$

$\mu$  appears as a link term, and the temperature is again the reciprocal of the imaginary time. The two formulations coincide in the limit  $a \rightarrow 0$ .

## 7.2 From the formulation to the results

Let us write again:

$$S = S_{YM}(U) + \bar{\psi}M(U)\psi \tag{38}$$

By taking advantage of  $S$  bilinearity in the fields  $\psi, \bar{\psi}$  we can write

$$\mathcal{Z} = \int e^{-S_{YM}(U)} \det M(U) dU \tag{39}$$

It is convenient to define an 'effective' Action

$$S_{eff}(U) = S_{YM}(U) - \ln(\det M(U)) \tag{40}$$

Averages of purely gluonic observables can be expressed as

$$\langle f(U) \rangle = Z^{-1} \int dU e^{-S_{eff}(U)} f(U) \tag{41}$$

while fermion bilinears can be evaluated with the help of Grassman algebra

$$\langle \bar{q}q \rangle = Z^{-1} \int dU e^{-S_{eff}(U)} \text{Det} M(U)^{-1} \tag{42}$$

In conclusion, if we know how to treat  $\int e^{-S_{eff}(U)} dU$  we have access to all of the gluonic observables, chiral condensate, meson and baryons propagators (masses, decay constant, etc.) etc. much in the same way as at  $T = 0$ .

In practical numerical works lattice discretization is combined with importance sampling: a configuration of gauge fields  $[U]$  is a 'point' in a multidimensional integration space. A Markov chain of points is then created according to the prescription:  $P([U]) \propto e^{-S_{eff}([U])}$ . Expectaction values are then given by simple averages:  $\langle O \rangle = \lim_{N \rightarrow \infty} 1/N \sum_{i=1}^N O(U)$ .

The prescription above relies on importance sampling:  $S_{eff}([U])$  must be positive.<sup>c</sup> In QCD (eq. above)  $M^\dagger(\mu) = -M(-\mu)$ : importance sampling, hence MonteCarlo evaluation of physical observables, works for purely imaginary chemical potential, including, of course,  $\mu = 0$ .

For QCD with two color, however, as well as for several fermionic models, the positivity condition is met by the Action at non zero  $\mu$ . All in all, we have a rather elaborate pattern of warnings and possibilities.

### 7.3 Results and possibilties for QCD at $\mu \neq 0$

I would classify the many questions one can ask along two main lines:

Firstly, what can be done in order to learn about general behaviour at nonzero baryon density?

Secondly, what can be done in order to learn about REAL QCD at nonzero baryon density?

I would say that to learn about the effects of a finite density of baryons, we can study two color QCD : here, not only one can study fermionic observables, but it is also possible to observe the effects of a density of baryons on the gauge fields. This is indeed an active field of research, and I refer to the proceedings of the Lattice meetings for details.

How about 'real' QCD? there is a growing consensus that at least the high temperature, small density region is accessible: by increasing temperature it is easier to fluctuate light baryons, hence to explore a region with a moderate baryon density. At least three different, complementary approaches stem from this consideration:direct evaluation of derivatives at  $\mu = 0$ , reweighting, analytic continuation from purely imaginary chemical potential. This last point has been discussed by M. D'Elia at this meeting. For the other we refer to the Lattice proceedings.

One final remark concerns the interplay of this 'exact' lattice approach and model calculations. Excellent examples are already to be found in the studies of two color QCD, whose fermionic sector compares well with the prediction of chiral perturbation theory.

---

<sup>c</sup>If this is not the case, one might think of using  $S^\dagger$  instead: this has to be used 'cum grano salis' because it introduces extra degrees of freedom which might well be dangerous.

A very interesting point is finally the possibility of using the critical line derived within a random matrix model approach<sup>13</sup> as an ansatz to analytically continue the critical line obtained at imaginary chemical potential to real chemical potential. Hopefully, this will complement and validate analytic continuations based on the Taylor expansion.

I hope to have managed to convey the feeling of a rapidly evolving field: I refer to a very recent and authoritative review<sup>14</sup> (not yet available at the time of the Frascati meeting) for a more detailed account on the recent progress.

## References

1. N. Cabibbo, introductory remarks, this volume.
2. H. Satz, *ibid.*
3. G. Nardulli, *ibid.*; M. Mannarelli, *ibid.*
4. F. Sannino, *ibid.*; W. Schaefer, *ibid.*
5. L. Del Debbio, *ibid.*; A. Drago, *ibid.*; D. Cosmai, *ibid.* ; A. Papa, *ibid.*
6. E. Meggiolaro, *ibid.*
7. M. d'Elia, *ibid.*
8. Introductory material on the lattice approach to field theory can be found in J. B. Kogut, Rev.Mod.Phys.51 (1979) 659; M. Creutz, *Quarks, Gluons and Lattice*, Cambridge; C. Itzykson-Douffre, *Statistical Field Theory*, Cambridge, Chapter 7;
9. M. Alford, [hep-ph/0102047](#); K. Rajagopal and F. Wilczek, in 'At the Frontier of Particle Physics / Handbook of QCD', M. Shifman, ed., (World Scientific); R. Rapp, T. Schafer, E.V. Shuryak, M. Velkovsky , Annals Phys.280 (2000)35;
10. For an introduction to numerical simulations of lattice QCD thermodynamics see C. DeTar, in Hwa, R.C. (ed.): Quark-gluon plasma, vol.2 , pag. 1 or F. Karsch, [hep-lat/0206034](#), which includes also a review of recent results.
11. R. D. Pisarski and F. Wilczek , Phys.Rev. D29 (1984)338 ;
12. J. Engels, S. Mashkevich, T. Scheideler, G. Zinovev , Phys.Lett.B365 (1996) 219;
13. M. Stephanov, K. Rajagopal, E. Shuryak, Phys. Rev. Lett. Phys.Rev.Lett.81 (1998) 4816; J. Berges and K. Rajagopal, Nucl.Phys. B538 (1999) 215; M.A. Halasz, A.D. Jackson, R.E. Shrock, M.A. Stephanov and J.J.M. Verbaarschot, Phys.Rev.D58 (1998) 096007; M. Stephanov, K. Rajagopal, E. Shuryak, Phys.Rev.D60 (1999) 114028.
14. J. B. Kogut, plenary talk at Lattice2002, to appear

# EFFECTIVE FIELDS IN DENSE QUANTUM CHROMODYNAMICS

G. NARDULLI

*Dipartimento di Fisica, Università di Bari, I-70124 Bari, Italia  
I.N.F.N., Sezione di Bari, I-70124 Bari, Italia  
E-mail: giuseppe.nardulli@ba.infn.it*

In the high density, low temperature limit, Quantum Chromodynamics exhibits a transition to phases characterized by color superconductivity and energy gaps in the fermion spectra. We review some fundamental results obtained in this area and in particular we describe the low energy effective lagrangian describing the motion of the quasi-particles in the high density medium (High Density Effective Theory).

## 1 Lecture I: Color superconductivity

### 1.1 Introduction

At high baryonic densities and small temperatures the color interaction favors the formation of quark-quark condensates in the color attractive antisymmetric channel:

$$\Delta = \langle \psi_{i\alpha}^T C \psi_{j\beta} \rangle \epsilon^{\alpha\beta\gamma} \epsilon^{ijk} \Omega_{\gamma k} \neq 0 \quad (1)$$

( $\alpha, \beta, \gamma = 1, 2, 3$  color indices;  $i, j, k = 1, 2, 3$  flavor indices). The condensates (1) depend on the matrix  $\Omega$  and act as order parameters of new phases where the  $SU(3)_c$  color symmetry is spontaneously broken. The densities are so high that these phenomena might probably occur only in the core of neutron stars. Since this mechanism is similar to electron superconductivity it is referred to as color superconductivity (CSC)<sup>1</sup>. This is one of the most fascinating advances in Quantum Chromo Dynamics (QCD) in recent years<sup>2,3,4</sup> (for reviews see<sup>5</sup>). The aim of these lectures is to describe an approach to this aspect of QCD that is based on the method of the effective lagrangians<sup>6,7,8,9</sup> and to stress possible astrophysical consequences.

Different phenomena take place depending on the value of the order parameter (1). One could have:  $\Omega_{\gamma k} = \delta_{\gamma 3} \delta_{k 3}$ , which corresponds to

$$\epsilon^{\alpha\beta\gamma} \epsilon_{ij} < \psi_{i\alpha}^T C \psi_{j\beta} > = \Delta \delta^{\gamma 3} \quad (2)$$

where the sum over the flavor indices run from 1 to 2 and  $\psi$  represents a left handed 2-component Weyl spinor (the right handed field satisfies a similar relation); moreover a sum over spinor indices is understood and  $C = i\sigma_2$ . This

case correspond to decoupling of the strange quark ( $m_s \rightarrow \infty$ ;  $m_u = m_d = 0$ ) and is called 2SC model. From dynamical analyses<sup>2,5</sup> one knows that, for  $\mu$  sufficiently large, the condensate (2) is non vanishing. Therefore it breaks the original symmetry group  $SU(3)_c \otimes SU(2)_L \otimes SU(2)_R \otimes U(1)_B$  down to  $SU(2)_c \otimes SU(2)_L \otimes SU(2)_R \otimes Z_2$ . The chiral group remains unbroken, while the original color symmetry group is broken to  $SU(2)_c$ , with generators  $T^A$  corresponding to the generators  $T^1, T^2, T^3$  of  $SU(3)_c$ ; an unbroken  $U(1)_{\tilde{B}}$  also remains. As a consequence, three gluons remain massless whereas the remaining five acquire a mass. One can construct an effective theory to describe the emergence of the unbroken subgroup  $SU(2)_c$  and the low energy excitations, much in the same way as one builds up chiral effective lagrangian with effective fields at zero density. For the two flavor case this development can be found in<sup>10</sup>.

For the three flavor case ( $m_u = m_d = m_s = 0$ ) the following case has been widely discussed<sup>3</sup>:

$$\langle \psi_{i\alpha}^L \psi_{j\beta}^L \rangle = -\langle \psi_{i\alpha}^R \psi_{j\beta}^R \rangle = \Delta \sum_{K=1}^3 \epsilon_{\alpha\beta K} \epsilon_{ijK} . \quad (3)$$

The condensate (3) breaks the original symmetry group  $SU(3)_c \otimes SU(3)_L \otimes SU(3)_R \otimes U(1)_B$  down to  $SU(3)_{c+L+R} \otimes Z_2$ . Both the chiral group,  $U(1)_B$  and the color symmetry are broken but a diagonal  $SU(3)$  subgroup remains unbroken in a way that locks together color and flavor (Color-Flavor-Locking=CFL model). There are 17 broken generators; since there is a broken gauge group, 8 of these generators correspond to 8 longitudinal degrees of freedom of the gluons, because the gauge bosons acquire a mass; there are 9 Nambu-Godstone Bosons (NGB's) organized in an octet associated to the breaking of the flavor group and in a singlet associated to the breaking of the baryonic number. The effective theory describing the NGB for the CFL model was studied in<sup>11</sup>.

Another interesting possibility arises when there is a difference  $\delta\mu$  between the chemical potentials of the two gapped quarks (for references see<sup>12</sup>; see also<sup>13,14</sup> and for earlier works<sup>15</sup>). As shown in<sup>12</sup> when the two fermions have different chemical potentials  $\mu_1 \neq \mu_2$ , for  $\delta\mu$  of the order of the gap the vacuum state is characterized by a non vanishing expectation value of a quark bilinear which breaks translational and rotational invariance. The appearance of this condensate is a consequence of the fact that for  $\mu_1 \neq \mu_2$ , and in a given range of  $\delta\mu = |\mu_1 - \mu_2|$ , the formation of a Cooper pair with a total momentum  $\vec{p}_1 + \vec{p}_2 = 2\vec{q} \neq \vec{0}$  is energetically favored in comparison with the normal BCS state. The possible form of these condensates is discussed in<sup>12</sup> and<sup>13</sup> (see also<sup>14</sup>); it is worthwhile to note that, for simplicity, these authors assume only two flavors. In<sup>12</sup> the ansatz of a plane wave behavior for the condensate is made :  $\propto e^{2i\vec{q}\cdot\vec{x}}$ ; in<sup>13</sup> it is shown that the configuration

that is energetically favored is a face centered cubic crystal. For simplicity I will consider here only the plane wave:

$$-\langle 0 | \epsilon_{ij} \epsilon_{\alpha\beta 3} \psi^{i\alpha}(\vec{x}) C \psi^{j\beta}(\vec{x}) | 0 \rangle = 2\Gamma_A^L e^{2i\vec{q}\cdot\vec{x}}; \quad (4)$$

besides the scalar condensate (4) there is also a vector condensate that can be however neglected since it is numerically small. The 2SC and/or the LOFF phases might exist for intermediate values of the chemical potentials, while for very high  $\mu$  the CFL phase should set in.

The phase transition and the non vanishing condensates result from a mechanism analogous to the formation of an electron Cooper pair in a BCS superconductor. At  $T = 0$  the only QCD interactions are those involving fermions near the Fermi surface. Quarks inside the Fermi sphere cannot interact because of the Pauli principle, unless the interactions involve large momentum exchanges. In this way the quarks can escape the Fermi surface, but these processes are disfavored, as large momentum transfers imply small couplings due to the asymptotic freedom property of QCD. Even though interactions of fermions near the Fermi surface involve momenta of the order of  $\mu$ , their effects are not necessarily negligible. As a matter of fact, even a small attractive interaction between fermions near the Fermi surface and carrying opposite momenta can create an instability and give rise to coherent effects. This is what really happens <sup>2,3</sup> and the result is the formation of a diquark condensate, as expressed by (2), (3) or (4). We stress again that the only relevant fermion degrees of freedom are therefore those near the Fermi surface. In <sup>6</sup> an effective theory for the CFL model was discussed, based on the approximation of the neglect of the negative energy states. This results in a rather terse formalism displaying as a characteristic note the existence of a Fermi velocity superselection rule and effective velocity-dependent fermion fields. We will refer to this effective lagrangian as the High Density Effective Theory (HDET). In <sup>7</sup> the 2SC model has been studied by the same formalism, while in <sup>8</sup> this effective theory has been applied to the crystalline color superconducting phase <sup>12</sup>, the so-called LOFF <sup>15</sup> phase.

The aim of these lectures is to review some developments in the description of Color Super Conductivity that are based on the HDET approach. This will be mainly done in the second lecture. Here I wish to discuss some possible astrophysical implications of CSC, in particular in the LOFF phase.

## 1.2 Astrophysical implications of the LOFF phase

Besides its theoretical interest for the study of the phase structure of QCD theory, the crystalline phase may result relevant for astrophysical dense sys-

tems, in particular in the explanation of the glitches in the pulsars.

The pulsars are rapidly rotating stellar objects, characterized by the presence of strong magnetic fields and by an almost continuous conversion of rotational energy into electromagnetic radiation. The rotation periods can vary in the range  $10^{-3}$  sec up to a few seconds; these periods increase slowly and never decrease except for occasional glitches, when the pulsar spins up with a variation in frequency that can be  $\delta\Omega/\Omega \approx 10^{-6}$  or smaller. Glitches are a typical phenomenon of the pulsars, in the sense that probably all the pulsar have glitches.

Pulsar are commonly identified with neutron stars; these compact stars are characterized by a rather complex structure comprising a core, an intermediate region with superfluid neutrons and a metallic crust. The ordinary explanation of the glitches is based on the idea that these sudden jumps of the rotational frequency are due to the movements outwards of rotational vortices in the neutron superfluid and their interaction with the crust. This is one of the main reasons that allow the identification of pulsars with neutron stars, as only neutron stars are supposed to have a metallic crust. Since the conventional models for glitches may be not familiar to an audience of nuclear and/or high energy physicists, I will briefly review them in the sequel.

It is known that a boson liquid at  $T \sim 0$  forms a condensate whose wavefunction

$$\Xi_0 = \sqrt{n_0(t, \vec{r})} e^{i\Phi(t, \vec{r})} \quad (5)$$

has a macroscopic meaning, due to the large number of particles in it. Also the probability current density

$$\vec{j}_{cond} = \frac{i\hbar}{2m} (\Xi_0 \nabla \Xi_0^* - \Xi_0^* \nabla \Xi_0) = \frac{\hbar}{m} n_0 \nabla \Phi \quad (6)$$

has such macroscopic meaning. Since  $\vec{j}_{cond} = n_0 \vec{v}_s$ , where  $\vec{v}_s$  is the condensate velocity that can be identified with the superfluid velocity, we get

$$\vec{v}_s = \frac{\hbar}{m} \vec{\nabla} \Phi . \quad (7)$$

The consequence of (7) is

$$\oint_{\gamma} \vec{v}_s \cdot d\vec{\ell} = 0 , \quad (8)$$

if the domain where the curve  $\gamma$  lies is simply connected. Given the arbitrariness of  $\gamma$ , a different way to write this result is

$$\vec{\nabla} \wedge \vec{v}_s = 0 . \quad (9)$$

Let us now suppose that the vessel containing the liquid is put in rotation with angular velocity  $\vec{\Omega}$ . A consequence of (8) is that the superfluid cannot rotate; to the same result one arrives by noting that the vessel cannot communicate the rotation to the superfluid component, as there is no friction between the recipient and the liquid. However it can be shown that the absence of rotation in the superfluid does not correspond to a state of minimal energy. As a matter of fact, if  $E$  and  $\vec{L}$  are energy and angular momentum in an inertial frame, the energy as computed in the rotating frame is  $E_{rot} = E - \vec{L} \cdot \vec{\Omega}$ . If  $\Omega$  is sufficiently high, then a lower energy can be achieved with

$$\vec{L} \cdot \vec{\Omega} > 0 \quad (10)$$

instead of  $\vec{L} \cdot \vec{\Omega} = 0$  that corresponds to the absence of rotation <sup>16</sup>.

Let us suppose for simplicity that the curve  $\gamma$  lies in a plane. For the result (10) to be compatible with (8) one has to suppose that inside the curve  $\gamma$  there is one point where (9) is violated. Physically this would correspond to the presence of a point with a normal, not superfluid component. Since now the domain is not simply connected, (8) is substituted by

$$\oint_{\gamma} \vec{v}_s \cdot d\vec{\ell} = 2\pi n\kappa , \quad (11)$$

where the integer  $n$  is a winding number counting the number of times the curve goes around the singular point, and  $\kappa$  is a constant with dimensions of *vorticity*, i.e.  $[L]^2 \cdot [T]^{-1}$ . To the same result one could arrive by noting that, by virtue of (7), as  $\Phi$  and  $\Phi + 2n\pi$  correspond to the same wavefunction, one may have

$$\oint_{\gamma} \vec{\nabla}\Phi \cdot d\vec{\ell} = 2\pi n , \quad (12)$$

which shows that  $\kappa = \hbar/m$ ;  $\kappa$  is called quantum of vorticity.

Clearly we can repeat the argument for any plane parallel to the previous one; we therefore conclude that there is an entire line (*vortex line*) of singular points. If this line is a straight line, then  $\vec{v}_s$  will be perpendicular to the vortex line and also perpendicular to the radius joining the singular point and the point at which we compute  $v_s$ . At a distance  $r$  from the singular point one has

$$v_s = \frac{n\kappa}{r} , \quad (13)$$

as can be immediately seen from (11). More generally:

$$\vec{v}_s = \frac{\kappa}{2} \int_{v.l.} \frac{d\vec{\ell} \wedge \vec{R}}{R^3} , \quad (14)$$

where  $\vec{R}$  is the distance vector from the vortex line (v.l.) to the point at which we compute the superfluid velocity.

We note some properties of the vortex lines. First, the integral (11) is independent of  $\gamma$ , provided the second curve contains the singular point; this result follows from the Stokes theorem. Second, the vortex line must be closed or it must stop at the boundary; were it open, for example at a point P, one might construct a surface  $\Sigma$  lying on the contour  $\gamma$  but large enough as to have no intersection with the vortex line; therefore by the Stokes theorem one would get that the vorticity constructed by  $\vec{v}_s$  would be zero. If the vortex line stops at the boundary and the vessel is rigid then the v.l. is pinned at the boundary, as it will be discussed in more detail below.

Let us compute the critical angular velocity  $\Omega$  for the formation of the first vortex line. The formation of a vortex line changes the energy  $E_{rot}$  by the amount  $\Delta E_{rot} = \Delta E - \Delta (\vec{L} \cdot \vec{\Omega})$ . We have  $\Delta E = \int \frac{\rho_s v_s^2}{2} dV$ . Here the integral is over the entire volume of the vessel that, for simplicity, we assume to be a cylinder of height  $b$  and radius  $R$ ; on the other hand  $v_s$  is given by the expression valid for a vortex line, i.e. (13). Therefore

$$\Delta E = \frac{\rho_s b}{2} 2\pi \int v_s^2 r dr = b \rho_s \pi \frac{\hbar^2 n^2}{m^2} \ln \frac{R}{a} \quad (15)$$

where  $a$  is a cutoff of the order of the interatomic distances, at which the macroscopic description fails down. The minimal energy  $E_{rot}$  is obtained for  $\vec{L}$  parallel to  $\vec{\Omega}$ , with  $L = \int \rho_s v_s r dV = b\pi R^2 \frac{n\hbar}{m} \rho_s$ . Vortex lines appear if  $\Delta E_{rot} < 0$ , i.e. if

$$\frac{n\hbar}{m} \ln \frac{R}{a} - \Omega R^2 < 0, \quad (16)$$

which corresponds to  $\Omega > \Omega_{crit} = \frac{\hbar}{mR^2} \ln \frac{R}{a}$ . Incidentally we note that, *ceteris paribus*, vortex lines with  $n = 1$  are more stable than those with  $n > 1$ , as the positive term in (16) has an extra power of  $n$ . Therefore from now on we put  $n = 1$ .

What happens when  $\Omega \gg \Omega_{crit}$ ? Clearly we expect there will be several v.l.'s. During the rotation these vortex lines follow the rotational motion of the vessel, which is clear because they are pinned at the boundary of the superfluid<sup>a</sup>. Their motion imitate the motion of the liquid as a whole, as it can

---

<sup>a</sup>For rotations around an axis, the vortex lines are, by symmetry, straight lines parallel to the rotation axis. For motion inside holes, slits, etc. there can be closed v.l.'s that are called *vortex rings*.

be seen by the following argument: in the formula for  $\Delta E_{crit}$  one can forget, for large  $\Omega$ , the first term  $\Delta E$  in comparison to the second one. Therefore minimizing  $\Delta E_{crit}$  correspond to maximize the angular momentum  $L$ , which is obtained if the liquid moves as a whole. A consequence of this feature of the motion of the v.l.'s is that also for the superfluid one can use the well known hydrodynamical formula  $\vec{\Omega} = \frac{1}{2} \vec{\nabla} \wedge \vec{v}_s$ , which strictly speaking is valid only for the normal component  $\vec{v}_n$ ; it can be used here only because it refers to the rotation of the superfluid as a whole.

The number of vortex lines that are present in the superfluid is proportional to  $\Omega$ , according to the formula ( $N$ =number of lines per unit area):

$$N = \frac{m\Omega}{\pi\hbar} \quad (17)$$

which shows that with increasing  $N$  the v.l.'s tend to fill in all the space. To prove (17) we consider a large closed curve  $C$  encircling the area  $A$  and containing in its interior  $NA$  v.l.'s. One has

$$\oint_C d\vec{\ell} \cdot \vec{v}_s = NA2\pi\kappa \quad (18)$$

but also

$$\oint_C d\vec{\ell} \cdot \vec{v}_s = \int_A d\vec{\sigma} \cdot \vec{\nabla} \wedge \vec{v}_s = 2A\Omega \quad (19)$$

from which (17) follows. As an example we can evaluate  $N$  for the pulsar in the Crab nebula. Here  $m = 2m_N$  (the condensate is formed by neutral bosons: pairs of neutrons) and  $\Omega = \Omega_{pulsar}$  gives  $N \simeq 1.9 \times 10^5 \text{ cm}^{-2}$  with an average distance between vortex lines  $d \sim N^{-1/2} \sim 10^{-2} \text{ cm}$ .

Let us consider again eqns. (12) and (18). If  $\nu(r)$  is the number of vortices per unit area at a distance  $r$  from the rotation axis, they give, if  $\vec{v} = \vec{v}_s$  is the superfluid velocity,

$$\oint d\vec{\ell} \cdot \vec{v} = \int_0^r d\vec{S} \cdot \vec{\nabla} \wedge \vec{v} = 2\pi\kappa \int_0^r 2\pi r' \nu(r') dr' . \quad (20)$$

We put

$$k = 2\pi\kappa = \frac{\hbar}{2m_n} \quad (21)$$

and write (20) as follows:

$$2\pi r^2 \Omega(r) = k \int_0^r 2\pi r' \nu(r') dr' , \quad (22)$$

which implies

$$k\nu(r) = 2\Omega(r) + r \frac{\partial\Omega}{\partial r}. \quad (23)$$

Since the total number of v.l.'s is conserved, one has

$$\frac{\partial\nu}{\partial t} + \vec{\nabla} \cdot (\nu \vec{v}_r) = 0 \quad (24)$$

where  $\vec{v}_r$  is the radial component of the superfluid velocity. We write (22) as

$$2\pi r^2 \Omega(r) = k \int_0^r \nu dS \quad (25)$$

and take the time derivative, using (23) to get

$$2\pi r^2 \frac{\partial\Omega}{\partial t} = -k \int_0^r dS \vec{\nabla}(\nu \vec{v}_r). \quad (26)$$

Using the Gauss theorem one gets  $2\pi r^2 \frac{\partial\Omega}{\partial t} = -k 2\pi r \nu v_r$ , i.e.

$$\frac{\partial\Omega}{\partial t} = -\frac{k\nu v_r}{r} = -\left(2\Omega(r) + r \frac{\partial\Omega}{\partial r}\right) \frac{v_r}{r}. \quad (27)$$

Eq. (27) shows that *the only possibility for the superfluid to change its angular velocity ( $\dot{\Omega} \neq 0$ ) is by means of a radial motion, i.e.  $v_r \neq 0$ .*

Let us now consider a rotating superfluid in contact with rotating normal matter on which an external torque is acting <sup>17</sup>. We denote by  $I_c$ ,  $\Omega_c$  moment of inertia and angular velocity of the normal components that, in a neutron star, includes the crust and possibly other normal components. The equation of motion of the normal component is

$$I_c \dot{\Omega}_c(t) = M_{ext} + M_{int}. \quad (28)$$

Besides the external torque  $M_{ext}$ , basically related to the spin down of the pulsar (or the steady accretion in binary pulsars), we have included internal torque  $M_{int}$ :

$$M_{int} = - \int dI_p \dot{\Omega}(r, t) \quad (29)$$

due to the interaction with the superfluid. Eqs.(27-29) are the equations of motion for the angular velocities  $\Omega$  and  $\Omega_c$  (superfluid and crust). The two velocities are coupled not only through  $M_{int}$ , but also by  $v_r$ , because we will show below that  $v_r = f(\Omega - \Omega_c)$ . We note again that fundamental for this model is the existence of radial motion, for, if  $v_r = 0$ , then  $\Omega = const.$  and only  $\Omega_c$  changes, due to the external torque alone.

In the neutron star, superfluid neutrons (in Cooper pairs) coexist with nuclei of the crust. Also in the crust there are superfluid neutrons, but they are characterized by a different (and smaller)  $\Delta$ . For superfluid neutrons in the volume  $V$ , the total energy can be estimated as follows:

$$E \simeq \frac{V}{(2\pi\hbar)^3} \int_{p_F}^{p_F + \Delta^2/E_F} p^3 dp \frac{d\Omega}{2} = \frac{V}{4\pi^2} \frac{\Delta^2 k_F^3}{E_F} \quad (30)$$

where  $p_F = \hbar k_F$ ; we integrate over half the solid angle as the superfluid neutrons only appear in pairs; we have taken into account that only neutrons in a shell of thickness  $\Delta^2/E_F$  participate in the pairing.

$E$  is also approximately given by the difference between the energies of superfluid neutrons outside the vortex line and neutrons inside, because those inside the vortex core have  $\Delta \rightarrow 0$ . Therefore neutrons inside the volume  $V$  of the vortex core are repelled from going outside the vortex towards the superfluid phase as it would cost more energy. However, if neutron rich nuclei are present, the repulsion will be less important, as  $\Delta_c$ , the gap for superfluid neutrons in the nuclei, is much smaller than  $\Delta_s$ , the gap of superfluid neutrons; therefore there will be a force pulling the vortex toward the nuclei; the pinning energy per nucleus will be

$$\delta E_p = \frac{V}{8} \left[ \left( \frac{\Delta^2 k_F^3}{\pi^2 E_F} \right)_s - \left( \frac{\Delta^2 k_F^3}{\pi^2 E_F} \right)_c \right] \approx \gamma \frac{V}{8} \left( \frac{\Delta^2 k_F^3}{\pi^2 E_F} \right)_s \quad (31)$$

with  $\gamma \sim 1$ .

Let now  $\xi$  be the *coherence length*, i.e. the spatial extension of the Cooper pair,  $\xi = \frac{\hbar v_F}{\pi \Delta}$ ; it can be proved that it gives an estimate of the radius of the vortex core. The maximum pinning force will be obtained, if  $2\xi < b$  ( $b$  the average distance between the nuclei) when the vortex passes through one layer of the lattice; the average distance between vortex core neutrons and superfluid neutrons is of the order of  $\xi$  and therefore the maximum force is  $F_p \simeq \frac{\delta E_p}{\xi}$  and the maximum force per unit length of vortex line ( $b$  is also the average distance between two consecutive pinning centers) is

$$f_p \simeq \frac{\delta E_p}{b\xi}. \quad (32)$$

Let us finally discuss a possible mechanism for the formation of glitches<sup>17</sup>; we consider the rotating neutron star with superfluid neutrons in its interior and a metallic crust, which is a simplified model, but adequate to our purposes. We distinguish between two angular velocities: the superfluid velocity  $\Omega$  and

the crust velocity  $\Omega_c$ . Let us suppose that they are initially equal, which is a consequence of the pinning. Due to the spinning down of the star,  $\Omega_c$  decreases; as long the vortex cores are pinned to the crust lattice, the neutron superfluid cannot spin down, because the radial motion is forbidden. There is therefore a relative velocity of the superfluid with respect to the pinned vortex core because  $\Omega > \Omega_c$ :

$$\delta\vec{v} = (\vec{\Omega} - \vec{\Omega}_c) \wedge \vec{r} . \quad (33)$$

The interaction between the normal matter in the core of the v.l. and the rest of normal matter (nuclei in the lattice, electrons, etc.) produces a Magnus force per unit length given by

$$\vec{f} = \rho \vec{k} \wedge \delta\vec{v} , \quad (34)$$

where  $k$  is the quantum of vorticity and the direction of  $\vec{k}$  coincides with the rotation axis.  $f$  is the force exerted on the vortex line; as it cannot be larger than  $f_p$  there is a maximum difference of angular velocity that the system can maintain:

$$\omega_{cr} = (\Omega - \Omega_c)_{max} = \frac{f_p}{\rho k r} = \frac{E_p}{\rho k \xi b} . \quad (35)$$

If  $\omega < \omega_{cr}$  the vortices remain pinned at the lattice sites instead of flowing with the superfluid as they generally in superfluid (see discussion above). On the contrary, if  $\omega > \omega_{cr}$ , the hydrodynamical forces arising from the mismatch between the two angular velocities ultimately break the crust and produce the conditions for the glitch.

We stop here this introduction to the standard model for glitches; see <sup>17</sup> for more details. The relevance for CSC is that the LOFF phase provides a lattice structure independently of the crust. Even in quark stars, if one is in a LOFF phase, one has a crystal structure: a lattice characterized by a geometric array where the gap parameter varies periodically. This would avoid the frequently raised objection by which one excludes the existence of strange stars because, if the strange matter exists, quark stars should be rather common, in contrast with the widespread appearance of glitches in pulsars. Therefore, if the color crystalline structure is able to produce glitches, the argument in favor of the existence of strange stars would be reinforced.

In a more conservative vein one can also imagine that the LOFF phase be realized in the inner core of a neutron star; in this case the crystalline color superconductivity could be partly responsible for the glitches of the pulsar. A detailed analysis of this scenario is however premature as one should first complete the study of the LOFF phase by including the third quark and by sorting out the exact form of the color lattice <sup>13,14</sup>.

## 2 Lecture II: High Density Effective Theory

In this section we derive the general formalism of High Density Effective Theory and we present an example of its use. This effective theory shows some resemblance with the Heavy Quark Effective Theory (see e.g. <sup>18</sup>); it is discussed in detail in the review paper <sup>9</sup>.

### 2.1 General Formalism

The main idea of the effective theory is the observation that the quarks participating in the dynamics have large ( $\sim \mu$ ) momenta. Wherefore one can introduce velocity dependent fields by extracting the large part  $\mu\vec{v}$  of this momentum. One starts with the Fourier decomposition of the quark field  $\psi(x)$ :

$$\psi(x) = \int \frac{d^4 p}{(2\pi)^4} e^{-i p \cdot x} \psi(p) , \quad (36)$$

and introduces the quark velocity by

$$p^\mu = \mu v^\mu + \ell^\mu , \quad (37)$$

where  $v^\mu = (0, \vec{v})$  with  $|\vec{v}| = 1$ . Let us put  $\ell^\mu = (\ell^0, \vec{\ell})$  and  $\vec{\ell} = \vec{v}\ell_{||} + \vec{\ell}_{\perp}$  with  $\vec{\ell}_{\perp} = \vec{\ell} - (\vec{\ell} \cdot \vec{v})\vec{v}$ . We can always choose the velocity parallel to  $\vec{p}$ , so that  $\vec{\ell}_{\perp} = 0$  and

$$\int d^4 p = \mu^2 \int d\Omega \int d\ell_{||} \int_{-\infty}^{+\infty} d\ell_0 = 4\pi\mu^2 \int \frac{d\vec{v}}{4\pi} \int d\ell_{||} \int_{-\infty}^{+\infty} d\ell_0 . \quad (38)$$

In this way the Fourier decomposition (36) takes the form

$$\psi(x) = \sum_{\vec{v}} e^{-i\mu v \cdot x} \int \frac{d^4 \ell}{(2\pi)^4} e^{-i\ell \cdot x} \psi_{\vec{v}}(\ell) = \sum_{\vec{v}} e^{-i\mu v \cdot x} \frac{4\pi\mu^2}{(2\pi)^4} \int d^2 \ell e^{-i\ell \cdot x} \psi_{\vec{v}}(\ell) , \quad (39)$$

where  $\psi_{\vec{v}}(\ell)$  are velocity-dependent fields. One can write

$$\psi(x) = \sum_{\vec{v}} e^{-i\mu v \cdot x} [\psi_+(x) + \psi_-(x)] , \quad (40)$$

where  $\psi_{\pm}$  are velocity dependent fields corresponding to positive and energy solutions of the Dirac equation.

Let us now define  $V^\mu = (1, \vec{v})$ ,  $\tilde{V}^\mu = (1, -\vec{v})$ ,  $\gamma_{||}^\mu = (\gamma^0, (\vec{v} \cdot \vec{\gamma}) \vec{v})$ ,  $\gamma_\perp^\mu = \gamma^\mu - \gamma_{||}^\mu$ . Using simple algebraic relations involving the gamma matrices <sup>9</sup> one

obtains

$$\mathcal{L}_D = \sum_{\vec{v}} \left[ \psi_+^\dagger iV \cdot D \psi_+ + \psi_-^\dagger (2\mu + i\tilde{V} \cdot D) \psi_- + (\bar{\psi}_+ iD_\mu \gamma_\perp^\mu \psi_- + \text{h.c.}) \right]; \quad (41)$$

$D_\mu$  is the covariant derivative:  $D^\mu = \partial^\mu + igA^\mu$ . We note that here quark fields are evaluated at the same Fermi velocity; off-diagonal terms are sub-leading due to the Riemann-Lebesgue lemma, as they are cancelled by the rapid oscillations of the exponential factor in the  $\mu \rightarrow \infty$  limit. One may call this phenomenon *Fermi velocity superselection rule*, in analogy with the behaviour of QCD in the  $m_Q \rightarrow \infty$  limit, where the corresponding effective theory, the Heavy Quark Effective Theory exhibits a similar phenomenon<sup>18</sup>. By the same analogy we may refer to the present effective theory as High Density Effective Theory (HDET),

We can get rid of the negative energy solutions by integrating out the  $\psi_-$  fields in the generating functional; in this way we get

$$\mathcal{L}_D \simeq \mathcal{L}_0 = \sum_{\vec{v}} \left[ \psi_+^\dagger iV \cdot \partial \psi_+ + \psi_-^\dagger i\tilde{V} \cdot \partial \psi_- \right], \quad (42)$$

where now  $\psi_\pm$  are both positive energy solutions with  $\psi_\pm = \psi_{\pm\vec{v}}$ . The construction described above is valid for any theory describing massless fermions at high density provided one excludes degrees of freedom very far from the Fermi surface. As discussed in the first lecture however, for small temperature and high density the fermions are likely to be gapped due to the phenomenon of the color superconductivity. We shall examine here the modification in the formalism for the LOFF model, with the condensate

$$\Delta(\vec{x}) = \Delta \exp\{2i\vec{q} \cdot \vec{x}\}. \quad (43)$$

The effect of the non vanishing vacuum expectation value can be taken into account by adding to the lagrangian the term:

$$\mathcal{L}_\Delta = -\frac{\Delta}{2} \exp\{2i\vec{q} \cdot \vec{x}\} \epsilon_{\alpha\beta\gamma} \epsilon_{ij} \psi_{i\alpha}^T(x) C \psi_{j\beta}(x) - (L \rightarrow R) + \text{h.c.} . \quad (44)$$

In order to introduce velocity dependent positive energy fields  $\psi_{\vec{v}_i; i\alpha}$  with flavor  $i$  we decompose both fermion momenta as in (37) and we have:

$$\begin{aligned} \mathcal{L}_\Delta = & -\frac{\Delta}{2} \sum_{\vec{v}_i, \vec{v}_j} \exp\{i\vec{x} \cdot \vec{\alpha}(\vec{v}_i, \vec{v}_j, \vec{q})\} \epsilon_{ij} \epsilon_{\alpha\beta\gamma} \psi_{-\vec{v}_i; i\alpha}(x) C \psi_{-\vec{v}_j; j\beta}(x) \\ & -(L \rightarrow R) + \text{h.c.}, \end{aligned} \quad (45)$$

where  $\vec{\alpha}(\vec{v}_i, \vec{v}_j, \vec{q}) = 2\vec{q} - \mu_i \vec{v}_i - \mu_j \vec{v}_j$ . We define

$$\mu = \frac{\mu_1 + \mu_2}{2}, \quad \delta\mu = -\frac{\mu_1 - \mu_2}{2}, \quad (46)$$

and perform the  $\mu \rightarrow \infty$  limit on a smeared amplitude as follows

$$\lim_{\mu \rightarrow \infty} \exp\{i\vec{x} \cdot \vec{\alpha}(\vec{v}_1, \vec{v}_2, \vec{q})\} \equiv \frac{1}{V} \int_{V(\vec{x})} d\vec{r} \exp\{i\vec{r} \cdot \vec{\alpha}(\vec{v}_1, \vec{v}_2, \vec{q})\}, \quad (47)$$

where  $V(\vec{x})$  is a small volume centered at  $\vec{x}$ . We evaluate (47) by taking  $\vec{q}$  along the  $z-axis$ , so that we get:  $\vec{v}_i \simeq -\vec{v}_j \equiv -\vec{v}$  by the  $x$  and  $y$  integrations, while the  $z$ -integration gives ( $\vec{n} = \vec{q}/q$ )

$$\frac{\pi}{R} e^{i2qhz} \delta_R[h(\vec{v} \cdot \vec{n})] \approx \frac{\pi}{R} \delta_R[h(\vec{v} \cdot \vec{n})]. \quad (48)$$

We have put  $R = q|\Delta\ell|$  where  $\Delta\ell$  is a smearing distance along the direction of  $\vec{q}$  ( $|\Delta\ell| \sim \frac{\pi}{q}$ ). We have introduced the "fat delta"  $\delta_R(x)$  defined by

$$\delta_R(x) \equiv \frac{\sin(Rx)}{\pi x}, \quad (49)$$

which, for large  $R$ , gives  $\delta_R(x) \rightarrow \delta(x)$ . Moreover in the  $\mu \rightarrow \infty$  limit  $h(x) = 1 - \frac{\delta\mu}{qx}$ . Therefore one has

$$\mathcal{L}_\Delta = -\frac{\Delta}{2} \frac{\pi}{R} \delta_R[h(\vec{v} \cdot \vec{n})] \sum_{\vec{v}} \epsilon_{ij} \epsilon_{\alpha\beta 3} \psi_{\vec{v}; i\alpha}(x) C \psi_{-\vec{v}; j\beta}(x) - (L \rightarrow R) + \text{h.c..} \quad (50)$$

In an appropriate basis the effective lagrangian is

$$\mathcal{L} = \mathcal{L}_0 + \mathcal{L}_\Delta = \sum_{\vec{v}} \sum_{A=0}^5 \chi^{A\dagger} \begin{pmatrix} i\delta_{AB} V \cdot \partial & \Delta_{AB} \\ \Delta_{AB} & i\delta_{AB} \tilde{V} \cdot \partial \end{pmatrix} \chi^B, \quad (51)$$

where the matrix  $\Delta_{AB}$  is as follows:  $\Delta_{AB} = 0$  ( $A$  or  $B = 4$  or  $5$ ), and, for  $A, B = 0, \dots, 3$ :

$$\Delta_{AB} = \Delta_{eff} \begin{pmatrix} 1 & 0 & 0 & 0 \\ 0 & -1 & 0 & 0 \\ 0 & 0 & -1 & 0 \\ 0 & 0 & 0 & -1 \end{pmatrix}_{AB}, \quad (52)$$

having put

$$\Delta_{eff} = \frac{\Delta\pi}{R} \delta_R[h(\vec{v} \cdot \vec{n})]. \quad (53)$$

From these equations one can derive the propagator for gapped quarks:

$$D_{AB}(\ell) = \frac{1}{V \cdot \ell \tilde{V} \cdot \ell - \Delta_{eff}^2} \begin{pmatrix} \tilde{V} \cdot \ell \delta_{AB} & -\Delta_{AB} \\ -\Delta_{AB} & V \cdot \ell \delta_{AB} \end{pmatrix}. \quad (54)$$

## 2.2 NGB and their parameters

Both in the CFL model and in the LOFF model with two flavors there are Nambu-Goldstone Bosons, associated in one case to the breaking of internal symmetries and in the other to the breaking of space-symmetries (phonon). In order to derive an effective low energy lagrangian for the NGB's one can use the gradient expansion, where the NGB's are introduced as external fields and acquire a kinetic term, thus becoming dynamical fields, by integrating out the fermion fields. I shall describe in some detail the calculation for the phonon field in the LOFF phase (other examples can be found in <sup>9</sup>).

$\mathcal{L}_\Delta$  in (44) explicitly breaks rotations and translations and induces a lattice structure given by plane waves. The crystal can fluctuate and its local deformations define one phonon field  $\phi$  that is the Nambu-Goldstone boson associated to the breaking of the translational symmetry. It is introduced by the substitution in (43)

$$z \rightarrow z + \frac{\phi}{2qf}, \quad (55)$$

with  $\langle \phi \rangle_0 = 0$ . We are interested in an effective description of the field  $\phi$  in the low energy limit, i.e. for wavelengths much longer than the lattice spacing  $\sim 1/q$ . In this limit the field  $\phi$  varies almost continuously and we can get rid of the lattice structure and use in the sequel the continuous notation.

At the first order one gets the couplings

$$\mathcal{L}_{\phi\psi\psi} = - \sum_{\vec{v}} \frac{\pi\Delta}{R} \delta_R[h(\vec{v} \cdot \vec{n})] \frac{i\phi}{f} \epsilon_{ij} \epsilon^{\alpha\beta 3} \psi_{i,\alpha,\vec{v}} C \psi_{j,\beta,-\vec{v}} - (L \rightarrow R) + h.c. \quad (56)$$

$$\mathcal{L}_{\phi\phi\psi\psi} = \sum_{\vec{v}} \frac{\pi\Delta}{R} \delta_R[h(\vec{v} \cdot \vec{n})] \frac{\phi^2}{2f^2} \epsilon_{ij} \epsilon^{\alpha\beta 3} \psi_{i,\alpha,\vec{v}} C \psi_{j,\beta,-\vec{v}} - (L \rightarrow R) + h.c. \quad (57)$$

In the basis of the  $\chi$  fields one has:

$$\mathcal{L}_3 + \mathcal{L}_4 = \sum_{\vec{v}} \sum_{A=0}^3 \tilde{\chi}^{A\dagger} \begin{pmatrix} 0 & g^\dagger \\ g & 0 \end{pmatrix} \tilde{\chi}^B. \quad (58)$$

Here

$$g = \left( \frac{\pi\Delta}{R} \delta_R[h(\vec{v} \cdot \vec{n})] \frac{i\phi}{f} - \frac{\pi\Delta}{R} \delta_R[h(\vec{v} \cdot \vec{n})] \frac{\phi^2}{2f^2} \right) \begin{pmatrix} 1 & 0 & 0 & 0 \\ 0 & -1 & 0 & 0 \\ 0 & 0 & -1 & 0 \\ 0 & 0 & 0 & -1 \end{pmatrix}_{AB} \quad (59)$$

To compute the effective lagrangian for the phonon field we use the propagator given in Eq. (54) and the interaction vertices in (58). The result of the calculation at the second order in the momentum expansion is <sup>b</sup>

$$\mathcal{L}_{eff}(p) = i \frac{4 \times 4 \mu^2}{16\pi^3 f^2} \sum_{\vec{v}} \frac{1}{2} \left( \frac{\pi \Delta}{R} \delta_R[h(\vec{v} \cdot \vec{n}_m)](i\phi) \right)^2 \int d^2 \ell \frac{2\Delta_{eff}^2 V \cdot p \tilde{V} \cdot p}{[D(\ell)]^3}. \quad (60)$$

One can handle the fat delta according to the Fermi trick in the Golden Rule; in expressions involving the gap parameters one makes in the numerator the substitution  $\delta_R[h(x)] \rightarrow \delta[h(x)]$ ; one fat delta is substituted by the Dirac delta while the other fat delta gives  $\frac{\pi \delta_R[h(x)]}{R} \rightarrow \frac{\pi \delta_R(0)}{R} \rightarrow 1$ . We finally get the effective lagrangian in the form

$$\mathcal{L}_{eff}(p) = - \frac{\mu^2 k_R}{2\pi^2 f^2} \sum_{\vec{v}} \delta \left\{ \vec{v} \cdot \vec{n} - \frac{\delta \mu}{q} \right\} V_\mu \tilde{V}_\nu p_\mu \phi p_\nu \phi. \quad (61)$$

Here  $k_R$  is kinematical factor of the order of 1 induced by the approximation of the Riemann-Lebesgue lemma <sup>8</sup>. The integration over fermi velocities can be easily performed and one obtains the effective lagrangian in the form

$$\mathcal{L}(\phi, \partial_\mu \phi) = \frac{1}{2} \left( \phi^2 - v_{\parallel}^2 |\vec{\nabla}_{\parallel} \phi|^2 - v_{\perp}^2 |\vec{\nabla}_{\perp} \phi|^2 \right), \quad (62)$$

if

$$f^2 = \frac{\mu^2 k_R}{2\pi^2}. \quad (63)$$

Here  $\vec{\nabla}_{\parallel} \phi = \vec{n}(\vec{n} \cdot \vec{\nabla})\phi$ ,  $\vec{\nabla}_{\perp} \phi = \vec{\nabla}\phi - \vec{\nabla}_{\parallel} \phi$ . Moreover

$$v_{\perp}^2 = \frac{1}{2} \sin^2 \theta_q, \quad (64)$$

$$v_{\parallel}^2 = \cos^2 \theta_q \quad (65)$$

and

$$\cos^2 \theta_q = \left( \frac{\delta \mu}{q} \right)^2. \quad (66)$$

Therefore the dispersion law for the phonon is anisotropic.

---

<sup>b</sup>One can easily control that the Goldstone theorem is satisfied and the phonon is massless.

## Acknowledgments

It is a pleasure to thank R. Casalbuoni, R. Gatto and M. Mannarelli for a very pleasant scientific collaboration on the themes of these lectures and the organizers of the GISELDA workshop at Frascati for an interesting and successful meeting.

## References

1. B. Barrois, *Nucl. Phys.* B **129**, 390 (1977); S. Frautschi, in *Proceedings of the workshop on hadronic matter at extreme density, Erice 1978*. See also: D. Bailin and A. Love, *Phys. Rept.* **107**, 325 (1984), and references therein.
2. M. Alford, K. Rajagopal and F. Wilczek, *Phys. Lett.* B **422**, 247 (1998) [[arXiv:hep-ph/9711395](#)].
3. M. Alford, K. Rajagopal and F. Wilczek, *Nucl. Phys.* B **537**, 443 (1999) [[arXiv:hep-ph/9804403](#)].
4. M. Alford, J. Berges and K. Rajagopal, *Nucl. Phys.* B **558**, 219 (1999) [[arXiv:hep-ph/9903502](#)]; T. Schäfer and F. Wilczek, *Phys. Rev. Lett.* **82**, 3956 (1999) [[arXiv:hep-ph/9811473](#)]; T. Schäfer and F. Wilczek, *Phys. Rev.* D **60**, 114033 (1999) [[arXiv:hep-ph/9906512](#)]; T. Schäfer and F. Wilczek, *Phys. Rev.* D **60**, 074014 (1999) [[arXiv:hep-ph/9903503](#)]; T. Schäfer and F. Wilczek, *Phys. Lett.* B **450**, 325 (1999) [[arXiv:hep-ph/9810509](#)]; G. W. Carter and D. Diakonov, *Phys. Rev.* D **60**, 16004 (1999) [[arXiv:hep-ph/9812445](#)]; E.V. Shuryak and M. Velkovsky, *Phys. Rev. Lett.* **81**, 53 (1998) [[arXiv:nucl-th/9711396](#)]; M. Alford, J. Berges K. and Rajagopal, *Nucl. Phys.* B **571**, 269 (2000) [[arXiv:hep-ph/9910254](#)]; R. D. Pisarski and D. H. Rischke, *Phys. Rev. Lett.* **83**, 37 (1999) [[arXiv:nucl-th/9811104](#)] and *Phys. Rev.* D **61**, 051501 (2000) [[arXiv:nucl-th/9907041](#)]; N. O. Agasian, B.O. Kerbikov and V. I. Schevchenko, *Phys. Rep.* **320**, 131 (1999) [[arXiv:hep-ph/9902335](#)]; E. Shuster and D.T. Son, *Nucl. Phys.* B **573**, 434 (2000) [[arXiv:hep-ph/9905448](#)]; D.K. Hong, V.A. Miransky, I.A. Shovkovy and L. C. R. Wijewardhana, *Phys. Rev.* D **61**, 056001 (2000), erratum, *ibidem*, **62** 59903 (2000) [[arXiv:hep-ph/9906478](#)]; F. Sannino and W. Shafer, *Phys. Lett.* B **527**, 142 (2002) [[arXiv:hep-ph/0111098](#)]; F. Sannino and W. Shafer [[arXiv:hep-ph/0204353](#)]. J. B. Kogut, M. P. Lombardo and D. K. Sinclair, *Phys. Rev.* D **51**, 1282 (1995) [[arXiv:hep-lat/9401039](#)]; *Nucl. Phys. Proc. Suppl.* **42**, 514 (1995) [[arXiv:hep-lat/9412057](#)].
5. K. Rajagopal and F. Wilczek, in *Handbook of QCD*, M.Shifman, ed.

- (World Scientific, 2001) [arXiv:hep-ph/0011333]. D. K. Hong [arXiv:hep-ph/0101025]; M. Alford [arXiv:hep-ph/0102047]; F. Sannino [arXiv:hep-ph/0205007]. S. D. H. Hsu [arXiv:hep-ph/0003140].
6. R. Casalbuoni, R. Gatto and G. Nardulli, *Phys. Lett. B* **498**, 179 (2001) [arXiv:hep-ph/0010321].
  7. R. Casalbuoni, R. Gatto, M. Mannarelli and G. Nardulli, *Phys. Lett. B* **524**, 144 (2001) [arXiv:hep-ph/0107024].
  8. R. Casalbuoni, R. Gatto, M. Mannarelli and G. Nardulli, *Phys. Lett. B* **511**, 218 (2001) [arXiv:hep-ph/0101326]. G. Nardulli [arXiv:hep-ph/0111178]. R. Casalbuoni, R. Gatto, M. Mannarelli and G. Nardulli [arXiv:hep-ph/0201059].
  9. G. Nardulli, to appear in *Riv. Nuovo Cimento* [arXiv:hep-ph/0202037].
  10. R. Casalbuoni, Z. Duan and F. Sannino, *Phys. Rev. D* **62**, 094004 (2000) [arXiv:hep-ph/0004207]; *Phys. Rev. D* **63**, 114026 (2001) [arXiv:hep-ph/0011394].
  11. R. Casalbuoni and R. Gatto, *Phys. Lett. B* **464**, 111 (1999) [arXiv:hep-ph/9908227].
  12. M. Alford, J. A. Bowers and K. Rajagopal *Phys. Rev. D* **63**, 074016 (2001) [arXiv:hep-ph/0008208]; J. A. Bowers, J. Kundu, K. Rajagopal and E. Shuster, *Phys. Rev. D* **64**, 014024 (2001) [arXiv:hep-ph/0101067]; A. K. Leibovich, K. Rajagopal and E. Shuster *Phys. Rev. D* **64**, 094005 (2001) [arXiv:hep-ph/0104073]; K. Rajagopal *Acta Phys. Polon. B* **31**, 3021 (2000) [arXiv:hep-ph/0009058]; M. Alford, J. A. Bowers and K. Rajagopal *J. Phys. G* **27**, 541 (2001) [arXiv:hep-ph/0009357]; T. Schäfer and E. Shuryak [arXiv:nucl-th/0010049]; K. Rajagopal in *QCD@Work*, P. Colangelo and G. Nardulli eds. (AIP, 2001) [arXiv:hep-ph/0109135].
  13. J.A. Bowers and K. Rajagopal [arXiv:hep-ph/0204079].
  14. R. Casalbuoni, R. Gatto and G. Nardulli, [arXiv:hep-ph/0205219].
  15. A. I. Larkin and Yu. N. Ovchinnikov *Zh. Eksp. Teor. Fiz.* **47**, 1136 (1964) (*Sov. Phys. JETP* **20**, 762 (1965)); P. Fulde and R. A. Ferrell *Phys. Rev.* **135**, A550 (1964).
  16. E. M. Lifshitz, L.P. Pitaevskii, *Statistical Physics, Part 2* (L.D.Landau and E.M. Lifshitz, *Course of Theoretical Physics, Vol. IX*), (Butterworth Heinemann, 1996).
  17. M. A. Alpar, P.W. Anderson, D.Pines and J. Shaham, *Astrophys. J.* **276**, 325 (1984); see also P.W.Anderson and N.Itoh, *Nature* **256**, 25 (1973).
  18. For reviews of the heavy quark effective theory see for example the textbook: A.V. Manohar and M. B. Wise, *Heavy Quark Physics* (Cambridge Univ. Press, 2000) and R. Casalbuoni et al., *Phys. Rept.*, **281** 145 (1997) [arXiv:hep-ph/9605342].

# ASPECTS OF THE QUANTUM CHROMO DYNAMICS PHASE DIAGRAM

FRANCESCO SANNINO

*NORDITA*

*Blegdamsvej 17, Copenhagen Ø, DK-2100 Denmark*

*E-mail:* francesco.sannino@nbi.dk

I briefly review some aspects of the Quantum Chromo Dynamics phase diagram at non zero temperature and quark chemical potential. I then suggest new possible phases which can appear in strongly interacting theories at non zero chemical potential. Finally I describe the phase diagram as function of the number of flavors and colors at zero quark chemical potential and zero temperature.

## 1 Introduction

There are already many excellent reviews on the QCD phase diagram, its possible applications and effective theories approaches<sup>1,2,3,4,5,6,7</sup>. Here I will first introduce some basic features of the phase diagram and then suggest new phases which can affect it such as vectorial-type condensation. I will also provide a brief summary of a possible plan for the phase diagram when varying the number of light flavors relative to the number of colors but keeping zero temperature and quark chemical potential and motivate the relevance for the physics beyond the standard model of particle interactions.

## 2 The Hot and Dense QCD Phase Diagram

### 2.1 Hadronic/Confining Phase

At zero temperature and density we do not observe free quarks and gluons. These states are permanently confined in hadronic particles like pions, vectors, nucleons etc. In this regime the interactions among hadrons can be efficiently described via effective Lagrangians built respecting the relevant symmetries of the underlying theory.

### 2.2 Hot and dilute QCD

At temperatures just above the deconfinement phase transition but small quark chemical potential the theory enters a quark gluon plasma phase (QGP) in which the underlying states are still strongly interacting but deconfined. Only at asymptotically high temperatures perturbative QCD calculations are

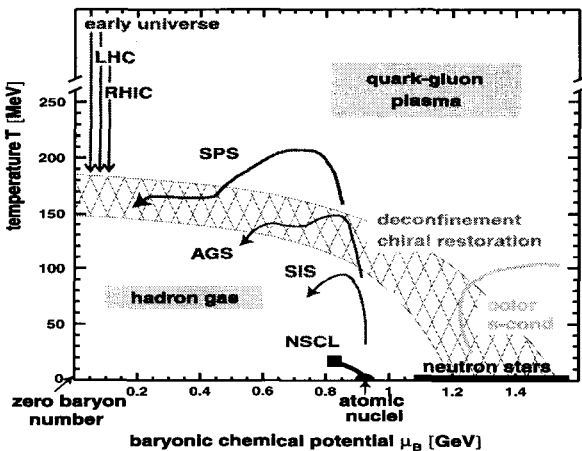


Figure 1. Possible physical applications and region of the QCD phase diagram explored by different experiments.

really reliable. This phase is relevant for the physics of the early universe and is accessible to earth based experiments like RHIC and LHC. Figure 1<sup>8</sup> shows the relevant experiments and possible physical applications.

The study of the temperature driven confining-deconfining phase transition has attracted much interest and work. Thanks to lattice simulations we now have a great deal of information. More specifically all of the relevant thermodynamical quantities have been computed with and without quarks<sup>9,10</sup> at zero quark chemical potential. Very recently new methods have been proposed which might help studying the phase diagram at non zero chemical potential via lattice simulations<sup>11</sup>. However still much is left to be understood about the nature of the transition of hot hadronic matter to a plasma of deconfined quarks and gluons<sup>2</sup>.

### 3 Dense and Cold QCD: Color Superconductivity

At zero temperature but very high quark chemical potential the perturbative (“naive”) vacuum is unstable. In this regime strong interactions favor the

formation of quark-quark condensates in the color antisymmetric channel <sup>1</sup>. Possible physical applications are related to the physics of compact objects <sup>1</sup>, supernovae cooling <sup>12</sup> and explosions <sup>13</sup> as well as to the Gamma Ray Bursts puzzle <sup>14</sup>.

The color superconductive phase is characterized by its gap energy ( $\Delta$ ) associated to quark-quark pairing which leads to the spontaneous breaking of the color symmetry. According to the number of light flavors in play we can have different phases.

### 3.1 Color Flavor Locked Phase

Let us start with the case of  $N_f = 3$  light flavors. At zero density only the confined Goldstone phase is allowed and the resulting symmetry group is  $SU_V(3) \times U_V(1)$ .

Turning on low baryon chemical potential we expect the theory to remain in the confined phase with the same number of Goldstone bosons (i.e. 8). At very high chemical potential, dynamical computations suggest that the preferred phase is a superconductive one and the following ansatz for a quark-quark type of condensate is energetically favored:

$$\epsilon^{\alpha\beta} \langle q_{L\alpha;a,i} q_{L\beta;b,j} \rangle \sim k_1 \delta_{ai} \delta_{bj} + k_2 \delta_{aj} \delta_{bi} . \quad (1)$$

A similar expression holds for the right transforming fields. The Greek indices represent spin,  $a$  and  $b$  denote color while  $i$  and  $j$  indicate flavor. The condensate breaks the gauge group completely while locking the left/right transformations with color. The final global symmetry group is  $SU_{c+L+R}(3)$ , and the low energy spectrum consists of 9 Goldstone bosons.

The low energy effective theory for 3 flavors (CFL) has been developed in <sup>15</sup>. We refer to <sup>1,6,7</sup> for a complete summary and review of this phase.

### 3.2 2 SC & Partial Deconfinement

QCD with 2 massless flavors has gauge symmetry  $SU_c(3)$  and global symmetry

$$SU_L(2) \times SU_R(2) \times U_V(1) . \quad (2)$$

At very low baryon chemical potential it is reasonable to expect that the confined Goldstone phase persists. However at very high density the ordinary Goldstone phase is no longer favored compared with a superconductive one associated to the following type of diquark condensates:

$$\langle L^\dagger{}^a \rangle \sim \langle \epsilon^{abc} \epsilon^{ij} q_{Lb,i}^\alpha q_{Lc,j;\alpha} \rangle , \quad \langle R^\dagger{}^a \rangle \sim -\langle \epsilon^{abc} \epsilon^{ij} q_{Rb,i;\dot{\alpha}} q_{Rc,j}^{\dot{\alpha}} \rangle , \quad (3)$$

$q_{Lc,i;\alpha}$ ,  $q_{Rc,i}^{\dot{\alpha}}$  are respectively the two component left and right spinors.  $\alpha, \dot{\alpha} = 1, 2$  are spin indices,  $c = 1, 2, 3$  stands for color while  $i = 1, 2$  represents the flavor. If parity is not broken spontaneously, we have  $\langle L_a \rangle = \langle R_a \rangle = f\delta_a^3$ , where we choose the condensate to be in the 3rd direction of color. The order parameters are singlets under the  $SU_L(2) \times SU_R(2)$  flavor transformations while possessing baryon charge  $\frac{2}{3}$ . The vev leaves invariant the following symmetry group:

$$[SU_c(2)] \times SU_L(2) \times SU_R(2) \times \tilde{U}_V(1) , \quad (4)$$

where  $[SU_c(2)]$  is the unbroken part of the gauge group. The  $\tilde{U}_V(1)$  generator is linear combination of the previous  $U_V(1)$  generator and the broken diagonal generator of the  $SU_c(3)$  gauge group  $T^8$ . The quarks with color 1 and 2 are neutral under  $\tilde{U}_V(1)$  and consequently the condensate is neutral too.

The superconductive phase for  $N_f = 2$  possesses the same global symmetry group as the confined Wigner-Weyl phase <sup>16</sup>. The effective theory for 2SC can be found in <sup>17</sup> while the effective theories describing the electroweak interactions for the low-energy excitations in the 2SC and CFL case can be found in <sup>18</sup>. The global anomalies matching conditions for 2 and 3 flavors and constraint are discussed in <sup>16</sup>.

An interesting property of the 2SC state is that the three color gauge group breaks via a dynamical higgs mechanism to a left over  $SU_c(2)$  subgroup. In Reference <sup>19</sup> it has been shown that the confining scale of the unbroken  $SU_c(2)$  color subgroup is lighter than the superconductive gap  $\Delta$ . The confined degrees of freedom, glueball-like particles, are expected to be light with respect to  $\Delta$ , and the effective theory based on the anomalous variation of the dilation current has been constructed in <sup>20</sup>. Using this model Lagrangian extended to include non zero temperature in <sup>21</sup> the following simple expression for the  $SU_c(2)$  critical temperature was found:

$$T_c = \sqrt[4]{\frac{90v^3}{2e\pi^2}} \hat{\Lambda} . \quad (5)$$

Here  $e$  is the Euler number,  $\hat{\Lambda}$  is the confining scale of the  $SU_c(2)$  gluodynamics in 2SC and  $v$  is the gluon <sup>19</sup> as well as light glueball velocity <sup>20</sup>. The deconfining/confining critical temperature is smaller than the critical temperature  $T_{2SC}$  for the superconductive state itself which is estimated to be  $T_{2SC} \approx 0.57 \Delta$  with  $\Delta$  the 2SC gap <sup>22</sup>. Knowing the explicit dependence of the  $SU_c(2)$  confining temperature on  $\mu$  and  $\Delta$  directly affects astrophysical models for compact stars like the one in Ref. <sup>14</sup>. A second order phase transition is also predicted. Finally in <sup>21</sup> it is suggested how ordinary lattice

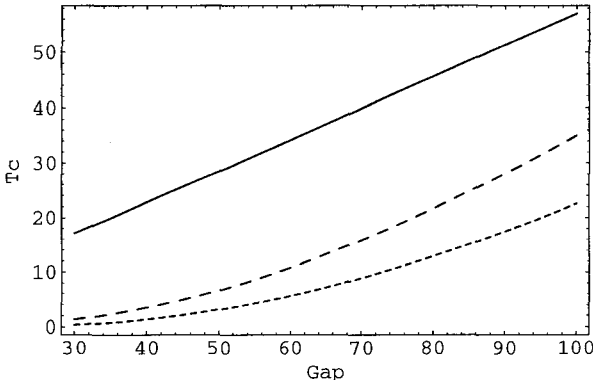


Figure 2. Plot of the  $SU_c(2)$  critical temperature for 2 values of the quark chemical potential ( $\mu = 400$  MeV long-dashed line;  $\mu = 500$  MeV short-dashed line) as function of the superconductive gap  $\Delta$ . The solid line corresponds to the critical temperature for the superconductive state  $0.57\Delta$ .

importance sampling techniques can be used to check these results and constitute, at the same time, the first simulations testing the high quark chemical potential but small temperature region of the QCD phase diagram. Interestingly recently it has also been shown that at high chemical potential the effective field theory of low energy modes in dense QCD has positive Euclidean path integral measure <sup>23</sup>. For temperatures in the range  $T_c < T < T_{2SC}$  the gapped quark dynamics is no longer negligible. Using the transport theory some of the quark temperature dependent effects have been investigated in <sup>24</sup>. It has also been recently argued that a 2SC phase might not appear in compact stars <sup>25</sup>.

In a world with two light and approximately degenerate quarks (the up and the down) and a relatively heavy strange quark a possible schematic theoretical representation of the phase diagram is shown in Fig. 3.

### 3.3 Crystalline Color Superconductivity/LOFF Phase

When considering physical applications one cannot neglect the effects of the quark masses or differences in the chemical potential among different quark flavors. If the two quarks participating in the Cooper pair posses different chemical potentials with the difference denoted by  $\delta\mu$  a quark-quark bilinear condensate breaking translational and rotational invariance may emerge for certain values of  $\delta\mu$  <sup>26</sup>. A similar phenomenon was suggested in the context

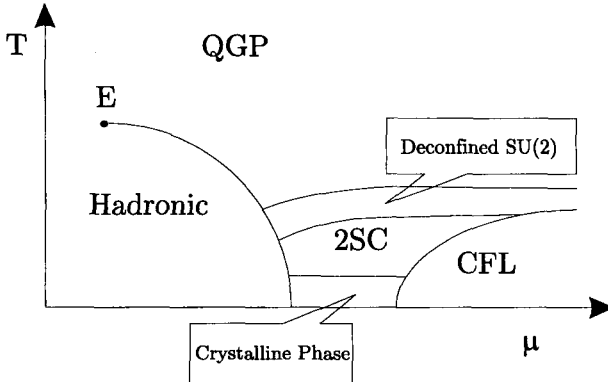


Figure 3. An oversimplified cartoon of the theoretical QCD phase diagram. The crystalline phase may exists only if we have different chemical potentials for the up and down quarks. The deconfined  $SU_c(2)$  corresponds to the phase where we have gapped up and down quarks and the remaining unbroken  $SU_c(2)$  of color deconfined.

of BCS theory for materials in presence of magnetic impurities by Larkin, Ovchinnikov, Fulde and Ferrel (LOFF) <sup>27</sup>. If present in the core of neutron stars an interesting application of the LOFF phase would be the generation of glitches <sup>26,7</sup>.

### 3.4 Kaon Condensation

The effects of the strange quark mass can be quite dramatic. In the CFL phase the  $K^+$  and  $K^0$  modes may be unstable for large values of the strange quark mass signaling the formation of a kaon condensate <sup>28</sup>. Vortex solutions in dense quark matter due to kaon condensation have been explored in <sup>29</sup>.

## 4 Higher Spin Condensates

At non zero quark chemical potential Lorentz invariance is explicitly broken down to the rotational subgroup  $SO(3)$  and higher spin fields can condense, thus enriching the phase diagram structure of QCD and QCD-like theories. The simplest non zero spin condensate which can appear is the spin one condensate. At this point we distinguish different types of spin one condensate.

#### 4.1 Superconductive Vectorial Gaps

Rotational symmetry can break in a color superconductor if two quarks of the same flavor gap. In this case the quarks must pair in a spin one state and a careful analysis has been performed in <sup>30</sup>. Whether this gap occurs or not in practice is a very dynamical issue recently investigated in <sup>31</sup>.

#### 4.2 Vectorial Bose-Einstein type condensation in 2 and 3 color QCD

Differently from superconductive higher spin gaps, the vectorial Bose-Einstein type of condensation requires some, already present in the theory, composite or elementary higher spin states to couple to an external chemical potential associated to a conserved current. A simple example is the standard QCD vector field  $\rho$  at non zero isospin chemical potential. It is not completely unexpected that vectors can be relevant at non zero chemical potential since they already play an important role in QCD at zero chemical potential <sup>32</sup> when trying to describe low energy dynamics.

Using an effective Lagrangian approach for relativistic vector fields it was shown how physical vector fields condense <sup>33</sup> and how the goldstone theorem is modified in this case <sup>34</sup>. Vector condensation for strongly interacting theories has also been suggested in <sup>35</sup> in the framework of two color QCD at non zero quark chemical potential where vector diquark states are present. A possible phase diagram of two color QCD for given number of light flavors augmented by a vector condensate phase is depicted in Fig. 4.

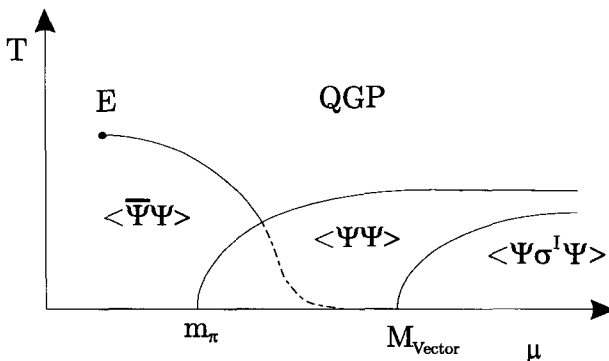


Figure 4. Schematic representation of the 2 colors phase diagram.  $m_\pi$  is the pion mass and  $M_{\text{Vector}}$  is the mass of the lightest vector state. We have chosen a normalization of the baryon number such that the diquark has unit baryon number.

In the third phase on the right we schematically represented the emergence of the vector condensate. It should coexists with the diquark condensate<sup>35</sup>. In this region not only we have spontaneous breaking of the baryon number but also breaking of the rotational invariance. The transition is predicted to be second order<sup>33</sup>.

Recent lattice simulations seem to support these predictions<sup>36</sup>. If these results are confirmed then for the first time we observe spontaneous rotational breaking due solely to strongly interacting matter. This fact would have far reaching consequences.

The subject of 2 color QCD at non zero quark chemical potential deserves a review on its own we just refer here to<sup>37,38</sup>.

We can already imagine a number of physical applications of topical interest. For example in the core of neutron stars or any compact object featuring a CFL state vector composite quasi-particles with masses of the order of the gap can condense due to the presence of a non zero isospin chemical potential and/or (as for kaon condensation) due to the effects of a non small strange mass. This may lead to the presence of new type of vortices affecting the compact star dynamics<sup>29</sup>.

Interestingly vectorial Bose-Einstein condensation recently has attracted much attention in condensed matter physics since it has been observed experimentally in alkali atom gases<sup>39</sup>.

## 5 Phases of Gauge Theories

To discuss the QCD phase diagram as function of the number of flavors and colors at zero quark chemical potential and zero temperature we need to discuss/define in somewhat more details the phases of gauge theories.

A reasonable way to characterize the phases of gauge theories is via the potential  $V(r)$  between electric test charges separated by a large distance  $r$ . The potential (up to a non-universal additive constant) is conjectured to behave as in the second column of Table 1. The first three phases have massless gauge fields and potentials of the form  $V(r) \sim e^2(r)/r$ . In the Coulomb phase, the electric charge  $e^2(r)$  is constant. In the free electric phase, massless electrically charged fields renormalize the charge to zero at long distances as  $e^{-2}(r) \sim \log(r\Lambda)$ . Similar behavior occurs when the long distance theory is a non-Abelian theory which is not asymptotically free. The free magnetic phase occurs when there are massless magnetic monopoles, which renormalize the electric coupling constant to infinity at large distance with a conjectured behavior  $e^2(r) \sim \log(r\Lambda)$ . In the Higgs phase, the condensate of an electrically charged field gives a mass gap to the gauge fields by the Anderson-Higgs

Phases	Electric $V(r)$	Magnetic $V(r)$
Coulomb	$\frac{1}{r}$	$\frac{1}{r}$
Free Electric	$\frac{1}{r \log r \Lambda}$	$\frac{\log r \Lambda}{r}$
Free Magnetic	$\frac{\log r \Lambda}{r}$	$\frac{1}{r \log r \Lambda}$
Higgs	Constant	$\rho r$
Confining	$\sigma r$	Constant

Table 1. Phases of Gauge Theories

mechanism and screens electric charges, leading to a potential which, up to the additive non-universal constant, has an exponential Yukawa decay to zero at long distances. In the confining phase, there is a mass gap with electric flux confined into a thin tube, leading to the linear potential with string tension  $\sigma$ .

All of the above phases can be non-Abelian as well as Abelian. In particular, in addition to the familiar Abelian Coulomb phase, there are theories which have a non-Abelian Coulomb phase with massless interacting quarks and gluons exhibiting the above Coulomb potential. This phase occurs when there is a non-trivial, infrared fixed point of the renormalization group. These are thus non-trivial, interacting four dimensional conformal field theories.

It is instructive to consider the behavior of the potential  $V(r)$  for magnetic test charges separated by a large distance  $r$  (3th column in Table 1). The behavior in the first three phases can be written as  $V(r) = g^2(r)/r$  where the effective magnetic charge  $g^2(r)$  is related to the effective electric charge appearing by the Dirac condition,  $e(r)g(r) \sim 1$ . The linear potential in the Higgs phase reflects the string tension in the Meissner effect.

The above behavior is modified when there are matter fields in the fundamental representation of the gauge group because virtual pairs can pop up from the vacuum and completely screen the sources.

Note that under electric-magnetic duality, which exchanges electrically charged fields with magnetically charged fields, the behavior in the free electric phase is exchanged with that of the free magnetic phase. Mandelstam and 't Hooft suggested that the Higgs and confining phases are exchanged by duality. Confinement can then be understood as the dual Meissner effect associated with a condensate of monopoles <sup>40</sup>. For supersymmetric theories

it is possible to argue that this picture is correct <sup>41</sup>. Dualizing a theory in the Coulomb phase, we remain in the same phase (the behavior of the potential is unchanged).

Unfortunately the previous classification of the phases of the gauge theories is not always possible. Besides if we are interested in the nature of the phase transition itself (by varying for example the temperature) the previous picture is not directly applicable. A better description/understanding can be achieved by introducing gauge invariant order parameters <sup>42</sup>.

For theories with global symmetries we can, quite often, construct simple order parameters. This is the case of the chiral phase transition where the quark – antiquark vacuum expectation value is the order parameter and is also directly related to the hadronic states of the theory (pions, etc..). Once the order parameter is identified a mean field theory approach can be adopted. There are cases, however, where the identification of the order parameter is not trivial. And even if the order parameter is found might not be connected straightforwardly to the physical states of the theory. This is the case of the pure  $SU(N_c)$  Yang-Mills theory where the finite temperature gauge invariant order parameter is the Polyakov loop  $\ell$  <sup>42,43</sup>. Here the global symmetry group is the center  $Z_{N_c}$  of  $SU(N_c)$ . On the other side the physical degrees of freedom of any asymptotically free gauge theory are hadronic states. Using the Yang-Mills trace anomaly and the exact  $Z_N$  symmetry in <sup>44</sup> a model able to communicate to the hadrons the information carried by the order parameter was constructed.

## 6 The Phase Diagram Along the Flavor Axes

Having introduced in the previous section the correct terminology we can now investigate, at zero temperature and quark matter density, the behavior of QCD as function of number of light flavors. Besides the academic interest we also hope to use these theories to model the electroweak symmetry breaking without using an elementary higgs field <sup>45</sup>. Indeed the infrared behavior of gauge theories changes dramatically when changing the number of light flavors. Predictions resulting from exact theoretical treatments are, at the moment, only possible for supersymmetric theories <sup>41</sup>. Nevertheless for non supersymmetric QCD theories it is still possible, using different methods and models, to sketch a plausible phase diagram which can be tested via lattice simulations. We focus here on zero quark chemical potential and temperature. We will however suggest how the dynamics of large number of flavors QCD might influence any other phase.

### 6.1 The Coulomb/Conformal Phase

For  $N_f > \frac{11}{2}N_c$ , the one-loop beta function of QCD changes sign and the theory loses asymptotic freedom. The resulting infrared free theory is now in a non-Abelian QED-like phase in which neither confinement nor chiral symmetry breaking is expected. For values of  $N_f$  near but below  $\frac{11}{2}N_c$ , the beta function develops a perturbative infrared stable fixed point at which the trace of the energy momentum tensor vanishes exactly and the theory is a non-Abelian conformal field theory (Coulomb phase). In this phase, the coupling constant is small on account of the large number of flavors and so we do not expect any of the global symmetries to break. However, as the number of flavors is decreased, the fixed point becomes nonperturbative and the coupling constant increases to a critical value above which chiral symmetry breaks spontaneously. A dynamical scale is generated and conformal symmetry is lost. The generation of this scale defines the critical number of massless flavors, i.e. the minimum number of flavors for which the gauge theory is still conformal and chiral symmetry is still intact. Below this critical number of flavors, the theory is expected to confine and the low energy spectrum is hadronic. This discussion assumes that the conformal and chiral phase transitions coincide as function of the number of flavors, but whether or not this is true is still controversial. This is not the case for supersymmetric QCD (see right panel in Fig. 5) where for a certain range of flavors the global symmetries do not break but the theory is still assumed to confine. We will assume here, as corroborated by lattice simulations for  $N_c = 3$ <sup>46</sup> (though more investigations are needed), that there is in fact a single conformal/chiral phase transition. Figure 5 (left panel) summarizes the possible phase structure for QCD as a function of the number of light flavors.

### 6.2 Conformal Critical Exponents

By way of a simple model it is possible to describe the conformal/chiral phase transition<sup>47</sup>. Since chiral symmetry, in the present scenario, is linked to the breaking of the conformal symmetry the model uses the chiral condensate  $\sigma \sim \bar{q}q$  as the order parameter. Trace and axial anomaly were also used to constrain part of the potential. In the absence of the quark masses the condensate vanishes exponentially fast as  $N_f$  approaches the critical value. More precisely the following result for the physical mass  $M_\sigma$  and  $\langle \sigma \rangle$  was derived in<sup>47</sup>:

$$\langle \sigma \rangle \simeq \left[ \frac{\gamma - 1}{2|C|} \right]^{\frac{1}{2(\gamma-1)}} \Lambda, \quad M_\sigma \simeq 2\sqrt{6}|C| \left[ \frac{\gamma - 1}{2|C|} \right]^{\frac{1}{2(\gamma-1)}} \Lambda. \quad (6)$$

Likewise, in the presence of the quark mass term we have

$$\langle \sigma \rangle_{\gamma=1} \simeq \left[ \frac{m N_f \Lambda}{2|C|} \right]^{\frac{1}{2}}, \quad [M_\sigma]_{\gamma=1} \simeq 2 [2m N_f \Lambda]^{\frac{1}{2}}. \quad (7)$$

Here  $\gamma \geq 1$  (in the confined and highly non perturbative phase) is the anomalous dimension of the quark mass operator and  $C$  an unknown coefficient. Thus the order parameter  $\sigma$  for  $\gamma = 1$  vanishes according to the power  $1/2$  with the quark mass in contrast with an ordinary second order phase transition where the order parameter is expected to vanish according to the power  $1/3$ . We expect that for a vanishing beta function close to the conformal point the theory becomes conformal at  $\gamma = 1$ . This fixes the critical value of the number of flavors to  $4 N_c$ . For more details and a complete list of references we refer the reader to the original paper <sup>47</sup>. Lattice simulations would certainly provide very useful in understanding the nature of this conformal phase and associated phase transition features.

### 6.3 Enhanced Symmetries Scenario

When the number of flavors is just below the critical value, the theory still exhibits chiral symmetry breaking but is possible that the vector spectrum changes quite significantly. In Refs. <sup>49,48</sup> it was suggested that a new global symmetry may be dynamically generated. This symmetry acts on the massive spectrum of the theory and is related to the modification of the second Weinberg spectral function sum rule near the critical number of flavors <sup>50</sup>.

If such an enhanced symmetry emerges, the vectors along the broken generators become degenerate with those along the orthogonal directions. For  $N_c = 3$  QCD, this corresponds to mass degenerate vector ( $\rho$ -type of field) and axial particles even in the presence of chiral symmetry breaking.

In the enhanced symmetry scenario, the interactions between the vectors and the Goldstone excitations are suppressed (in the derivative expansion). The enhanced symmetry scenario imposes very stringent constraints on the possible form of the negative intrinsic parity terms (the ones involving the  $\epsilon_{\mu\nu\rho\sigma}$ -terms) as well <sup>48 a</sup>

We conjecture the following phase structure before entering the conformal phase:

---

<sup>a</sup>Nota Bene: In reference <sup>48</sup> the gauging of the Wess-Zumino term needed for the saturation of the 't Hooft global anomaly matching has been computed for 2-colors QCD. The effective theories for 2 color QCD at zero density for the linear and non linear realization extended, as well, to include the Electroweak theory and to contain physical vectors states were first constructed in <sup>49,48</sup> for an arbitrary number of flavors.

- Approximate local chiral symmetry for small  $N_f$
- Parity doubling and an extra global symmetry near the critical  $N_f$ .

At very low number of flavors the vectors can be included in the low energy effective theory as almost gauge vectors of the chiral symmetry. By “almost” we mean that the vector masses are considered as minimal sources of breaking of the local chiral symmetry. This hypothesis is at the base of “vector dominance” model, it strongly reduces the number of unknown coefficients in the effective Lagrangian and it has been widely used in the past for successful phenomenological investigations. Near the critical  $N_f$ , according to our conjecture, a new dynamically generated global symmetry sets in. Due to this new symmetry the vectors are almost degenerate while chiral symmetry still breaks spontaneously. In this regime the new global symmetry strongly constrains the effective Lagrangian theory.

Interestingly enough when extending this theory to model the spontaneous symmetry breaking sector of the electroweak theory the major contribution to the  $S$ -parameter (proportional schematically to the difference between the square of the mass of the axial vector and vector  $M_A^2 - M_V^2$ ) is protected by the new enhanced symmetry and leads to phenomenologically viable technicolor models of the type of the BESS models<sup>51</sup>.

For a fixed, nonzero chemical potential, the phase structure as the number of light flavors is increased should be very rich<sup>52</sup>. For instance, when  $N_f > \frac{11}{2}N_c$ , the theory is no longer asymptotically free and the low energy theory is simply the QCD Lagrangian. In this regime perturbation theory is reliable also at low energy scales.

## 7 Conclusions

The Phase Diagrams in Fig. 3 and in Fig. 5 are just educated guesses of the true QCD phase diagram. Indeed other interesting phases may emerge in the future recalling the richness of the phases encountered in other physical systems studied in the condensed matter framework.

## Acknowledgments

It is a pleasure to thank P. Damgaard, A.D. Jackson, K. Rummukainen, J. Schechter, W. Schäfer and K. Splittorff for discussions and careful reading of the manuscript. I also thank R. Casalbuoni, J.T. Lenaghan, M.P. Lombardo and G. Nardulli for useful discussions. This work is supported by the Marie-Curie fellowship under contract MCFI-2001-00181.

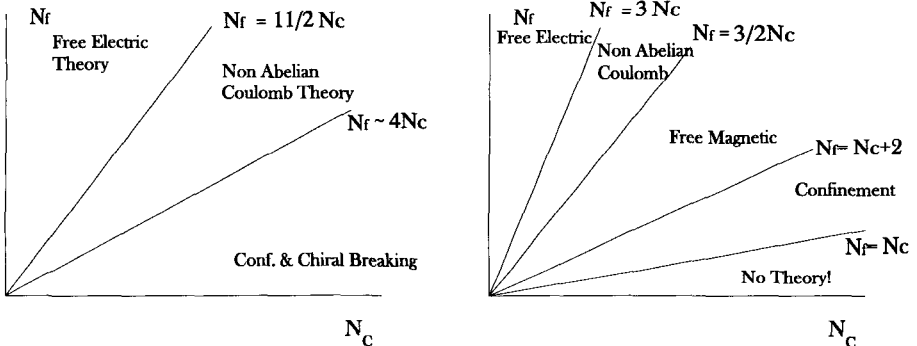


Figure 5. Left Panel: Represent a possible plan for the QCD phase diagram at zero quark density and temperature but for different number of flavors and colors. The origin in both schemes of the number of color axes corresponds to  $N_c = 2$ . Right Panel: Same phase diagram for supersymmetric QCD.

## References

1. See K. Rajagopal and F. Wilczek, hep-ph/0011333; M.G. Alford, hep-ph/0102047 for an overview on the subject; S.D.H. Hsu, hep-ph/0003140 for the renormalization group approach review; D.K. Hong, Acta Phys. Polon. B32:1253, 2001, hep-ph/0101025 for the effective theories close to the fermi surface.
2. H. Satz, arXiv:hep-ph/0201051.
3. E. V. Shuryak, arXiv:hep-ph/0110130.
4. M. A. Halasz, A. D. Jackson, R. E. Shrock, M. A. Stephanov and J. J. Verbaarschot, Phys. Rev. D **58**, 096007 (1998) [arXiv:hep-ph/9804290].
5. M. P. Lombardo, arXiv:hep-ph/0103141.
6. R. Casalbuoni, hep-th/0108195 for the effective Lagrangians approach.
7. G. Nardulli, hep-ph/0202037 for the effective theory approach to CSC and the LOFF phase and possible applications of the LOFF phase to the physics of compact stars.
8. U. W. Heinz, AIP Conf. Proc. **602**, 281 (2001) [arXiv:hep-ph/0109006].
9. G. Boyd, J. Engels, F. Karsch, E. Laermann, C. Legeland, M. Lutgemeier and B. Petersson, Nucl. Phys. B **469**, 419 (1996) [arXiv:hep-lat/9602007].
10. M. Okamoto *et al.* [CP-PACS Collaboration], Phys. Rev. D **60**, 094510 (1999) [arXiv:hep-lat/9905005].
11. Z. Fodor and S. D. Katz, arXiv:hep-lat/0204029.
12. G. W. Carter and S. Reddy, Phys. Rev. D **62**, 103002 (2000), hep-

- ph/0005228.
13. D. K. Hong, S. D. Hsu and F. Sannino, Phys. Lett. B **516**, 362 (2001), hep-ph/0107017.
  14. R. Ouyed and F. Sannino, astro-ph/0103022. To appear in *Astronomy & Astrophysics*.
  15. R. Casalbuoni and R. Gatto, Phys. Lett. B**464**, 11 (1999).
  16. F. Sannino, Phys. Lett. B**480**, 280, (2000). S. D. Hsu, F. Sannino and M. Schwetz, Mod. Phys. Lett. A **16**, 1871 (2001), hep-ph/0006059.
  17. R. Casalbuoni, Z. Duan and F. Sannino, Phys. Rev. D **62** (2000) 094004, hep-ph/0004207.
  18. R. Casalbuoni, Z. Duan and F. Sannino, Phys. Rev. D **63**, 114026 (2001), hep-ph/0011394
  19. D. H. Rischke, D. T. Son and M. A. Stephanov, Phys. Rev. Lett. **87**, 062001 (2001), hep-ph/0011379.
  20. R. Ouyed and F. Sannino, Phys. Lett. B **511**, 66 (2001).
  21. F. Sannino, N. Marchal and W. Schafer, arXiv:hep-ph/0202248.
  22. R.D. Pisarski and D.H. Rischke, Phys. Rev. D**61**, 051501 (2000); Phys. Rev. D**61**, 074017 (2000).
  23. D. K. Hong and S. D. Hsu, arXiv:hep-ph/0202236.
  24. D. F. Litim and C. Manuel, Phys. Rev. Lett. **87**, 052002 (2001), hep-ph/0103092.
  25. M. Alford and K. Rajagopal, arXiv:hep-ph/0204001.
  26. J. A. Bowers and K. Rajagopal, arXiv:hep-ph/0204079 and references therein.
  27. A.I. Larkin and Yu.N. Ovchinnikov, Zh. Eksp. Teor. Fiz., **47**, (1964) 1136 (Sov. Phys. JETP, **20**, (1965) 762); P. Fulde and R.A. Ferrell, Phys. Rev. **135**, (1964) A550.
  28. T. Schafer, Phys. Rev. Lett. **85**, 5531 (2000) [arXiv:nucl-th/0007021].  
T. Schafer, D. T. Son, M. A. Stephanov, D. Toublan and J. J. Verbaarschot, Phys. Lett. B **522**, 67 (2001) [arXiv:hep-ph/0108210].  
D. B. Kaplan and S. Reddy, Phys. Rev. D **65**, 054042 (2002) [arXiv:hep-ph/0107265].
  29. D. B. Kaplan and S. Reddy, Phys. Rev. Lett. **88**, 132302 (2002).
  30. R. D. Pisarski and D. H. Rischke, Phys. Rev. D **61**, 074017 (2000) [arXiv:nucl-th/9910056].
  31. M. Buballa, J. Hosek and M. Oertel, arXiv:hep-ph/0204275.
  32. M. Harada, F. Sannino and J. Schechter, Phys. Rev. D **54**, 1991 (1996) [arXiv:hep-ph/9511335]. M. Harada, F. Sannino and J. Schechter, Phys. Rev. Lett. **78**, 1603 (1997), [arXiv:hep-ph/9609428].
  33. F. Sannino and W. Schäfer, Phys. Lett. B **527**, 142 (2002) hep-

- ph/0111098; F. Sannino and W. Schäfer. These proceedings hep-ph/0204353.
34. H.B. Nielsen and S. Chadha, Nucl. Phys. **B105**, 445 (1976). V. A. Miransky and I. A. Shovkovy, Phys. Rev. Lett. **88**, 111601 (2002) [arXiv:hep-ph/0108178].
  35. J. T. Lenaghan, F. Sannino and K. Splittorff, Phys. Rev. D **65**, 054002 (2002) [arXiv:hep-ph/0107099].
  36. M.P. Lombardo, these proceedings.
  37. J. B. Kogut, D. K. Sinclair, S. J. Hands and S. E. Morrison, Phys. Rev. D **64**, 094505 (2001) [arXiv:hep-lat/0105026]; I. Montvay, S. Hands, L. Scorzato and J. I. Skullerud, arXiv:hep-lat/0112046.
  38. J.B. Kogut, M.A. Stephanov, and D. Toublan, Phys. Lett. **B 464** (1999) 183; J.B. Kogut, M.A. Stephanov, D. Toublan, J.J.M. Verbaarschot, and A. Zhitnitsky, Nucl.Phys. **B 582** (2000) 477; K. Splittorff, D. Toublan, and J.J.M. Verbaarschot, Nucl. Phys. **B620**, 290 (2002) [arXiv:hep-ph/0108040], [arXiv:hep-ph/0204076].
  39. D.M. Stamper-Kurn, M.R. Andrews, A.P. Chikkatur, S. Inouye, H.-J. Miesner, J. Stenger, and W. Ketterle, Phys. Rev. Lett. **80**, 2027 (1998).
  40. A. D. Giacomo, arXiv:hep-lat/0204001.
  41. K. Intriligator and N. Seiberg, Nucl. Phys. Proc. Suppl. **45BC**, 1 (1996).
  42. B. Svetitsky and L. G. Yaffe, Nucl. Phys. B **210**, 423 (1982). L. G. Yaffe and B. Svetitsky, Phys. Rev. D **26**, 963 (1982). B. Svetitsky, Phys. Rept. **132**, 1 (1986).
  43. R. D. Pisarski, hep-ph/0112037; R.D. Pisarski, Phys. Rev. D**62**, 111501 (2000).
  44. F. Sannino, arXiv:hep-ph/0204174.
  45. K. Lane, arXiv:hep-ph/0202255.
  46. R. D. Mawhinney, Nucl. Phys. Proc. Suppl. **60A**, 306 (1998), hep-lat/9705030; D. Chen, R. D. Mawhinney, Nucl. Phys. Proc. Suppl. **53**, 216 (1997).
  47. F. Sannino and J. Schechter, Phys. Rev. D**60**, 056004, (1999).
  48. Z. Duan, P.S. Rodrigues da Silva and F. Sannino, Nucl. Phys. **B 592**, 371 (2001), hep-ph/0001303.
  49. T. Appelquist, P.S. Rodrigues da Silva and F. Sannino, Phys. Rev. D**60**, 116007 (1999), hep-ph/9906555.
  50. T. Appelquist and F. Sannino, Phys. Rev. D**59**, 067702 (1999).
  51. R. Casalbuoni, S. De Curtis and M. Redi, Eur. Phys. J. C **18**, 65 (2000) [arXiv:hep-ph/0007097].
  52. T. Schäfer, Nucl. Phys. B **575**, 269 (2000) [arXiv:hep-ph/9909574].

# THE $U(1)$ AXIAL SYMMETRY AND THE CHIRAL TRANSITION IN QCD

ENRICO MEGGIOLARO

*Dipartimento di Fisica “E. Fermi”, Università di Pisa,  
Via Buonarroti 2, I-56127 Pisa, Italy  
E-mail: enrico.meggiolaro@df.unipi.it*

We discuss the role of the  $U(1)$  axial symmetry for the phase structure of QCD at finite temperature. We expect that, above a certain critical temperature, also the  $U(1)$  axial symmetry will be restored. We will try to see if this transition has (or has not) anything to do with the usual chiral transition: various possible scenarios are discussed. In particular, we analyse a scenario in which the  $U(1)$  axial symmetry is still broken above the chiral transitions. We will show that this scenario can be consistently reproduced using an effective Lagrangian model. A new order parameter is introduced for the  $U(1)$  axial symmetry.

## 1 Introduction

It is generally believed that a phase transition which occurs in QCD at a finite temperature is the restoration of the spontaneously broken  $SU(L) \otimes SU(L)$  chiral symmetry in association with  $L$  massless quarks. At zero temperature the chiral symmetry is broken spontaneously by the condensation of  $q\bar{q}$  pairs and the  $L^2 - 1$   $J^P = 0^-$  mesons are just the Nambu–Goldstone (NG) bosons associated with this breaking. At high temperatures the thermal energy breaks up the  $q\bar{q}$  condensate, leading to the restoration of chiral symmetry. We expect that this property not only holds for massless quarks but also continues for a small mass region. The order parameter for the chiral symmetry breaking is apparently  $\langle\bar{q}q\rangle \equiv \sum_{i=1}^L \langle\bar{q}_i q_i\rangle$ : the chiral symmetry breaking corresponds to the non-vanishing of  $\langle\bar{q}q\rangle$  in the chiral limit  $\text{sup}(m_i) \rightarrow 0$ . From lattice determinations of the chiral order parameter  $\langle\bar{q}q\rangle$  one knows that the  $SU(L) \otimes SU(L)$  chiral phase transition temperature  $T_{ch}$ , defined as the temperature at which the chiral condensate  $\langle\bar{q}q\rangle$  goes to zero (in the chiral limit  $\text{sup}(m_i) \rightarrow 0$ ), is nearly equal to the deconfining temperature  $T_c$  (see, e.g., Ref. <sup>1</sup>). But this is not the whole story: QCD possesses not only an approximate  $SU(L) \otimes SU(L)$  chiral symmetry, for  $L$  light quark flavours, but also a  $U(1)$  axial symmetry (at least at the classical level). The role of the  $U(1)$  symmetry for the finite temperature phase structure has been so far not well studied and it is still an open question of hadronic physics whether the fate of the  $U(1)$  chiral symmetry of QCD has or has not something to do with the fate of the  $SU(L) \otimes SU(L)$  chiral symmetry. In the following sections we

shall try to answer these questions:

- At which temperature is the  $U(1)$  axial symmetry restored? (if such a critical temperature does exist!)
- Does this temperature coincide with the deconfinement temperature and with the temperature at which the  $SU(L)$  chiral symmetry is restored?

## 2 Topological and chiral susceptibilities

In the “Witten–Veneziano mechanism”<sup>2,3</sup> for the resolution of the  $U(1)$  problem, a fundamental role is played by the so-called “topological susceptibility” in a QCD without quarks, i.e., in a pure Yang–Mills (YM) theory, in the large- $N_c$  limit ( $N_c$  being the number of colours):

$$A = \lim_{k \rightarrow 0} \lim_{N_c \rightarrow \infty} \left\{ -i \int d^4x e^{ikx} \langle TQ(x)Q(0) \rangle \right\}, \quad (1)$$

where  $Q(x) = \frac{g^2}{64\pi^2} \varepsilon^{\mu\nu\rho\sigma} F_{\mu\nu}^a F_{\rho\sigma}^a$  is the so-called “topological charge density”. This quantity enters into the expression for the squared mass of the  $\eta'$ :  $m_{\eta'}^2 = \frac{2LA}{F_\pi^2}$ , where  $L$  is the number of light quark flavours taken into account in the chiral limit. Therefore, in order to study the role of the  $U(1)$  axial symmetry for the full theory at non-zero temperatures, one should consider the YM topological susceptibility  $A(T)$  at a given temperature  $T$ , formally defined as in Eq. (1), where now  $\langle \dots \rangle$  stands for the expectation value in the full theory at a given temperature  $T$ .<sup>4</sup> The problem of studying the behaviour of  $A(T)$  as a function of the temperature  $T$  was first addressed, in lattice QCD, in Refs.<sup>5,6</sup>. Recent lattice results<sup>7</sup> (obtained for the  $SU(3)$  pure-gauge theory) show that the YM topological susceptibility  $A(T)$  is approximately constant up to the critical temperature  $T_c \simeq T_{ch}$ , it has a sharp decrease above the transition, but it remains different from zero up to  $\sim 1.2 T_c$ . In the Witten–Veneziano mechanism, a (no matter how small!) value different from zero for  $A$  is related to the breaking of the  $U(1)$  axial symmetry, since it implies the existence of a pseudo–Goldstone particle with the same quantum numbers of the  $\eta'$ . Therefore, the available lattice results show that the  $U(1)$  chiral symmetry is restored at a temperature  $T_{U(1)}$  greater than  $T_{ch}$ .

Another way to address the same question is to look at the behaviour at non-zero temperatures of the susceptibilities related to the propagators for the following meson channels<sup>8</sup> (we consider for simplicity the case of  $L = 2$  light flavours): the isoscalar  $I = 0$  scalar channel  $\sigma$  (also known as  $f_0$  in the modern language of hadron spectroscopy), interpolated by the operator  $O_\sigma = \bar{q}q$ ; the

isovector  $I = 1$  scalar channel  $\delta$  (also known as  $a_0$ ), interpolated by the operator  $\vec{O}_\delta = \bar{q} \frac{\vec{\tau}}{2} q$ ; the isovector  $I = 1$  pseudoscalar channel  $\pi$ , interpolated by the operator  $\vec{O}_\pi = i \bar{q} \gamma_5 \frac{\vec{\tau}}{2} q$ ; the isoscalar  $I = 0$  pseudoscalar channel  $\eta'$ , interpolated by the operator  $O_{\eta'} = i \bar{q} \gamma_5 q$ . Under  $SU(2)_A$  transformations,  $\sigma$  is mixed with  $\pi$ : thus the restoration of this symmetry at  $T_{ch}$  requires identical correlators for these two channels. Another  $SU(2)$  chiral multiplet is  $(\delta, \eta')$ . On the contrary, under the  $U(1)_A$  transformations,  $\pi$  is mixed with  $\delta$ : so, a “practical restoration” of the  $U(1)$  axial symmetry should imply that these two channels become degenerate, with identical correlators. Another  $U(1)$  chiral multiplet is  $(\sigma, \eta')$ . (Clearly, if both chiral symmetries are restored, then all  $\pi$ ,  $\eta'$ ,  $\sigma$  and  $\delta$  correlators should become the same.) In practice, one can construct, for each meson channel  $f$ , the corresponding chiral susceptibility

$$\chi_f = \int d^4x \langle O_f(x) O_f^\dagger(0) \rangle, \quad (2)$$

and then define two order parameters:  $\chi_{SU(2) \otimes SU(2)} \equiv \chi_\sigma - \chi_\pi$ , and  $\chi_{U(1)} \equiv \chi_\delta - \chi_\pi$ . If an order parameter is non-zero in the chiral limit, then the corresponding symmetry is broken. Present lattice data for these quantities seem to indicate that the  $U(1)$  axial symmetry is still broken above  $T_{ch}$ , up to  $\sim 1.2 T_{ch}$ , where the  $\delta$ - $\pi$  splitting is small but still different from zero.<sup>9,10,11</sup> In terms of the left-handed and right-handed quark fields [ $q_{L,R} \equiv \frac{1}{2}(1 \pm \gamma_5)q$ ], one has the following expression for the difference between the correlators for the  $\delta^+$  and  $\pi^+$  channels:

$$\begin{aligned} \mathcal{D}_{U(1)}(x) &\equiv \langle O_{\delta^+}(x) O_{\delta^+}^\dagger(0) \rangle - \langle O_{\pi^+}(x) O_{\pi^+}^\dagger(0) \rangle \\ &= 2 [\langle \bar{u}_R d_L(x) \cdot \bar{d}_R u_L(0) \rangle + \langle \bar{u}_L d_R(x) \cdot \bar{d}_L u_R(0) \rangle]. \end{aligned} \quad (3)$$

(The integral of this quantity,  $\int d^4x \mathcal{D}_{U(1)}(x)$ , is just equal to the  $U(1)$  chiral parameter  $\chi_{U(1)} = \chi_\delta - \chi_\pi$ .) What happens below and above  $T_{ch}$ ? Below  $T_{ch}$ , in the chiral limit  $\text{sup}(m_i) \rightarrow 0$ , the left-handed and right-handed components of a given light quark flavour (*up* or *down*, in our case with  $L = 2$ ) can be connected through the quark condensate, giving rise to a non-zero contribution to the quantity  $\mathcal{D}_{U(1)}(x)$  in Eq. (3) (i.e., to the quantity  $\chi_{U(1)}$ ). But above  $T_{ch}$  the quark condensate is zero: so, how can the quantity  $\mathcal{D}_{U(1)}(x)$  (i.e., the quantity  $\chi_{U(1)}$ ) be different from zero also above  $T_{ch}$ , as indicated by present lattice data? The only possibility in order to solve this puzzle seems to be that of requiring the existence of a genuine four-fermion local condensate, which is an order parameter for the  $U(1)$  axial symmetry and which remains different from zero also above  $T_{ch}$ . This will be discussed in section 4.

### 3 Which chiral symmetry is restored in hot QCD?

Let us define the following temperatures:

- $T_{ch}$ : the temperature at which the chiral condensate  $\langle \bar{q}q \rangle$  goes to zero. The chiral symmetry  $SU(L) \otimes SU(L)$  is spontaneously broken below  $T_{ch}$  and it is restored above  $T_{ch}$ .
- $T_{U(1)}$ : the temperature at which the  $U(1)$  axial symmetry is (approximately) restored. If  $\langle \bar{q}q \rangle \neq 0$  also the  $U(1)$  axial symmetry is broken, i.e., the chiral condensate is an order parameter also for the  $U(1)$  axial symmetry. Therefore we must have:  $T_{U(1)} \geq T_{ch}$ .
- $T_\chi$ : the temperature at which the pure-gauge topological susceptibility  $A$  (approximately) drops to zero. Present lattice results indicate that  $T_\chi \geq T_{ch}$ .<sup>7</sup> Moreover, the Witten–Veneziano mechanism implies that  $T_{U(1)} \geq T_\chi$ .

The following scenario, that we shall call “SCENARIO 1”, in which  $T_\chi < T_{ch}$ , is, therefore, immediately ruled out. In this case, in the range of temperatures between  $T_\chi$  and  $T_{ch}$  the  $U(1)$  axial symmetry is still broken by the chiral condensate, but the anomaly effects are absent. In other words, in this range of temperatures the  $U(1)$  axial symmetry is spontaneously broken (*à la* Goldstone) and the  $\eta'$  is the corresponding NG boson, i.e., it is massless in the chiral limit  $sup(m_i) \rightarrow 0$ , or, at least, as light as the pion  $\pi$ , when including the quark masses. This scenario was first discussed (and indeed really supported!) in Ref.<sup>12</sup>. It is known that the  $U(1)$  chiral anomaly effects are connected with instantons.<sup>13</sup> It is also known that at high temperature  $T$  the instanton-induced amplitudes are suppressed by the so-called “Pisarski–Yaffe suppression factor”, due to the Debye-type screening:

$$d\mathcal{N}_{inst}(T) \sim d\mathcal{N}_{inst}(T=0) \cdot \exp \left[ -\pi^2 \rho^2 T^2 \left( \frac{2N_c + L}{3} \right) \right], \quad (4)$$

$\rho$  being the instanton radius. The argument of Pisarski and Wilczek in Ref.<sup>12</sup> was the following: “If instantons themselves are the primary chiral-symmetry-breaking mechanism, then it is very difficult to imagine the unsuppressed  $U(1)_A$  amplitude at  $T_{ch}$ .” So, what was wrong in their argument? The problem is that Eq. (4) can be applied only in the quark–gluon plasma phase, since the Debye screening is absent below  $T_{ch}$ . Indeed, Eq. (4) is applicable only for  $T \geq 2T_{ch}$  and one finds instanton suppression by at least two orders of magnitude at  $T \simeq 2T_{ch}$  (see Ref.<sup>8</sup> and references therein). Moreover, the qualitative picture of instanton–driven chiral symmetry restoration which is

nowadays accepted has significantly changed since the days of Ref. <sup>12</sup>. It is now believed (see Ref. <sup>8</sup> and references therein) that the suppression of instantons is not the only way to “kill” the quark condensate. Not only the number of instantons is important, but also their relative positions and orientations. Above  $T_{ch}$ , instantons and anti-instantons can be rearranged into some finite clusters with zero topological charge, such as well-formed “instanton–anti-instanton molecules”.

Therefore, we are left essentially with the two following scenarios.

SCENARIO 2:  $T_{ch} \leq T_{U(1)}$ , with  $T_{ch} \sim T_\chi \sim T_{U(1)}$ . If  $T_{ch} = T_\chi = T_{U(1)}$ , then, in the case of  $L = 2$  light flavours, the restored symmetry across the transition is  $U(1)_A \otimes SU(2)_L \otimes SU(2)_R \sim O(2) \otimes O(4)$ , which may yield a first-order phase transition (see, for example, Ref. <sup>14</sup>).

SCENARIO 3:  $T_{ch} \ll T_{U(1)}$ , that is, the complete  $U(L)_L \otimes U(L)_R$  chiral symmetry is restored only well inside the quark–gluon plasma domain. In the case of  $L = 2$  light flavours, we then have at  $T = T_{ch}$  the restoration of  $SU(2)_L \otimes SU(2)_R \sim O(4)$ . Therefore, we can have a second-order phase transition with the  $O(4)$  critical exponents.  $L = 2$  QCD at  $T \simeq T_{ch}$  and the  $O(4)$  spin system should belong to the same universality class. An effective Lagrangian describing the softest modes is essentially the Gell-Mann–Levy linear sigma model, the same as for the  $O(4)$  spin systems (see Ref. <sup>12</sup>). If this scenario is true, one should find the  $O(4)$  critical indices for the quark condensate and the specific heat:  $\langle \bar{q}q \rangle \sim |(T - T_{ch})/T_{ch}|^{0.38 \pm 0.01}$ , and  $C(T) \sim |(T - T_{ch})/T_{ch}|^{0.19 \pm 0.06}$ . Present lattice data partially support these results.

#### 4 The $U(1)$ chiral order parameter

We make the assumption (discussed in the previous sections) that the  $U(1)$  chiral symmetry is broken independently from the  $SU(L) \otimes SU(L)$  symmetry. The usual chiral order parameter  $\langle \bar{q}q \rangle$  is an order parameter both for  $SU(L) \otimes SU(L)$  and for  $U(1)_A$ : when it is different from zero,  $SU(L) \otimes SU(L)$  is broken down to  $SU(L)_V$  and also  $U(1)_A$  is broken. Thus we need another quantity which could be an order parameter only for the  $U(1)$  chiral symmetry. <sup>15,16</sup> The most simple quantity of this kind was found by 'tHooft in Ref. <sup>13</sup>. For a theory with  $L$  light quark flavours, it is a  $2L$ -fermion interaction that has the chiral transformation properties of:

$$\mathcal{L}_{eff} \sim \det_{st}(\bar{q}_{sL} q_{tR}) + \det_{st}(\bar{q}_{sR} q_{tL}), \quad (5)$$

where  $s, t = 1, \dots, L$  are flavour indices, but the colour indices are arranged in a more general way (see below). It is easy to verify that  $\mathcal{L}_{eff}$  is invariant under  $SU(L) \otimes SU(L) \otimes U(1)_V$ , while it is not invariant under  $U(1)_A$ . To

obtain an order parameter for the  $U(1)$  chiral symmetry, one can simply take the vacuum expectation value of  $\mathcal{L}_{eff}$ :  $C_{U(1)} = \langle \mathcal{L}_{eff} \rangle$ . The arbitrariness in the arrangement of the colour indices can be removed if we require that the new  $U(1)$  chiral condensate is “independent” of the usual chiral condensate  $\langle \bar{q}q \rangle$ , as explained in Refs.<sup>15,16</sup>. In other words, the condensate  $C_{U(1)}$  is chosen to be a *genuine*  $2L$ -fermion condensate, with a zero “disconnected part”, the latter being the contribution proportional to  $\langle \bar{q}q \rangle^L$ , corresponding to retaining the vacuum intermediate state in all the channels and neglecting the contributions of all the other states. As a remark, we observe that the condensate  $C_{U(1)}$  so defined turns out to be of order  $\mathcal{O}(g^{2L-2}N_c^L) = \mathcal{O}(N_c)$  in the large- $N_c$  expansion, exactly as the quark condensate  $\langle \bar{q}q \rangle$ .

In the case of the  $SU(L) \otimes SU(L)$  chiral symmetry, one finds the following Ward identity (WI):

$$\int d^4x \langle T\partial^\mu A_\mu^a(x) i\bar{q}\gamma_5 T^b q(0) \rangle = i\delta_{ab} \frac{1}{L} \langle \bar{q}q \rangle, \quad (6)$$

where  $A_\mu^a = \bar{q}\gamma_\mu\gamma_5 T^a q$  is the  $SU(L)$  axial current. If  $\langle \bar{q}q \rangle \neq 0$  (in the chiral limit  $sup(m_i) \rightarrow 0$ ), the anomaly-free WI (6) implies the existence of  $L^2 - 1$  non-singlet NG bosons, interpolated by the hermitean fields  $O_b = i\bar{q}\gamma_5 T^b q$ . Similarly, in the case of the  $U(1)$  axial symmetry, one finds that:

$$\int d^4x \langle T\partial^\mu J_{5,\mu}(x) i\bar{q}\gamma_5 q(0) \rangle = 2i\langle \bar{q}q \rangle, \quad (7)$$

where  $J_{5,\mu} = \bar{q}\gamma_\mu\gamma_5 q$  is the  $U(1)$  axial current. But this is not the whole story! One also derives the following WI:

$$\int d^4x \langle T\partial^\mu J_{5,\mu}(x) O_P(0) \rangle = 2Li\langle \mathcal{L}_{eff} \rangle, \quad (8)$$

where  $O_P \sim i[\det(\bar{q}_{sL}q_{tR}) - \det(\bar{q}_{sR}q_{tL})]$ . If the  $U(1)$  chiral symmetry is still broken above  $T_{ch}$ , i.e.,  $\langle \mathcal{L}_{eff} \rangle \neq 0$  for  $T > T_{ch}$  (while  $\langle \bar{q}q \rangle = 0$  for  $T > T_{ch}$ ), then this WI implies the existence of a (pseudo-)Goldstone boson (in the large- $N_c$  limit!) coming from this breaking and interpolated by the hermitean field  $O_P$ . Therefore, the  $U(1)_A$  (pseudo-)NG boson (i.e., the  $\eta'$ ) is an “exotic”  $2L$ -fermion state for  $T > T_{ch}$ !

## 5 The new chiral effective Lagrangian

We shall see in this section how the proposed scenario, in which the  $U(1)$  axial symmetry is still broken above the chiral transition, can be consistently reproduced using an effective-Lagrangian model.<sup>15</sup>

It is well known that the low-energy dynamics of the pseudoscalar mesons, including the effects due to the anomaly and the quark condensate, and expanding to the first order in the light quark masses, can be described, in the large- $N_c$  limit, by an effective Lagrangian,<sup>17,18,19,20</sup> written in terms of the mesonic field  $U_{ij} \sim \bar{q}_{jR} q_{iL}$  (up to a multiplicative constant) and the topological charge density  $Q$ . If we make the assumption that the  $U(1)$  chiral symmetry is restored at a temperature  $T_{U(1)}$  greater than  $T_{ch}$ , we need another order parameter for the  $U(1)$  chiral symmetry, the form of which has been discussed in the previous section. We must now define a field variable  $X$ , associated with this new condensate, to be inserted in the chiral Lagrangian. The translation from the fundamental quark fields to the effective-Lagrangian meson fields is done as follows. The operators  $i\bar{q}\gamma_5 q$  and  $\bar{q}q$  entering in the WI (7) are essentially equal to (up to a multiplicative constant)  $i(\text{Tr}U - \text{Tr}U^\dagger)$  and  $\text{Tr}U + \text{Tr}U^\dagger$  respectively. Similarly, the operators  $\mathcal{L}_{eff} \sim \det(\bar{q}_{sL} q_{tR}) + \det(\bar{q}_{sR} q_{tL})$  and  $O_P \sim i[\det(\bar{q}_{sL} q_{tR}) - \det(\bar{q}_{sR} q_{tL})]$  entering in the WI (8) can be put equal to (up to a multiplicative constant)  $X + X^\dagger$  and  $i(X - X^\dagger)$  respectively, where  $X \sim \det(\bar{q}_{sR} q_{tL})$  is the new field variable (up to a multiplicative constant), related to the new  $U(1)$  chiral condensate, which must be inserted in the chiral effective Lagrangian. It was shown in Refs.<sup>15</sup> that the most simple effective Lagrangian, constructed with the fields  $U$ ,  $X$  and  $Q$ , is:

$$\begin{aligned} \mathcal{L}(U, U^\dagger, X, X^\dagger, Q) = & \frac{1}{2}\text{Tr}(\partial_\mu U \partial^\mu U^\dagger) + \frac{1}{2}\partial_\mu X \partial^\mu X^\dagger + \\ & -V(U, U^\dagger, X, X^\dagger) + \frac{1}{2}iQ(x)\omega_1\text{Tr}[\log(U) - \log(U^\dagger)] + \\ & +\frac{1}{2}iQ(x)(1 - \omega_1)[\log(X) - \log(X^\dagger)] + \frac{1}{2A}Q^2(x), \end{aligned} \quad (9)$$

where the potential term  $V(U, U^\dagger, X, X^\dagger)$  has the form:

$$\begin{aligned} V(U, U^\dagger, X, X^\dagger) = & \frac{1}{4}\lambda_\pi^2\text{Tr}[(U^\dagger U - \rho_\pi \cdot \mathbf{I})^2] + \frac{1}{4}\lambda_X^2(X^\dagger X - \rho_X)^2 \\ & -\frac{B_m}{2\sqrt{2}}\text{Tr}[MU + M^\dagger U^\dagger] - \frac{c_1}{2\sqrt{2}}[\det(U)X^\dagger + \det(U^\dagger)X]. \end{aligned} \quad (10)$$

$M$  represents the quark mass matrix,  $M = \text{diag}(m_1, \dots, m_L)$ , and  $A$  is the topological susceptibility in the pure YM theory. All the parameters appearing in the Lagrangian are to be considered as functions of the physical temperature  $T$ . In particular, the parameters  $\rho_\pi$  and  $\rho_X$  are responsible for the behaviour of the theory respectively across the  $SU(L) \otimes SU(L)$  and the  $U(1)$  chiral phase

transitions, according to the following table:

	$T < T_{ch}$	$T_{ch} < T < T_{U(1)}$	$T > T_{U(1)}$
$\rho_\pi$	$\frac{1}{2}F_\pi^2 > 0$	$-\frac{1}{2}B_\pi^2 < 0$	$-\frac{1}{2}B_\pi^2 < 0$
$\rho_X$	$\frac{1}{2}F_X^2 > 0$	$\frac{1}{2}F_X^2 > 0$	$-\frac{1}{2}B_X^2 < 0$

[Tab.1]

[That is:  $\rho_\pi(T_{ch}) = 0$  and  $\rho_X(T_{U(1)}) = 0$ .] The  $U(1)$  chiral symmetry remains broken also in the region of temperatures  $T_{ch} < T < T_{U(1)}$ , where on the contrary the  $SU(L) \otimes SU(L)$  chiral symmetry is restored. The  $U(1)$  chiral symmetry is restored above  $T_{U(1)}$ . We also assume that the topological susceptibility of the pure YM theory,  $A(T)$ , drops to zero at a temperature  $T_\chi$  greater than  $T_{ch}$ . Then, for the consistency of the model, it must be  $T_\chi \leq T_{U(1)}$ .

One can study the mass spectrum of the theory for  $T < T_{ch}$  and  $T_{ch} < T < T_{U(1)}$ . First of all, let us see what happens for  $T < T_{ch}$ , where both the  $SU(L) \otimes SU(L)$  and the  $U(1)$  chiral symmetry are broken. Integrating out the field variable  $Q$  and taking only the quadratic part of the Lagrangian, one finds that, in the chiral limit  $\sup(m_i) \rightarrow 0$ , there are  $L^2 - 1$  zero-mass states, which represent the  $L^2 - 1$  Goldstone bosons coming from the breaking of the  $SU(L) \otimes SU(L)$  chiral symmetry down to  $SU(L)_V$ . Then there are two singlet eigenstates:

$$\begin{aligned}\eta' &= \frac{1}{\sqrt{F_\pi^2 + LF_X^2}}(\sqrt{L}F_X S_X + F_\pi S_\pi), \\ \eta_X &= \frac{1}{\sqrt{F_\pi^2 + LF_X^2}}(-F_\pi S_X + \sqrt{L}F_X S_\pi),\end{aligned}\quad (11)$$

(where  $S_\pi$  is the usual  $SU(L)$  singlet meson field associated with  $U$ , while  $S_X$  is the meson field associated with  $X$ ) with non-zero masses. One of them ( $\eta'$ ) has a “light” mass, in the sense of the  $N_c \rightarrow \infty$  limit, being

$$m_{\eta'}^2 = \frac{2LA}{F_\pi^2 + LF_X^2} = \mathcal{O}\left(\frac{1}{N_c}\right). \quad (12)$$

This mass is intimately related to the anomaly and they both vanish in the  $N_c \rightarrow \infty$  limit. On the contrary the field  $\eta_X$  has a sort of “heavy hadronic” mass of order  $\mathcal{O}(1)$  in the large- $N_c$  limit. We immediately see that, if we put  $F_X = 0$  in the above-written formulae (i.e., if we neglect the new  $U(1)$  chiral

condensate), then  $\eta' = S_\pi$  and  $m_{\eta'}^2$  reduces to  $\frac{2A}{F_\pi^2}$ , which is the “usual”  $\eta'$  mass in the chiral limit.<sup>2,3</sup> Yet, in the general case  $F_X \neq 0$ , the two states which diagonalize the squared mass matrix are linear combinations of the “quark–anti-quark” singlet field  $S_\pi$  and of the “exotic” field  $S_X$ . Both the  $\eta'$  and the  $\eta_X$  have the same quantum numbers (spin, parity and so on), but they have a different quark content: one is mostly  $\sim i(\bar{q}_L q_R - \bar{q}_R q_L)$ , while the other is mostly  $\sim i[\det(\bar{q}_{sL} q_{tR}) - \det(\bar{q}_{sR} q_{tL})]$ . What happens when approaching the chiral transition temperature  $T_{ch}$ ? We know that  $F_\pi(T) \rightarrow 0$  when  $T \rightarrow T_{ch}$ . From Eq. (12) we see that  $m_{\eta'}^2(T_{ch}) = \frac{2A}{F_X^2}$  and, from the first Eq. (11),  $\eta'(T_{ch}) = S_X$ . We have continuity in the mass spectrum of the theory through the chiral phase transition at  $T = T_{ch}$ . In fact, if we study the mass spectrum of the theory in the region of temperatures  $T_{ch} < T < T_{U(1)}$  (where the  $SU(L) \otimes SU(L)$  chiral symmetry is restored, while the  $U(1)$  chiral symmetry is still broken), one finds that there is a singlet meson field  $S_X$  (associated with the field  $X$  in the chiral Lagrangian) with a squared mass given by (in the chiral limit):  $m_{S_X}^2 = \frac{2A}{F_X^2}$ . This is nothing but the *would-be* Goldstone particle coming from the breaking of the  $U(1)$  chiral symmetry, i.e., the  $\eta'$ , which, for  $T > T_{ch}$ , is a sort of “exotic” matter field of the form  $\sim i[\det(\bar{q}_{sL} q_{tR}) - \det(\bar{q}_{sR} q_{tL})]$ . Its existence could be proved perhaps in the near future by heavy-ions experiments.

## 6 Conclusions

We have tried to gain a physical insight into the breaking mechanism of the  $U(1)$  axial symmetry, through a study of the behaviour of the theory at finite temperature. In the following, we briefly summarize the main points that we have discussed and the results that we have obtained.

- One expects that, above a certain critical temperature, also the  $U(1)$  axial symmetry will be (approximately) restored. We have tried to see if this transition has (or has not) anything to do with the usual  $SU(L) \otimes SU(L)$  chiral transition: various possible scenarios have been discussed.
- We have proposed a scenario (supported by lattice results) in which the  $U(1)$  axial symmetry is still broken above the chiral transition. A new order parameter is introduced for the  $U(1)$  axial symmetry.
- We have shown that this scenario can be consistently reproduced using an effective Lagrangian model. We have analysed the effects that one should observe on the mass spectrum of the theory, both below and above  $T_{ch}$ .

In this scenario, the  $\eta'$  survives across the chiral transition at  $T_{ch}$  in the form of an “exotic”  $2L$ -fermion state.

This scenario could perhaps be verified in the near future by heavy-ions experiments, by analysing the spectrum in the singlet sector. Some tests and verifications of this picture could also be provided by Monte Carlo simulations on the lattice.

## References

1. T. Blum, L. Karkkäinen, D. Toussaint and S. Gottlieb, Phys. Rev. D **51** (1995) 5153.
2. E. Witten, Nucl. Phys. B **156** (1979) 269.
3. G. Veneziano, Nucl. Phys. B **159** (1979) 213.
4. E. Meggiolaro, Phys. Rev. D **58** (1998) 085002.
5. M. Teper, Phys. Lett. B **171** (1986) 81.
6. A. Di Giacomo, E. Meggiolaro and H. Panagopoulos, Phys. Lett. B **277** (1992) 491.
7. B. Allés, M. D’Elia and A. Di Giacomo, Nucl. Phys. B **494** (1997) 281.
8. E. Shuryak, Comments Nucl. Part. Phys. **21** (1994) 235.
9. C. Bernard *et al.*, Nucl. Phys. B (Proc. Suppl.) **53** (1997) 442;  
C. Bernard *et al.*, Phys. Rev. Lett. **78** (1997) 598.
10. F. Karsch, Nucl. Phys. B (Proc. Suppl.) **83–84** (2000) 14.
11. P.M. Vranas, Nucl. Phys. B (Proc. Suppl.) **83–84** (2000) 414.
12. R.D. Pisarski, F. Wilczek, Phys. Rev. D **29** (1984) 338.
13. G. ’t Hooft, Phys. Rev. Lett. **37** (1976) 8;  
G. ’t Hooft, Phys. Rev. D **14** (1976) 3432.
14. D. Kharzeev, R.D. Pisarski and M.H.G. Tytgat, Phys. Rev. Lett. **81** (1998) 512.
15. E. Meggiolaro, Z. Phys. C **62** (1994) 669;  
E. Meggiolaro, Z. Phys. C **62** (1994) 679;  
E. Meggiolaro, Z. Phys. C **64** (1994) 323.
16. A. Di Giacomo and E. Meggiolaro, Nucl. Phys. B (Proc. Suppl.) **42** (1995) 478.
17. P. Di Vecchia and G. Veneziano, Nucl. Phys. B **171** (1980) 253.
18. E. Witten, Annals of Physics **128** (1980) 363.
19. C. Rosenzweig, J. Schechter and C.G. Trahern, Phys. Rev. D **21** (1980) 3388.
20. P. Nath and R. Arnowitt, Phys. Rev. D **23** (1981) 473.

# MECHANISMS OF CONFINEMENT

L. DEL DEBBIO

*Dipartimento di Fisica, Università di Pisa  
Via Buonarroti 2, 56127 Pisa, Italy  
E-mail: ldd@df.unipi.it*

We discuss current proposals for the mechanism of color confinement in QCD. The role of topological excitations like vortices and monopoles is analyzed, starting from the numerical evidence produced by Monte Carlo simulations. Trying to characterize the deconfinement phase transition in terms of symmetry, we argue that the confined phase can be characterized as a dual superconducting phase, i.e. a phase where a dual magnetic symmetry is spontaneously broken *à la Higgs*. We discuss the definition of a disorder parameter that is capable of monitoring dual superconductivity and present numerical data in favour of a deconfining phase transition in pure gluodynamics driven by monopole condensation. This picture can be naturally extended to the case of QCD with dynamical fermions: in this case, the disorder parameter becomes a unique tool to identify the phase transition.

## 1 Introduction: confinement and symmetry

Experimental bounds on the existence of free quarks are very stringent. Such small numbers are “naturally” explained if one postulates that there are no free colored particles in nature, i.e. that confinement is an absolute property of strong interactions at large distances, possibly protected by a symmetry. The success of lattice QCD in computing hadron masses, decay constants, and hadronic matrix elements, suggests that QCD remains an adequate description of strong interactions even at the hadronic scale. For this description to be complete, one should identify, within QCD, a mechanism that is responsible for color confinement.

First results from heavy-ion experiments are consistent with the existence of two phases in QCD. At low temperature, the system is characterized by the Regge trajectories in the hadronic spectrum, a linear potential between constituent quarks, and chiral symmetry breaking. In the high temperature phase, where quarks and gluons become the elementary excitations in the spectrum, the potential between the quarks is a Debye potential, and chiral symmetry is restored. (The connection between chiral symmetry breaking and confinement is another interesting aspect of the non-perturbative dynamics of strong interactions.) One should understand whether these two phases are separated by a phase transition or analytically connected by a crossover. If there is indeed a phase transition, one would like to identify the symme-

tries that characterize the two phases, define a suitable order parameter, and predict the order of the transition and the critical exponents. Finally, the phenomenological consequences of the structure of the phase diagram should be investigated in view of the experimental results that will be produced at RHIC and ALICE.

For pure gluodynamics, the confined phase is characterized in terms of global symmetries and suitable order parameters can be defined. There is a clear evidence from numerical simulations in favour of a confined and a deconfined phase, separated by a phase transition. The confined phase is unambiguously identified by a linear potential at large distances:

$$V(R) = \sigma R \quad (1)$$

which yields the characteristic *area law* for large Wilson loops. At finite temperature, the expectation value of the Polyakov line yields the free energy of an isolated quark:

$$\langle P(\vec{x}) \rangle \propto \exp \{ -F_q(\vec{x})/T \} \quad (2)$$

As suggested by Eq. 2,  $\langle P(\vec{x}) \rangle$  vanishes in the confined phase, where  $F_q$  is divergent, while it has a finite value in the deconfined phase. The non-vanishing expectation value of the Polyakov loop in the deconfined phase signals the spontaneous breaking of center symmetry. The Svetitsky and Yaffe (SY) conjecture<sup>1</sup> yields a correspondence between the dynamics of the phase transition in a Yang-Mills theory in  $(d+1)$  dimensions and a spin system in  $d$  dimensions: the system is described by the most general effective lagrangian for the order parameter, that describes the breaking of the center symmetry, including all the relevant operators that are compatible with the symmetry. Hence, the critical dynamics of  $SU(N)$  gauge theories in 4 dimensions is described by a  $Z_N$  spin system in 3 dimensions. The order of the phase transition and the critical exponents are obtained on simple symmetry grounds. Numerical simulations have confirmed the predictions of the SY conjecture. The transition is second order for  $SU(2)$  and first order for  $SU(3)$ . The transition temperatures are<sup>2,3</sup>:

$$\frac{T_c}{\sqrt{\sigma}} = \begin{cases} 0.69 \pm 0.02, & SU(2) \\ 0.60 \pm 0.04, & SU(3) \end{cases}$$

Preliminary results are available for larger values of  $N$ <sup>4,5</sup>. As their precision is improved, these simulations should enable us to check the order of the phase transition as the number of colors grows large<sup>1,6</sup>.

Within this well-defined framework, we review some aspects of two mechanisms of confinement: the center vortex model and dual superconductivity.

Both identify topological excitations as the configurations that are responsible for confinement. They are respectively vortex lines and monopoles. For the case of monopoles, it is possible to associate confinement with the breaking of a *dual* symmetry. We discuss the definition of an order parameter, which detects the spontaneous breaking of this dual symmetry. Such an operator is called a disorder parameter, by analogy with statistical mechanics. The disorder parameter proves to be a valuable tool to investigate quantitatively the characteristics of the phase transition by Monte Carlo simulations.

Introducing dynamical fermions complicates the scenario in many ways. Most importantly, the characterization of confinement becomes more difficult. Due to string breaking, one can no longer rely on the linear behaviour of the potential at large distances to identify the confined phase. Similarly, center symmetry is explicitly broken by the fermionic action. We argue that the pattern of dual symmetry breaking remains valid and that the disorder parameter introduced for the case of pure gauge theories is still useful to study the deconfinement phase transition in QCD.

## 2 Pure gluodynamics

### 2.1 Vortex model of the QCD vacuum

The vortex model of QCD vacuum was originally proposed in <sup>7,8,9,10,11,12,13</sup> as an attempt to identify the configurations that are responsible for confinement: the area law for large Wilson loops is produced by the fluctuations in the number of vortex lines that cross the minimal surface spanned by the loop. A vortex is defined as a topological defect associated to a closed curve  $C$ , that contributes a non-trivial phase to any Wilson line that has non-trivial winding number with it. The creation operator for such a vortex configuration,  $A(C)$ , is characterized by the commutation relation with  $W(C')$ , a generic Wilson loop associated with the curve  $C'$ <sup>7</sup>:

$$A(C)W(C') = W(C')A(C) \exp\left(\frac{2\pi i n_{CC'}}{N}\right) \quad (3)$$

where  $n_{CC'}$  is the linking number of the curves  $C$  and  $C'$  and  $N$  is the number of colors. In other words, the Wilson loop is multiplied by an element of the center every time the vortex line crosses its surface. The presence of vortices helps disordering the system and therefore produces a non-vanishing string tension. A numerical recipe to identify center vortices in lattice configurations was proposed in Refs. <sup>14,15</sup>. Several aspects of the above mechanism have been checked in numerical simulations.

**Vortices and string tension.** In SU(2), if the configurations with an odd number of vortices piercing the Wilson loop are excluded, the string tension at zero temperature vanishes. The same result is obtained if one excludes the configurations with an even number of vortices piercing the loop, showing that confinement is produced by the balance of positive and negative contributions to the Wilson loop<sup>14</sup>. Similarly, the finite temperature phase transition appears to be driven by vortices<sup>16,17</sup>.

**Chiral symmetry and topology.** The vortex contribution to chiral symmetry breaking<sup>18</sup> and to the topological charge<sup>19,20</sup> has also been established. In Ref.<sup>18</sup>, a “modified” field configuration is constructed by removing “by hand” the vortices that were found in the Monte Carlo generated ensemble. The value of the chiral condensate is computed for small values of the quark mass on both ensembles, and extrapolated to the chiral limit. A non-vanishing chiral condensate in the zero-mass limit is obtained only when the vortices are taken into account.

**'t Hooft operator.** More insight on the dynamics of vortices has been obtained studying the behaviour of the 't Hooft operator, which is related to the free energy of a vortex configuration<sup>21,22,23,24,25,26,27,28,29</sup>. As expected from the commutation relation in Eq. 3, the 't Hooft operator shows a behaviour that is dual to that of the Wilson loop, namely it displays an area law in the deconfined phase, characterized by a dual string tension. In Ref.<sup>27,28</sup> a vortex creation operator is defined on the lattice, and its vacuum expectation value is monitored across the finite temperature phase transition. The operator is the dual of a Polyakov line, as such it is related to the free energy cost for creating a pair of vortices, and the deconfined phase is signalled by the vanishing of its expectation value. In practice, one computes  $\rho = \frac{d}{d\beta} \log\langle\mu\rangle$ , which should exhibit a negative peak at the phase transition. The critical temperature and the critical exponents have been extracted from a fit to the finite size scaling of  $\rho$ . Another independent determination of the critical exponent  $\nu$  is obtained from the temperature dependence of the dual string tension<sup>29</sup> for SU(2). The dual string tension is an order parameter to monitor the breaking of a magnetic  $Z_N$  symmetry. It would be interesting to see the temperature dependence of the dual string tension for the SU(3) lattice gauge theory, where the phase transition is known to be of the first order.

**Effective descriptions.** Using dual plaquettes as fundamental fields, an effective lagrangian for the dynamics of the vortex sheets has been proposed and used to study the deconfinement phase transition<sup>30</sup>. It is interesting to see that a formulation in terms of dual variables allows the string tension and the critical temperature to be determined. Clearly, the couplings of the effective lagrangian need to be tuned and hence most of the predictive power

of this approach is lost. Moreover, the effective lagrangian approach does not yield any information neither on the order of the phase transition, nor on the critical exponents. The deconfinement phase transition has also been linked to the transition to a phase where vortices percolate<sup>17</sup>. Unfortunately, the characterization of a phase of percolating networks of vortices is not completely unambiguous<sup>31</sup>.

## 2.2 *Dual superconductivity*

The dual superconductor model of confinement was proposed independently by 't Hooft<sup>32</sup> and Mandelstam<sup>33</sup>. In this scenario, magnetic charge is condensed in the confined phase of QCD, leading to the formation of chromoelectric flux tubes by dual Meissner effect and hence to a linear potential between chromoelectric charges. Substantial evidence in favour of this picture comes from numerical investigations of the field configurations in the QCD vacuum that have highlighted the existence of flux tubes and have investigated their profile in detail<sup>34,35,36,37</sup>.

Dual superconductivity provides an appealing mechanism for confinement. Duality is a deep property that appears in a variety of systems with topological excitations. These systems admit two equivalent descriptions: one in terms of the canonical variables that appear in the hamiltonian, with solitonic solutions describing the topological excitations; the other is based on the topological excitations considered as elementary fields, with an appropriate (dual) hamiltonian to describe their dynamics. In this second picture, the elementary fields of the original theory appear as topological excitations. Usually, duality maps strong into weak coupling and viceversa. The transformation relating the original fields to the dual ones and the original hamiltonian to the dual hamiltonian is known explicitly only in a few systems. The most celebrated example is the Ising model in two dimensions, which happens to be self-dual.

The duality that we are going to consider here is the electric-magnetic duality. A dual superconductor is therefore characterized by condensation of magnetic charge and dual Meissner effect with formation of chromoelectric flux tubes. In order to investigate this scenario beyond the simple study of the field configurations, a definition of monopoles in non-abelian gauge theories is needed. Stable monopole solutions are classified by the elements of the first homotopy group of the gauge group: in the case of  $SU(N)$ , the first homotopy group is trivial, meaning that there are no stable monopole solutions. Stable Magnetic charges can be defined with respect to the abelian fields defined in the Cartan subalgebra  $U(1)^{N-1}$  via a procedure called abelian projection<sup>38,39</sup>.

In order to check the dual superconductor picture, one needs to define an operator that detects condensation of magnetic charge. Confinement is thereby related to the breaking of a symmetry, namely the dual magnetic symmetry. Following the Dirac prescription<sup>40</sup>, one constructs an operator with non-vanishing magnetic charge and measures its vacuum expectation value by numerical simulations. Being related to the breaking of a dual symmetry, such an operator is usually called a disorder operator. A disorder operator was first written in the continuum formulation generalizing to field theory the idea of a shift operator<sup>41</sup>. Consider for simplicity an abelian theory, in the Schrödinger representation. The electric field  $E_i$  is the conjugate momentum to the canonical variables  $A_i$ , so that the operator:

$$\mu(x) = \exp \left\{ \int_y E_i(y) b_i(y - x) \right\} \quad (4)$$

shifts the potential by an amount  $b(y - x)$ :

$$\mu(x)|A_i(y)\rangle = |A_i(y) + b_i(y - x)\rangle \quad (5)$$

$\mu$  is gauge invariant by construction. If  $b_i$  is the potential corresponding to a monopole, then  $\mu$  is also magnetically charged.

The construction of a disorder operator  $\mu(x)$  on the lattice for the abelian U(1) theory and for abelian projected monopoles was first introduced in<sup>42,43,44</sup>. The formulation was then clarified in<sup>45</sup> and extensive numerical investigations have been performed both in SU(2) and SU(3) lattice gauge theories<sup>46,47</sup>.

The correlator  $\langle \mu(t)\bar{\mu}(0) \rangle$  describes the propagation of a magnetic charge from time 0 to time  $t$ :

$$\langle \mu(t)\bar{\mu}(0) \rangle \simeq C e^{-Mt} + |\langle \mu \rangle|^2 \quad (6)$$

where  $M$  is the mass of the lightest state with magnetic charge, and a non-vanishing value for  $|\langle \mu \rangle|^2$  signals the breaking of the dual magnetic symmetry. Alternatively, the vacuum expectation value of a single operator can be measured, e.g. at finite temperature, using  $C^*$  boundary conditions in the time-direction<sup>48,49</sup>.

The vacuum expectation value of  $\mu$  is actually the ratio of two partition functions. As such it is affected by large fluctuations and turns out to be very difficult to estimate numerically. In order to overcome this problem, one measures:

$$\rho = \frac{d}{d\beta} \log \langle \mu \rangle \quad (7)$$

which yields the same information as  $\mu$ .

A sharp negative peak for  $\rho$  should signal a phase transition driven by the breaking of a dual magnetic symmetry. Such a peak is observed for both  $SU(2)$  and  $SU(3)$ , independently of the abelian projection used. For  $SU(3)$ , different choices of the abelian subgroup identify different magnetic charges, however all of them condense in the confined phase. In order to detect the remnants of a phase transition in a finite volume, a careful finite size scaling analysis is required. For pure gluodynamics in a finite volume, finite size scaling predicts that  $\rho$  only depends on the rescaled variable  $L^{1/\nu}t$ , where  $L$  is the lattice size and  $t$  is the reduced temperature. Assuming a functional form for the rescaled order parameter, the critical temperature and the critical exponent  $\nu$  can be fitted, yielding results in agreement with the ones reported above. The same analysis in the case of the  $SU(3)$  lattice gauge theory, yields data consistent with a first order phase transition.

### 2.3 Comments

Many results show that vortices are responsible for the characteristic features of the confined phase of QCD. However they do not identify confinement in terms of symmetry. Besides, vortices can hardly reproduce the ratios of  $k$ -string tensions for  $N > 3$ , that are now available from numerical simulations<sup>50,51</sup>, as suggested in Ref.<sup>52</sup>.

Dual superconductivity is the mechanism responsible for confinement in  $\mathcal{N} = 2$  supersymmetric Yang-Mills theories, explicitly broken to  $\mathcal{N} = 1$  by an adjoint mass term<sup>53</sup>. At given points in the moduli space, the monopoles become massless and therefore enter in the effective description of IR physics. The effective theory is a supersymmetric  $U(1)$  theory with monopoles as matter fields, and the form of the superpotential constrained by supersymmetry. Minimizing the superpotential yields explicitly a monopole condensate  $\langle \bar{q}q \rangle \neq 0$ . The original result, obtained for the  $SU(2)$  Yang-Mills theory, has been extended to show that monopole condensation also occurs for  $SU(N)$ ,  $N \geq 3$ <sup>54,55,56</sup>. This implies a very specific pattern for the ratios of  $k$ -string tensions in supersymmetric theories and there are conjectures that the same could also be true in the non supersymmetric case<sup>57</sup>. These conjectures are supported by the recent calculations for  $SU(N)$  gauge theories mentioned above<sup>50,51</sup>. Nonetheless, one should be very careful in extending supersymmetric results to the non-supersymmetric case. Indeed, as a consequence of supersymmetry, a fundamental scalar field appears in the lagrangian, and is responsible for breaking the symmetry down to the Cartan subgroup, so that solitonic monopole solutions naturally emerge. Moreover, the form of the potential is constrained by supersymmetry. None of these important ingredi-

ents are present in the non-supersymmetric case. Still, the numerical results on monopole condensation provide solid evidence that dual superconductivity is also at work in QCD, suggesting that more theoretical work is necessary to understand the relation between supersymmetric and non-supersymmetric theories.

Numerical results show that monopoles do condense, regardless of the abelian projection used to identify them. This is in agreement with the idea that there are no preferred directions in color space, and that abelian projection should be regarded simply as a tool to define magnetic charges.

It should also be noted that the disorder parameter defined above describes the propagation of an abelian projected magnetic charge only up to corrections that are  $O(a^2)$ . We believe that this should not be numerically relevant, if the simulations are performed in the scaling region.

Further properties of the disorder operator have been investigated in Refs. <sup>58,59</sup>. We recall here two important results. For the pure U(1) gauge theory, a duality transformation can be written explicitly, mapping the partition function of the theory into a dual non-compact abelian Higgs (ncH) model <sup>60</sup>. Under this transformation, the correlator of two disorder operators is mapped into the correlator of two gauge-invariant charged fields constructed using the Dirac prescription. Hence, for the case of an abelian theory, one can see explicitly that the disorder parameter is exactly a Dirac charged dual field, written as a non-local operator in the original theory. Refs. <sup>58,59</sup> also point out that the disorder parameter  $\mu$  is inconsistent in the treatment of small scales, because it violates Dirac's quantization condition of fluxes. As a consequence, one should observe an unphysical dependence on the Dirac string attached to the monopole. A new order parameter is proposed, that overcomes these difficulties. Unfortunately the new order parameter is more complicated to estimate by numerical simulations, while it is expected to behave like  $\mu$  in the scaling region. It is very interesting to point out that the construction in <sup>58,59</sup>, which relies primarily on center vortex sheets, leads to a natural connection between the percolation of vortices and monopole condensation, a phenomenon that certainly deserves further investigations.

Ref. <sup>61</sup> presents an interesting approach to relate the dynamics of the order parameter to the observed hadronic spectrum. Further progress along these lines could bridge the gap between the hadronic states that appear in the spectrum and the elementary degrees of freedom of the QCD lagrangian.

### 3 Full QCD

As a conclusion, let us analyze how some of the arguments reported above can be extended to the case where dynamical quarks are also taken into account.

#### 3.1 *Residual symmetries*

Introducing dynamical fermions leads to several difficulties. First of all, as already mentioned in the introduction, is the characterization of confinement itself. Due to string breaking, the linear potential between quarks flattens out at large distances and the confined phase is no longer identified by an asymptotic string tension. Moreover, the center symmetry is explicitly broken by the fermionic part of the action, and hence the Svetitsky-Yaffe conjecture does not apply in this case. Finally, a mass term for fermions introduces an explicit breaking of chiral symmetry. Therefore, if the system is studied using chiral observables, the confined and deconfined phases do not look separated by a singularity as long as the mass of the quarks does not vanish. Finally, one expects the phase diagram to depend on the quark masses.

However, the experimental results already mentioned above do refer to the real world, that is to a system where fermions are dynamical degrees of freedom. Moreover, if confinement is still present in the large- $N$  limit of  $SU(N)$  gauge theories, the suppression of quark loops by factors of  $1/N$  should suggest that the mechanism of confinement is actually not very sensitive to the unquenching of the fermionic degrees of freedom.

In this respect, it is worthwhile to remark that dual superconductivity is still a viable scenario. Indeed, according to the mechanism proposed by 't Hooft, every particle that is charged with respect to the abelian subgroups, including quarks, will be confined by dual Meissner effect. Moreover, the dual symmetry breaking pattern remains unchanged. Therefore, we argue that the disorder parameter introduced for the pure gauge case, is still a valid tool to locate the deconfinement phase transition and to determine its order.

#### 3.2 *Numerical results*

Preliminary results for the  $\rho$  parameter in full QCD with two flavors of staggered quarks are now available<sup>62</sup>. The temperature is varied by changing the lattice spacing  $a$ , which is a function of both the coupling and the bare mass. The physical mass of the quark is kept constant by requiring that the ratio  $m_\pi/m_\rho$  at zero temperature remains constant as  $\beta$  and  $m$  are varied. The negative peak suggests that there is indeed a monopole condensate. The location of the peak coincides with the chiral phase transition. The finite

size scaling analysis in this case is complicated by the fact that the disorder parameter becomes a function of several scaling variables. In order to evidence a scaling behaviour, one needs to have data at different temperatures and volumes, while rescaling the mass with the volume. It is a very intensive numerical task, especially when the values for the mass become very small. Further progress is expected along these lines.

**Acknowledgements.** I have been working on and discussing about these topics with Adriano Di Giacomo for many years. It is a pleasure to acknowledge his contribution to many of the results presented in this talk. I have also greatly benefitted from collaborating at various stages with Jeff Greensite and Biagio Lucini. I am grateful to Massimo D'Elia, Mike Teper and Ettore Vicari for many interesting discussions.

## References

1. B. Svetitsky, L. Yaffe, Nucl. Phys. B **210** (1982) 423.
2. J. Fingberg, U. Heller, F. Karsch, Nucl. Phys. B **392** (1993) 493.
3. G. Boyd, J. Engels, F. Karsch, E. Laermann, C. Legeland, M. Lütgemeier, B. Petersson, Nucl. Phys. B **469** (1996) 419.
4. M. Wingate and S. Ohta, Phys. Rev. D **63** (2001) 094502 [arXiv:hep-lat/0006016].
5. R. V. Gavai, arXiv:hep-lat/0203015.
6. R. D. Pisarski and M. Tytgat, arXiv:hep-ph/9702340.
7. G. 't Hooft, Nucl. Phys. B **138** (1978) 1.
8. Y. Aharonov, A. Casher, S. Yankielowicz, Nucl. Phys. B **146** (1978) 256.
9. J.M. Cornwall, Nucl. Phys. B **157** (1979) 392.
10. G. Mack, V.B. Petkova, Ann. Phys. (NY) **123** (1979) 442.
11. G. Mack, Phys. Rev. Lett. **45** (1980) 1378.
12. H.B. Nielsen and P. Olesen, Nucl. Phys. B **160** (1979) 380.
13. P. Olesen, Nucl. Phys. B **200** [FS4] (1982) 381.
14. L. Del Debbio, M. Faber, J. Greensite and S. Olejnik, Phys. Rev. D **53** (1996) 5891 [arXiv:hep-lat/9510028].
15. L. Del Debbio, M. Faber, J. Giedt, J. Greensite and S. Olejnik, Phys. Rev. D **58** (1998) 094501 [arXiv:hep-lat/9801027].
16. K. Langfeld, O. Tennert, M. Engelhardt, H. Reinhardt, Phys. Lett. B **452** (1999) 301.
17. M. Engelhardt, K. Langfeld, H. Reinhardt, O. Tennert, Phys. Rev. D **61** (2000) 054504 [arXiv:hep-lat/9904004].
18. Ph. de Forcrand, M. D'Elia, Phys. Rev. Lett. **82** (1999) 4582.

19. M. Engelhardt, H. Reinhardt, Nucl. Phys. B **567** (2000) 249.
20. J.M. Cornwall, Phys. Rev. D **61** (2000) 085012.
21. C. Hoelbling, C. Rebbi and V. A. Rubakov, Phys. Rev. D **63** (2001) 034506 [arXiv:hep-lat/0003010].
22. C. Hoelbling, C. Rebbi and V. A. Rubakov, Nucl. Phys. Proc. Suppl. **83** (2000) 485 [arXiv:hep-lat/9909023].
23. C. Hoelbling, C. Rebbi and V. A. Rubakov, Nucl. Phys. Proc. Suppl. **73** (1999) 527 [arXiv:hep-lat/9809113].
24. S. Cheluvaraja, Nucl. Phys. Proc. Suppl. **94** (2001) 490 [arXiv:hep-lat/0010042].
25. S. Cheluvaraja, arXiv:hep-th/0006055.
26. S. Cheluvaraja, arXiv:hep-lat/0006011.
27. L. Del Debbio, A. Di Giacomo and B. Lucini, Nucl. Phys. B **594** (2001) 287 [arXiv:hep-lat/0006028].
28. L. Del Debbio, A. Di Giacomo and B. Lucini, Phys. Lett. B **500** (2001) 326 [arXiv:hep-lat/0011048].
29. Ph. de Forcrand, M. D'Elia, Phys. Rev. Lett. **86** (2001) 1438.
30. M. Engelhardt, H. Reinhardt, hep-lat/9912003.
31. K. Kajantie, M. Laine, T. Neuhaus, A. Rajantie, K. Rummukainen, Phys. Lett. B **482** (2000) 114.
32. G. 't Hooft, in "High Energy Physics", Proceedings of the EPS International Conference, Palermo 1975, ed. A. Zichichi, Bologna 1976.
33. S. Mandelstam, Phys. Rept. **23** (1976) 245.
34. A. Di Giacomo, M. Maggiore, S. Olejnik, Nucl. Phys. B **347** (1990) 441.
35. G. S. Bali, K. Schilling and C. Schlichter, Phys. Rev. D **51** (1995) 5165 [arXiv:hep-lat/9409005].
36. P. Cea and L. Cosmai, Phys. Rev. D **52** (1995) 5152 [arXiv:hep-lat/9504008].
37. R. W. Haymaker, V. Singh, Y. C. Peng and J. Wosiek, Phys. Rev. D **53** (1996) 389 [arXiv:hep-lat/9406021].
38. G. 't Hooft, Nucl. Phys. B **190**, 455 (1981).
39. A. S. Kronfeld, G. Schierholz and U. J. Wiese, Nucl. Phys. B **293**, 461 (1987).
40. P.A.M. Dirac, Can. J. Phys. **33** (1955) 650.
41. E. C. Marino, B. Schroer and J. A. Swieca, Nucl. Phys. B **200** (1982) 473.
42. L. Del Debbio, A. Di Giacomo and G. Paffuti, Phys. Lett. B **349** (1995) 513 [arXiv:hep-lat/9403013].
43. L. Del Debbio, A. Di Giacomo, G. Paffuti and P. Pieri, Phys. Lett. B **355** (1995) 255 [arXiv:hep-lat/9505014].

44. M. Chernodub, M. Polikarpov, A. Veselov, JETP Lett. **63** (1996) 411.
45. A. Di Giacomo, G. Paffuti, Phys. Rev. D **56**, 6816 (1997).
46. A. Di Giacomo, B. Lucini, L. Montesi, G. Paffuti, Phys. Rev. D **61** 034504 (2000).
47. A. Di Giacomo, B. Lucini, L. Montesi, G. Paffuti, Phys. Rev. D **61** 034505 (2000).
48. U.J. Wiese, Nucl. Phys. B **375** (1992) 45.
49. A.S. Kronfeld, U.J. Wiese, Nucl. Phys. B **401** (1992) 190.
50. L. Del Debbio, H. Panagopoulos, P. Rossi and E. Vicari, JHEP **0201** (2002) 009 [arXiv:hep-th/0111090].
51. B. Lucini and M. Teper, Phys. Rev. D **64** (2001) 105019 [arXiv:hep-lat/0107007].
52. L. Del Debbio and D. Diakonov, in preparation.
53. N. Seiberg and E. Witten, Nucl. Phys. B **426** (1994) 19 [Erratum-ibid. B **430** (1994) 485] [arXiv:hep-th/9407087].
54. P. C. Argyres and A. E. Faraggi, Phys. Rev. Lett. **74** (1995) 3931 [arXiv:hep-th/9411057].
55. A. Klemm, W. Lerche, S. Yankielowicz and S. Theisen, Phys. Lett. B **344** (1995) 169 [arXiv:hep-th/9411048].
56. M. R. Douglas and S. H. Shenker, Nucl. Phys. B **447**, 271 (1995).
57. A. Hanany, M. J. Strassler, and A. Zaffaroni, Nucl. Phys. B **513**, 87 (1998).
58. J. Fröhlich, P.A. Marchetti, Phys. Rev. D **64** (2001) 014505 [arXiv:hep-lat/00110246].
59. J. Fröhlich, P.A. Marchetti, Nucl. Phys. Proc. Suppl. **106** (2002) 47 [arXiv:hep-lat/0110193].
60. F.J. Wegner, J. Math. Phys. **12** (1971) 2259.
61. F. Sannino, arXiv:hep-ph/0204174.
62. J. M. Carmona, M. D'Elia, L. Del Debbio, A. Di Giacomo, B. Lucini and G. Paffuti, Nucl. Phys. Proc. Suppl. **106** (2002) 607 [arXiv:hep-lat/0110058].

# VECTOR SPECTRUM AND COLOR SCREENING IN TWO COLOR QCD AT NONZERO $T$ AND $\mu$

BARTOLOME ALLÉS

*Dipartimento di Fisica, Università di Milano-Bicocca and INFN Sezione di Milano, I-20126-Milano, Italy*

MASSIMO D'ELIA

*Dipartimento di Fisica, Università di Genova and INFN Sezione di Genova, I-16146-Genova, Italy*

MARIA-PAOLA LOMBARDO

*INFN Sezione di Padova, I-34123-Padova, Italy*

MICHELE PEPE

*Laboratoire de Physique Théorique, Université de Paris XI, Bâtiment 210, 91405 Orsay Cedex, France*

We discuss a few topics from our ongoing investigation of the phase diagram of  $SU(2)$  Lattice Gauge Theory: we analyse a first set of results for vector mesons and diquarks, we discuss long distance screening, inferred from the behaviour of interquark potential at large separation, and we contrast and compare features at high temperature and density.

## 1 Introduction

We are investigating the phase diagram in the temperature–chemical potential plane of two color QCD by use of lattice simulations, which are possible since the Action remains positive at nonzero baryon density<sup>1,2</sup>.

Various physical questions have been addressed so far<sup>3</sup>: mean field and chiral perturbation theory are applicable at low temperature, and lattice simulations can be used either to confront these predictions, and to study the behaviour at high temperature and the effects of a finite density of baryons on the gauge fields.

The phase diagram in the temperature–density space, and a nonzero bare quark mass has been studied in great detail<sup>4</sup>. There are three different phases: an hadronic phase with confinement and spontaneous (approximate) symmetry breaking, a superfluid phase with diquark condensation, a plasma phase. For a nonzero quark mass, and a zero diquark source, which is our case, only the superfluid line is a bona fide phase transition, the other lines are crossover. It has been shown<sup>4</sup> that, for some values of  $\mu$ ,  $\langle\bar{\psi}\psi\rangle(T)$  is a non-monotonic

function. An earlier, sketchy proposal of the phase diagram<sup>5</sup> suggests a non-monotonic behavior for the diquark condensate. Such re-entrant behaviours are rather common in condensed matter (e.g. superconductors) but unusual in particle physics: that adds to the interest of two color QCD.

Our aim is to characterize the various phases and their associated phenomena, by continuing the study of the spectrum and by exploring more deeply the behaviour of purely gluonic observables.

Here we will present only a subset of our results, including results for the Polyakov loop and its correlators, and first results for the vector meson and diquark spectrum. A complete presentation, comprehensive of topological<sup>6</sup> and thermodynamics results will appear in a future publication<sup>7</sup>.

## 2 The simulations

We carried out simulations by use of an HMD algorithm used in previous work<sup>2</sup>, on a  $14^3 \times 6$  lattice for several values of temperatures, masses and chemical potentials. The chemical potentials ranges from zero to the lattice saturation, while the temperature ranges from  $T \simeq 0$  to  $T > T_c$ . Typically, on our larger lattices we run for  $O(10000)$  MD steps, with  $dt = .02$  and taking measures every 40 steps. A few test runs were performed with  $dt = .04$  and  $dt = .08$  and we confirm that discretization errors are small at  $dt = .02$ . The accuracy of the inversion of the Dirac operator has been checked by use of the lattice Ward identity.

## 3 Color screening

Consider the correlations  $\langle PP^\dagger(R) \rangle$  of the zero momentum Polyakov loops, averaged over spatial directions. Remember that this quantity is related to the interquark potential  $V(R)$ :  $\langle PP^\dagger(R) \rangle \propto e^{-V(R)/T}$ ,  $R$  being the spatial separation and  $T$  the temperature.

In a pure Yang-Mills (quenched) system, the  $Z(N_c)$  global symmetry which is broken at high temperature dictates the large distance behaviour

$$\begin{aligned} \lim_{R \rightarrow \infty} \langle PP^\dagger(R) \rangle &= |\langle P \rangle|^2 \propto e^{-V(\infty)/T} = 0 & T < T_c \\ &= K \neq 0 & T > T_c \end{aligned} \quad (1)$$

i.e. the Polyakov loop is the order parameter for confinement. As  $\lim_{R \rightarrow \infty} V(R) \propto \sigma R$ ,  $\sigma$  being the string tension, the interquark potential in the quenched theory is characterized by a non-vanishing string tension in the confined phase.

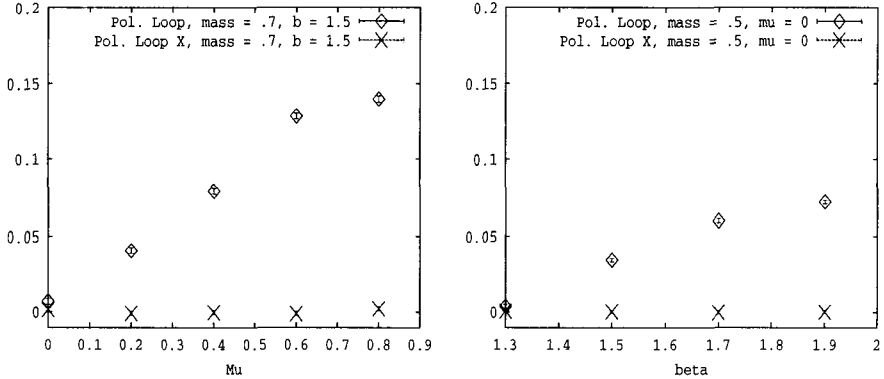


Figure 1. Polyakov loop, and spatial Polyakov loop, as a function of  $\beta$  (right) and chemical potential. In both cases only the temporal Polyakov loop feels the transition

When dynamical quarks are added, the picture, as it is well known, becomes more complicated due to a new phenomenon: the color flux tubes between heavy quarks can break by creation of a light quark pair:  $Q\bar{Q} \rightarrow (Q\bar{q})(q\bar{Q})$ . The potential does not rise linearly with the distance, but it is effectively screened (string breaking). The typical length scale  $R_0$  of this phenomenon can be estimated by  $V(R_0) = 2M_{q\bar{Q}}$ ,  $M_{q\bar{Q}}$  being the mass of the heavy-light meson. String breaking in the hadronic phase has been observed at a moderately high temperature and it has also been suggested that the real particles present in a dense system further favors the breaking of the string<sup>8</sup>.

Consider the Polyakov loop at spatial coordinates  $\vec{n} = (n_1, n_2, n_3)$

$$P(\vec{n}) = (1/N_c) \text{Tr} \prod_{\tau=0}^{N_\tau-1} U_0(\vec{n}, \tau) \quad (2)$$

We average  $P(\vec{n})$  on spatial planes to build, for each spatial coordinate  $x_i$ :

$$P(x_i) = (1/N_s)^2 \sum_{n_i=x_i} P(\vec{n}) \quad (3)$$

By use of  $P(x_i)$  we finally arrive at the zero-th momentum projected correlation function of the Polyakov line

$$\langle PP^\dagger(R) \rangle = \frac{1}{3N_s} \sum_{i=1}^3 \sum_{x_i=1}^{N_s} \langle P_i(x_i) P_i^\dagger(x_i + R) \rangle \quad (4)$$

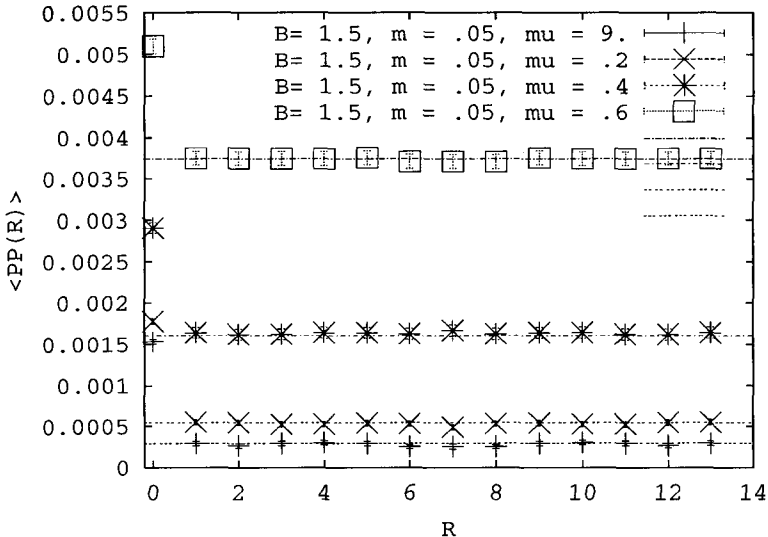


Figure 2. Polyakov loop correlation for different chemical potentials: screening and string breaking grows rapidly around  $\mu_c$ . The horizontal lines are drawn in correspondence of  $\langle P^2 \rangle$ , demonstrating the cluster property of the correlators.

It is interesting to remark that for two color  $P$  is a real quantity: hence, the Polyakov loop correlator defining the strength of the quark-quark, interaction  $\langle PP(R) \rangle / \langle |P|^2 \rangle$ , would be the same as the quark-antiquark one  $\langle PP^\dagger(R) \rangle / \langle |P|^2 \rangle$ : that remains true also at  $\mu \neq 0$ .

We show the results for the Polyakov loop correlators at various values of the chemical potential correlators in Fig. 2. At high temperature we observe the expected long range enhanced screening. We note that the trends with temperature and chemical potential are quite similar: in both cases we have signals of long range ordering, i.e. deconfinement. The gap between the plateaux at  $\mu = .2$  and  $\mu = .4$  in Fig. 2 suggests increased fermion screening and the passage to a deconfined phase. We have then a direct evidence of the effect of the chemical potential on the gauge fields (similar results have been obtained also on smaller, symmetric lattices).

The results provide a *first direct observation of long range screening in a dense gauge system*, obtained from a first principle study of the model. They are thus providing an important confirmation of the standard expectation of the structure of a dense medium.

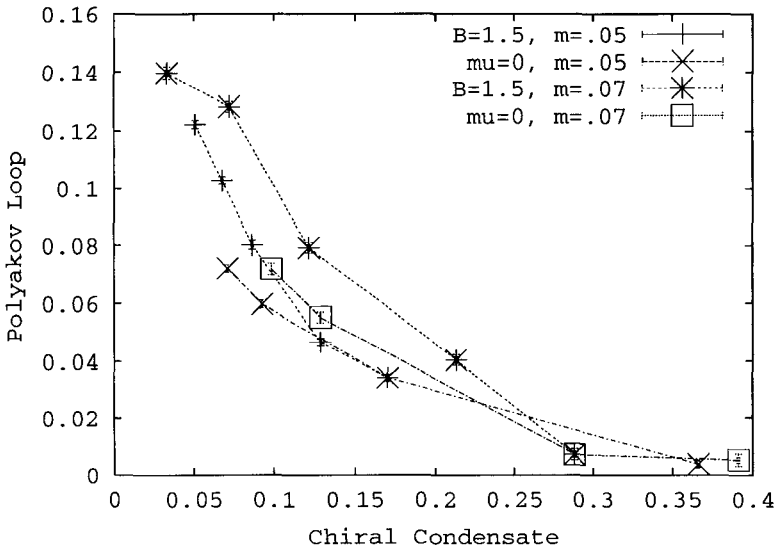


Figure 3. Chiral condensate vs. Polyakov loop: see text

A more detailed analysis can give us more information on the screening properties. We note that some theoretical guidance can also be offered by low energy effective string models<sup>9</sup>, which provide the following expression (simplified for the sake of the present discussion):

$$\langle PP^\dagger(R) \rangle = c_1 e^{-\sigma_0 R N_t} + (N_c N_f)^2 c_2^{-\sigma_0 R_0 N_t}. \quad (5)$$

We see the expected exponential dependence on the breaking length  $R_0$ , hence on the mass scale, and we also note the dynamical factors  $c_1$  and  $c_2$ . It is then reasonable to assume that they depend on temperature and density: we will address this point in more detail in the future.

In Fig. 1 the dependence of the Polyakov loop on  $\mu$  (left hand side) and on  $T$  (right hand side) is contrasted with that of the spatial Polyakov loop. The behaviour at high temperature and high density is qualitatively similar: in both cases, only the temporal loop is affected.

Finally, in Fig. 3 we study the correlation between  $|\langle P \rangle|$  and  $\langle \bar{\psi} \psi \rangle$ . We see that 1. chiral condensate and Polyakov loop are well correlated both as a function of temperature and chemical potential 2. the Polyakov loop looks consistently larger when  $\mu \neq 0$  supporting the idea of a somehow larger string breaking at finite density<sup>8</sup>.

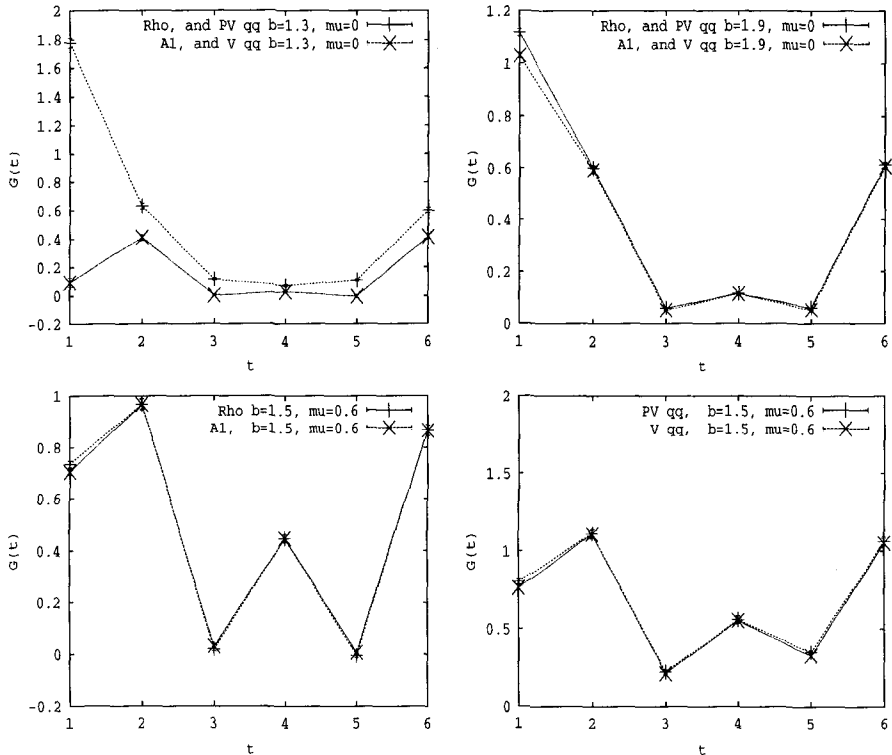


Figure 4. Vector mesons and diquarks propagators  $G(t)$  as a function of Euclidean time  $t$ . Upper, left: vector and pseudovector meson propagators in the hadronic phases. Vector diquarks are degenerate. Upper, right: as in left part of the diagram, but in the plasma phase: chiral symmetry is restored. Lower, left: vector mesons at high density; the propagators are degenerate, as it happens at high  $T$ , but chiral symmetry is still broken. Note anomalous spectral behaviour. Lower, right: vector diquarks at high density; time reversal symmetry is broken, and we note possible hints of vector condensation

#### 4 The vector sector

The vector meson  $(\bar{q}\gamma_i q)$  and diquark  $(q\gamma_i q)$  and antidiquark  $(\bar{q}\gamma_i \bar{q})$  propagators at  $\mu = 0$  are constructed from the quark propagator, as explained in early work<sup>2</sup> for the scalar spectrum, modulo the inclusion of the appropriate  $\gamma$  matrix (or, rather, of its staggered fermion representation).

From the Pauli-Gursey symmetry of the SU(2) Action follows the exact

degeneracies of the vector (V) meson propagator with the pseudovector (PV) diquark propagator, and that of the pseudovector meson propagator with the vector diquark propagator. This can also be understood as being due to quarks and anti-quarks having opposite intrinsic parities, whereas the  $qq$  and  $q\bar{q}$  interactions due to gluon exchange are identical.

Finite density spectroscopy analysis has been already introduced and discussed<sup>10</sup>. The following symmetries should hold true in the ensemble:

$$G(t) = G(T - t) \quad \text{for mesons} \quad (6)$$

$$G(t, \mu) = G(T - t, -\mu) \quad \text{for diquarks} \quad (7)$$

In addition to that, remember that staggered mesons contain states with different lattice parity (the 'oscillating' channel) : for instance, the vector meson contains both the  $\rho$  and the B particle, while the pseudovector contains the A1 and again the  $\rho$ :

$$G_V(t) = a(e^{(-m_\rho t)} + e^{m_\rho(T-t)}) + (-1)^t b(e^{(-m_B t)} + e^{m_B(T-t)}) \quad (8)$$

$$G_{PV}(t) = a(e^{(-m_{A1} t)} + e^{m_{A1}(T-t)}) + (-1)^t b(e^{(-m_\rho t)} + e^{m_\rho(T-t)}) \quad (9)$$

Since the mesons do not "feel" the effects of the chemical potential the masses of the forward and backward propagating meson states are identical.

For  $\mu \neq 0$  we expect different forward and backwards masses in the diquark channels, reflecting the different backwards and forward propagations in the dense medium.

Let us look now at the diagrams, Fig.4: the upper left diagram shows the vector and pseudovector meson propagators at low temperature, zero chemical potential. We have verified that they are degenerate with the vector diquarks of opposite parity. By increasing temperature, we observe chiral symmetry restoration in the vector channel (Fig.4, upper right diagram) : all of the four vector states (mesons and diquarks) are now degenerate. By increasing density, the degeneracy between mesons and diquarks is removed, as anticipated. Let us follow independently mesons and diquarks then.

In Fig.4 , left lower diagram, we see the vector and pesudovector mesons for  $\mu > \mu_c$ : they are degenerate, as it happens at high T: of course this does not signal chiral symmetry restoration , since chiral symmetry is still broken by the diquark condensate. Simply, it tells us that the chiral condensate, which is responsible for the difference between these two propagators, is now zero. This is the same which happened with scalars. We observe also an important difference : the oscillating componenent is increased, as if the B particle contribution were more important at high density. This might indicate a significant difference of the spectral functions at high temperature and density,

suggesting that the spectral concentration of the  $\rho$  decreases at high density in comparison to that of the B meson.

One last remark concerns the behavior of vector diquarks: in addition of the expected asymmetry, we observe (Fig.4 , right lower diagram) some indication of a plateau. All the usual caveat apply to this observation : first of all we should study colder lattices, where condensation phenomena are more prominent. Secondly, we should check finite size scaling. If this trend were to persist for a range of lattice volumes then it could be interpreted as evidence for the predicted <sup>11</sup> vector condensation.

## 5 Summary

We have observed enhanced screening and string breaking in the critical region for chiral symmetry. We have shown that chiral condensate and screening properties are correlated both at finite temperature and finite density. These observations suggest that the (pseudo)critical line for chiral condensate and confinement run close to each other in the phase diagram of two color QCD. Moreover we noticed that, at comparable values of chiral condensate, string breaking is slightly more pronounced at finite density, and low temperature, than at zero density and finite temperature. This supports the view that recombination with real quarks in a dense system favors deconfinement <sup>8</sup>.

We have noted and observed exact degeneracies in the vector sector of the spectrum. We have observed chiral symmetry restorations for meson and diquarks at finite temperature. We have observed a peculiar behaviour in the meson vector sector at high density, noticeably different from that at high temperature: spectral concentration of the B particle seems dominating over the  $\rho$ , while at high temperature the opposite holds true. We have observed possible signals for vector condensation in the diquark sector.

These results should be framed in a broader perspective of ongoing studies of the phase diagram of two color QCD at nonzero chemical potential, either by us and other groups.

One final remarks concerns the possibility to use two color QCD as a testbed for methods for simulating QCD at nonzero density. Some experiments with the Glasgow reweighting have already been performed <sup>12</sup>, while test of the analytic continuation from imaginary chemical potential <sup>13</sup> are in progress <sup>14</sup>.

## Acknowledgments

This work has been partially supported by MIUR. M.P. is supported by the European Union Human Potential Program under contract HPRN-CT-2000-00145, Hadrons/Lattice QCD.

## References

1. E. Dagotto, F. Karsch and A. Moreo, Phys. Lett. **169B** (1986) 421; E.Dagotto, A.Moreo and U.Wolff, Phys. Lett. **186B** (1987) 395.
2. S.J. Hands, J. B. Kogut, M.-P. Lombardo, S.E. Morrison, Nucl.Phys. **B558** (1999) 327.
3. J.B. Kogut, M. A. Stephanov, D. Toublan, J.J.M. Verbaarschot , Nucl.Phys.B 582 (2000) 477; K. Splittorff, D. Toublan, J.J.M. Verbaarschot, hep-ph/0204076; K. Splittorff, J. B. Kogut, D. Toublan, D.K. Sinclair, Phys.Lett.B514 (2001) 77 ;K. Splittorff, D. Toublan, J.J.M. Verbaarschot, Nucl.Phys.B620 (2002) 290; J.T. Lenaghan, F. Sannino, K. Splittorff, Phys.Rev. D65 (2002) 054002; J.B. Kogut, D.K. Sinclair, S.J. Hands, S.E. Morrison; Phys.Rev.D64 (2001) 094505; E. Bittner, M.-P. Lombardo, H. Markum, R. Pullirsch, Nucl.Phys.Proc.Suppl.94 (2001) 445; R. Aloisio, V. Azcoiti, G. Di Carlo, A. Galante, A.F. Grillo , Phys.Lett.B 493 (2002) 189; S. Muroya, A. Nakamura, C. Nonaka, nucl-th/0111082; Y. Liu, O. Miyamura, A. Nakamura, T. Takaishi in Non-perturbative methods and lattice QCD p. 132; M-P Lombardo, hep-lat/9907025.
4. J.B. Kogut, D. Toublan and D.K. Sinclair, hep-lat/0205019
5. M.-P. Lombardo, Proceedings of *Understanding Deconfinement in QCD*, World Scientific, p.24
6. B. Alles, M. D'Elia, M.-P. Lombardo, M. Pepe, Nucl.Phys.Proc.Suppl.94 (2001) 441
7. B. Allés, M. D'Elia, M.-P. Lombardo and M. Pepe, to appear.
8. J. Engels, O. Kaczmarek, F. Karsch, E. Laermann, Nucl. Phys. **B558** (1999) 307.
9. F. Gliozzi and P. Provero, Nucl. Phys. **B558** (1999) 357.
10. M.-P. Lombardo, J.B. Kogut, D.K. Sinclair, Phys.Rev. D54 (1996) 2303.
11. F. Sannino and W. Schaefer , Phys.Lett.B527 (2002) 142; this volume
12. P.R. Crompton Nucl.Phys.B626 (2002) 228
13. M. D'Elia and M.-P. Lombardo, this volume and hep-lat/0205022.
14. A. Papa e P. Giudice, in progress, private communications.

# STUDY OF CONFINEMENT USING THE SCHRÖDINGER FUNCTIONAL

PAOLO CEA

*INFN and Dept. of Physics, Univ. of Bari, via Amendola 173, 70126 Bari, Italy*  
*E-mail: Paolo.Cea@ba.infn.it*

LEONARDO COSMAI

*INFN - Sezione di Bari, via Amendola 173, 70126 Bari, Italy*  
*E-mail: Leonardo.Cosmai@ba.infn.it*

We use a gauge-invariant effective action defined in terms of the lattice Schrödinger functional to investigate vacuum dynamics and confinement in pure lattice gauge theories. After a brief introduction to the method, we report some numerical results.

## 1 Introduction

To study the vacuum structure of the lattice gauge theories we introduced <sup>1,2,3</sup> a gauge invariant effective action, defined by using the lattice Schrödinger functional.

The Schrödinger functional can be expressed as a functional integral <sup>4,5</sup>

$$\mathcal{Z}[\mathbf{A}^{(f)}, \mathbf{A}^{(i)}] = \int \mathcal{D}\mathbf{A}_\mu e^{-\int_0^T dx_4 \int d^3\vec{x} \mathcal{L}_{YM}(x)}, \quad (1)$$

with the constraints  $\mathbf{A}(x_0 = 0) = \mathbf{A}^{(i)}$ ,  $\mathbf{A}(x_0 = T) = \mathbf{A}^{(f)}$ , where  $\mathbf{A}(\vec{x})$  are static classical gauge fields. The Schrödinger functional Eq. (1) is invariant under arbitrary static gauge transformations of  $\mathbf{A}(\vec{x})$ 's fields. The lattice implementation of the Schrödinger functional is discussed in Ref. <sup>6</sup>.

Our lattice effective action for the static background field  $\mathbf{A}^{\text{ext}}(\vec{x}) = \mathbf{A}_a^{\text{ext}}(\vec{x})\lambda_a/2$  ( $\lambda_a/2$  generators of the SU(N) algebra) is defined as

$$\Gamma[\mathbf{A}^{\text{ext}}] = -\frac{1}{T} \ln \left\{ \frac{\mathcal{Z}[U_\mu^{\text{ext}}]}{\mathcal{Z}[0]} \right\}, \quad \mathcal{Z}[U_\mu^{\text{ext}}] = \int_{U_k(x)|_{x_4=0}=U_k^{\text{ext}}(x)} \mathcal{D}\mathbf{U} e^{-S_W}. \quad (2)$$

$\mathcal{Z}[U_\mu^{\text{ext}}]$  is the lattice Schrödinger functional (invariant, by definition, for lattice gauge transformations of the external links),  $U_\mu^{\text{ext}}(x)$  is the lattice version of the external continuum gauge field  $\mathbf{A}^{\text{ext}}(x)$ , and  $S_W$  is the standard Wilson action.  $\mathcal{Z}[0]$  is the lattice Schrödinger functional with  $\mathbf{A}^{\text{ext}} = 0$  ( $U_\mu^{\text{ext}} = \mathbf{1}$ ).

Our definition of lattice effective action can be extended to gauge systems

at finite temperature as

$$\mathcal{Z}_T [\mathbf{A}^{\text{ext}}] = \int_{U_k(\beta_T, \vec{x}) = U_k(0, \vec{x}) = U_k^{\text{ext}}(\vec{x})} \mathcal{D}U e^{-S_W}, \quad \beta_t = L_4 = \frac{1}{aT}. \quad (3)$$

The integrations are over the dynamical links with periodic boundary conditions in the time direction. If we send the physical temperature to zero the thermal functional Eq. (3) reduces to the zero-temperature Schrödinger functional.

## 2 Abelian Monopoles and Vortices

Monopole or vortex condensation can be detected by means of a disorder parameter  $\mu$  defined in terms of the lattice Schrödinger functional  $\mathcal{Z}[\mathbf{A}^{\text{ext}}]$  introduced in the previous Section. At zero-temperature

$$\mu = e^{-E_{\text{b.f.}} L_4} = \frac{\mathcal{Z}[\mathbf{A}^{\text{ext}}]}{\mathcal{Z}[0]}, \quad (4)$$

$\mathbf{A}^{\text{ext}}$  is the monopole or vortex static background field. According to the physical interpretation of the effective action Eq. (2)  $E_{\text{b.f.}}$  is the energy to create a monopole or a vortex in the quantum vacuum. If there is condensation, then  $E_{\text{b.f.}} = 0$  and  $\mu = 1$ .

At finite temperature the disorder parameter is defined in terms of the thermal partition function Eq. (3) in presence of the given static background field

$$\mu = e^{-F_{\text{b.f.}}/T_{\text{phys}}} = \frac{\mathcal{Z}_T [\mathbf{A}^{\text{ext}}]}{\mathcal{Z}_T [0]}, \quad (5)$$

$F_{\text{b.f.}}$  is now the free energy to create a monopole or a vortex (if there is condensation  $F_{\text{b.f.}} = 0$  and  $\mu = 1$ ).

Our disorder parameter  $\mu$  is invariant for time-independent gauge transformations of the external background fields. This implies that we have not to fix the gauge before performing the Abelian projection. Indeed, after choosing the Abelian direction, needed to define the Abelian monopole or vortex fields through the Abelian projection, due to gauge invariance of the Schrödinger functional for transformations of background field, our results do not depend on the selected Abelian direction, which, actually, can be varied by a gauge transformation.

## 2.1 *U(1) monopoles and vortices*

In the U(1) l.g.t. we considered a Dirac magnetic monopole background field. In the continuum

$$e\vec{b}(\vec{x}) = \frac{n_{\text{mon}}}{2} \frac{\vec{x} \times \vec{n}}{|\vec{x}|(|\vec{x}| - \vec{x} \cdot \vec{n})}, \quad (6)$$

$\vec{n}$  is the direction of the Dirac string,  $e$  is the electric charge and, according to the Dirac quantization condition,  $n_{\text{mon}}$  is an integer (magnetic charge  $= n_{\text{mon}}/2e$ ). The lattice implementation of the continuum field Eq. (6) is straightforward. As well we can consider a vortex background field:

$$A_{1,2}^{\text{ext}} = \mp \frac{n_{\text{vort}}}{e} \frac{x_{2,1}}{(x_1)^2 + (x_2)^2}, \quad A_3^{\text{ext}} = 0. \quad (7)$$

We can evaluate, by lattice numerical simulation, the energy to create a Dirac monopole or a vortex. It is easier to first evaluate the derivative  $E'_{\text{mon}} = \partial E_{\text{mon}} / \partial \beta$  ( $\beta = 1/g$ ,  $g$  is the gauge coupling constant):

$$E'_{\text{mon,vort}} = V [ < U_{\mu\nu} >_{n_{\text{mon,vort}}=0} - < U_{\mu\nu} >_{n_{\text{mon,vort}} \neq 0} ], \quad (8)$$

$V$  is the lattice spatial volume.  $E_{\text{mon,vort}}$  is then computed by means of a numerical integration in  $\beta$ . Our numerical results<sup>3</sup> show that Dirac monopoles condense in the confined phase (i.e. for  $\beta \lesssim 1.01$ ) of U(1) lattice gauge theory. While in the case of vortices we do not find a signal of condensation.

Thus, we may conclude that in U(1) lattice theory the strong coupling confined phase is intimately related to magnetic monopole condensation<sup>7</sup>.

## 2.2 *SU(2) Abelian monopoles and Abelian vortices*

It is well known that SU(2) lattice gauge theory at finite temperature undergoes a transition between confined and deconfined phase. We studied if Abelian monopoles or Abelian vortices condense in the confined phase of SU(2). To this purpose we considered in turn an Abelian monopole and an Abelian vortex background field. We found<sup>3</sup> that both Abelian monopoles and Abelian vortices condense in the confined phase of SU(2).

## 2.3 *SU(3) Abelian monopoles and Abelian vortices*

For SU(3) gauge theory the maximal Abelian group is U(1)  $\times$  U(1), therefore we may introduce two independent types of Abelian monopoles or Abelian vortices associated respectively to the  $\lambda_3$  and the  $\lambda_8$  diagonal generator (one can also consider<sup>3</sup> linear combinations of  $\lambda_3$  and  $\lambda_8$ ).

Let us focus on the  $\lambda_8$  Abelian monopole ( $T_8$  monopole):

$$U_{1,2}^{\text{ext}}(\vec{x}) = \begin{bmatrix} e^{i\theta_{1,2}^{\text{mon}}(\vec{x})} & 0 & 0 \\ 0 & e^{i\theta_{1,2}^{\text{mon}}(\vec{x})} & 0 \\ 0 & 0 & e^{-2i\theta_{1,2}^{\text{mon}}(\vec{x})} \end{bmatrix}, \quad U_3^{\text{ext}}(\vec{x}) = \mathbf{1}, \quad (9)$$

with

$$\theta_{1,2}^{\text{mon}}(\vec{x}) = \frac{1}{\sqrt{3}} \left[ \mp \frac{n_{\text{mon}}}{4} \frac{(x_{2,1} - X_{2,1})}{|\vec{x}_{\text{mon}}|} \frac{1}{|\vec{x}_{\text{mon}}| - (x_3 - X_3)} \right]. \quad (10)$$

Analogously, we can define the  $T_3$  Abelian vortex.

Fig. 1 shows that both  $T_8$  Abelian monopoles and Abelian vortices condense in the confined phase of SU(3) l.g.t. at finite temperature (simulations have been performed on  $32^3 \times 4$  lattice using the APE100 crate in Bari).

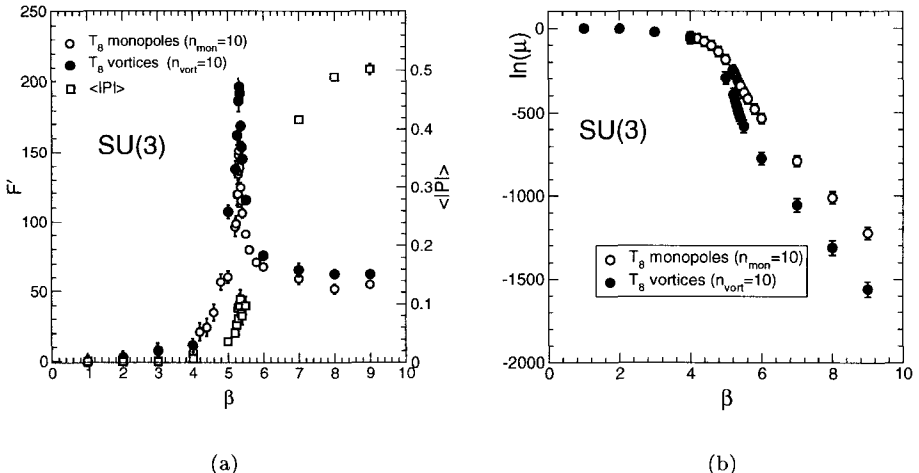


Figure 1. (a) The derivative of the free energy versus  $\beta$  for monopoles (open circles) and vortices (full circles). The absolute value of the Polyakov loop is also displayed (open squares). (b) The logarithm of the disorder parameter, Eq. (5), versus  $\beta$  for  $T_8$  monopoles (open circles) and  $T_8$  vortices (full circles).

## 2.4 $SU(3)$ Center Vortices

In the case of center vortices the thermal partition function  $\mathcal{Z}_T[\mathcal{P}_{\mu\nu}]$  is defined<sup>8,9</sup> by multiplying by the center element  $\exp(i2\pi/3)$  the set  $\mathcal{P}_{\mu\nu}$  of plaquettes  $\mathcal{P}_{\mu\nu}(x_1, x_2, x_3, x_4)$  with  $(\mu, \nu) = (4, 2)$ ,  $x_4 = x_4^*$ ,  $x_2 = \frac{L_s}{2}$  and  $L_s^{\min} \leq x_{1,3} \leq L_s^{\max}$ , with  $L_s$  the lattice spatial linear size. By numerical integration of  $F'_{\text{vort}}$  we can compute  $F_{\text{vort}}$  and the disorder parameter  $\mu$  (see

Eq. (5)). Our numerical results (see Fig. 2) suggest that in the confined phase  $F_{\text{vort}} = 0$  (in the thermodynamic limit) and center vortices condense.

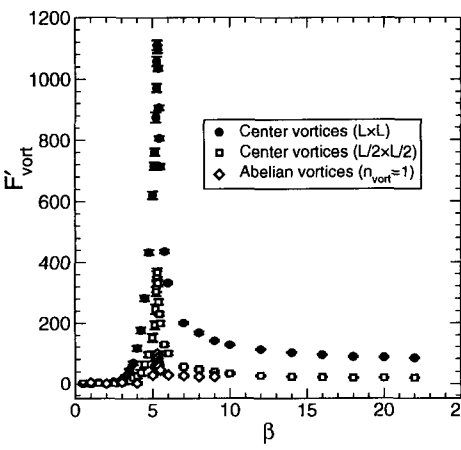


Figure 2.  $F'_{\text{vort}}$  for center vortices and Abelian vortices (vortex charge  $n_{\text{vort}} = 1$ ).

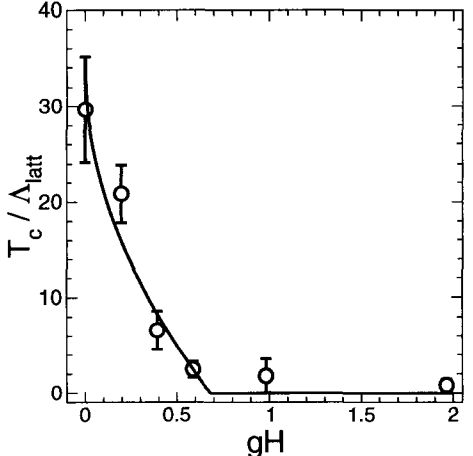


Figure 3.  $T_c / \Lambda_{\text{latt}}$  versus the applied external field strength  $gH$ .

### 3 Constant Abelian Chromomagnetic Field

We want to study the SU(3) gauge system at finite temperature in presence of an external constant Abelian magnetic field

$$\vec{A}_a^{\text{ext}}(\vec{x}) = \vec{A}^{\text{ext}}(\vec{x})\delta_{a,3}, \quad \vec{A}_k^{\text{ext}}(\vec{x}) = \delta_{k,2}x_1 H. \quad (11)$$

Spatial links belonging to a given time slice are fixed to

$$U_1^{\text{ext}}(\vec{x}) = U_3^{\text{ext}}(\vec{x}) = \mathbf{1}, \quad U_2^{\text{ext}}(\vec{x}) = \begin{bmatrix} e^{i\frac{gHx_1}{2}} & 0 & 0 \\ 0 & e^{-i\frac{gHx_1}{2}} & 0 \\ 0 & 0 & 1 \end{bmatrix}, \quad (12)$$

that corresponds to the continuum gauge field in Eq. (11). The magnetic field  $H$  turns out to be quantized (due to periodic boundary conditions):  $a^2 gH/2 = (2\pi)/L_1 n_{\text{ext}}$  ( $n_{\text{ext}}$  integer).

Since the gauge potential in Eq. (11) gives rise to a constant field strength we can consider the density  $f[\vec{A}^{\text{ext}}]$  of the free energy functional  $F[\vec{A}^{\text{ext}}]$

$$f[\vec{A}^{\text{ext}}] = \frac{1}{V} F[\vec{A}^{\text{ext}}] = -\frac{1}{VL_t} \ln \frac{\mathcal{Z}_T[\vec{A}^{\text{ext}}]}{\mathcal{Z}_T[0]}, \quad V = L_s^3. \quad (13)$$

As is well known, the pure gauge system undergoes the deconfinement phase transition by increasing the temperature. The deconfinement temperature in  $\Lambda_{\text{latt}}$  units is

$$\frac{T_c}{\Lambda_{\text{latt}}} = \frac{1}{L_t} \frac{1}{f_{SU(3)}(\beta^*(L_t))}, \quad (14)$$

where  $f_{SU(3)}(\beta)$  is the two-loop asymptotic scaling function and  $\beta^*(L_t)$  is the pseudocritical coupling  $\beta^*(L_t)$  at a given temporal size  $L_t$ , and can be determined by fitting the peak of  $f'[\vec{A}^{\text{ext}}] = \partial f[\vec{A}^{\text{ext}}]/\partial\beta$  for the given  $L_t$ .

Following <sup>10</sup> we can perform a linear extrapolation to the continuum of our data for  $T_c/\Lambda_{\text{latt}}$ . We vary the strength of the applied external Abelian chromomagnetic background field in order to analyze a possible dependence of  $T_c$  on  $gH$ . We perform numerical simulations on  $64^3 \times L_t$  lattices with  $n_{\text{ext}} = 1, 2, 3, 5, 10$ . Our numerical results show that the critical temperature decreases by increasing the external Abelian chromomagnetic field. For dimensional reasons one expects that  $T_c^2 \sim gH$ . Indeed we get a satisfying fit to our data with

$$\frac{T_c(gH)}{\Lambda_{\text{latt}}} = t + \alpha\sqrt{gH}. \quad (15)$$

From Fig. 3 one can see that there exists a critical field  $H_c$  such that the deconfinement temperature  $T_c = 0$  for  $H > H_c$ .

## References

1. P. Cea, L. Cosmai and A. D. Polosa, *Phys. Lett. B* **392**, 177 (1997).
2. P. Cea and L. Cosmai, *Phys. Rev. D* **60**, 094506 (1999).
3. P. Cea and L. Cosmai, *JHEP* **0111**, 064 (2001).
4. D. J. Gross, R. D. Pisarski and L. G. Yaffe, *Rev. Mod. Phys.* **53**, 43 (1981).
5. G. C. Rossi and M. Testa, *Nucl. Phys. B* **163**, 109 (1980).
6. M. Luscher, R. Narayanan, P. Weisz and U. Wolff, *Nucl. Phys. B* **384**, 168 (1992).
7. E. H. Fradkin and L. Susskind, *Phys. Rev. D* **17**, 2637 (1978).
8. T. G. Kovacs and E. T. Tomboulis, *PRL* **85**, 704 (2000).
9. L. Del Debbio, A. Di Giacomo and B. Lucini, *Nucl. Phys. B* **594**, 287 (2001).
10. J. Fingberg, U. Heller and F. Karsch, *Nucl. Phys. B* **392**, 493 (1993).

# IMAGINARY CHEMICAL POTENTIAL IN QCD AT FINITE TEMPERATURE

MASSIMO D'ELIA

*Dipartimento di Fisica dell'Università di Genova and INFN, I-16146, Genova,  
Italy  
E-mail: delia@ge.infn.it*

MARIA-PAOLA LOMBARDO

*Istituto Nazionale di Fisica Nucleare, Sezione di Padova, I-35131, Padova, Italy  
E-mail: lombardo@pd.infn.it*

After presenting a brief review of how simulations of QCD with imaginary chemical potential can be used to extract physical results, we analyse the phase structure of QCD with four flavours of dynamical fermions in the finite temperature - imaginary chemical potential plane, and discuss perspectives for realistic calculations.

## 1 Introduction

The zero density QCD partition function,  $Z(V, T) = \text{Tr} \left( e^{-\frac{H_{\text{QCD}}}{T}} \right)$ , with  $H_{\text{QCD}}$  the QCD Hamiltonian, can be discretized on an euclidean lattice with finite temporal extent  $\tau = 1/T$

$$Z = \int (\mathcal{D}U \mathcal{D}\psi \mathcal{D}\bar{\psi}) e^{-\beta S_G[U]} e^{-S_F[U, \psi, \bar{\psi}]} = \int (\mathcal{D}U) e^{-\beta S_G[U]} \det M[U] \quad (1)$$

where  $U$  are the gauge link variables and  $\psi$  and  $\bar{\psi}$  the fermionic variables,  $S_G$  is the pure gauge action,  $S_F$  is the fermionic action which can be expressed as a quadratic form in the fermionic fields in terms of the fermionic matrix  $M[U]$ ,  $S_F = \bar{\psi} M[U] \psi$ .

To describe QCD at finite density the grand canonical partition function,  $Z(V, T, \mu) = \text{Tr} \left( e^{-\frac{H_{\text{QCD}} - \mu N}{T}} \right)$ , where  $N = \int d^3x \psi^\dagger \psi$  is the quark number operator, can be used. The correct way to introduce a finite chemical potential  $\mu$  on the lattice <sup>1</sup> is to modify the temporal links appearing in the integrand in Eq. (1) as follows:

$$\begin{aligned} U_t &\rightarrow e^{a\mu} U_t && \text{(forward temporal link)} \\ U_t^\dagger &\rightarrow e^{-a\mu} U_t^\dagger && \text{(backward temporal link)}, \end{aligned} \quad (2)$$

where  $a$  is the lattice spacing. Whilst  $S_G$  is left invariant by this transformation,  $\det M[U]$  is not and gets a complex phase which makes importance sampling, and therefore standard lattice MonteCarlo simulations, unfeasible.

The situation is different when the chemical potential is purely imaginary. This is implemented on the lattice as described in Eq. (2), but in this case  $U_t \rightarrow e^{ia\mu_I} U_t$ ,  $U_t^\dagger \rightarrow e^{-ia\mu_I} U_t^\dagger$ . This is like adding a constant  $U(1)$  background field to the original theory;  $\det M[U]$  is again real and positive and simulations are as easy as at  $\mu = 0$ .

The question then arises how simulations at imaginary chemical potential may be of any help to get physical interesting information.

One possibility is analytic continuation<sup>2</sup>.  $Z(V, T, \mu)$  is expected to be an analytical even function of  $\mu$  away from phase transitions. For small enough  $\mu$  one can write:

$$\log Z(\mu) = a_0 + a_2\mu^2 + a_4\mu^4 + O(\mu^6) \quad (3)$$

$$\log Z(\mu_I) = a_0 - a_2\mu_I^2 + a_4\mu_I^4 + O(\mu_I^6). \quad (4)$$

Simulations at small  $\mu_I$  will thus allow a determination of the expansion coefficients for the free energy and, analogously, for other physical quantities, which can be cross-checked with those obtained by standard reweighting techniques<sup>3,4</sup>. This method is expected to be useful in the high temperature regime, where the first coefficients should be sensibly different from zero; moreover the region of interest for present experiments (RHIC, LHC) is that of high temperatures and small chemical potential, with  $\mu/T \sim 0.1$ . This method has been already investigated in the strong coupling regime<sup>2</sup>, in the dimensionally reduced 3-d QCD theory<sup>5</sup>, and in full QCD with two flavours<sup>6</sup>. The Taylor expansion coefficients can also be measured as derivatives with respect to  $\mu$  at  $\mu = 0$ <sup>7,8</sup>.

$Z(V, T, i\mu_I)$  can also be used to reconstruct the canonical partition function  $Z(V, T, n)$  at fixed quark number  $n$ <sup>9</sup>, *i.e.* at fixed density:

$$Z(V, T, n) = \text{Tr} \left( (e^{-\frac{H_{\text{QCD}}}{T}} \delta(N - n)) \right) = \frac{1}{2\pi} \text{Tr} \left( e^{-\frac{H_{\text{QCD}}}{T}} \int_0^{2\pi} d\theta e^{i\theta(N-n)} \right) \\ = \frac{1}{2\pi} \int_0^{2\pi} d\theta e^{-i\theta n} Z(V, T, i\theta T). \quad (5)$$

As  $n$  grows, the factor  $e^{-i\theta n}$  oscillates more and more rapidly and the error in the numerical integration grows exponentially with  $n$ : this makes the application of the method difficult especially at low temperatures where  $Z(V, T, i\mu_I)$  depends very weakly on  $\mu_I$ . The method has been applied in the 2-d Hubbard model<sup>10</sup>, where  $Z(V, T, n)$  has been reconstructed up to  $n = 6$ .

The phase structure of QCD in the  $T - i\mu_I$  plane is also interesting by its own. Writing for brief  $Z(\theta) \equiv Z(V, T, i\theta T) = \text{Tr} \left( e^{i\theta N} e^{-\frac{H_{\text{QCD}}}{T}} \right)$ ,  $Z(\theta)$  is clearly periodic in  $\theta$  with period  $2\pi$  and a period  $2\pi/3$  is expected in the

confined phase, where only physical states with  $N$  multiple of 3 are present. However it has been shown<sup>9</sup> that  $Z(\theta)$  has always period  $2\pi/3$  for any physical temperature. Moreover the suggestion has been made<sup>9</sup>, based on a calculation in the weak coupling approximation, that discontinuities in the first derivatives of the free energy at  $\theta = 2\pi/3(k + 1/2)$  should appear in the high temperature phase. This suggests a very interesting scenario for the phase diagram of QCD in the  $T - i\mu_I$  plane which needs confirmation by lattice calculations.

We have recently started a program of simulations of QCD at finite imaginary chemical potential, with both the aim of determining the phase diagram of QCD in the entire  $T - i\mu_I$  plane, and exploring by analytic continuation the high T – small real chemical potential region.

We have studied QCD with four degenerate staggered flavours of bare mass  $a \cdot m = 0.05$  on a  $16^4 \times 4$  lattice, where the phase transition is expected at a critical coupling  $\beta_c \simeq 5.04$ <sup>11</sup> (the two flavour case has been studied as well<sup>6</sup>). The algorithm used is the standard HMC  $\Phi$  algorithm. We will present here only a subset of our results and analysis. A complete presentation will appear soon<sup>12</sup>.

## 2 Results

In order to understand the phase structure of the theory, it is very useful to look at the phase of the trace of the Polyakov loop,  $P(\vec{x})$ . Let us parametrize  $P(\vec{x}) \equiv |P(\vec{x})|e^{i\phi}$ , and let  $\langle\phi\rangle$  be the average value of the phase. In the pure gauge theory the average Polyakov loop is non zero only in the deconfined phase, where the center symmetry is spontaneously broken and  $\langle\phi\rangle = 2k\pi/3$ ,  $k = -1, 0, 1$ , *i.e.* the Polyakov loop effective potential is flat in the confined phase and develops three degenerate minima above the critical temperature. In presence of dynamical fermions  $P(\vec{x})$  enters explicitly the fermionic determinant and  $Z_3$  is broken: the effect of the determinant is therefore like that of an external magnetic field which aligns the Polyakov loop along  $\langle\phi\rangle = 0$ . In the high temperature phase the  $Z_3$  degeneracy is lifted:  $\langle\phi\rangle = 0$  is the true vacuum and  $\langle\phi\rangle = \pm 2\pi/3$  are now metastable minima.

When  $\mu_I \neq 0$ , what enters the fermionic determinant is  $P(\vec{x})e^{i\theta}$ ,  $\theta \equiv \mu_I/T$ , instead of  $P(\vec{x})$ . Therefore the determinant now tends to align  $\langle\phi\rangle + \theta$  along zero: its effect is like that of an external magnetic field pointing in the  $\theta$  direction. Hence one expects  $\langle\phi\rangle = -\theta$  at low temperatures; at high temperatures the external magnetic field will still lift the  $Z_3$  degeneracy, but now which is the true vacuum will depend on the value of  $\theta$ . In particular one expects that for  $(k - 1/2) < \frac{3}{2\pi}\theta < (k + 1/2)$  the true vacuum is the one with  $\langle\phi\rangle = 2k\pi/3$  and that  $\theta = 2(k + 1/2)\pi/3$  corresponds to first order phase

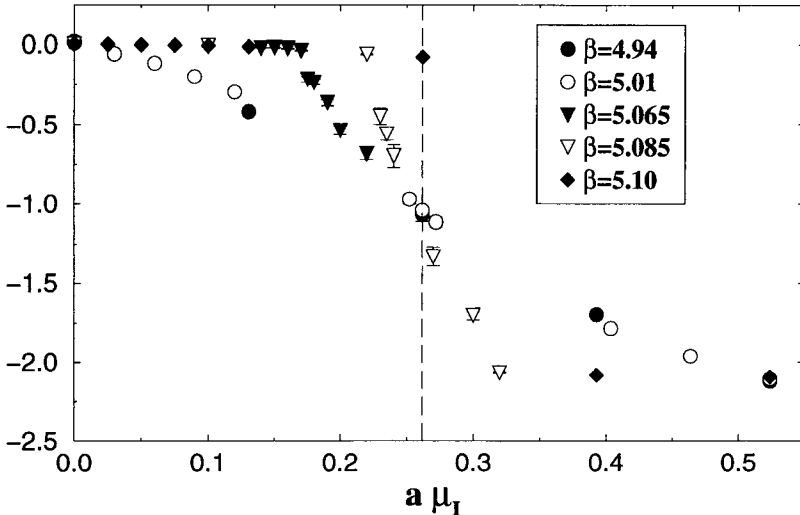


Figure 1. Average value of the Polyakov loop phase as a function of the imaginary chemical potential for different values of  $\beta$ . The vertical dashed line corresponds to  $\theta = \mu_I/T = \pi/3$ .

transitions from one  $Z_3$  sector to the other: this is indeed the prediction of Roberge and Weiss.

In Fig. 1 we report our results for  $\langle \phi \rangle$  versus the imaginary chemical potential for different values of  $\beta$ . Since  $T = 1/(N_t a)$  and  $N_t = 4$  in our case, we have  $\theta = 4a\mu_I$ . For  $\beta = 4.94$  and  $5.01$ , which are below the critical  $\beta$  at  $\mu_I = 0$ ,  $\beta_c(\mu_I = 0) \equiv \beta_c \simeq 5.04$ , one has  $\langle \phi \rangle \simeq -\theta = -4a\mu_I$ , *i.e.*  $\langle \phi \rangle$  is driven continuously by the fermionic determinant. For  $\beta = 5.10$ , which is well above  $\beta_c$  we see that  $\langle \phi \rangle \simeq 0$ , almost independently of  $\mu_I$ , as long as  $\theta < \pi/3$ , while for  $\theta > \pi/3$  there is a sudden change to  $\langle \phi \rangle \simeq -\pi/3$ : we are clearly crossing the Roberge-Weiss phase transition from one  $Z_3$  sector to the other. At intermediate values,  $\beta = 5.065$  and  $5.085$ ,  $\langle \phi \rangle \simeq 0$  until a critical value of  $a\mu_I$ , where it starts moving almost linearly with  $\mu_I$  crossing continuously the  $Z_3$  boundary: in this case there is no Roberge-Weiss phase transition, but there is anyway a critical value of  $\mu_I$  after which  $\langle \phi \rangle$  is no more constrained to be  $\simeq 0$  and can be driven again by  $\theta$ : as we will soon clarify, this critical value of  $\mu_I$  corresponds to the crossing of the chiral critical line, *i.e.* the continuation in the  $T-\mu_I$  plane of the chiral phase transition.

We display our results for the chiral condensate in Fig. 2. We expect a periodicity with period  $2\pi/3$  in terms of  $\theta$ . Moreover  $\langle \bar{\psi} \psi \rangle$ , like the partition function, is an even function of  $\mu_I$ : this, combined with the periodicity, leads to symmetry around all points  $\theta = n\pi/3$ , with  $n$  an integer number, for  $\langle \bar{\psi} \psi \rangle$

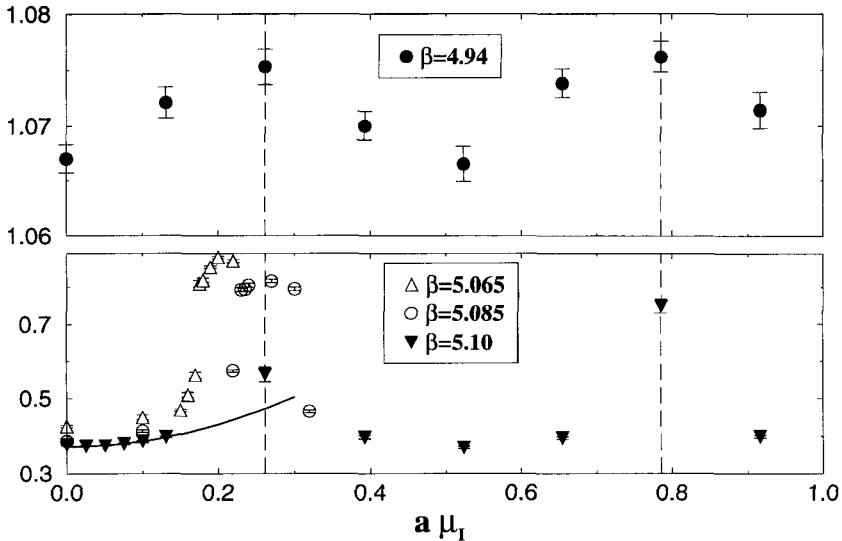


Figure 2. Average value of the chiral condensate as a function of the imaginary chemical potential for different values of  $\beta$ . The vertical dashed lines correspond to  $\theta = \mu_I/T = (2k+1)\pi/3$ . The continuous line in the lower picture is the result of a quadratic fit at small values of  $a\mu_I$  obtained at  $\beta = 5.10$ .

as well as for the partition function itself. For  $\beta < \beta_c$ ,  $\langle \bar{\psi}\psi \rangle$  has a continuous dependence on  $a\mu_I$  with the expected periodicity and symmetries. For  $\beta > \beta_c$  the correct periodicity and symmetries are still observed but the dependence is less trivial. At  $\beta = 5.065$  there is a critical value  $a\mu_I \simeq 0.17$  for which the theory has a transition to a spontaneously broken chiral symmetry phase: we are clearly going through the chiral critical line. The same happens for  $\beta = 5.085$  at  $a\mu_I \simeq 0.22$ : in this case we have proceeded further, observing also the transition back to a chirally restored phase at  $a\mu_I \simeq 0.30$ , which is, correctly, the symmetric point with respect to  $\theta = \pi/3^a$ . At  $\beta = 5.10$  we never cross, when moving in  $\mu_I$ , the chiral critical line, but only the Roberge-Weiss critical lines <sup>b</sup>.

We have also performed runs at fixed  $\mu_I$  and variable  $\beta$  to look for other locations of the chiral line in the  $T-\mu_I$  plane, a detailed summary of all results will be presented elsewhere <sup>12</sup>. We present, in Fig. 3, a sketch of the phase dia-

<sup>a</sup>We notice a discrepancy in the results obtained at the same  $\beta$  by multireweighting techniques <sup>4</sup>, where the same symmetry cannot be observed.

<sup>b</sup>Error bars for the determinations at  $\beta = 5.10$  and on the critical lines ( $\theta = \pi/3$  and  $\theta = \pi$ ) are probably underestimated.

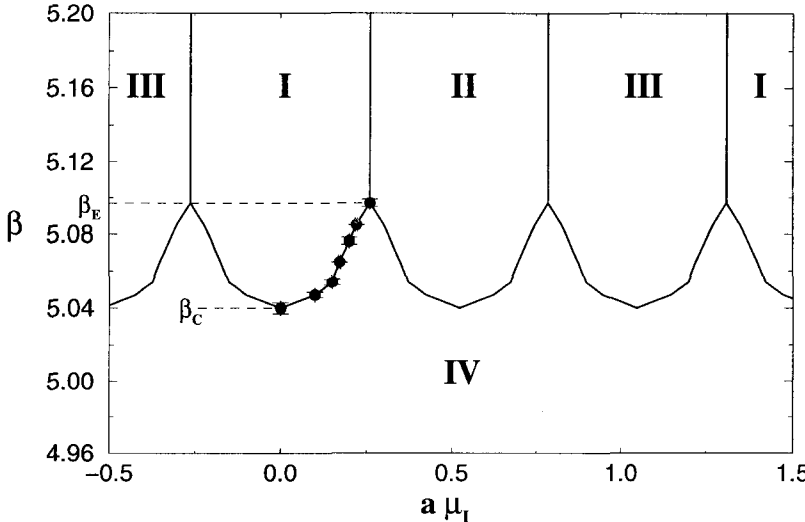


Figure 3. Sketch of the phase diagram in the  $\mu_I - \beta$  plane. The filled circles represent direct determinations of the chiral critical line location from our simulations. The rest of the chiral line has been obtained by interpolation and by exploiting the symmetries of the partition function.

gram in the  $\beta - \mu_I$  plane, as emerges from our data and by exploiting the above mentioned symmetries. We can distinguish a region where chiral symmetry is spontaneously broken (indicated as IV in the figure) and three regions (I, II and III), which correspond to different  $Z_3$  sectors and repeat periodically, where chiral symmetry is restored. The chiral critical line separates region IV from other regions, while the Roberge-Weiss critical lines separate regions I, II and III among themselves. In QCD with 4 staggered flavours,  $am = 0.05$  and  $\mu_I = 0$ , the phase transition is expected to be first order<sup>11</sup>: assuming it continues to be first order also at  $\mu_I \neq 0$ , we expect all the regions to be separated by first order critical lines.

It is interesting to illustrate the determination of the endpoint of the Roberge-Weiss critical line,  $\beta_E = 5.097(2)$ . We have performed a simulation at exactly  $\theta = \pi/3$ : starting thermalization at an high value of  $\beta$  from a zero field configuration we always stay on the border of region I, since on the  $16^3 \times 4$  lattice that we have used it is practically impossible to flip into region II through the critical line. As we decrease  $\beta$ , always staying on the border of region I, we will meet the chiral critical line at  $\beta = \beta_E$ . Various quantities can obviously be considered to signal this transition, but it is interesting to notice that in this case the baryon density can be taken as an exact order parameter. Indeed the baryon density,  $\langle b \rangle = \frac{T}{V} \frac{\partial}{\partial \mu} \ln Z$ , is an odd function of  $\mu$ , being

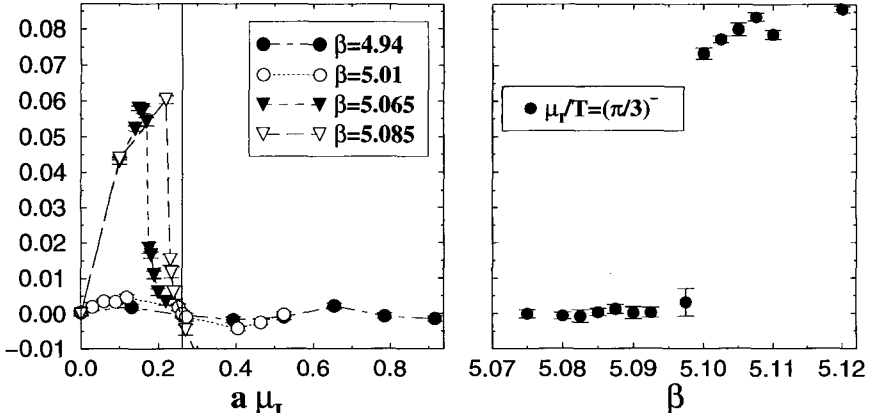


Figure 4. Imaginary part of the barion density as a function of  $\mu_I$  for different values of  $\beta$  (left-hand side), and as a function of  $\beta$  at  $\theta = \mu_I/T = \frac{\pi}{3}$  (right-hand side).

$Z$  an even function. Therefore, for an imaginary chemical potential,  $\langle b \rangle$  is also purely imaginary and an odd function of  $\mu_I$ . This, combined with the periodicity in  $\mu_I$ , leads to the expectation that  $\langle b \rangle(\theta = \frac{\pi^-}{3}) = -\langle b \rangle(\theta = \frac{\pi^+}{3})$ . The last relation clearly implies that  $\langle b \rangle = 0$  at  $\theta = \pi/3$ , unless  $\langle b \rangle$  is not continuous on that point. Thus a non-zero value of  $\langle b \rangle = 0$  at  $\theta = \frac{\pi^-}{3}$  implies the presence of the Roberge-Weiss critical line. On the right hand side of Fig. 4 the imaginary part of  $\langle b \rangle$  at  $\theta = \frac{\pi^-}{3}$  is plotted as a function of  $\beta$ : one can clearly see a transition from a zero to a non-zero expectation value, which permits the determination of  $\beta_E$ . We have verified that the transition through  $\beta_E$  is also visible in the chiral condensate: this implies that the Roberge-Weiss critical line ends on the chiral critical line. On the left hand side of Fig. 4 we present instead the imaginary part of  $\langle b \rangle$  as a function of  $\mu_I$  for different values of  $\beta < \beta_E$ : in this case  $\langle b \rangle$  is always zero and continuous at  $\theta = \frac{\pi}{3}$ , but it is interesting to note how it starts developing the discontinuity as  $\beta \rightarrow \beta_E$ .

In order to translate results for  $\beta_c(\mu_I)$  into results for the physical critical temperature,  $T_c(\mu_I)$ , we need the lattice spacing,  $a = a(\beta)$ , in physical units. For instance using the values  $a(5.04) = 0.30(2)$  fm and  $a(5.097) = 0.272(10)$  fm<sup>13</sup> we obtain  $T_c = 164(10)$  MeV and  $T_E = 181(7)$  MeV.

Finally we notice that for high temperatures and away from the critical lines, physical quantities show a clear non-zero dependence on the imaginary chemical potential, which is encouraging in starting the program of fitting the first terms of their Taylor expansion in  $\mu_I$  and performing the analytic continuation to real chemical potential. As an example we have reported, in Fig. 2, the result of a quadratic fit in  $\mu_I$  for the chiral condensate at  $\beta = 5.10$ .

### 3 Summary and discussion

We have clarified the phase structure in the imaginary chemical potential – temperature plane for full QCD with four staggered flavours. In particular we have confirmed the existence of the Roberge Weiss critical lines, located their endpoints and assessed their interplay with the chiral critical lines.

We have checked that data at high temperature and small imaginary chemical potential can be safely fitted by a polynomial, when away from phase transition lines, making the analytic continuation to real  $\mu$  feasible.

The physical interesting region of high temperature and small chemical potential can now be studied by essentially three different techniques: 1) Direct calculations of derivatives; 2) Reweighting; 3) Analytic continuation from imaginary  $\mu$ . Each method has its own merits and limitations, and cross checks among the three approaches should produce reliable results.

### Acknowledgments

This work has been partially supported by MIUR. We thank the computer center of ENEA for providing us with time on their QUADRICS machines.

### References

1. J.B. Kogut *et al.*, *Nucl. Phys. B* **225**, 93 (1983); P. Hasenfratz and F. Karsch, *Phys. Lett. B* **125**, 308 (1983).
2. M.P Lombardo, *Nucl. Phys. B*(Proc. Suppl.) **83**, 375 (2000).
3. I.M. Barbour *et al.*, *Nucl. Phys. B*(Proc. Suppl.) **60A**, 220 (1998).
4. Z. Fodor and S.D. Katz, arXiv:hep-lat/0104001
5. A. Hart, M. Laine and O. Philipsen, *Nucl. Phys. B* **586**, 443 (2000); *Phys. Lett. B* **505**, 141 (2001).
6. Ph. de Forcrand and O. Philipsen, arXiv:hep-lat/0205016; O. Philipsen, arXiv:hep-lat/0110051.
7. S. Gottlieb *et al.*, *Phys. Rev. D* **38**, 2888 (1988); R.V. Gavai and S. Gupta, arXiv:hep-lat/0202006.
8. C.R. Allton *et al.*, arXiv:hep-lat/0204010; S. Choe *et al.*, *Phys. Rev. D* **65**, 054501 (2002).
9. A. Roberge and N. Weiss, *Nucl. Phys. B* **275**, 734 (1986).
10. M. G. Alford, A. Kapustin, F. Wilczek, *Phys. Rev. D* **59**, 054502 (1999).
11. F.R. Brown *et al.*, *Phys. Lett. B* **251**, 181 (1990).
12. M. D'Elia, M.P. Lombardo, in preparation.
13. B. Alles, M. D'Elia, A. Di Giacomo, *Phys. Lett. B* **483**, 139 (2000).

# EFFECTIVE DESCRIPTION OF THE LOFF PHASE OF QCD

M.MANNARELLI

*Dipartimento di Fisica, Università di Bari, I-70124 Bari, Italia*

*I.N.F.N., Sezione di Bari, I-70124 Bari, Italia*

*E-mail: massimo.mannarelli@ba.infn.it*

We present an effective field theory for the crystalline color superconductivity phase of QCD. It is known that at high density and at low temperature QCD exhibits a transition to a color superconducting phase characterized by energy gaps in the fermion spectra. Under specific circumstances the gap parameter has a crystalline pattern, breaking translational and rotational invariance. The corresponding phase is the crystalline color superconductive phase (or *LOFF* phase). We compute the parameters of the low energy effective lagrangian describing the motion of the free phonon in the high density medium and derive the phonon dispersion law.

## 1 Introduction

In this talk We will discuss the recently proposed crystalline color superconducting phase of QCD<sup>1,2</sup>. This state is the QCD analogus to a state studied in QED by Larkin and Ovchinnikov<sup>3</sup> and Fulde and Ferrell<sup>4</sup>. Therefore it has been named after them *LOFF* state.

It is known that at very high density and at low temperature quark matter exhibits color superconductivity<sup>5</sup>. Color superconductivity is a phenomenon analogous to the *BCS* superconductivity of QED. According to the *BCS* theory, whenever there is an arbitrary small attractive interaction between electrons, the Fermi sea becomes unstable with respect to the formation of bound pairs of electrons. Indeed the creation of a Cooper pair costs no free energy, because each electron is on its own Fermi surface. On the other hand there is an energy gain due to the attraction of electrons. We call  $\Delta$  the binding energy of each pair with respect to the Fermi level. It is possible to show that the most energetically favored arrangement of electrons is made of two electrons with opposite momenta and spins. That is the condensate has spin zero and momentum zero. This is a normal superconductor. Now let us see what is a *LOFF* superconductor.

## 2 *LOFF* phase in QED

Let us consider a system made of a ferromagnetic alloy containing paramagnetic impurities. In first approximation the action of the impurities on the electrons may be viewed as a constant self-consistent exchange field. Due to

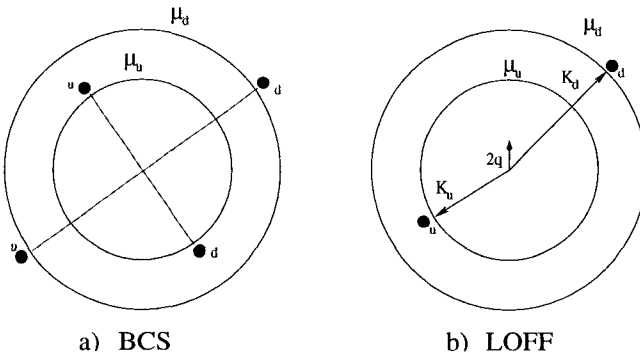


Figure 1. Fermi surfaces of down (d) and up (u) electrons (quarks). Black dots are electrons (quarks). The *BCS* pair, in a), gains energy  $\Delta$  but has  $p_F^u = p_F^d$  and therefore pays free energy price. Indeed one of the two electrons (quarks) of the pair has to stay far from its own Fermi surface. The *LOFF* pair, in b), gains energy  $\Delta_{LOFF} \ll \Delta$  but does not pay any free energy price, because each electron (quark) is on its own Fermi surface. For more details on figure b) see the text below.

this field the Fermi surfaces of up and down electrons (with respect to the direction of polarization of the medium) split, see figure (1). The half-separation of the Fermi surfaces will be<sup>3</sup>

$$I = NSa , \quad (1)$$

where  $N$  is the concentration of impurities,  $S$  is their spin and  $a$  is the integral of the exchange potential. To determine the energetically favored state we have to compare the *BCS* free energy with the free energy of the unpaired state. One has<sup>3</sup>:

$$F_{BCS} - F_{free} \propto I^2 - \Delta^2/2 . \quad (2)$$

Therefore for  $I > \Delta/\sqrt{2}$  the *BCS* state is no more energetically favorite. For  $I = \Delta/\sqrt{2}$  one expects that a first order phase transition takes place from the *BCS* to the normal state. Or at least this is what one should naively expect. Instead it has been shown<sup>3,4</sup> that for

$$\frac{\Delta}{\sqrt{2}} < I < .75\Delta , \quad (3)$$

it is energetically favorite a superconducting phase characterized by a condensate of spin zero but with non zero total momentum. We call  $\Delta_{LOFF} \equiv \Delta_{LOFF}(I)$  the electron binding energy when the distance between the Fermi surfaces is  $2I$ . Increasing the half-distance between the Fermi spheres, from

$\frac{\Delta}{\sqrt{2}}$  to  $.75\Delta$ , the *LOFF* gap decreases to zero. Therefore, for  $I \simeq .75\Delta$ , a second order phase transition from the *LOFF* phase to the normal phase takes place. In the *LOFF* phase pairs are made of fermions which remain close to their own Fermi surfaces as shown in figure (1). Therefore the creation of a pair costs no free energy. The pair has total momentum  $2\vec{q}$ , given by the formula

$$\vec{K}_u + \vec{K}_d = 2\vec{q}, \quad (4)$$

where  $\vec{K}_u$  and  $\vec{K}_d$  are the momenta of up and down electrons. The magnitude of  $q$  is determined by minimizing the free energy of the *LOFF* state. The direction of  $\vec{q}$  is chosen spontaneously by the condensate. We observe that not all electrons can condense in *LOFF* pairs. Only the electrons of a restricted region of the phase space can pair because of equation (4). Therefore  $\Delta_{LOFF} \ll \Delta_{BCS}$  because of the reduced phase space available for coupling. Moreover  $\Delta_{LOFF}$  turns out to be a periodic function of the coordinates and we have a crystalline structure described by  $\Delta_{LOFF}(\vec{r})$ .

### 3 *LOFF* phase in QCD

Let us consider quark matter at asymptotic density and at low temperature. In the previous section we have learnt that the *LOFF* phase may arise when fermions have different chemical potentials, and the potential difference lies inside a certain window<sup>1,6,7,8,9,10</sup>. Crystalline color superconductivity is also expected to occur in case of different quark masses<sup>11</sup>. In what follows we shall consider matter made of massless quarks and electrons, in weak equilibrium and electrically neutral. If we impose weak equilibrium we have  $\mu_u = \bar{\mu} - \frac{2}{3}\mu_e$  and  $\mu_{d,s} = \bar{\mu} + \frac{1}{3}\mu_e$  where  $\mu_{u,d,s,e}$  are quarks and electrons chemical potential. Requiring electrical neutrality we get:

$$\frac{2}{3}N_u - \frac{1}{3}N_d - \frac{1}{3}N_s - N_e = 0, \quad (5)$$

where  $N_{u,d,s,e}$  are the concentrations of quarks and electrons. When  $m_s = 0$  we get  $N_u = N_d = N_s$ ,  $N_e = 0$  and we expect matter to be in the color-flavor locked phase (CFL)<sup>5</sup>. For  $m_s \sim \bar{\mu}$  we have  $\mu_u = \bar{\mu} - \delta\mu$ ,  $\mu_d = \bar{\mu} + \delta\mu$ , and there are just two active flavors.

### 4 Velocity dependent effective lagrangian

In this Section we give a brief review of the effective lagrangian approach for the *LOFF* phase<sup>7</sup>, based on velocity-dependent fields. We perform a Fourier

transformation of the fermion field

$$\psi(x) = \int \frac{d^4 p}{(2\pi)^4} e^{-ip \cdot x} \psi(p) , \quad (6)$$

and we decompose the fermion momentum as

$$p_i^\mu = \mu_i v_i^\mu + \ell_i^\mu , \quad (7)$$

where  $i = 1, 2$  is a flavor index,  $v_i^\mu = (0, \vec{v}_i)$  and  $\vec{v}_i$  the Fermi velocity (for massless fermions  $|\vec{v}| = 1$ ); finally  $\ell_i^\mu$  is a residual momentum. By the decomposition (7) only the positive energy component  $\psi_+$  of the fermion field survives in the lagrangian in the  $\mu \rightarrow \infty$  limit while the negative energy component  $\psi_-$  can be integrated out. These effective fields are velocity dependent and are related to the original fields by

$$\psi(x) = \sum_{\vec{v}} e^{-i\mu v \cdot x} [\psi_+(x) + \psi_-(x)] , \quad (8)$$

where

$$\psi_\pm(x) = \frac{1 \pm \vec{\alpha} \cdot \vec{v}}{2} \int \frac{d\vec{\ell}}{(2\pi)^3} \int_{-\infty}^{+\infty} \frac{d\ell_0}{2\pi} e^{-i\ell \cdot x} \psi_{\vec{v}}(\ell) . \quad (9)$$

Here  $\sum_{\vec{v}}$  means an average over the Fermi velocities and

$$\psi_\pm(x) \equiv \psi_{\pm, \vec{v}}(x) \quad (10)$$

are velocity-dependent fields.

Now we write the condensates. We have a scalar condensate (sc)

$$< \epsilon_{ij} \epsilon_{\alpha\beta 3} \psi^{i\alpha}(\vec{x}) C \psi^{j\beta}(\vec{x}) > \propto \Delta_A e^{2i\vec{q} \cdot \vec{x}} \quad (11)$$

and a spin 1 vector condensate (vc)

$$< \sigma_{ij}^1 \epsilon_{\alpha\beta 3} \psi^{i\alpha}(\vec{x}) C \sigma^{03} \psi^{j\beta}(\vec{x}) > \propto \Delta_B e^{2i\vec{q} \cdot \vec{x}} . \quad (12)$$

The lagrangian for the (sc) is

$$\begin{aligned} \mathcal{L}_\Delta^{(s)} = & -\frac{\Delta_A}{2} \sum_{\vec{v}_1, \vec{v}_2} \exp\{i\vec{x} \cdot \vec{\alpha}(\vec{v}_1, \vec{v}_2, \vec{q})\} \epsilon_{ij} \epsilon^{\alpha\beta 3} \psi_{-\vec{v}_i\alpha}(x) C \psi_{-\vec{v}_j\beta}(x) \\ & -(L \rightarrow R) + \text{h.c.} , \end{aligned} \quad (13)$$

where  $\vec{\alpha}(\vec{v}_1, \vec{v}_2, \vec{q}) = 2\vec{q} - \mu_1 \vec{v}_1 - \mu_2 \vec{v}_2$ . We take  $\vec{q} = (0, 0, q)$ , therefore the components of  $\vec{\alpha}$  satisfy the equations

$$\begin{aligned} \alpha_x &= -\mu_1 \sin \alpha_1 \cos \phi_1 - \mu_2 \sin \alpha_2 \cos \phi_2 , \\ \alpha_y &= -\mu_1 \sin \alpha_1 \sin \phi_1 - \mu_2 \sin \alpha_2 \sin \phi_2 , \end{aligned}$$

$$\alpha_z = 2q - \mu_1 \cos \alpha_1 - \mu_2 \cos \alpha_2 . \quad (14)$$

In the limit  $\mu_1, \mu_2 \rightarrow \infty$  we get

$$\phi_2 = \phi_1 + \pi \quad (15)$$

$$\alpha_2 \equiv \theta_q = \arccos \frac{\delta\mu}{q} + \mathcal{O}\left(\frac{\delta\mu}{\mu}\right), \quad (16)$$

$$\alpha_1 = \alpha_2 + \pi + \mathcal{O}\left(\frac{\delta\mu}{\mu}\right) . \quad (17)$$

Therefore the velocities are almost opposite  $\vec{v}_1 \simeq -\vec{v}_2$ , and we have to deal with a no more symmetric sum over velocities<sup>2</sup>, because the angle  $\alpha_2$  is fixed.

## 5 Phonon quark interaction

The condensates (11) and (12) explicitly break rotations and translations. We have an induced lattice structure given by parallel planes perpendicular to  $\vec{n} = \vec{q}/|\vec{q}|$ :

$$\vec{n} \cdot \vec{x} = \frac{\pi k}{q} \quad (k = 0, \pm 1, \pm 2, \dots) . \quad (18)$$

Lattice planes are allowed to fluctuate in two ways. We describe these fluctuations by means of two fields  $\phi$  and  $R$ :

$$\vec{n} \cdot \vec{x} \rightarrow \vec{n} \cdot \vec{x} + \frac{\phi}{2qf} \equiv \frac{\Phi}{2q} , \quad (19)$$

$$\vec{n} \rightarrow \vec{R} . \quad (20)$$

But  $\phi$  and  $R$  are not independent, indeed it is possible to show<sup>2</sup> that

$$\vec{R} = \frac{\vec{\nabla} \Phi}{|\vec{\nabla} \Phi|} . \quad (21)$$

Therefore there is just one independent degree of freedom, i.e. the phonon.

## 6 Effective lagrangian

By a bosonization procedure<sup>2</sup> it is possible to get the effective action for the phonon and to calculate the polarization tensor. At the lowest order in the momentum  $\vec{p}$  of the phonon we have

$$\Pi(0) = \Pi(0)_{s.e.} + \Pi(0)_{tad} = 0 , \quad (22)$$

$$\Pi(p) = -\frac{\mu^2}{4\pi^2 f^2} \left[ p_0^2 - v_{\perp}^2 (p_x^2 + p_y^2) - v_{\parallel}^2 p_z^2 \right], \quad (23)$$

where

$$v_{\perp}^2 = \frac{1}{2} \sin^2 \theta_q + \mathcal{O} \left( \frac{\Delta^{(v)}}{q} \right)^2, \quad (24)$$

$$v_{\parallel}^2 = \cos^2 \theta_q, \quad (25)$$

are the velocities perpendicular and parallel to  $\vec{q}$ . From eq.(22) we see that the phonon is massless. From eq.(23) we have the dispersion law for the phonon:

$$E(\vec{p}) = \sqrt{v_{\perp}^2 (p_x^2 + p_y^2) + v_{\parallel}^2 p_z^2}. \quad (26)$$

In conclusion we can say that the dispersion law for the phonon is anisotropic in two ways. Indeed the velocity of propagation of the phonon in the plane perpendicular to  $\vec{q}$ , i.e.  $v_{\perp}$ , is not equal to  $v_{\parallel}$ , that is the velocity of propagation of the phonon along  $\vec{q}$ . Moreover  $p_z$  is a quasi-momentum.

## References

1. M. Alford, J. A. Bowers and K. Rajagopal, *Phys. Rev. D* **63**, 074016 (2001), hep-ph/0008208.
2. R. Casalbuoni, R. Gatto, M. Mannarelli and G. Nardulli, hep-ph/0201059.
3. A. I. Larkin and Yu. N. Ovchinnikov, *Zh. Eksp. Teor. Fiz.* **47**, 1136 (1964) (*Sov. Phys. JETP* **20**, 762 (1965)).
4. P. Fulde and R. A. Ferrell, *Phys. Rev* **135**, A550 (1964).
5. For a review see K. Rajagopal and F. Wilczek, in *Handbook of QCD*, ed. M. Shifman (World Scientific, 2001), hep-ph/0011333. For earliest papers on color superconductivity see B. Barrois, *Nucl. Phys. B* **129**, 390 (1977); S. Frautschi in *Proceedings of workshop on hadronic matter at extreme density*, (Erice 1978). See also: D. Bailin and A. Love, *Phys. Rept.* **107**, 325 (1984) and references therein.
6. J. A. Bowers, J. Kundu, K. Rajagopal and E. Shuster, *Phys. Rev. D* **64**, 014024 (2001), hep-ph/0101067.
7. R. Casalbuoni, R. Gatto, M. Mannarelli and G. Nardulli, *Phys. Lett. B* **511**, 218 (2001), hep-ph/0101326.
8. A. K. Leibovich, K. Rajagopal and E. Shuster, *Phys. Rev. D* **64**, 094005 (2001), hep-ph/0104073.
9. D. K. Hong, Y. J. Sohn, hep-ph/0107003.
10. D. K. Hong, hep-ph/0112028.
11. J. Kundu and K. Rajagopal, hep-ph/0112206.

# DECONFINEMENT TRANSITION AND HIGH TEMPERATURE PHASE IN LATTICE GAUGE THEORIES

ALESSANDRO PAPA

*Dipartimento di Fisica, Università della Calabria  
 & Istituto Nazionale di Fisica Nucleare, Gruppo Collegato di Cosenza  
 I-87036 Arcavacata di Rende, Cosenza, Italy  
 E-mail: papa@cs.infn.it*

This paper is organized in two parts. In the first one, I present a recent determination of the critical exponent  $\nu$  of the correlation length in 3D SU(3) and in 4D SU(2) pure gauge theories at finite temperature, by a new approach inspired by universality and based on finite size scaling. Moreover, I discuss possible implications of universality on the spectrum of screening masses in 4D SU(2) just above the critical temperature. In the second part, I propose two topics, well known in the literature, to be investigated by numerical simulations on the lattice, namely the Polyakov loop model by Pisarski for the high temperature phase of 4D SU(N) pure gauge theories and the Roberge-Weiss formulation of 4D SU(N) gauge theories with fermions and with *imaginary* chemical potential.

## 1 Introduction

This paper is concerned with SU(N) *lattice* gauge theories at finite temperature and is organized in two separate parts.

The first part is based on the concept of *universality* and on its consequences. Universality means that the critical behavior of a system near a phase transition is determined by the long-range fluctuations of the order parameter and depends essentially on symmetries rather than on microscopic interactions. An example of the predictive power of universality is presented in Section 2, where universality is applied to gauge theories undergoing a *second order* deconfinement transition at a critical temperature  $T_c$ . In particular, a new method is described for the determination of the critical exponent  $\nu$  of the correlation length in SU(N) gauge theories. Another issue of universality is discussed in Section 3, where the correspondence between the spectrum of *bound states* in the broken phase of 3D Ising model and the spectrum of *screening masses* in the deconfined phase of 4D SU(2) is investigated.

In the second part of this paper, two interesting scenarios will be illustrated of the high temperature phase of 4D SU(N) gauge theories and of the quark-gluon plasma. The first one, recently proposed by R. Pisarski, is the scenario of the quark-gluon plasma as a condensate of Polyakov loops (Section 4). The second one, proposed by Roberge and Weiss many years ago

but till now not so much investigated, is based on the formulation with an *imaginary* chemical potential of 4D SU(N) in presence of fermions. According to this scenario, the quark-gluon plasma would be the state of QCD matter in the high temperature phase only at short (order  $1/T$ ) distances, while long distance correlations would be still dominated by colorless degrees of freedom (Section 5). Both these scenarios can be studied in a straightforward way by numerical simulations on the lattice.

## 2 The critical index $\nu$ of the correlation length

### 2.1 The Svetitsky-Yaffe conjecture

Let us consider a  $(d + 1)$ -dimensional SU(N) pure gauge theory undergoing a *continuous* deconfinement transition at a critical temperature  $T_c$ . The order parameter of this transition is the Polyakov loop, defined as  $l(\vec{x}) \equiv \text{Tr} \prod_{n_4=1}^{N_t} U_4(\vec{x}, a\bar{n}_4)$ , where  $U_\mu(x)$  is the link variable at the site  $x \equiv (\vec{x}, t)$  in the  $\mu$  direction and  $a$  is the lattice size.<sup>1</sup> Under the transformation  $U_4(\vec{x}, a\bar{n}_4) \rightarrow z U_4(\vec{x}, a\bar{n}_4)$  with  $z$  belonging to the *center* of the gauge group, Z(N), and  $a\bar{n}_4$  any fixed time coordinate, the lattice action is left invariant. The Polyakov loop  $l(\vec{x})$  transforms instead in  $z l(\vec{x})$ . If the Z(N) symmetry were unbroken,  $l$  should always vanish; instead,  $l \neq 0$  above a critical temperature  $T_c$ .

It is always possible to construct an effective statistical model of the order parameter. This can be done starting from the partition function written in terms of the link variables and integrating out all degrees of freedom, except the order parameter. The resulting  $d$ -dimensional effective model  $S_{\text{eff}}$  is symmetric under Z(N), possesses only short-range interactions and its critical dynamics is dominated by long-range fluctuations in the order parameter.<sup>2</sup> Moreover,  $S_G$  and  $S_{\text{eff}}$  belong to the same universality class and therefore their critical properties (such as critical indices, finite-size scaling, correlation functions at criticality, etc.) are predicted to coincide.<sup>2</sup> In particular, 3D and 4D SU(2) belong to the universality class of 2D and 3D Z(2) (Ising) model, respectively, while 3D SU(3) belongs to the universality class of 2D Z(3) (3-state Potts) model. The validity of the Svetitsky-Yaffe conjecture has been confirmed in several Monte Carlo analyses.<sup>3</sup>

### 2.2 Finite-size behavior at criticality

A convenient way to determine critical indices is to study the finite-size behavior of suitable operators at criticality. Let us consider for instance the

determination of the critical index  $\nu$  of the correlation length  $\xi$ , defined as  $\xi \sim |t|^{-\nu}$ , where  $t \equiv (T - T_c)/T_c$ . In the  $d$ -dimensional statistical model, it can be done by the finite-size scaling (FSS) behavior of the (lattice) energy operator  $E$ :<sup>4</sup>

$$\langle E \rangle_L \sim \langle E \rangle_\infty + k L^{\frac{1}{\nu} - d}, \quad (1)$$

where  $L$  is the lattice size, taken to be large enough, and  $k$  is a non-universal constant. In order to apply the same method to the  $(d+1)$ -dimensional gauge theory, it is necessary to compute expectation values of operators having the same FSS behavior of the energy in the  $d$ -dimensional statistical model. This is the case of any gauge invariant operator  $\hat{O}$  that is invariant also under the global symmetry given by the center of the gauge group, such as any Wilson loop or any correlator of the form  $l(\vec{x})l^\dagger(\vec{y})$ , where  $\vec{x}$  and  $\vec{y}$  are different sites of the  $d$ -dimensional space. It is natural to expect that the operator product expansion (OPE) of any such operator at criticality has the same form as the one of  $E$ :

$$\hat{O} = c_I I + c_\epsilon \epsilon + \dots \quad (2)$$

Here  $I$  and  $\epsilon$  are, respectively, the identity and the (scaling) energy operator in the statistical model, and the dots represent contributions of operators with higher dimension. The above ansatz was introduced and tested in Ref.<sup>5</sup>, and used in Ref.<sup>6</sup>. In particular, Eq. (2) implies that the FSS behavior of the expectation value  $\langle \hat{O} \rangle$  will have the same form as Eq. (1), with  $E$  replaced by  $\langle \hat{O} \rangle$  and a different non-universal constant. The contributions of the irrelevant operators will be subleading for  $L \rightarrow \infty$ . The obvious advantage of this approach is that one can use operators, such as the plaquette, whose expectation value can be computed to high accuracy with relatively modest computational effort.

### 2.3 Numerical results

The method described in the previous subsection has been applied to the cases of 3D SU(3) and of 4D SU(2).<sup>7,8</sup> The lattice operators considered are (i) space-like (“magnetic”) plaquette, (ii) time-like (“electric”) plaquette, (iii) correlator  $l(\vec{x})l^\dagger(\vec{y})$ , with  $\vec{x}$  and  $\vec{y}$  neighbor sites in the spatial lattice.

For the case of 3D SU(3), we performed simulations on lattices  $L^2 \times N_t$ , with  $N_t=2$  and  $L$  ranging from 7 to 30 at the critical value of the lattice (inverse) coupling constant  $\beta$  for the chosen  $N_t$ . We fixed  $\beta$  at the critical value taken from Ref.<sup>9</sup>:  $\beta_c(N_t=2)=8.155$ . We collected 400K “measurements” of each operator for each value of  $L$  and performed a multibranched fit on

uncorrelated measurements with the scaling law (1), obtaining  $\nu = 0.827(22)$  with  $\chi^2/\text{d.o.f.}=0.84$ . This result is in excellent agreement with the *exact* value in the 2D Z(3) (3-state Potts) model,  $\nu = 5/6 = 0.833\cdots$ , as predicted by the Svetitsky-Yaffe conjecture. The standard Monte Carlo determination of  $\nu$  (based on the  $\chi^2$  analysis of the Polyakov loop susceptibility) gave  $\nu_{\text{MC}}=0.90(20)$ .<sup>9</sup>

For the case of 4D SU(2), we performed simulations on lattices  $L^3 \times 2$ , with  $L$  ranging from 5 to 26. Simulations were performed at  $\beta_c(N_t = 2) = 1.8735$ , taken from Ref.<sup>10</sup> and the collected “measurements” ranged from 50K (for the larger lattices) to 4.8M (for the smaller ones). We found  $\nu = 0.6298(28)$ , with  $\chi^2/\text{d.o.f.}=0.96$ . As predicted by the Svetitsky-Yaffe conjecture, this value is in excellent agreement with that of the 3D Z(2) (Ising) model, for which the most accurate determination so far, obtained by the high-temperature expansion method<sup>11</sup>, is  $\nu = 0.63012(16)$ . There is agreement also with the standard Monte Carlo determination ( $\chi^2$  analysis of the Polyakov loop susceptibility), giving  $\nu_{\text{MC}} = 0.630(9)$ .<sup>10</sup>

### 3 Spectrum of screening masses in 4D SU(2)

There are both numerical and analytical evidences<sup>12,13,14</sup> that in the broken symmetry phase of 3D Ising model and lattice 3D  $\Phi^4$  theory, both belonging to the same universality class, there is a bound state ( $J^P = 0^+$ , mass  $m^*$ ) with  $m^*/m \simeq 1.83$  for  $T \rightarrow T_c^-$ ,  $m(0^+)$  being the fundamental mass.

In the 3D Ising model, this appears, for instance, in the connected wall-wall correlation function:

$$\begin{aligned} G(z - z') &\equiv \left\langle \left[ \frac{1}{N_x N_y} \sum_{x,y} s(x, y, z) \right] \left[ \frac{1}{N_x N_y} \sum_{x,y} s(x, y, z') \right] \right\rangle_{\text{conn}} \\ &= Ae^{-m|z-z'|} + Be^{-m^*|z-z'|} + \dots, \end{aligned} \quad (3)$$

where  $s(\vec{x})$  is the spin at the site  $\vec{x}$ .<sup>a</sup>

Now, according to the Svetitsky-Yaffe conjecture, 4D SU(2) gauge theory belongs to the universality class of 3D Ising model, with the order parameter of the former (Polyakov loop) mapped into the order parameter of the latter (magnetization) and the broken symmetry phase of the former (high temperature phase) corresponding to the broken symmetry phase of the latter (low temperature phase). This arises the question if the  $0^+$  bound state(s) of

<sup>a</sup>It should be observed, however, that the most convenient way to determine  $m^*$  is the variational method<sup>13</sup> in its improved version.<sup>15</sup>

3D Ising (and of 3D lattice  $\Phi^4$ ) should have a counterpart in the high temperature phase of 4D SU(2) near criticality. This counterpart would appear in the connected wall-wall correlation of Polyakov loops, defined similarly to Eq. (3), where  $m, m^*$  represent now “screening masses” in the  $0^+$  channel. In particular, the expectation is that  $m^*/m \simeq 1.83$  as  $T \rightarrow T_c^+$ . This question is presently under investigation.<sup>16</sup> The argument can of course be generalized to bound states of the 3D Ising model for all  $J^P$  channels.

#### 4 Polyakov loop model in 4D SU(2) and SU(3)

Numerical simulations on the lattice of 4D SU(2) and SU(3) pure gauge theories (see, for instance, Ref. <sup>17</sup>) show that:

- the pressure  $p(T)$  vanishes below the critical temperature  $T_c$ ; this is because glueball masses are much larger than  $T_c$ , so that the free energy necessary to excite them is suppressed in Boltzmann fashion below  $T_c$ ;
- the pressure shows a sharp increase starting from  $T_c$ , thus reflecting the liberation of degrees of freedom associated with deconfinement, then it flattens already at  $T \sim 2T_c$  at around 80% of the ideal gas limit value,  $p_{\text{SB}} = n_\infty T^4$ ,  $n_\infty$  being  $\pi^2/90$  times the number of (bosonic) degrees of freedom;
- $p(T)/n_\infty$  as a function of  $T/T_c$  is almost universal (also in presence of quarks);
- screening masses (correlation lengths), obtained from 2-point functions of Polyakov loops, decrease (increase) as  $T$  tends to  $T_c$  from above; this is true also for 4D SU(3), where the deconfinement transition is first order; we have indeed that  $m/T \simeq 2.5$  at  $T = 2T_c$  and  $\simeq 0.25$  at  $T = T_c$ .<sup>18</sup>

These evidences suggest <sup>19</sup> that the pressure itself behaves as an order parameter of the transition, in a way quite independent on the number of colors, reflecting the same behavior of the true order parameter, i.e. the Polyakov loop. Moreover, although the vanishing of  $p(T)$  below  $T_c$  would require increasing typical masses as  $T_c$  is approached from above, screening masses determined from Polyakov loop correlation tend instead to decrease. All this lead R. Pisarski to propose a *mean field theory* description of the high temperature phase of SU(N) gauge theories.<sup>19,20</sup> The effective potential in its simplest version is:

$$V = \left[ -2b_2|l|^2 + b_3(l^3 + (l^*)^3) + (|l|^2)^2 \right] b_4 T^4 , \quad (4)$$

with  $b_3 \neq 0$  and small for  $SU(3)$ , in order to drive the transition to be (weakly) first order and  $b_3 = 0$  for  $SU(2)$ , where  $l$  is real and the transition is second order. Sticking for simplicity to the case of  $SU(2)$ ,  $\langle l \rangle \equiv l_0$  is given by the condition  $V(l_0) = V_{\min}$  and we have therefore  $l_0^2 = 0$  for  $T < T_c$  and  $l_0^2 = b_2$  for  $T > T_c$ . The dependence on the temperature of  $l_0$  in the high temperature phase can be adjusted therefore by  $b_2(T)$ . As for the pressure in the high temperature phase, we have  $p(T) = -V_{\min} = +b_2^2 b_4 T^4$ . Since  $l_0$ , and therefore  $b_2$ , approach 1 for  $T \rightarrow \infty$ ,  $b_4$  in this limit approaches  $n_\infty$ . It can be assumed, in the spirit of mean field, that  $b_4$  is constant for all  $T$  above  $T_c$ .<sup>20</sup> In this way, the strong variation of  $p(T)$  around  $T_c$  would be accounted by the variation of  $l_0(T)$ . This scenario of the quark-gluon plasma as “condensate of  $Z(N)$  spins”<sup>19</sup> looks attractive and can be tested by numerical simulations,<sup>21</sup> although its predictive power is questionable.

## 5 $Z(N)$ symmetry and imaginary chemical potential

In this Section, I review a not so recent work by Roberge and Weiss,<sup>22</sup> where many interesting consequences are drawn from the formulation of  $SU(N)$  gauge theories with fermions and *imaginary* chemical potential ( $\mu = i\nu$ ) (see also Ref.<sup>23</sup>). The starting point is the partition function  $Z(\theta)$  defined as

$$Z(\theta) = \text{Tr} \exp(-\beta \hat{H} + i\theta \hat{N}) , \quad \hat{N} = \int d^3x (\psi^\dagger \psi) , \quad \theta = \beta\nu . \quad (5)$$

Now, if the spectrum contains quarks (integer fermion number) then  $Z(\theta)$  is periodic with period  $2\pi$ . Otherwise, if the spectrum contains only color singlet states (eigenvalues of  $\hat{N}$  multiples of  $N$ ) then  $Z(\theta)$  is periodic with period  $2\pi/N$ . This would mean that the periodicity of  $Z(\theta)$  should change across  $T_c$ . However, it is possible to prove that, as long as  $T \neq 0$ ,  $Z(N)$  symmetry implies that  $Z(\theta)$  *must have* periodicity  $2\pi/N$ .<sup>22</sup> For  $T = 0$ , instead, the imaginary chemical potential can be removed by a phase redefinition of the fermionic fields. There are several interesting consequences of the  $2\pi/N$  periodicity:<sup>22</sup>

- all long-wavelength excitations should be *color singlets*; the theory could appear to be a quark-gluon plasma only at short distances (order  $1/T$ );
- *in pure gauge theories*,  $Z(N)$  symmetry implies  $\langle l \rangle$  always equal to zero, but the symmetry is broken at high temperature, leading to confinement; *in presence of fermions*,  $Z(N)$  symmetry implies that  $Z(\theta)$  has periodicity  $2\pi/N$ , so the confinement-deconfinement transition should manifest itself in the behavior of the theory as a function of  $\theta$ .

Roberge and Weiss<sup>22</sup> studied the free energy  $F(\theta)$  in SU(2) by perturbation theory, in the high temperature phase, finding that  $F(\theta)$  behaves *smoothly* as function of  $\theta$ , and by using the strongly-coupled Wilson lattice theory in leading hopping parameter expansion, in the low temperature phase, finding that  $F(\theta)$  is *discontinuous* at  $\theta = 2\pi(k + 1/2)/N$ ,  $k$  integer. A firmer confirmation of this result and of its consequences could come from lattice Monte Carlo simulations.<sup>23,24</sup>

Finally, I would like to stress that the formulation of a gauge theory with imaginary chemical potential has also a practical importance. First of all, in the physically relevant case of QCD, a *real* chemical potential leads to a complex determinant for the fermion matrix,<sup>25</sup> thus preventing the numerical simulation of the system on a lattice, except for small values of  $\mu$ , where “reweighting” can be applied on simulations performed at  $\mu=0$ . The formulation with imaginary chemical potential is instead free of the problem of complex determinant and can always be applied in numerical simulations. The price to pay here is the analytical continuation of the results to real chemical potential. Whenever this continuation can be performed in safe way, it is possible to cross-check the results of the reweighting method in the region of small  $\mu$  and to make accessible to lattice numerical simulations also other regions of the QCD phase diagram.<sup>25</sup> Second, by means of a Fourier transform in the parameter  $\theta$ , the grandcanonical partition function  $Z(\theta)$  is turned into the *true* canonical one  $Z_B$ , where  $B$  is the net number of fermions in the system. Indeed,

$$Z_B = \int_0^{2\pi} \frac{d\theta}{2\pi} e^{-iB\theta} Z(\theta) = \text{Tr} \int_0^{2\pi} \frac{d\theta}{2\pi} e^{-iB\theta} e^{-\beta\hat{H} + i\theta\hat{N}} = \text{Tr}[e^{-\beta\hat{H}} \delta(B - \hat{N})]. \quad (6)$$

Unfortunately, the oscillations of the phase term in the integrand of Eq. (6) make a numerical determination of  $Z_B$  reliable only for small values of  $B$ . As a consequence of the result by Roberge-Weiss that the long-wavelength excitations must be color singlets at any temperature  $T$ , the canonical partition function  $Z_B$  is always zero, except when  $B$  is multiple of  $N$ , which means that an infinite free energy is needed to create from the vacuum a single fermion at any temperature.

## Acknowledgments

I am grateful to M.P. Lombardo for many stimulating discussions. I thank also my collaborators (M. Barberio, R. Fiore, P. Giudice, P. Provero and C. Vena) for their contribution to this paper.

## References

1. G. Martinelli, these proceedings; R. Petronzio, these proceedings.
2. B. Svetitsky and L. G. Yaffe, *Nucl. Phys. B* **210**, 423 (1982).
3. J. Engels *et al.*, *Nucl. Phys. B* **332**, 737 (1990); J. Engels *et al.*, *Nucl. Phys. B* **387**, 501 (1992); M. Caselle and M. Hasenbusch, *Nucl. Phys. B* **470**, 435 (1996); K. Pinn and S. Vinti, *Nucl. Phys. B* (Proc. Suppl.) **63**, 457 (1998), *Phys. Rev. D* **57**, 3923 (1998); M. Teper, *Phys. Lett. B* **313**, 417 (1993).
4. M. Hasenbusch and K. Pinn, *J. Phys. A* **31**, 6157 (1998).
5. F. Gliozzi and P. Provero, *Phys. Rev. D* **56**, 1131 (1997).
6. R. Fiore *et al.*, *Phys. Rev. D* **58**, 114502 (1998), *Nucl. Phys. B* (Proc. Suppl.) **73**, 429 (1999).
7. R. Fiore *et al.*, *Phys. Rev. D* **63**, 117503 (2001), *Nucl. Phys. B* (Proc. Suppl.) **106**, 486 (2002).
8. A. Papa and C. Vena, hep-lat/0203007.
9. J. Engels *et al.*, *Nucl. Phys. B* (Proc. Suppl.) **53**, 420 (1997).
10. S. Fortunato *et al.*, *Nucl. Phys. B* (Proc. Suppl.) **94**, 398 (2001).
11. M. Campostrini *et al.*, cond-mat/0201180.
12. M. Caselle *et al.*, *Nucl. Phys. B* **556**, 575 (1999).
13. M. Caselle *et al.*, *Phys. Rev. D* **62**, 017901 (2000).
14. D. Lee *et al.*, *Phys. Lett. B* **502**, 329 (2001).
15. A.S. Kronfeld, *Nucl. Phys. B* (Proc. Suppl.) **17**, 313 (1990); M. Lüscher and U. Wolff, *Nucl. Phys. B* **339**, 222 (1990).
16. M. Barberio, R. Fiore, A. Papa and P. Provero, in progress.
17. F. Karsch, hep-lat/0106019.
18. O. Kaczmarek *et al.*, *Phys. Rev. D* **62**, 034021 (2000).
19. R.D. Pisarski, hep-ph/0101168.
20. A. Dumitru and R.D. Pisarski, *Nucl. Phys. B* (Proc. Suppl.) **106**, 483 (2002) and references therein.
21. M. Barberio, R. Fiore and A. Papa, in progress.
22. A. Roberge and N. Weiss, *Nucl. Phys. B* **275**, 734 (1986).
23. M. D'Elia, these proceedings.
24. P. Giudice and A. Papa, in progress.
25. M. P. Lombardo, these proceedings.

# VECTOR CONDENSATION AT LARGE CHEMICAL POTENTIAL

F. SANNINO AND W. SCHÄFER

*NORDITA, Blegdamsvej 17, DK-2100 Copenhagen Ø, Denmark*

*E-mail: francesco.sannino@nbi.dk, schaefer@nordita.dk*

We discuss the condensation of relativistic spin-one fields at high chemical potential. This phenomenon leads to the spontaneous breaking of rotational invariance, together with the breaking of internal symmetries.

## 1 Introduction

There has been much interest recently in the phase structure of Quantum Chromodynamics (QCD) and QCD-like theories. An overview has been given at this workshop<sup>1</sup>. Here the phase diagram not only depends on temperature and density, but also on the number of flavors  $N_f$ , and colors  $N_c$ . Most of our knowledge on the QCD phase diagram at finite temperature derives from lattice simulations<sup>2</sup>. Lattice studies of the high density, low temperature region are however seriously obstructed by a complex fermion determinant. No such difficulties exist for  $N_c = 2$ , and hence predictions for two-color QCD can be compared with numerical solutions from the lattice. Such a theory with  $N_f$  flavors has a global  $SU(2N_f)$  symmetry. There are color-singlet diquark states which play the role of baryons. Interestingly, it has been predicted<sup>3</sup> that at sufficiently high baryon chemical potential, spin-1 diquark states will condense. Indeed there appears to be preliminary evidence for this phenomenon from lattice calculations<sup>4</sup>. With this physical application in mind we shall study a vector field transforming in the adjoint representation of a global  $SU(2)$  group<sup>5</sup>. The chemical potential is chosen along one of the generator's direction (the “baryon charge” operator), and breaks the global symmetry explicitly to  $U(1) \times Z_2$ . Apparently condensation of a vector field singles out a direction in space, the rotational  $SO(3)$ -invariance is spontaneously broken to an  $SO(2)$  subgroup.

Introduction of a chemical potential explicitly breaks the Lorentz invariance, and in such a situation the relation between broken symmetries and Goldstone modes (gapless excitations) is of special interest. Here the particle-physics textbook folklore that every broken generator corresponds to a Goldstone boson does not apply. Instead, following Nielsen and Chadha, one should properly distinguish between two types of Goldstone modes, depending on whether in the long-wavelength limit their energy varies with an odd

(type I) or even (type II) power of momentum. The following inequality holds:

$$N_{bg} \leq N_I + 2 \cdot N_{II}, \quad (1)$$

between the numbers of broken generators  $N_{bg}$ , and type I/II Goldstone modes  $N_{I/II}$ <sup>6</sup>. In order to elucidate these aspects in case of the vector condensation, we proceed with constructing the simplest effective Lagrangian for a vector field.

## 2 A lagrangian model for vector condensation

We introduce a vector field  $A_\nu^a, a = 1, 2, 3$  of mass  $m$  transforming under the adjoint representation of a global  $SU(2)$  symmetry. The Lagrangian, endowed with a potential of fourth order in the field, reads:

$$\mathcal{L} = -\frac{1}{4}F_{\mu\nu}^a F^{a\mu\nu} + \frac{m^2}{2}A_\mu^a A^{a\mu} - \frac{\lambda}{4}(A_\mu^a A^{a\mu})^2 + \frac{\lambda'}{4}(A_\mu^a A^{a\nu})^2, \quad (2)$$

with  $F_{\mu\nu}^a = \partial_\mu A_\nu^a - \partial_\nu A_\mu^a$ , and metric convention  $\eta^{\mu\nu} = \text{diag}(+, -, -, -)$ . Here we confine ourselves to positive  $\lambda$  and  $\lambda'$ . Stability of the potential furthermore demands  $\lambda > \lambda'$ . The effect of a nonzero chemical potential associated to a given conserved charge - related to the generator  $B = T_3$  - can be readily included<sup>3</sup> by modifying the derivatives acting on the vector fields:

$$\partial_\nu A_\rho \rightarrow \partial_\nu A_\rho - i[B_\nu, A_\rho], \quad (3)$$

with  $B_\nu = \mu \delta_{\nu 0} B \equiv V_\nu B$  where  $V = (\mu, \vec{0})$ . The chemical potential thus resembles an external field in temporal direction. The kinetic term can then be cast in the form

$$\mathcal{L}_{kinetic} = \frac{1}{2}A_\rho^a K_{ab}^{\rho\nu} A_\nu^b \quad (4)$$

with

$$\begin{aligned} K_{ab}^{\rho\nu} = & \delta_{ab} [g^{\rho\nu} \partial^2 - \partial^\rho \partial^\nu] - 4i\gamma_{ab} \left[ g^{\rho\nu} V \cdot \partial - \frac{V^\rho \partial^\nu + V^\nu \partial^\rho}{2} \right] \\ & + 2\chi_{ab} [V \cdot V g^{\rho\nu} - V^\rho V^\nu], \end{aligned} \quad (5)$$

where

$$\gamma_{ab} = \text{Tr} [T^a [B, T^b]], \quad \chi_{ab} = \text{Tr} [[B, T^a] [B, T^b]]. \quad (6)$$

For  $B = T^3$  we have

$$\gamma_{ab} = -\frac{i}{2}\epsilon^{ab3}, \quad \chi_{11} = \chi_{22} = -\frac{1}{2}, \quad \chi_{33} = 0. \quad (7)$$

The chemical potential induces a “magnetic-type” mass term for the vectors at tree-level. The symmetries of the potential are more easily understood using the following Euclidean notation:

$$\varphi_M^a = (A_M^1, A_M^2), \quad \psi_M = A_M^3, \quad (8)$$

with  $A_M = (iA_0, \vec{A})$  and metric signature  $(+, +, +, +)$ . In these variables the potential reads:

$$V_{Vector} = \frac{m^2}{2} [|\vec{\varphi}_0|^2 + \psi_M^2] + \frac{m^2 - \mu^2}{2} |\vec{\varphi}_I|^2 + \frac{\lambda}{4} [|\vec{\varphi}_M|^2 + \psi_M^2]^2 - \frac{\lambda'}{4} [\vec{\varphi}_M \cdot \vec{\varphi}_N + \psi_M \psi_N]^2 \quad (9)$$

with  $I = X, Y, Z$  while  $M, N = 0, X, Y, Z$  and repeated indices are summed over. At zero chemical potential  $V_{Vector}$  is invariant under the  $SO(4)$  Lorentz transformations while only the  $SO(3)$  symmetry is manifest at non zero  $\mu$ . As noted above, the chemical potential explicitly breaks the global  $SU(2)$  symmetry to  $U(1) \times Z_2$ . Note that for the special parameter choice  $\lambda' = 0$ , the potential alone is invariant under an  $SO(6)$  rotation group.

It is apparent, that due to the presence of the term proportional to  $(m^2 - \mu^2)$ , we have to distinguish the cases  $\mu \leq m$  and  $\mu > m$ .

## 2.1 The Symmetric Phase: $0 < \mu \leq m$

Here the  $SO(4)$  Lorentz and  $SU(2)$  symmetries are explicitly broken to  $SO(3)$  and  $U(1)$  respectively by the chemical potential. All fields have a vanishing expectation value in the vacuum:  $\langle \vec{\varphi}_M \rangle = \langle \psi_M \rangle = 0$ . The curvatures of the potential on the vacuum (the masses) are:

$$M_{\varphi_0^a}^2 = M_{\psi_M}^2 = m^2, \quad M_{\varphi_I^a}^2 = m^2 - \mu^2. \quad (10)$$

We obtain the dispersion relations by diagonalizing the 12 by 12 matrix  $\mathcal{K}$  (5). This leads to 3 physical vectors (i.e. each of the following states has 3 components) with the dispersion relations:

$$E_{\varphi^\mp} = \pm \mu + \sqrt{\vec{p}^2 + m^2}, \quad E_\psi = \sqrt{\vec{p}^2 + m^2}. \quad (11)$$

We observe that for  $\mu \rightarrow m$  the 3 physical components associated with  $E_{\varphi^\mp}$  will become massless signaling an instability. Indeed, for higher values of the chemical potential larger than  $m$  a vector condensation sets in.

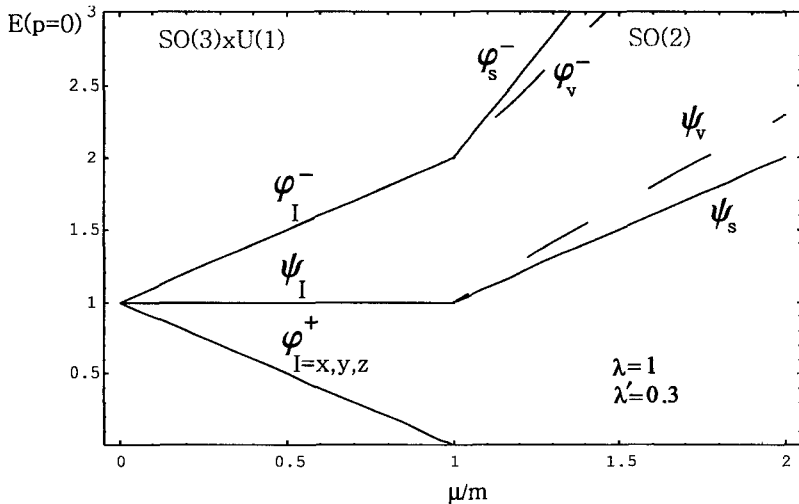


Figure 1. The mass gaps  $E(0)$  as a function of the chemical potential  $\mu$ .

## 2.2 The Spin-Flavor Broken Phase: $\mu > m$

In this phase at the global minimum of the potential we still have  $\langle \varphi_0^a \rangle = \langle \psi_M \rangle = 0$ . However there emerges a condensate:

$$\langle \varphi_X^1 \rangle = \sqrt{\frac{\mu^2 - m^2}{\lambda - \lambda'}} . \quad (12)$$

We have a manifold of equivalent vacua which are obtained rotating the chosen one under a  $Z_2 \times U(1) \times SO(3)$  transformation. The choice of the vacuum partially locks together the Lorentz group and the internal symmetry while leaving unbroken only the subgroup  $Z_2 \times SO(2)$ . Two generators associated to the Lorentz rotations are now spontaneously broken together with the  $U(1)$  generator.

To proceed with the calculation of the dispersion relation of the vector states in the broken phase we first have to evaluate the curvatures of the potential on the new vacuum. The explicit formulas can be found elsewhere<sup>5</sup>. We find in general three states with null curvature. An exception occurs for the choice  $\lambda' = 0$  in which case there are five zero curvature states. To explain this behavior we note that for  $\lambda' = 0$  the potential possesses an enhanced  $SO(6)$  global symmetry which breaks to  $SO(5)$  when the vector field condenses. The associated five states would correspond to the ordinary Goldstone modes in

the absence of an explicit Lorentz breaking. Now the symmetry breaking pattern of our theory is  $SO(3) \times U(1) \times Z_2 \rightarrow SO(2) \times Z_2$  and we find the three expected gapless excitations irrespective of the parameters of the potential.

In Fig.1 we show how the mass gaps evolve as a function of the chemical potential  $\mu$ . In the unbroken phase, for  $\mu \leq m$  all gaps are threefold degenerate and the splitting of the states of different baryon charge is clearly visible. For  $\mu > m$  the modes with nonvanishing gap split further. The dashed lines are twofold degenerate ( $SO(2)$ -vectors) while the solid lines correspond to  $SO(2)$  scalar states. There are three gapless modes, whose dispersion relations however show some subtleties.

### 2.3 Dispersion relations and Goldstone counting

The gapless states also fall into a doublet forming an  $SO(2)$  vector and an  $SO(2)$  singlet. Their dispersion relations at small momenta have the form

$$E_{\varphi_V^+}^2 = v_{\varphi_V^+}^2 \vec{p}^2 + \mathcal{O}(p^4), \quad E_{\varphi_S^+}^2 = v_{\varphi_S^+}^2 \vec{p}^2 + \mathcal{O}(p^4), \quad (13)$$

where we introduced the “superfluid velocities”  $v_{\varphi_V^+}, v_{\varphi_S^+}$ . One can easily show that these velocities can be expressed directly in terms of the curvatures in the directions orthogonal to the gapless modes as follows:

$$v_{\varphi_V^-}^2 = \frac{M_{\varphi_Y^2}^2}{M_{\varphi_Y^2}^2 + 4\mu^2}, \quad v_{\varphi_S^-}^2 = \frac{M_{\varphi_X^1}^2}{M_{\varphi_X^1}^2 + 4\mu^2}. \quad (14)$$

It now turns out, that always  $M_{\varphi_X^1}^2 \neq 0$ . Therefore the scalar state will always have a linear dispersion relation  $E \propto p$ . Not so the  $SO(2)$  vector states. In the case of enhanced potential symmetry  $SO(6)$ , the curvature  $M_{\varphi_Y^2}^2$  vanishes and with it the velocity  $v_{\varphi_V^-}^2$ . The dispersion relation hence becomes a quadratic one,  $E \propto p^2$ , the  $SO(2)$  state turns into a type II Goldstone boson. We emphasize, that were Lorentz invariance unbroken, the curvatures  $M_i^2$  would precisely be masses and there would be a Goldstone for each flat direction of the potential. Obviously the chemical potential prevents the emergence of extra Goldstone bosons in the case  $\lambda' = 0$ . Simply the full Lagrangian (kinetic plus potential terms) does not share the potential’s larger symmetry. Still, the additional flat directions of the potential have a physical effect: *they are responsible for turning some of the Goldstones into type II modes*. This appears to be a perfectly general phenomenon for the type of kinetic term that arises at finite chemical potential. Finally we count: for  $\lambda' \neq 0$  there are three broken generators and three type I Goldstones, hence  $N_{bg} = N_I$ , the standard situation. For  $\lambda' = 0$  we have still three broken generators, but on

the right hand side of the Nielsen–Chadha inequality (1) we count  $1 \times$  type I +  $2 \times 2$  type II = 5. This is larger than the number of broken generators, which appears to be a novel observation. We note that five is precisely the number of broken generators of the potential symmetry group, which would correspond to the breaking pattern  $SO(6) \rightarrow SO(5)$ .

We finally point out that the choice of coupling constants discussed here gives rise to the “polar” phase with a real order parameter. In principle, an interaction with negative  $\lambda'$  might give rise to “ferromagnetic” type phases characterized by a complex order parameter and a different symmetry breaking pattern<sup>7</sup>.

### 3 Where to find vector condensates – some examples

We already mentioned the condensation of vector fields in two–color QCD, which has been the main focus of our work. In three color QCD at high quark chemical potential the 2SC phase allows a spin-1 diquark condensate with albeit smaller gap than the spin-0 condensate. This case has been recently investigated<sup>8</sup>. We also note that spin-1 condensation is expected to give rise to a rich phenomenology of vortices<sup>7</sup>, which have been discussed in the context of atomic Bose–Einstein condensates.

In the color–flavor locked phase of color superconducting quark matter, the possibilities of condensation of vector states in presence of a nonvanishing isospin chemical potential are as yet unexplored.

### Acknowledgments

The work of F.S. is supported by the Marie–Curie Fellowship under contract MCFI–2001–00181. W.S. has been supported in part by DAAD and NORDITA.

### References

1. F. Sannino, these proceedings, and references therein.
2. S. Hands, *Nucl. Phys. Proc. Suppl.* **106**, 142 (2002) [arXiv:hep-lat/0109034].
3. J. T. Lenaghan, F. Sannino and K. Splittorff, *Phys. Rev. D* **65**, 054002 (2002) [arXiv:hep-ph/0107099].
4. M.P. Lombardo, a talk given at GISELDA meeting, Firenze, October 20001 and these proceedings.
5. F. Sannino and W. Schäfer, *Phys. Lett. B* **527**, 142 (2002).

6. H.B. Nielsen and S.Chadha, *Nucl. Phys. B* **105**, 445 (1976).
7. G. Volovik, *J. Low. Temp. Phys.* **121**, 357 (2000) [arXiv:cond-mat/0005431] and references therein; U. Leonhardt and G. E. Volovik, *JETP Lett.* **72**, 46 (2000) [arXiv:cond-mat/0003428].
8. R. D. Pisarski and D. H. Rischke, *Phys. Rev. D* **61**, 074017 (2000) [arXiv:nucl-th/9910056]; M. Buballa, J. Hošek and M. Oertel, arXiv:hep-ph/0204275.

# QUARK-GLUON PLASMA and HEAVY ION COLLISIONS

This book offers the unique possibility of tackling the problem of hadronic deconfinement from different perspectives. After general introductions to the physical issues, from both the theoretical and the experimental point of view, the book presents the most recent expertise on field theory approaches to the QCD phase diagram, many-body techniques and applications, the dynamics of phase transitions, and phenomenological analysis of relativistic heavy ion collisions.

One of the major goals of this book is to promote interchange among those fields of research, which have traditionally been cultivated by different communities of physicists. The contributions in the book help in obtaining deep comprehension of this new state of matter, a system of deconfined quarks and gluons. At the same time the book offers a few examples of how the seeds of the deconfined state are looked for in the phenomenological analysis of the observables measured in relativistic heavy ion collisions. The main topics are dealt with in a pedagogical style, suitable for beginners as well as experienced researchers.